Selective Deposition: Fabrication of Coherent Nano-Dimensioned Metal Oxide Films by Monolayer Polymer Brush Template Assisted Inclusion

Trinity College Dublin
Coláiste na Tríonóide, Baile Átha Cliath
The University of Dublin

A Thesis Presented to the Trinity College Dublin for the Degree of

Doctor of Philosophy

By

Pravind Kumar Yadav

Under the Supervision of Professor Michael Morris

School of Chemistry

Trinity College Dublin

February 2022

Declaration

I declare that this thesis has not been submitted as an exercise for a degree at this or any other university and it is entirely my own work.

I agree to deposit this thesis in the University's open access institutional repository or allow the library to do so on my behalf, subject to Irish Copyright Legislation and Trinity College Library conditions of use and acknowledgement.

I consent to the examiner retaining a copy of the thesis beyond the examining period, should they so wish (EU GDPR May 2018).

____

Pravind Kumar Yadav

Abstract:

Selective Deposition: Fabrication of Coherent Nano-Dimensioned Metal Oxide Films by Monolayer Polymer Brush Template Assisted Inclusion

Pravind Yadav

Shrinking feature sizes in electronic devices and demands of more processing power have generated new integration challenges. Advances in top-down lithography techniques successfully reduced the size of nano-electronic devices to sub 10 nm. Further size reduction poses major challenges, such as line edge roughness, material placement error, size irregularity, and most importantly high production cost. The photolithography technique most commonly employed requires multiple steps to achieve the desired patterns. These steps are; the selective removal of the resist material, the patterning of the active material, and the removal of excess resist material. Currently the fidelity needed is only achieved with very expensive fabrication tools. Multiple patterning processes (where larger features are trimmed by further photolithographic steps) increases production cost further. In contrast, a bottom-up area selective deposition (ASD) technique allows direct inclusion of the functional material on a targeted area to achieve the desired patterns while reducing the number of steps.

Several groups have reported ASD techniques coupled with atomic layer deposition (ALD) for the selective inclusion of active materials on the substrate. Substrate surface patterning using the self-assembled monolayer (SAM) techniques have also been investigated extensively for this purpose. The selective surface coating developed through the SAM approach provide the ability to selectively deposit or block the material of choice. However, the pinhole effect, generated by SAMs technique and the long processing times makes it industrially less favourable.

In this work, we have investigated the possibilities of using polymer brush monolayer coatings to realize homogeneous inorganic material infiltration and their subsequent processing to ultrathin metal oxide films. The applicability of the reactive polymer brushes such as poly (2-vinyl pyridine) (P2VP), poly (4-vinyl pyridine) (P4VP), and poly (methyl methacrylate) (PMMA) were examined. Uses of unreactive polystyrene (PS) brush to block materials growth was also investigated. First, the polymer brush grafting parameters on SiO_2 substrate were optimised. Solution concentration, molecular weight, end group density, grafting time and temperature were investigated in order to obtained homogeneous monolayer coverage. This is a critical step in avoiding non-uniform thickness and pinhole formation.

After defining the monolayer coverage of polymer brushes, we infiltrated a range of inorganic ions from a solvated liquid phase on to the developed polymer brush films. Formation of the films, from ethanolic solutions of aluminium nitrate, ruthenium chloride, and zirconium oxynitrate were investigated in detail. Subsequent oxidation using oxygen plasma or UV ozone treatment produced thin oxide films while eliminating organic polymer. Additionally, we developed an innovative vapour phase technique for the deposition of TiO_2 thin films with precise thickness control. Further, we demonstrated the thin film coating of high-k dielectric materials (HfO_2 and ZrO_2) on topographically patterned substrates using P4VP-OH as the templating layer. We established that the fabrication of a high coverage molecular system is essential in developing thin metal oxide films across the trenches. Finally, we established the selective deposition of dielectric (ZrO_2) material on a copper substrate by activating the metal surface using PMMA-SH brush.

Acknowledgements:

First, I would like to express my gratitude and deep regards to my supervisor Prof. Mick Morris for his patience and exemplary guidance throughout the course of my work. His feedback and insights have been invaluable and helped me to complete my work on time. Working with him was a great experience. His precious suggestions and discussions helped me to comprehend concepts on diverse topics.

Secondly, I want to thank Intel Corporation and SFI for their funding to carry out this research work. I am very thankful to Intel researchers Matt Shaw, Jennifer Mckenna, and Peter Gleeson for their suggestions during our monthly meetings and continual support. I wish to acknowledge Colm for his help as project manager. I am very thankful to my collaborators in DCU, Dr. Robert O'Connor, Dr. Miles M. Turner and their researchers Jim, Matthew and Caitlin for providing XPS and GA-FTIR analysis. All the staff who worked in the AML, Clive, Dermot and Megan were very helpful. I am also thankful to my past teachers especially Shakunthala Mam and Dr. Atul Chaudhari who motivated me to Pursue a PhD.

I would like to thank Dr. Ross Lundy, for his ideas, supervision, and constant support. I am extremely thankful to senior research fellows (past and present) in the group, Sibu, Arantxa, Cian, Lipika, David, Niall, and Riley, for their feedbacks and discussions in improving my research. I am very thankful to Nadia, Brid and Tom for their constant encouragement and support throughout the PhD study. I would like to thank my group members in unit 9, Sukhana, Jhonathan, Eleanor, Philip, Andrew, Aislan, Hande, and Elsa, for creating a positive workplace environment. Every one of them have been truly supportive in every possible way irrespective of their different backgrounds and research areas.

I will take this opportunity to thank each member of my family. Each one of them had immense confidence in me and wanted me to pursue PhD. I dedicate this degree to them. My heartfelt gratitude to my mother for having an unperturbed faith in my abilities.

I would especially like to thank my wife Chhaya for her patience and encouragements. I thank all the kids in my family Advait, Ayush, Akshat, whom I ignored last three and half years for this achievement.

List of Publications:

1) Yadav, P.; Lundy, R.; Prochukhan, N.; Giraud, E.C.; O'Mohany, T.F.; Selkirk, A.; Mullen, E.; Conway, J.; Turner, M.; Daniels, S.; Mani-Gonzalez, P.G.; Snelgrove, M.; Bogan, J.; McFeely, C.; O'Conor, R.; McGlynn, E.; Hughes, G.; Cummins, C.; Morris, M.A. Precise Definition of a "Monolayer Point" in Polymer Brush Films for Fabricating Highly Coherent TiO_2 Thin Films by Vapor-Phase Infiltration. *Langmuir* **2020**, *36* (41), 12394–12402.

2) Yadav, P.; Lundy, R.; Selkirk, A.; Mullen, E.; Ghoshal, T.; Cummins, C.; Morris M. A.; Optimizing Polymer Brush Coverage to Develop Highly Coherent Sub-5nm Oxide Films by Ion Inclusion. *Chem. Mater.* **2019**.

3) Snelgrove, M.; Zehe, C.; Lundy, R.; **Yadav, P**.; Rueff, J.-P.; O'Connor, R.; Bogan, J.; Hughes, G.; McGlynn, E.; Morris, M.; Mani-Gonzalez, P. G. Surface Characterization of Poly-2-Vinylpyridine—A Polymer for Area Selective Deposition Techniques. *J. Vac. Sci. Technol. A* **2019**, *37* (5), 050601.

4) Mani-Gonzalez, P. G.; Snelgrove, M.; Rueff, J.-P.; Lundy, R.; **Yadav, P**.; Bogan, J.; O'Connor, R.; Morris, M.; Hughes, G. Analysis of Al and Cu Salt Infiltration into a Poly 2-Vinyl pyridine (P2VP) Polymer Layer for Semiconductor Device Patterning Applications. *J. Phys. D. Appl. Phys.* **2019**, 1–20.

5) Snelgrove, M.; **Yadav, P**.; McGlynn, E.; Morris, M.; O'Connor, R. Hard X-Ray Photoelectron Spectroscopy Study of Copper Formation by Metal Salt Inclusion in a Polymer Film. *J. Phys. D. Appl. Phys.* **2019**, *52* (43).

6) Snelgrove, M.; **Yadav, P**.; Morris, M. A.; O'Connor, R. Aluminium Oxide Formation via Atomic Layer Deposition Using a Polymer Brush Mediated Selective Infiltration Approach. *Appl. Surf. Sci.* **2020**, *515* (March), 145987.

7) Snelgrove, M.; McFeely, C.; Shiel, K.; Hughes, G.; **Yadav, P**.; Weiland, C.; Woicik, J. C.; Mani-Gonzalez, P. G.; Lundy, R.; Morris, M. A.; McGlynn, E.; O'Connor, R. Analysing Trimethylaluminum Infiltration into Polymer Brushes Using a Scalable Area Selective Vapor Phase Process. *Mater. Adv.* **2021**, *2* (2), 769–781.

1) Yadav, P.; Gatensby, R.; Padmanabham, S.; Lundy, R.; Prochukhan, N.; Snelgrove, M.; Morris, M.A. Fabrications of High-κ Dielectric Metal Oxide Films on Patterned Substrates: Polymer Brush Assisted Depositions for Modern Device Architectures. *Appl. Mater. Interfaces* 2022, 14, 28, 32729–32737.

In Preparation:

1) Yadav, P.; Conway, J.; Davo-Quinonero, A.; R.; Padmanabham, S.; Lundy, R.; Prochukhan, N.; Snelgrove, M.; Morris, M.A. Polymethyl Methacrylate Template Assisted Deposition of Uniform Zirconium Oxide Films on Copper Substrate through Liquid Phase for Area Selective Deposition Applications.

List of Abbreviations

ICs Integrated Circuits

EBL Electron beam lithography

UV Ultraviolet

BCP block copolymer

SA Self assembly

ASD Area selective deposition

ALD Atomic layer deposition

SAM Self assembled monolayer

PMMA Polymethyl methacrylate

P2VP Poly (2-vinylpyridine)

PS Polystyrene

P4VP Poly (4-vinylpyridine)

IPA Isopropyl alcohol

THF Tetrahydrofuran

SEM Scanning electron microscopy

TEM Transmission electron microscopy

AFM Atomic force microscopy

XPS X-ray photoelectron spectroscopy

CA Contact angle

FIB Focused ion beam

TGA Thermogravimetric analysis

STEM Scanning-tunnelling electron microscopy

HAADF High angle annular dark field images

BF Bright field

Table of Contents

Declaration:……… i
Abstract:……… ii
Acknowledgements:……… iii
List of publications:……… v
List of abbreviations:……… vi
Chapter 1. Introduction and background:……… 1
1.1 Background and motivation:……… 1
1.2 Area selective deposition:……… 5
1.3 Polymer brush:……… 8
1.4 Inorganic oxide nano film fabrications:……… 17
1.5 Main goal and outline:……… 21
1.6 References:……… 23

Chapter 2. Optimizing polymer brush coverage to develop highly coherent sub 5 nm oxide film by ion inclusion. 37
2.1 Abstract:……… 37
2.2 Introduction:……… 38
2.3 Experimental section:……… 40
2.4 Results:……… 43
2.5 Conclusions:……… 51
2.6 References:……… 53
2.7 Appendix:……… 58

Chapter 3. Precise definition of monolayer point in polymer brush films for fabricating highly coherent TiO2 thin films by vapour phase infiltration. 67
3.1 Abstract:……… 67
3.2 Introduction:……… 68
3.3 Experimental section:……… 71
3.4 Results and discussion:……… 74
3.5 Conclusions:……… 82
3.6 References:……… 83
3.7 Appendix……… 89

Chapter 4. Fabrication of high-k dielectric metal oxide films on patterned substrates: polymer brush assisted depositions for modern device architectures. 102
4.1 Abstract:……… 102
4.2 Introduction:……… 103
4.3 Experimental section:……… 106
4.4 Results and discussion:……… 109
4.5 Conclusions:……… 118
4.6 References:……… 119
4.7 Appendix:……… 125

Chapter 5. Polymethyl methacrylate template assisted deposition of uniform zirconium oxide films on copper substrate through liquid phase for area selective deposition application 128
5.1 Abstract:………………………………………………………………… 128
5.2 Introduction:………………………………………………………………. 129
5.3 Experimental section:…………………………………………………... 131
5.4 Results and discussion:…………………………………………………. 134
5.5 Conclusions:………………………………………………………………. 141
5.6 References:……………………………………………………………… 142
5.7 Appendix:…………………………………………………………………. 149

Chapter 6. Conclusions and future work 154
6.1 Conclusions:………………………………………………………………. 154
6.2 Future work:……………………………………………………………….. 158
6.3. References:……………………………………………………………... 160

Chapter 1. Introduction and background:

1.1 Background and motivation:

Over the past several decades the size of electronic and optoelectronic devices has consistently decreased. Integrated circuits (ICs) are composed of transistors structured on a single segment of semiconducting material. Expanding the number of transistors on a circuit is a promising way to increase both the processing power and reducing production costs. In 1965, Gordon Moore envisioned that the number of transistors per computer microchip would double every two years.[1] This prediction became the roadmap for the semiconductor industry and efforts have been successful in consistently achieving these biyearly milestones. Progress in downscaling of devices has led to the transition from planar 2D transistors to ingenious 3D transistors with fin field effect (FinFETs) features.[2,3] However, this continuous downscaling of device feature size has led to several integration challenges.

The most common techniques for material patterning are top-down lithography methods, which include photolithography, electron beam lithography, and nanoimprint lithography. In the photolithography technique,[4] a photoresist consisting of a polymer and photoactive compound mixed in a solvent is spin cast onto the substrate and annealed at a temperature higher than the boiling point of the chosen solvent to dry the resist. After drying, the resist layer is exposed to UV light through a photomask with the desired geometric pattern. The exposed regions undergo photochemical changes that affect the resist solubility. Depending on the nature of the resist, (positive or negative) exposed or unexposed regions are selectively removed with a solvent. For positive tone resist, exposed areas are more soluble in developing solution compared to negative tone resist where unexposed areas are easily eliminated by a developer solution (see **Figure 1.1**).[5–8] After developing the resist in solution, a post bake is carried out to harden the resist pattern to make it stable under the conditions needed for implantation, deposition etc. and subsequent etching for resist

removal. Following the formation of the resist pattern, pattern transfer is performed. Pattern transfer processes involve subtractive transfer (etching), additive transfer (selective deposition), and ion implantation (impurity doping). Most common of these is etching in which exposed substrate is removed using various etch processes.[7,8] After this, a striping process is carried out using an organic or inorganic solution or by dry plasma chemistry in order to remove the remaining photoresist.[9]

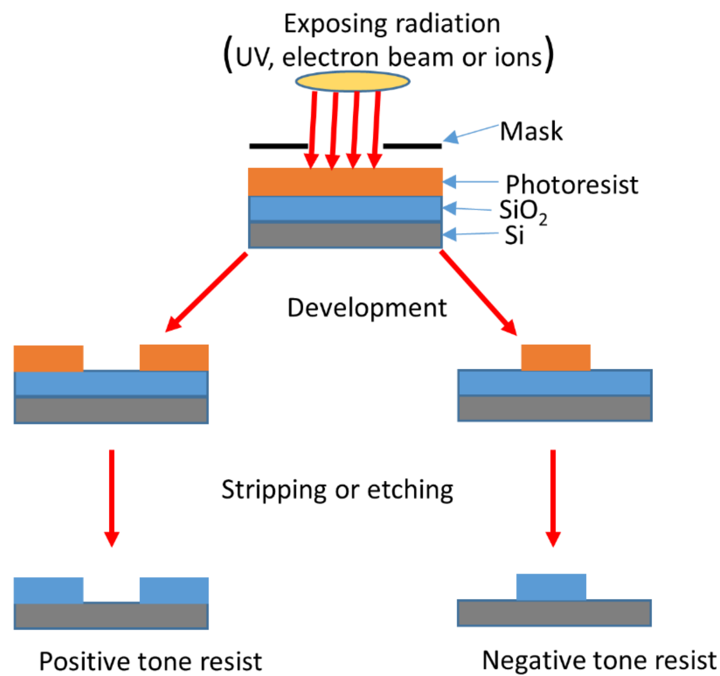

Figure 1.1: The overview of photolithography process.

The semiconductor industry's most common patterning technique for wafer scale production is photolithography. The following equations approximate the minimum feature size or critical dimension (CD) that can be defined:

$$CD = k\frac{\lambda}{NA}$$

Where k is a process related coefficient, λ is the wavelength of light and NA is the numerical aperture of the lens.

The resolution of photolithography has been improved by replacing gas discharge lamps with excimer lasers (from 465 nm MUV in 1980 to the currently used ArF 193 nm DUV laser).[10] Some issues with existing photolithography technique include edge placement error. The high cost associated with the transition from deep UV to extreme EUV (13.5 nm) and development of new photosensitive resists.[11] Progress towards implementation of extreme ultraviolet (EUV) lithography are expected to overcome some processing challenges.[12]

In the late 90's, aggressive research was directed towards the development of mask-less lithographic techniques to produce nanostructure pattern of required feature size. Some common mask-less lithography techniques include electron beam lithography (EBL),[13] and nanoimprint lithography (NIL).[14] The working principle of EBL is similar to that of photolithography except EBL technique uses electron beam instead of light. This electron beam produces chemical changes (*i.e.* monomerization or cross-linking) in the resist film upon exposure.[15–17]

EBL was frequently adapted with polymethyl-methacrylate (PMMA) resists for the fabrication of dot and line arrays at pitches and periods down to sub 30 and 40 nm.[18] *Karl et al*. have produced 2 nm feature size patterns on hydrogen silsesquioxane with electron beam condensed from scanning tunnelling electron microscopy.[19] However, the EBL application is limited by the high cost of instrumentation, poor large area resolution, mechanical toughness of the resist, electron scattering and slow manufacturing speeds since patterns are written by moving the beam.[17]

Nanoimprint lithography (NIL),[20] or hot embossing, involves a hard mould with a predefined topological pattern brought into direct contact with a substrate covered with a layer of organic polymeric material. After the removal of the mould, an inverse reproduction of the feature is imprinted on the substrate.[21–23] In the last decade, sub 10 nm patterns have been

developed successfully using NIL approach.[17] Some of the prevalent problems in NIL technique are low throughput and defects generated due to alignment issues.[25]

These limitations are pushing the electronic industry to establish new cost-effective bottom-up techniques.[26,27] Directed self-assembly of block copolymer (BCP) and area selective deposition are promising techniques to complement traditional top down patterning methods.[28] Block copolymer lithography is the self-assembly (SA) of block copolymers consisting of two (or more) chemically dissimilar polymeric blocks connected by a covalent bond. SA is the process of forming highly ordered periodic structures (~5 nm to over 100 nm) such as dots, space, and lines.[29–31] The self-assembly of BCPs occurs to minimise the interaction of similar blocks (repulsive forces) and maximise interaction of dissimilar blocks (attractive forces) and so produces distinct structural arrangements. The self-assembly and morphology of block copolymers depend on the block volume fraction, rigidity of each segment in the block, molecular weight, polymer-polymer interaction parameter (chi denoted as χ) value the interaction of the block with underlying substrate.[32–36] Analysing and understanding the thermodynamic mechanism of microphase separation has been the key component in BCP research and in the recent year number of development have been made using the variety of self-assembly technology.[32,33] Microphase separated BCP can be formed using thermal annealing, solvent vapour annealing (SVA), or laser annealing process. Advances in BCP process have enabled the accurate synthesis of number of a thin films and bulk morphologies employing numerous BCP system. Morphology developed using BCP system can be used for the various application such as integrated circuits, nano porous membranes, electrocatalytic system, photonic devices and anti-reflective coating to name a few.

Research in the area of BCPs has overcome some limitations of conventional lithography processes; for example, line edge/width roughness, minimizing defect level and aspect ratio of the pattern transfer.[37] Despite the obvious benefits of BCP-based techniques, a number of

significant difficulties persist, and have been the focus of extensive research. The primary issues are establishing substrate-normal patterns and ii) developing very large scale integration (VLSI) [32,35,38,39] while reducing defects in the patterns.

1.2 Area selective deposition:

Area selective deposition (ASD) is an emerging method and a potential bottom-up approach for nanoscale material patterning.[40,41] ASD is referred as any chemical or physical process that allows the controlled deposition of desired material on particular portions of a specified substrate. ASD uses chemical functionalities available on the substrate surface and the reactant to deposit materials. This technique can decrease the number of processing steps by allowing the growth of materials on predefined structures on the substrate. ASD has been achieved through different methods, many of which have been based on a combination of surface modification followed by vapour phase deposition techniques such as chemical vapour deposition (CVD)[42] or atomic layer deposition (ALD).[43]

Surface modifications are combined with ALD to reduce the precursor molecule adsorption on adjacent undesired area of the substrate.[44,45] Schematic representation of deactivation of non-growth area are shown in **Figure 1.2**. In the ASD technique, selective deposition of material can be performed either by, 1) activation of target substrate region (growth area), (see **Figure 1.2**) or 2) deactivation of the non-target region of substrate (non-growth) area.[46,47] The substrate can be activated by depositing self-assembled monolayers (SAMs) with reactive head group (reaction centre) or by using a polymer with availability of heteroatoms in the backbone for uptake of metal ions.[48] A region can be deactivated with organic or polymeric material (saturated) with no available reaction centre for material binding.[48,49]

Selectivity is defined in the ASD approach as the ability to selectively allow or refuse material infiltrations on the growth area. Material nucleation in non-growth regions may occur as a result of poor selectivity during material deposition (e.g. ALD). Previous studies

shows that, exposing a substrate to an organic inhibitor lowers precursor adsorption on the untargeted non-growth area.[50] Most commonly used inhibitor in the literature is acetylacetone abbreviated as Hacac. The optimal inhibitor is one that absorbs on the majority of the surface except where deposition is required. Selectivity is described as the deposition of material onto the targeted growth area relative to the undesired non-growth area and it is given by:

$$\text{Selectivity}=(\theta_{GA}-\theta_{NGA})/(\theta_{GA}+\theta_{NGA})$$

Where θ_{GA} and θ_{NGA} are the surface coverage of material on the growth and non-growth areas respectively.

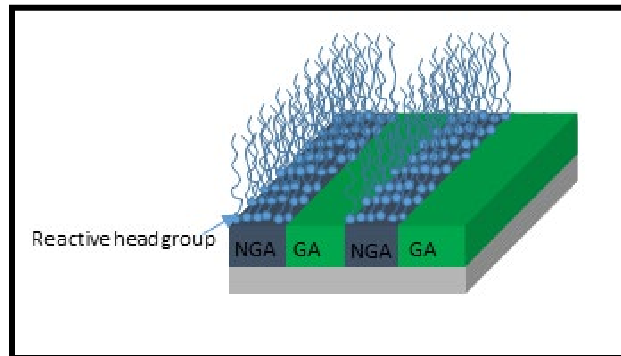

Figure 1.2: Schematic representation of area selective deposition of organic material (blocking layer) on the non-growth area (NGA) in order to carry out metal ion infiltration on the growth area (GA).

Area selective ALD has been developed to deposit different combinations of material sets for semiconductor manufacturing such as metal on dielectric, dielectric on metal and dielectric on dielectric.[28,51,52] Previous studies have demonstrated the use of organic materials as blocking layers for preventing material growth on adjacent surface.[44,47,53] Polymers have been extensively studied for the purpose of material blocking or growth. ASD of unreactive polymer layers such as PMMA,[54] polyimide,[53,55] octafluorocyclobutane (C_4F_8) and polyvinylpyrrolidone (PVP)[56] were studied earlier, with PMMA, polyimide, and PVP being deposited by spin casting methods and C_4F_8 was coated using inductively coupled plasma polymerization.[57] The blocking capability of these materials are governed by the type

of polymeric material used for the deactivation and different ALD growth recipes such as precursors used, dosage, no. of cycles, process time, reactor pressure and substrate temperature.[58] In addition to this, some physical methods of modifying the substrate have been discussed in the literature.[59] Surface activation/deactivation using physical methods can be achieved by high power laser treatment,[60,61] ionic plasma technique,[62] or ion beam bombardment.[63]

The majority of ASD research, however, combines SAM deposition with ALD.[41,64] SAMs are monolayer organic films containing long chain of hydrocarbons (typically 10 – 20 units long) as the backbone and a reactive head group at one or both ends. Typically, these head groups covalently bind with the substrate surface and the hydrocarbon backbone is exposed normal to the surface. Altering the functional group at the tail end can influence the adsorption or blocking of the inorganic materials. Frequently studied SAMs contains alkanoic acid, organosilicon, and phosphonic acid as head groups. These reactive head group have higher affinity towards surfaces of metals, metal oxides and semiconductors. One such example of SAM molecule is the octadecyl trichlorosilane (ODTS) having structural formula [$CH_3(CH_2)_{17}SiCl_3$]. ODTS can form covalent bond with the hydroxy functionalized silicon substrate and once deposition process is completed terminal unreactive -CH_3 group is exposed at the interface. The function of ODTS is to block the ALD precursor deposition on the region where the ODTS molecule is placed. A limited number of ALD deposition can be blocked by the SAM molecule. Bent *et al*. investigated octadecylphosphonic acid (ODPA) SAMs for selectively blocking Cu line in a patterned Cu/SiO_2 substrate in order to deposit materials on SiO_2 utilizing an ALD technique.[65] They also employed vapour and liquid phase deposition methods to assess the potential of alkane thiol groups to passivate metal surfaces, and found that both approaches were successful. However, when compared to liquid phase deposition, SAM vapour phase methods require a longer deposition time.[66] Furthermore, They used octadecyltrichlorosilane (ODTS) SAMs to preferentially block SiO_2 over Si-H

for polyuria molecular layer deposition (MLD).[41] Retala and Leskela have also developed a semiconductor-compatible SAM patterning approach that selectively activates/deactivates a specific region of the wafer to generate features on copper or silicon.[67,68]

Although there has been progress in using SAMs for ASD applications, a fundamental difficulty with SAM-based ASD systems is poor broad area coverage (pinholes) and long deposition periods (24–48 h), which has prohibited their use in large-scale integration.[69–71]

1.3 Polymer brush

The term polymer brush is not well defined. However, we can use it in the following manner: a polymer brush is a thin film of polymer that is covalently end bonded to the surface with a high coverage area (see **Figure 1.3**). As the polymer chain grafts to the surface, the chains interact with one another through van der Walls and electrostatic interactions. Therefore, at sufficiently high density (chain/nm^2), polymer chains stretch perpendicular to the surface to minimize their free energy.[72,73] This is only possible in relatively short chain systems and longer brushes probably adopt a strained/distorted random coil structure.[74] Polymer brushes have higher affinity (through end-group or chain chemistry) to bind strongly with silicon,[75]gold,[76] indium,[77] and the walls of various nanotubes.[78] These brushes were attached to silicon, indium, and gold surfaces using dispersive, van der Waals, and electrostatic forces, as well as hydrogen and covalent bonds.

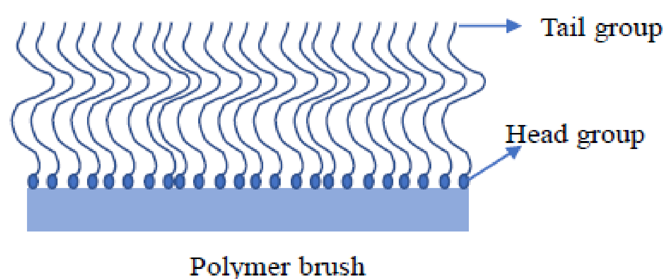

Figure 1.3: Schematic showing the anchoring of the reactive head group of the polymer brush to the substrate.

The polymer brush term was coined by Brittain and Minko.[79] They proposed that these can be described by the following equation:

$\sum = \sigma \pi R_g^2$,

where, $\sigma = h\rho N_A / M_n$,

σ is the brush grafting density

h is the dry brush thickness

ρ is the bulk density of the polymer

N_A is the Avogadro's number

M_n is the number average molecular weight.

$\sum$ is defined as area occupied by single polymer chain to the total no of chains per unit area of the substrate, R_g is radius of gyration of the polymer brush on the substrate.[80]

Depending on the value of $\sum$, formation of brush is categorised in three different regimes:

(1) the mushroom or weekly interacting regime ($\Sigma<1$),

(2) the crossover regime ($\Sigma\sim1$)

(3) highly stretched regime ($\Sigma>1$).[79]

Conformation of the polymer also depends on the solvent "quality" *i.e.* in an ideal solvent, monomer-monomer interactions are less, and in such a solvent $H>>R_g$, (H-dry brush thickness) thus the polymer stretch vertically and brush conformation is formed. For stretching to occur, the distance between two adjacent grafted polymer brushes should be less than the radius of gyration of the polymer chains.[80] mushroom regime begins to form when the R_g value approaches H. in a poor solvent where $H << R_g$ the monomer-monomer

interactions become sufficiently strong causing the polymer coil to collapse. **Figure 1.4** shows various confirmation of the polymer.

Alexander, was the first to carry out research on the behaviour of polymer brushes using theoretical analysis.[81] To date, several studies have been conducted to analyse the internal structure of the polymer using numerical and analytical self-consistent field (SCF) theory and by simulation.[82,83]

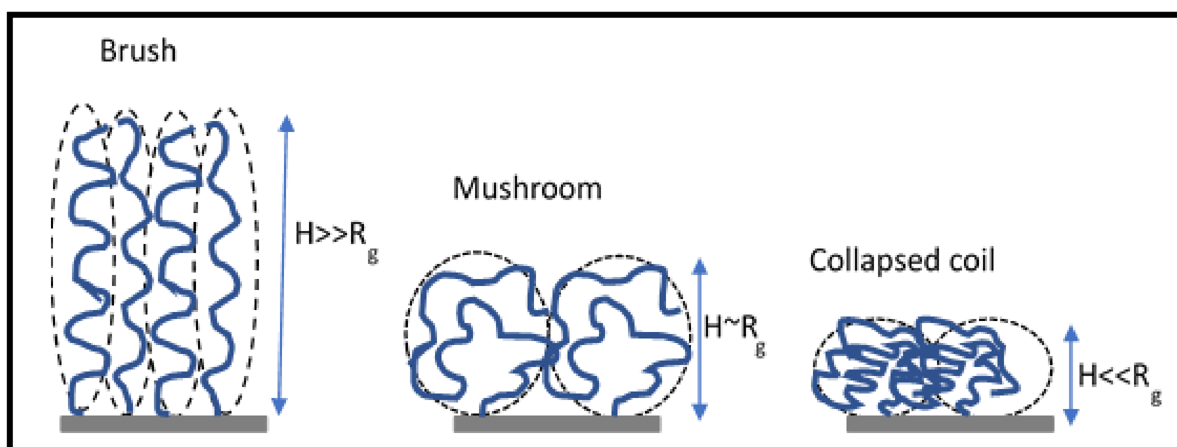

Figure 1.4 : Shows the brush (left) and mushroom (middle) conformation in good solvent as well as the formation of collapsed coil in poor solvent (right).[80]

Polymer brushes can be adhered to the substrate surface using either "grafting from" or "grafting to" techniques. Grafting from technique, also known as surface-initiated polymerization, is a polymerization technique in which the surface is modified with an initiator prior to the polymerization, which takes place solely on the surface. Most polymerization methods including nitroxide mediated polymerisation,[84] atom transfer radical polymerization (ATRP),[85] ring opening metathesis polymerization (ROMP),[86] and reversible addition fragmentation chain transfer (RAFT)[87] are categorised in grafting from technique. By contrast, “grafting to” technique is experimentally simple and uses a previously synthesized polymer with a reactive end groups (hydroxyl, thiol, silanes, amino, carboxylic acid and phosphoric acid) to react with the complementary group present on the surface. The “grafting to” technique is advantageous over “grafting from” method as this

technique allows the molecule to be readily synthesized, purified and characterized before the grafting process, *e.g.* polymer characterizations such as the chain length and polydispersity index (PDI).[88] The "grafting from" technique can also be susceptible to poor surface immobilization of the initiator and the rate of diffusion of reactant to the active site of the initiator for polymerization.

In the current scenario, 1D, 2D, and 3D polymer brushes have sparked considerable interest, with the polymer chains being attached to linear polymer, planar substrate, and spherical or trench substrate. The structural construction of 1D polymer brushes consists of a highly concentrated terminal chain that is covalently or non-covalently bonded to the backbone. Grafting from or grafting to procedures are used to create a variety of 1D polymer brushes. In contrast to 1D, 2D and 3D polymer brushes are class of material that can uniformly deposited in a very high coverage to various substrate. Substrate surface coating using polymer brush have numerous applications ranging from household material to complicated ICs. Polymer brushes are effectively used in food storage, water purification technology, and medical equipment.[89] Polymer brush technique have already been emerged as crucial platform for the advancement of the applied nanotechnology. Modification of nanoparticle using water soluble polymer brush offer them the solubility in water and colloidal stability.[90] The grafted polymer brush repels each other, preventing the particle from aggregation. Polymer brushes are a preferred choice to alter the physical properties of surfaces as these molecules exhibit exquisite long-term mechanical toughness and chemical durability coupled with the synthetic flexibility to introduce different functionality. In the beginning, polymer brushes were used for limited applications, namely, control of wetting properties,[91] corrosion,[92] and colloidal stabilization.[90] In the last couple of decades, research has emerged for the practical use of polymer brushes in energy storage devices,[93] catalysis,[94] and nanotechnology applications.[95] Further advancements in this field are expected as polymer brushes exhibit highly tailored films, where the thickness and monolayer coverage of brushes

can be tuned with nanoscale precision by controlling the molecular weight and polydispersity index (PDI) of the dissolved polymers in the solution.

Polymer brush and SAMs molecule have nearly the same bonding strength and operates in the similar application. Polymer brushes can be chemically bound to the substrate and provide selective material deposition via the tail group. In comparison to SAM, polymer brushes are quick to graft to the substrate and have complete coverage. Fabrication process of the polymer brush are discussed in details in chapter 2 and 3.

Polymer brush-based area selective deposition process represent possibly low-priced option to accomplish semiconductor fabrication. There are various polymer brush deposition and material infiltration process, each with the specific parameter that needs to be precisely optimized for different substrate and inorganic materials.

1.3.1 P2VP, P4VP, and PMMA as surface activating polymer brushes

Polymers are excellent candidates for surface modification of dielectrics and metals. They are considered as the simplest and most effective materials to form films of varying/controllable thickness, possessing fast deposition times, and yield high coverage compared to SAMs.[71,96] Polymers were initially attached to surface via non-covalent interactions (physical adsorption)[97] and were thus unstable under different material deposition conditions. To increase the robustness of the polymer films it is critical to generate covalently grafted polymer films. In this study we have used chemically grafted poly (2-vinyl pyridine) (P2VP), poly (4-vinyl pyridine) and poly methyl methacrylate (PMMA) for activating the surface and to allow the infiltration of inorganic materials.

P2VP is a weak polybasic molecule consisting of six membered heterocyclic compounds with a nitrogen atom in the aromatic domain and an aliphatic chain attached to adjacent carbon. The lone pair of electrons on the pyridinyl nitrogen does not take part in the resonance stabilization of the aromatic ring. The presence of electronegative nitrogen atom

in the benzene ring prevents the equal distribution of electron density in the ring. This loan pair of electron on nitrogen atom directed outward and influence the chemical environment of the ring. This accessible lone pair on pyridine nitrogen could be utilized as a Lewis base to make coordination bonds with lewis acids. It is a weak basic that interacts with acids to form pyridinium salt, with a pKa of 5.25 for conjugate acid (pyridinium cation). Because of its Lewis basic nature based in its nitrogen lone pair, pyridine qualifies as a transition metal ligand capable of forming metal complexes with most of the metals in the periodic table. For example, Aizawa *et.al.* examined the P2VP bonding with gold and silver.[98] They have produced a sub-100 nm gold feature surrounded by silver using the P2VP self-assembly approach. Similarly, Orhan *et.al*. studied the infiltration of Co, Cr, and Au, in to the P2VP Matrix.[99] P2VP end functionalised with hydroxyl group have the ability to graft covalently on hydroxyl functionalised silicon substrates whereas amino and thiol terminated polymer can deposit uniformly onto metal surfaces. **Figure 1.5** shows P2VP brush grafting on silicon substrate.

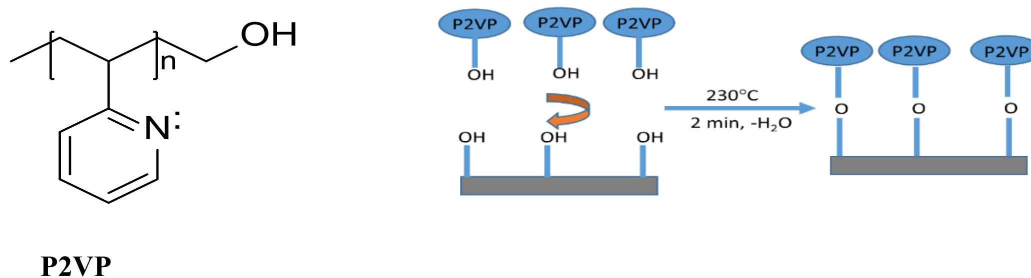

Fig 1.5: structure of P2VP (left), schematic representation of chemically grafted P2VP brush on silicon substrate (right).

P2VP has been used for various applications such as the promotion of the adhesion of micro and nanoscopic particles or molecules for the use as catalysts,[100] sensors,[101] and electronic devices.[102] Manfred Stamm *et al.* have demonstrated the process for immobilising Ag nanoparticles on chemically grafted P2VP brush to understand its optical behaviours with respect to the pH of the surrounding medium by UV-Vis spectroscopy.[103] In another work, his group extended the applicability of P2VP by modifying sp^2 hybridised carbon atoms of

carbon nanotubes with P2VP to disperse it in water and organic solvents.[104] P2VP was chosen as it has the ability to form complexes with metals and its solution behaviour can be altered significantly.[104] P2VP has also been used as the active block in a BCP template for selective infiltration of the metal oxide film.[105] Previous research in the Morris group has demonstrated P2VP-*b*-PS to create metal nano structure via liquid phase (salt) infiltrations.[106,69]

P4VP is structurally similar to P2VP, except for the position of the nitrogen atom in the aromatic ring. Metal-pyridine chemistry employs pyridine and its derivatives such as bipyridine as bidentate or tridentate ligands in the formation of metal complexes. Bipyridine metal chemistry can be seen in the unusual photochemistry and luminous ruthenium bipyridine complexes.[107] Since a long time ago, the transition metal chemistry has been focused on phenanthroline, terpyridine, and other multidentate ligands. The discussion here will be limited to pyridine and its coordination to transition metals. Titanium pyridine complexes are typically found in the Ti (IV) state. However, they can also exhibit (II – IV) valence states. Pyridine produces complex with Zr in III & IV states. Both Ti and Zr complexes are stable in +4 state. Ru, Cr, and Cu also exhibit rich chemistry with the pyrindene. Ru exhibits eight distinct oxidation states, the most stable of which is the +3-oxidation state.

Positioning of pyridinyl nitrogen atom in P2VP and P4VP exhibits different bonding strength with metal or positive organic ions. Large nanoparticles will encounter additional challenges due to the limited geometry of P2VP when compared to smaller inorganic ions or hydrogen halide. P2VP can react with smaller metal atoms like Al, and Zr, but it hinders binding with bulkier metal cations due to steric repulsion of the side chain.[108] Large molecular guests and nanoparticles can bind to P4VP considerably more accessibility, which significantly improves binding stability.[109] P2VP is soluble in THF whereas P4VP require addition of polar solvent such as isopropyl alcohol (IPA) to THF.

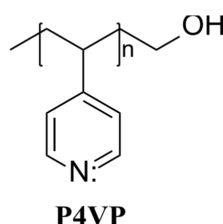

P4VP

Due to strong electron donating ability of P4VP, it displays great potential to form complexes with transition metal ions. P4VP has been studied as the strong metal coordinating agent for the uptake of bulkier metal ions such as gold (Au) and silver (Ag) to exhibit optical, antimicrobial, surface enhanced Raman and catalytic properties.[110,111] P4VP has demonstrated as the template of block copolymer to produce nanometer range structure for the microelectronic industry.[112] P4VP was studied widely as a complexing material for metals in catalysis,[113] humidity sensors,[114] and for antimicrobial materials.[115]

PMMA is an aliphatic lightweight polymer. It is less harmful as compared to P2VP and P4VP and has excellent mechanical properties which are making it potential material for bone tissue regeneration.[116] PMMA blended with polycarbonate produces a material that is used in biomaterial application.[117] The inert properties of PMMA with its long term stability permits them to be used in hip joint transplantation.[117] PMMA has also been blended with graphite for electrical conductivity and dielectric properties.[118] For gas sensing application PMMA composites containing carbon nanotubes and surface altered carbon nanotubes were studied.[119] Due to the electron sensitivity of the PMMA ester bond, it is also used as high-resolution resist

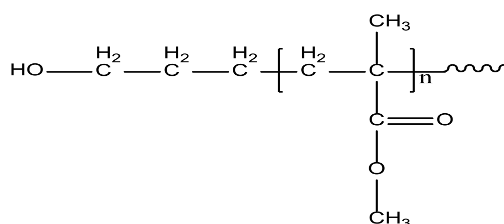

PMMA

for electron beam lithography and UV microlithography. PMMA has also been demonstrated as an important active block in the self-assembly of BCPs for developing highly ordered nano structures.[18]

PMMA is soluble in toluene and has negligible swelling in water.[120] The establishment of high adhesion strength is one of the goals of surface engineering, and PMMA has the capacity to bind to oxides and metals.[13] At the interfaces, intermolecular interaction between substrate and polymer decides the durability of the polymer film. In general, covalently grafted PMMA are stable when exposed to toluene whereas physically adsorbed PMMA is washed away in toluene. PMMA is immobilised easily on silica by UV irradiation in presence of photo initiator.[121] XPS analysis and infrared spectroscopic technique reveal that carbonyl oxygen of PMMA binds with the metal.[122] In particular, the characteristic band of PMMA υ(C=O) at $1730 cm^{-1}$ in the IR region disappear after it forms the bond with the metal.[123] PMMA can be degraded thermally at high temperature or it can be monomerised by oxidative degradation in presence of oxygen. In our study we have employed hydroxyl and thiol terminated PMMA to selectively graft on silicon and copper substrate respectively for the metal ion infiltration.

1.3.2 Polystyrene as polymer brush for deactivation of substrate

Ultrathin polystyrene (PS) layers selectively coated on a substrate can significantly affect the surface properties of the substrate without altering its bulk properties.[124] End terminated hydroxyl, amino and carboxylic acid of different molecular weight have been extensively studied to increase adhesion of the polystyrene to the polar surfaces.[88,125] A polystyrene brush can be uniformly deposited on the surface by grafting to or grafting from technique. Hydroxyl end terminated polystyrene (PS-OH) has strong affinity to form covalent bonds with complementary silanol groups on the substrate through a condensation (water elimination) reaction. Example of PS-OH grafting on silicon substrate is shown in **figure**

1.6. End terminated polystyrene is soluble in toluene and used for various applications including food packaging and laboratory ware.[126,127]

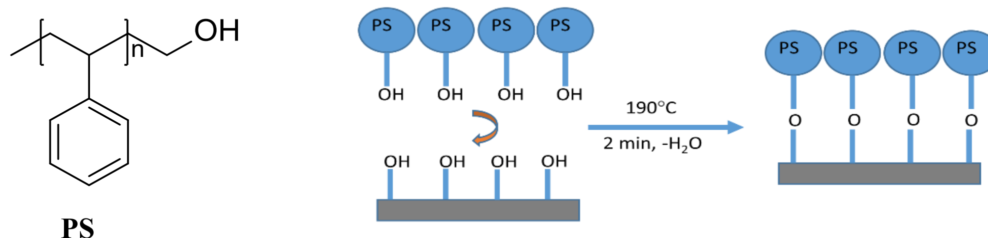

Figure 1.6: structure of PS (left), process for the chemical grafting of hydroxy terminated polystyrene (right).

Cummins et al. has demonstrated the use of amino terminated PS for selective blocking of the Cu line of patterned Cu/SiO_2 in order to perform gold deposition onto the SiO_2.[128] By simply altering the PS end amino functional group to hydroxyl, the SiO_2 region can be deactivated instead. Multiple patterning directed self-assembly of PS-b-PMMA was employed to manufacture diverse morphologies using pre deposited hydroxyl terminated PS brush.[129] Depending on the surface energy and polarity of the block, this method enable to adjust the surface chemical characteristics and induce higher affinity for one block over another.

1.4 Inorganic oxide nano film fabrications:

Metal is the most commonly used material in the production of highly conductive and stable electronic devices.[130] Metallisation is the process which connects semiconductor components by fine conducting lines.[131] In this thesis, we have studied aluminium oxide (Al_2O_3), copper oxide (CuO), titanium oxide (TiO_2), ruthenium oxide (RuO_2), hafnium oxide (HfO_2), and zirconium oxide (ZrO_2) precursor infiltration onto the optimized homogeneous polymer brush films.

The metal deposition process is broadly classified into two types *i.e.* chemical vapour deposition (CVD) and physical vapour deposition (PVD) which can be further divided into subclasses.[132] In CVD techniques, a chemical reaction occurs between precursors in the gas phase in a heterogeneous manner and products are deposited onto the substrate surface.[133] CVD processes can also be performed using plasma deposition chemistry.[134] Here, a gas plasma generated by nitrogen or argon is formed into which reactant gases are introduced.[135] Reaction between plasma and reactant gases results in radical formation and recombination of radicals occurs at the substrate. CVD is mostly used for the fabrications of organic and inorganic film. CVD has a number of advantages, including conformal film deposition. This means that the thickness of the top-deposited film is comparable to the thickness of the side walls-deposited film. [133] CVD has a number of disadvantages. The primary disadvantage of the CVD process is due to the properties of the precursors. In the CVD process the precursors needs to be volatile. This is not suitable for the number of elements in the periodic table. However, the use of organometallic precursors has helped to alleviate this situation. CVD precursor can also be extremely toxic for example $Ni(Co_4)$ or explosive B_2H_6 or corrosive $Si(Cl)_4$. Some of the organometallic precursors are extremely expensive. Furthermore, some of the processes are carried out at higher temperatures, which limits the type of substrate that can be coated. More importantly, It creates tensions in films formed on materials with different thermal expansion coefficients (TEC), which can cause mechanical instabilities in the produced films.

In comparison to CVD, physical vapor deposition (PVD) involve the various vacuum deposition methods that can be utilize to create thin films of materials.[136] PVD technique consists of process of material transitions from condensed phase to vapor phase and then back to thin films. PVD process is used to deposit materials of thickness ranging from nanometre to thousands of nanometres. Evaporative deposition, ion plating, pulsed laser deposition, and sputter deposition are a few examples of commonly used PVD methods.

PVD depositions are environmentally friendly. Negative side of PVD include slow process, high cost and sophisticated instrument that require skilled labour to operate it.

ALD is a technique similar to CVD; however, unlike continuous film growth, which occurs in the same chamber at the same time, ALD is a step-by-step process. ALD is popular technique for depositing uniform thin films with the ability to fabricate materials with atomic layer control.[137] ALD is mainly used in CMOS and other electronic components fabrications. It allows a conformal growth of materials through sequential chemical interactions.[138]

ALD is a technique that consists of four distinct steps, each of which is self-limiting, allowing for precise control over the resulting films. The first step involves the reaction of the substrate surface with the vapour phase precursor (monolayer), such as the interaction of trimethyl aluminum (TMA) with hydroxy terminated silicon substrate shown in the equation below.

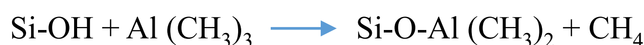

$$\text{Si-OH} + \text{Al}\,(\text{CH}_3)_3 \longrightarrow \text{Si-O-Al}\,(\text{CH}_3)_2 + \text{CH}_4$$

In the second step, excess precursor molecules (unreacted) and by-products are removed by purging gas. The third step involves the addition of a second precursor molecule, which reacts with the first.

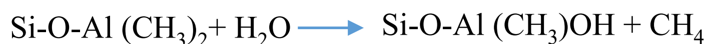

$$\text{Si-O-Al}\,(\text{CH}_3)_2 + \text{H}_2\text{O} \longrightarrow \text{Si-O-Al}\,(\text{CH}_3)\text{OH} + \text{CH}_4$$

Excess co-reactant and formed by-product are then eliminated by another purge, completing the cycle process and resulting in the homogeneous formation of single atomic layer aluminium oxide in the fourth step. The net thus can be written as,

$$\text{Al}(\text{CH}_3)_3 + 3/2\ \text{H}_2\text{O} \longrightarrow 1/2\ \text{Al}_2\text{O}_3 + 3\text{CH}_4$$

Liquid phase deposition is useful methods to create organic oxide from aqueous or organic solutions at ambient condition.[71] Effectiveness of liquid phase infiltration is governed by two primary factors: first, the diffusivity of inorganic precursors into the reactive polymer brushes, and second, the binding interaction between the precursor and the active functional

group within the polymer. Chemical properties of both polymer brushes and the inorganic precursor have strong influence on the percentage of metal inclusion.[139] Commonly used reactive polymer brushes are P2VP, P4VP, and PMMA. In P2VP and P4VP polymer brushes, the metal precursor interacts with the nitrogen atom via a loan pair of electrons, forming a very strong coordinate bond, whereas in PMMA brush, the metal precursor interacts with the carbonyl oxygen atom. In addition to this, solvent plays an important role in inorganic infiltration. To successfully infiltrate material, reactive polymer brushes must swell in the solvent in which inorganic precursor are dissolved. Metal salt infiltrated polymer brushes can be removed using variety of methods including oxidative process such as O_2 plasma, or UV-ozone, or reductive process such as Ar/H_2 plasma. Following oxidative/reductive processes a uniform layer of metal oxide/metal is produced on the substrate.[140]

1.5 Main goal and outline

The main goal of this study is to research novel methods for carrying out selective deposition of materials. As discussed earlier, ASD is a potential method that can improve edge placement errors and effectively reduce the number of processing steps for IC fabrications. Semiconductor industries such as INTEL, LAM, and Microsoft corporation, etc. are devoting more attention to the development of this technique, however, key understandings are still at the R&D stage. One of the main steps in developing an ASD methodology is to develop a facile process for fabricating highly coherent sub 5 nm metal oxide films and understand the mechanism of the infiltration. To fabricate nanostructured materials, it is critical to generate chemistry that can enable the inclusion of the metal ions. Polymer brush methods may provide this chemistry and is emerging as a powerful tool to selectively coat materials on metal or dielectric surfaces. The advantage of using polymer brushes is that it deposits uniformly on the substrate and can be used to prepare the nanoscale metal oxide film of varied thickness by adjusting the molecular weight of the polymer.

Chapter 1 includes background knowledge of area selective deposition, polymer brush and the motivation for using it. In chapter 2, we prepared uniform robust P2VP films in seconds by optimizing annealing temperature, and time. The developed polymer film was then infiltrated with aluminium nitrate solution to obtained sub 5 nm metal oxide films. Pravind Yadav performed the experiments, and study the thin films using contact angle, AFM and SEM. Ross Lundy and Nadezda Prochukhan performed the XPS, calculated surface energy and coverage.

In chapter 3, we investigated the effect of the polymer concentration, molecular weight, and end group density, to develop monolayer coverage for sterically hindered (P2VP) and unhindered polymers (PS and PMMA). Here, we utilized simple apparatus to perform vapour phase infiltration of volatile organometallic titanium precursor onto the prepared monolayer films to develop highly coherent TiO_2 nano oxide film. Pravind Yadav conceived the experiments and prepared the samples. The characterization of thin films such as AFM, SEM and contact angle was carried out by Pravind Yadav and Ross Lundy. Nadezda Prochukhan and Ross Lundy calculated the surface energy and coverage. While XPS analysis was performed by Matthew Snelgrove and Jim Conway.

In chapter 4, we demonstrated the fabrication of conformal high-κ dielectric metal oxide films through liquid phase infiltrations onto non-planar surface (topographically patterned substrate) using P4VP as a template. The ion uptake in reactive polymer systems such as P2VP, PMMA, and P4VP is also compared in this chapter. The use of an unreactive polystyrene brush to block material on a topographically patterned substrate has also been developed. Pravind Yadav Performed the sample preparation and characterization via AFM. Nadezda Prochukhan and Ramshankar analysed the sample using SEM. Matthew Snelgrove and Caitlin performed monochromatic XPS analysis, while O_2 plasma etching was done by Jim.

In chapter 5, we developed the uniform coating of PMMA-SH brush on copper surface, and further we examined the infiltration of zirconium oxy-nitrate on the formed polymer layer. We developed a hydrogen plasma reduction process for the simultaneous reductions of the metal precursor and reductive elimination of the polymer. Pravind Yadav performed the sample fabrication and analysis. Matthew Snelgrove and Caitlin conducted XPS measurement. While H_2 plasma etching was done by Jim Conway.

1.6 References:

(1) Moore, G. M. Cramming More Components onto Integrated Circuits With Unit Cost. *Electronics* **1965**, *38* (8), 114.

(2) Lee, Y. J.; Limbrick, D.; Lim, S. K. Power Benefit Study for Ultra-High Density Transistor-Level Monolithic 3D ICs. *Proc. - Des. Autom. Conf.* **2013**. https://doi.org/10.1145/2463209.2488863.

(3) Chang, C. Y.; Lee, T. L.; Wann, C.; Lai, L. S.; Chen, H. M.; Yeh, C. C.; Chang, C. S.; Ho, C. C.; Sheu, J. C.; Kwok, T. M.; Yuan, F.; Yu, S. M.; Hu, C. F.; Shen, J. J.; Liu, Y. H.; Chen, C. P.; Chen, S. C.; Chen, L. S.; Chen, L.; Chiu, Y. H.; Fu, C. Y.; Huang, M. J.; Huang, Y. L.; Hung, S. T.; Liaw, J. J.; Lin, H. C.; Lin, H. H.; Lin, L. T. S.; Lin, S. S.; Mii, Y. J.; Eric, O. Y.; Shieh, M. F.; Su, C. C.; Tai, S. P.; Tao, H. J.; Tsai, M. H.; Tseng, K. T.; Wang, K. W.; Wang, S. B.; Xu, J. J.; Yang, F. K.; Yang, S. T.; Yeh, C. N. A 25-Nm Gate-Length FinFet Transistor Module for 32nm Node. *Tech. Dig. - Int. Electron Devices Meet. IEDM* **2009**, 293–296. https://doi.org/10.1109/IEDM.2009.5424367.

(4) Holmes, P. J.; Snell, J. E. A Vapour Etching Technique for the Photolithography of Silicon Dioxide. *Microelectron. Reliab.* **1966**, *5* (4), 337–341. https://doi.org/10.1016/0026-2714(66)90162-4.

(5) Garner, C. M. Lithography for Enabling Advances in Integrated Circuits and Devices. *Philos. Trans. R. Soc. A Math. Phys. Eng. Sci.* **2012**, *370* (1973), 4015–4041. https://doi.org/10.1098/rsta.2011.0052.

(6) Yeh, W.-M.; Noga, D. E.; Lawson, R. A.; Tolbert, L. M.; Henderson, C. L. Comparison of Positive Tone versus Negative Tone Resist Pattern Collapse Behavior. *J. Vac. Sci. Technol. B, Nanotechnol. Microelectron. Mater. Process. Meas. Phenom.* **2010**, *28* (6), C6S6-C6S11. https://doi.org/10.1116/1.3518136.

(7) Sun, Y.; Khang, D. Y.; Hua, F.; Hurley, K.; Nuzzo, R. G.; Rogers, J. A. Photolithographic Route to the Fabrication of Micro/Nanowires of III-V Semiconductors. *Adv. Funct. Mater.* **2005**, *15* (1), 30–40. https://doi.org/10.1002/adfm.200400411.

(8) Pang, S. W. Etching of Photoresist Using Oxygen Plasma Generated by a Multipolar Electron Cyclotron Resonance Source. *J. Vac. Sci. Technol. B Microelectron. Nanom. Struct.* **1992**, *10* (3), 1118. https://doi.org/10.1116/1.586087.

(9) Yang, S. K.; Cho, J. H.; Lee, S. W.; Lee, C. W.; Park, S. J.; Chae, H. S. Hydrogen Plasma Characteristics for Photoresist Stripping Process in a Cylindrical Inductively Coupled Plasma. *J. Semicond. Technol. Sci.* **2013**, *13* (4), 387–394. https://doi.org/10.5573/JSTS.2013.13.4.387.

(10) Shibata, T.; Nakagawa, S.; Sato, Y.; Sho, K.; Hayashi, H.; Abe, J. Material and Process Development of Tri-Level Resist System in KrF and ArF Lithography.

Adv. Resist Technol. Process. XIX **2002**, *4690*, 773. https://doi.org/10.1117/12.474278.

(11) Rankin, J.; Qi, Z. J.; Lawliss, M.; Narita, E.; Seki, K.; Badger, K.; Bonam, R.; Halle, S.; Turley, C. EUV Photomask Defects: What Prints, What Doesn't, and What Is Required for HVM. *Photomask Technol. 2015* **2015**, *9635*, 96350L. https://doi.org/10.1117/12.2197476.

(12) Wu, B.; Kumar, A. Extreme Ultraviolet Lithography and Three Dimensional Integrated Circuit - A Review. *Appl. Phys. Rev.* **2014**, *1* (1). https://doi.org/10.1063/1.4863412.

(13) Wang, X.; Xu, J.; Quan, X.; Li, Y.; Wang, Y.; Cheng, X. Fast Fabrication of Silicon Nanopillar Array Using Electron Beam Lithography with Two-Layer Exposure Method. *Microelectron. Eng.* **2020**, *227* (August 2019), 111311. https://doi.org/10.1016/j.mee.2020.111311.

(14) Modaresialam, M.; Chehadi, Z.; Bottein, T.; Abbarchi, M.; Grosso, D. Nanoimprint Lithography Processing of Inorganic-Based Materials. *Chem. Mater.* **2021**. https://doi.org/10.1021/acs.chemmater.1c00693.

(15) Tritchkov, A. Use of Positive and Negative Chemically Amplified Resists in Electron-Beam Direct-Write Lithography. *J. Vac. Sci. Technol. B Microelectron. Nanom. Struct.* **1995**, *13* (6), 2986. https://doi.org/10.1116/1.588293.

(16) Tseng, A. A.; Chen, K.; Chen, C. D.; Ma, K. J. Electron Beam Lithography in Nanoscale Fabrication: Recent Development. *IEEE Trans. Electron. Packag. Manuf.* **2003**, *26* (2), 141–149. https://doi.org/10.1109/TEPM.2003.817714.

(17) Chen, Y. Nanofabrication by Electron Beam Lithography and Its Applications: A Review. *Microelectron. Eng.* **2015**, *135*, 57–72. https://doi.org/10.1016/j.mee.2015.02.042.

(18) Hu, W.; Sarveswaran, K.; Lieberman, M.; Bernstein, G. H. Sub-10 Nm Electron Beam Lithography Using Cold Development of Poly(Methylmethacrylate). *J. Vac. Sci. Technol. B Microelectron. Nanom. Struct.* **2004**, *22* (4), 1711–1716. https://doi.org/10.1116/1.1763897.

(19) Manfrinato, V. R.; Zhang, L.; Su, D.; Duan, H.; Hobbs, R. G.; Stach, E. A.; Berggren, K. K. Resolution Limits of Electron-Beam Lithography toward the Atomic Scale. *Nano Lett.* **2013**, *13* (4), 1555–1558. https://doi.org/10.1021/nl304715p.

(20) Sreenivasan, S. V. Nanoimprint Lithography Steppers for Volume Fabrication of Leading-Edge Semiconductor Integrated Circuits. *Microsystems Nanoeng.* **2017**, *3* (1), 1–19. https://doi.org/10.1038/micronano.2017.75.

(21) Sreenivasan, S. V. Nanoimprint Lithography Steppers for Volume Fabrication of Leading-Edge Semiconductor Integrated Circuits. *Microsystems Nanoeng.*

2017, *3* (1), 1–19. https://doi.org/10.1038/micronano.2017.75.

(22) Barcelo, S.; Li, Z. Nanoimprint Lithography for Nanodevice Fabrication. *Nano Converg.* **2016**, *3* (1). https://doi.org/10.1186/s40580-016-0081-y.

(23) Guo, L. J. Nanoimprint Lithography: Methods and Material Requirements. *Adv. Mater.* **2007**, *19* (4), 495–513. https://doi.org/10.1002/adma.200600882.

(24) Krauss, P. R.; Chou, S. Y. Sub-10 Nm Imprint Lithography and Applications. *Annu. Device Res. Conf. Dig.* **1997**, No. September, 90–91. https://doi.org/10.1116/1.589752.

(25) Cegielski, P. J.; Bolten, J.; Kim, J. W.; Schlachter, F.; Nowak, C.; Wahlbrink, T.; Giesecke, A. L.; Lemme, M. C. Overlay Accuracy Limitations of Soft Stamp UV Nanoimprint Lithography and Circumvention Strategies for Device Applications. *Microelectron. Eng.* **2018**, *197*, 83–86. https://doi.org/10.1016/j.mee.2018.06.004.

(26) Lu, W.; Lieber, C. M. Nanoelectronics from the Bottom Up. *Nanosci. Technol. A Collect. Rev. from Nat. Journals* **2009**, 137–146. https://doi.org/10.1142/9789814287005_0014.

(27) Mackus, A. J. M.; Merkx, M. J. M.; Kessels, W. M. M. From the Bottom-Up: Toward Area-Selective Atomic Layer Deposition with High Selectivity †. *Chem. Mater.* **2019**, *31* (1), 2–12. https://doi.org/10.1021/acs.chemmater.8b03454.

(28) Parsons, G. N.; Clark, R. D. Area-Selective Deposition: Fundamentals, Applications, and Future Outlook. *Chem. Mater.* **2020**, *32* (12), 4920–4953. https://doi.org/10.1021/acs.chemmater.0c00722.

(29) Cummins, C.; Weingärtner, T.; Morris, M. A. Enabling Large-Area Selective Deposition on Metal-Dielectric Patterns Using Polymer Brush Deactivation. *J. Phys. Chem. C* **2018**, *122* (26), 14698–14705. https://doi.org/10.1021/acs.jpcc.8b04092.

(30) Cummins, C.; Gangnaik, A.; Kelly, R. A.; Borah, D.; O'Connell, J.; Petkov, N.; Georgiev, Y. M.; Holmes, J. D.; Morris, M. A. Aligned Silicon Nanofins *via* the Directed Self-Assembly of PS- *b* -P4VP Block Copolymer and Metal Oxide Enhanced Pattern Transfer. *Nanoscale* **2015**, *7* (15), 6712–6721. https://doi.org/10.1039/C4NR07679F.

(31) Cummins, C.; Ghoshal, T.; Holmes, J. D.; Morris, M. A. Strategies for Inorganic Incorporation Using Neat Block Copolymer Thin Films for Etch Mask Function and Nanotechnological Application. *Adv. Mater.* **2016**, 5586–5618. https://doi.org/10.1002/adma.201503432.

(32) Yang, X. M.; Wan, L.; Xiao, S.; Xu, Y.; Weller, D. K. Directed Block Copolymer Assembly versus Electron Beam Lithography for Bit-Patterned Media with Areal Density of 1 Terabit/Inch2 and Beyond. *ACS Nano* **2009**, *3*

(7), 1844–1858. https://doi.org/10.1021/nn900073r.

(33) Arras, M. M. L.; He, B.; Jandt, K. D. High Molar Mass Amphiphilic Block Copolymer Enables Alignment and Dispersion of Unfunctionalized Carbon Nanotubes in Melt-Drawn Thin-Films. *Polymer (Guildf).* **2017**, *127*, 15–27. https://doi.org/10.1016/j.polymer.2017.08.030.

(34) Borah, D.; Cummins, C.; Rasappa, S.; Senthamaraikannan, R.; Salaun, M.; Zelsmann, M.; Liontos, G.; Ntetsikas, K.; Avgeropoulos, A.; Morris, M.; Borah, D.; Cummins, C.; Rasappa, S.; Senthamaraikannan, R.; Salaun, M.; Zelsmann, M.; Liontos, G.; Ntetsikas, K.; Avgeropoulos, A.; Morris, M. A. Nanopatterning via Self-Assembly of a Lamellar-Forming Polystyrene-Block-Poly(Dimethylsiloxane) Diblock Copolymer on Topographical Substrates Fabricated by Nanoimprint Lithography. *Nanomaterials* **2018**, *8* (1), 32. https://doi.org/10.3390/nano8010032.

(35) Jeong, S. J.; Kim, J. Y.; Kim, B. H.; Moon, H. S.; Kim, S. O. Directed Self-Assembly of Block Copolymers for next Generation Nanolithography. *Mater. Today* **2013**, *16* (12), 468–476. https://doi.org/10.1016/j.mattod.2013.11.002.

(36) Gotrik, K. W.; Hannon, A. F.; Son, J. G.; Keller, B.; Alexander-katz, A.; Ross, C. A. Morphology Control in Block Copolymer Films Using Mixed Solvent Vapors, 2012.

(37) Borah, D.; Shaw, M. T.; Holmes, J. D.; Morris, M. A. Sub-10 Nm Feature Size PS-b-PDMS Block Copolymer Structures Fabricated by a Microwave-Assisted Solvothermal Process. *ACS Appl. Mater. Interfaces* **2013**, *5* (6), 2004–2012. https://doi.org/10.1021/am302830w.

(38) Gu, X.; Gunkel, I.; Russell, T. P.; Russell, T. P. Pattern Transfer Using Block Copolymers Subject Areas : Author for Correspondence : *Philos. Trans. R. Soc.* **2013**.

(39) Liu, C.-C.; Nealey, P. F.; Raub, A. K.; Hakeem, P. J.; Brueck, S. R. J.; Han, E.; Gopalan, P. Integration of Block Copolymer Directed Assembly with 193 Immersion Lithography. *J. Vac. Sci. Technol. B, Nanotechnol. Microelectron. Mater. Process. Meas. Phenom.* **2010**, *28* (6), C6B30-C6B34. https://doi.org/10.1116/1.3501348.

(40) Tsubouchi, K.; Masu, K. Area-Selective CVD of Metals. *Thin Solid Films* **1993**, *228* (1–2), 312–318. https://doi.org/10.1016/0040-6090(93)90624-X.

(41) Prasittichai, C.; Pickrahn, K. L.; Minaye Hashemi, F. S.; Bergsman, D. S.; Bent, S. F. Improving Area-Selective Molecular Layer Deposition by Selective SAM Removal. *ACS Appl. Mater. Interfaces* **2014**, *6* (20), 17831–17836. https://doi.org/10.1021/am504441e.

(42) Han, J. H.; Lee, S. W.; Choi, G. J.; Lee, S. Y.; Hwang, C. S.; Dussarrat, C.; Gatineau, J. Chemical Vapor Deposition of Ru Thin Films with an Enhanced Morphology, Thermal Stability, and Electrical Properties Using a RuO4

Precursor. *Chem. Mater.* **2009**, *21* (2), 207–209. https://doi.org/10.1021/cm802485r.

(43) Richey, N. E.; De Paula, C.; Bent, S. F. Understanding Chemical and Physical Mechanisms in Atomic Layer Deposition. *J. Chem. Phys.* **2020**, *152* (4), 1–17. https://doi.org/10.1063/1.5133390.

(44) Zhang, Z.; Dwyer, T.; Sirard, S. M.; Ekerdt, J. G. Area-Selective Atomic Layer Deposition of Cobalt Oxide to Generate Patterned Cobalt Films. *Journal of Vacuum Science & Technology A*. 2019, p 020905. https://doi.org/10.1116/1.5066437.

(45) Rong Chen, †; Hyoungsub Kim, ‡; Paul C. McIntyre, ‡ and; Stacey F. Bent*, §. Investigation of Self-Assembled Monolayer Resists for Hafnium Dioxide Atomic Layer Deposition. **2005**. https://doi.org/10.1021/CM0486666.

(46) Minaye Hashemi, F. S.; Prasittichai, C.; Bent, S. F. Self-Correcting Process for High Quality Patterning by Atomic Layer Deposition. *ACS Nano* **2015**, *9* (9), 8710–8717. https://doi.org/10.1021/acsnano.5b03125.

(47) Bobb-semple, D.; Nardi, K. L.; Draeger, N.; Hausmann, D. M.; Bent, S. F. Area-Selective Atomic Layer Deposition Assisted by Self-Assembled Monolayers: A Comparison of Cu, Co, W, and Ru. **2019**. https://doi.org/10.1021/acs.chemmater.8b04926.

(48) Zyulkov, I.; Madhiwala, V.; Voronina, E.; Snelgrove, M.; Bogan, J.; O'Connor, R.; De Gendt, S.; Armini, S. Area-Selective ALD of Ru on Nanometer-Scale Cu Lines through Dimerization of Amino-Functionalized Alkoxy Silane Passivation Films. *ACS Appl. Mater. Interfaces* **2020**, *12* (4), 4678–4688. https://doi.org/10.1021/acsami.9b14596.

(49) Chen, R.; Kim, H.; McIntyre, P. C.; Porter, D. W.; Bent, S. F. Achieving Area-Selective Atomic Layer Deposition on Patterned Substrates by Selective Surface Modification. *Appl. Phys. Lett.* **2005**, *86* (19), 1–3. https://doi.org/10.1063/1.1922076.

(50) Mameli, A.; Merkx, M. J. M.; Karasulu, B.; Roozeboom, F.; Kessels, W. (Erwin) M. M.; Mackus, A. J. M. Area-Selective Atomic Layer Deposition of SiO 2 Using Acetylacetone as a Chemoselective Inhibitor in an ABC-Type Cycle. *ACS Nano* **2017**, *11* (9), 9303–9311. https://doi.org/10.1021/acsnano.7b04701.

(51) Xiang, C.; Kung, S. C.; Taggart, D. K.; Yang, F.; Thompson, M. A.; Güell, A. G.; Yang, Y.; Penner, R. M. Lithographically Patterned Nanowire Electrodeposition: A Method for Patterning Electrically Continuous Metal Nanowires on Dielectrics. *ACS Nano* **2008**, *2* (9), 1939–1949. https://doi.org/10.1021/nn800394k.

(52) Singh, J. A.; Thissen, N. F. W.; Kim, W.-H.; Johnson, H.; Kessels, W. (Erwin) M. .; Bol, A. A.; Bent, S. F.; Mackus, A. J. M. Area-Selective Atomic Layer

Deposition of Metal Oxides on Noble Metals through Catalytic Oxygen Activation. *Chem. Mater.* **2017**, acs.chemmater.7b03818. https://doi.org/10.1021/acs.chemmater.7b03818.

(53) Forouzmehr, M.; Zambou, S.; Lahtonen, K.; Honkanen, M.; Nazmul Anam, R. M.; Ruhanen, A.; Rokaya, C.; Lupo, D.; Berger, P. R. Selective Atomic Layer Deposition on Flexible Polymeric Substrates Employing a Polyimide Adhesive as a Physical Mask. *J. Vac. Sci. Technol. A* **2021**, *39* (1), 012405. https://doi.org/10.1116/6.0000566.

(54) Färm, E.; Kemell, M.; Ritala, M.; Leskelä, M. Selective-Area Atomic Layer Deposition Using Poly(Methyl Methacrylate) Films as Mask Layers. *J. Phys. Chem. C* **2008**, *112* (40), 15791–15795. https://doi.org/10.1021/jp803872s.

(55) Zhang, C.; Vehkamäki, M.; Pietikäinen, M.; Leskelä, M.; Ritala, M. Area-Selective Molecular Layer Deposition of Polyimide on Cu through Cu-Catalyzed Formation of a Crystalline Interchain Polyimide. *Chem. Mater.* **2020**, *32* (12), 5073–5083. https://doi.org/10.1021/acs.chemmater.0c00898.

(56) Färm, E.; Kemell, M.; Santala, E.; Ritala, M.; Leskelä, M. Selective-Area Atomic Layer Deposition Using Poly(Vinyl Pyrrolidone) as a Passivation Layer. *J. Electrochem. Soc.* **2010**, *157* (1), K10. https://doi.org/10.1149/1.3250936.

(57) Haider, A.; Yilmaz, M.; Deminskyi, P.; Eren, H.; Biyikli, N. RSC Advances TiO 2 Using E-Beam Patterned Polymers †. **2016**, 106109–106119. https://doi.org/10.1039/c6ra23923d.

(58) Obuchovsky, S.; Frankenstein, H.; Vinokur, J.; Hailey, A. K.; Loo, Y. L.; Frey, G. L. Mechanism of Metal Oxide Deposition from Atomic Layer Deposition inside Nonreactive Polymer Matrices: Effects of Polymer Crystallinity and Temperature. *Chem. Mater.* **2016**, *28* (8), 2668–2676. https://doi.org/10.1021/acs.chemmater.6b00159.

(59) Damborenea, J. De. Surface Modification of Metals by High Power Lasers. **1998**, *101*.

(60) Rakesh, K. R.; Bontha, S.; Ramesh, M. R.; Arya, S. B.; Das, M.; Balla, V. K.; Srinivasan, A. Laser Surface Modification of Mg-Zn-Gd Alloy: Microstructural, Wettability and in Vitro Degradation Aspects. *Mater. Res. Express* **2018**, *5* (12). https://doi.org/10.1088/2053-1591/aadec6.

(61) Quazi, M. M.; Fazal, M. A.; Haseeb, A. S. M. A.; Yusof, F.; Masjuki, H. H.; Arslan, A. Laser-Based Surface Modifications of Aluminum and Its Alloys. *Crit. Rev. Solid State Mater. Sci.* **2016**, *41* (2), 106–131. https://doi.org/10.1080/10408436.2015.1076716.

(62) Cvelbar, U.; Markoli, B.; Poberaj, I.; Zalar, A.; Kosec, L.; Spaić, S. Formation of Functional Groups on Graphite during Oxygen Plasma Treatment. *Appl. Surf. Sci.* **2006**, *253* (4), 1861–1865.

https://doi.org/10.1016/j.apsusc.2006.03.028.

(63) Park, J. W.; Sohn, C. W.; Choi, B. H. Some Characteristics of Materials Surface-Modified by Ions Beam Bombardment. **2006**, *6*, 188–193. https://doi.org/10.1016/j.cap.2005.07.038.

(64) Minaye Hashemi, F. S.; Birchansky, B. R.; Bent, S. F. Selective Deposition of Dielectrics: Limits and Advantages of Alkanethiol Blocking Agents on Metal–Dielectric Patterns. *ACS Appl. Mater. Interfaces* **2016**, *8* (48), 33264–33272. https://doi.org/10.1021/acsami.6b09960.

(65) Sadat, F.; Hashemi, M.; Prasittichai, C.; Bent, S. F.; Science, M.; Engineering, C.; Present, U. S. Self-Correcting Process for High Quality Patterning by Atomic Layer Deposition. **2015**, No. 9, 8710–8717. https://doi.org/10.1021/acsnano.5b03125.

(66) Minaye Hashemi, F. S.; Birchansky, B. R.; Bent, S. F. Selective Deposition of Dielectrics: Limits and Advantages of Alkanethiol Blocking Agents on Metal–Dielectric Patterns. *ACS Appl. Mater. Interfaces* **2016**, *8* (48), 33264–33272. https://doi.org/10.1021/acsami.6b09960.

(67) Octadecyltrimethoxysilane, S.; Atomic, M. E. S. Layer Deposition of Iridium **. **2006**, 415–417. https://doi.org/10.1002/cvde.200604219.

(68) Farm, E. Passivation of Copper Surfaces for Selective-Area ALD Using a Thiol Self-Assembled Monolayer. **2012**. https://doi.org/10.1088/0268-1242/27/7/074004.

(69) Cummins, C.; Shaw, M. T.; Morris, M. A. Area Selective Polymer Brush Deposition. **2017**, *1700252*, 1–6. https://doi.org/10.1002/marc.201700252.

(70) Lundy, R.; Yadav, P.; Prochukhan, N.; Giraud, E. C.; O'Mahony, T. F.; Selkirk, A.; Mullen, E.; Conway, J.; Turner, M.; Daniels, S.; Mani-Gonzalez, P. G.; Snelgrove, M.; Bogan, J.; McFeely, C.; O'Connor, R.; McGlynn, E.; Hughes, G.; Cummins, C.; Morris, M. A. Precise Definition of a "Monolayer Point" in Polymer Brush Films for Fabricating Highly Coherent TiO2Thin Films by Vapor-Phase Infiltration. *Langmuir* **2020**, *36* (41), 12394–12402. https://doi.org/10.1021/acs.langmuir.0c02512.

(71) Lundy, R.; Yadav, P.; Selkirk, A.; Mullen, E.; Ghoshal, T.; Cummins, C.; Morris, M. A. Optimizing Polymer Brush Coverage To Develop Highly Coherent Sub-5 Nm Oxide Films by Ion Inclusion. *Chem. Mater.* **2019**, *31* (22), 9338–9345. https://doi.org/10.1021/acs.chemmater.9b02856.

(72) Azzaroni, O. Polymer Brushes Here , There , and Everywhere : Recent Advances in Their Practical Applications and Emerging Opportunities in Multiple Research Fields. **2012**, 3225–3258. https://doi.org/10.1002/pola.26119.

(73) Chen, W.-L.; Cordero, R.; Tran, H.; Ober, C. K. *50th Anniversary Perspective* :

Polymer Brushes: Novel Surfaces for Future Materials. *Macromolecules* **2017**, *50* (11), 4089–4113. https://doi.org/10.1021/acs.macromol.7b00450.

(74) Feng, C.; Huang, X. Polymer Brushes: Efficient Synthesis and Applications. *Acc. Chem. Res.* **2018**, *51* (9), 2314–2323. https://doi.org/10.1021/acs.accounts.8b00307.

(75) Jiang, L.; Bagán, H.; Kamra, T.; Zhou, T.; Ye, L. Nanohybrid Polymer Brushes on Silica for Bioseparation. *J. Mater. Chem. B* **2016**, *4* (19), 3247–3256. https://doi.org/10.1039/c6tb00241b.

(76) Balko, S. M.; Kreer, T.; Mulder, D. J.; Costanzo, P. J.; Patten, T. E.; Kuhl, T. L. Using Thiol-Gold Bond Formation to Bridge Surfaces with a Polymer Brush: Sfa Experiments and Md Simulations. *Macromolecules* **2013**, *46* (24), 9826–9836. https://doi.org/10.1021/ma4015356.

(77) Kim, B.; Ratcliff, E. L.; Armstrong, N. R.; Kowalewski, T.; Pyun, J. Ferrocene Functional Polymer Brushes on Indium Tin Oxide via Surface-Initiated Atom Transfer Radical Polymerization. *Langmuir* **2010**, *26* (3), 2083–2092. https://doi.org/10.1021/la902590u.

(78) Khan, M. U.; Reddy, K. R.; Snguanwongchai, T.; Haque, E.; Gomes, V. G. Polymer Brush Synthesis on Surface Modified Carbon Nanotubes via in Situ Emulsion Polymerization. *Colloid Polym. Sci.* **2016**, *294* (10), 1599–1610. https://doi.org/10.1007/s00396-016-3922-7.

(79) Brittain, W. J.; Minko, S.; Brittain, W. A Structural Definition of Polymer Brushes. **2007**, *45*, 3505–3512. https://doi.org/10.1002/pola.22180.

(80) Galvin, C. J.; Genzer, J. Progress in Polymer Science Applications of Surface-Grafted Macromolecules Derived from Post-Polymerization Modification Reactions. *Prog. Polym. Sci.* **2012**, *37* (7), 871–906. https://doi.org/10.1016/j.progpolymsci.2011.12.001.

(81) Alexander, S.; Polymer, S. A.; Physique, J. De; Alexander, S. Polymer Adsorption on Small Spheres . A Scaling Approach To Cite This Version : HAL Id : Jpa-00208665. **1977**.

(82) Shull, K. R.; Shull, K. R. Theory of Endadsorbed Polymer Brushes in Polymeric Matrices Theory of End-Adsorbed Polymer Brushes in Polymeric Matrices. **2011**, *5723* (1991). https://doi.org/10.1063/1.460456.

(83) Version, D.; Vos, D. Switching the Interpenetration of Confined Asymmetric Polymer Brushes . Switching the Interpenetration of Confined Asymmetric Polymer Brushes . **2016**. https://doi.org/10.1021/acs.macromol.6b00310.

(84) Chevigny, C.; Gigmes, D.; Bertin, D.; Jestin, J.; Boué, F. Polystyrene Grafting from Silica Nanoparticles via Nitroxide-Mediated Polymerization (NMP): Synthesis and SANS Analysis with the Contrast Variation Method. *Soft Matter* **2009**, *5* (19), 3741–3753. https://doi.org/10.1039/b906754j.

(85) Liu, Y.; Klep, V.; Zdyrko, B.; Luzinov, I. Polymer Grafting via ATRP Initiated from Macroinitiator Synthesized on Surface. *Langmuir* **2004**, *20* (16), 6710–6718. https://doi.org/10.1021/la049465j.

(86) Johnson, J. A.; Lu, Y. Y.; Burts, A. O.; Lim, Y. H.; Finn, M. G.; Koberstein, J. T.; Turro, N. J.; Tirrell, D. A.; Grubbs, R. H. Core-Clickable PEG-Branch-Azide Bivalent-Bottle-Brush Polymers by ROMP: Grafting-through and Clicking-To. *J. Am. Chem. Soc.* **2011**, *133* (3), 559–566. https://doi.org/10.1021/ja108441d.

(87) Liu, C. H.; Pan, C. Y. Grafting Polystyrene onto Silica Nanoparticles via RAFT Polymerization. *Polymer (Guildf).* **2007**, *48* (13), 3679–3685. https://doi.org/10.1016/j.polymer.2007.04.055.

(88) Zdyrko, B.; Luzinov, I. Polymer Brushes by the "Grafting to" Method. *Macromol. Rapid Commun.* **2011**, *32* (12), 859–869. https://doi.org/10.1002/marc.201100162.

(89) Pester, C. W.; Poelma, J. E.; Narupai, B.; Patel, S. N.; Su, G. M.; Mates, T. E.; Luo, Y.; Ober, C. K.; Hawker, C. J.; Kramer, E. J. Ambiguous Anti-Fouling Surfaces: Facile Synthesis by Light-Mediated Radical Polymerization. *J. Polym. Sci., Part A Polym. Chem* **2015**, *54*, 253–262. https://doi.org/10.1002/pola.27748.

(90) Witten, T. A.; Pincus, P. A.; Pincus, P. A. Colloid Stabilization by Long Grafted Polymers. *Macromolecules* **1986**, *19* (10), 2509–2513. https://doi.org/10.1021/ma00164a009.

(91) Kobayashi, M.; Terayama, Y.; Yamaguchi, H.; Terada, M.; Murakami, D.; Ishihara, K.; Takahara, A. Wettability and Antifouling Behavior on the Surfaces of Superhydrophilic Polymer Brushes. *Langmuir* **2012**, *28* (18), 7212–7222. https://doi.org/10.1021/la301033h.

(92) Kutnyanszky, E.; Vancso, G. J. Nanomechanical Properties of Polymer Brushes by Colloidal AFM Probes. *Eur. Polym. J.* **2012**, *48* (1), 8–15. https://doi.org/10.1016/j.eurpolymj.2011.09.008.

(93) Giussi, J. M.; Cortez, M. L.; Marmisollé, W. A.; Azzaroni, O. Practical Use of Polymer Brushes in Sustainable Energy Applications: Interfacial Nanoarchitectonics for High-Efficiency Devices. *Chem. Soc. Rev.* **2019**, *48* (3), 814–849. https://doi.org/10.1039/c8cs00705e.

(94) Costantini, F.; Bula, W. P.; Salvio, R.; Huskens, J.; Gardeniers, H. J. G. E.; Reinhoudt, D. N.; Verboom, W. Nanostructure Based on Polymer Brushes for Efficient Heterogeneous Catalysis in Microreactors. *J. Am. Chem. Soc.* **2009**, *131* (5), 1650–1651. https://doi.org/10.1021/ja807616z.

(95) Cheng, S.; Stevens, M. J.; Grest, G. S. Ordering Nanoparticles with Polymer Brushes. *J. Chem. Phys.* **2017**, *147* (22). https://doi.org/10.1063/1.5006048.

(96) Senaratne, W.; Andruzzi, L.; Ober, C. K. Self-Assembled Monolayers and Polymer Brushes in Biotechnology: Current Applications and Future Perspectives. *Biomacromolecules* **2005**, *6* (5), 2427–2448. https://doi.org/10.1021/bm050180a.

(97) Somasundaran, P.; Krishnakumar, S. Adsorption of Surfactants and Polymers at the Solid-Liquid Interface. *Colloids Surfaces A Physicochem. Eng. Asp.* **1997**, *123–124* (96), 491–513. https://doi.org/10.1016/S0927-7757(96)03829-0.

(98) Aizawa, M.; Buriak, J. M. Nanoscale Patterning of Two Metals on Silicon Surfaces Using an ABC Triblock Copolymer Template. *J. Am. Chem. Soc.* **2006**, *128* (17), 5877–5886. https://doi.org/10.1021/JA060366X.

(99) Orhan Lekesiz, T.; Kaleli, K.; Kayran, C.; Hacaloglu, J. Preparation and Characterization of Polystyrene-b-Poly(2-Vinylpyridine) Coordinated to Metal or Metal Ion Nanoparticles. *J. Anal. Appl. Pyrolysis* **2014**, *106*, 81–85. https://doi.org/10.1016/j.jaap.2014.01.002.

(100) Nabid, M. R.; Bide, Y.; Aghaghafari, E.; Rezaei, S. J. T. PdNPs@P2VP-Fe3O4 Organic-Inorganic Hybrid Microgels as a Nanoreactor for Selective Aerobic Oxidation of Alcohols. *Catal. Letters* **2014**, *144* (2), 355–363. https://doi.org/10.1007/s10562-013-1107-2.

(101) Linke, A.; Schmidt, M.; Waldvogel, S. R. Poly(2-Vinylpyridine)-Based Polymers as an Efficient Affinity Material for the Detection of Airborne Phenol. *Chempluschem* **2015**, *80* (7), 1096–1099. https://doi.org/10.1002/cplu.201500108.

(102) Tsutsumi, K.; Funaki, Y.; Hirokawa, Y.; Hashimoto, T. Selective Incorporation of Palladium Nanoparticles into Microphase-Separated Domains of Poly(2-Vinylpyridine)-Block-Polyisoprene. *Langmuir* **1999**, *15* (16), 5200–5203. https://doi.org/10.1021/la990246l.

(103) Gupta, S.; Uhlmann, P.; Agrawal, M.; Chapuis, S.; Oertel, U.; Stamm, M. Immobilization of Silver Nanoparticles on Responsive Polymer Brushes. **2008**, 2874–2879.

(104) Lou, X.; Detrembleur, C.; Pagnoulle, C.; Jérôme, R.; Bocharova, V.; Kiriy, A.; Stamm, M. Surface Modification of Multiwalled Carbon Nanotubes by Poly(2-Vinylpyridine): Dispersion, Selective Deposition, and Decoration of the Nanotubes. *Adv. Mater.* **2004**, *16* (23–24), 2123–2127. https://doi.org/10.1002/adma.200400298.

(105) Cummins, C.; Bell, A. P.; Morris, M. A. Creating Active Device Materials for Nanoelectronics Using Block Copolymer Lithography. *Nanomaterials* **2017**, *7* (10). https://doi.org/10.3390/nano7100304.

(106) Mokarian-Tabari, P.; Senthamaraikannan, R.; Glynn, C.; Collins, T. W.; Cummins, C.; Nugent, D.; O'Dwyer, C.; Morris, M. A. Large Block

Copolymer Self-Assembly for Fabrication of Subwavelength Nanostructures for Applications in Optics. *Nano Lett.* **2017**, *17* (5), 2973–2978. https://doi.org/10.1021/acs.nanolett.7b00226.

(107) Balzani, V.; Ceroni, P.; Credi, A.; Venturi, M. Ruthenium Tris(Bipyridine) Complexes: Interchange between Photons and Electrons in Molecular-Scale Devices and Machines. *Coord. Chem. Rev.* **2021**, *433*. https://doi.org/10.1016/J.CCR.2020.213758.

(108) Kennemur, J. G. Poly(Vinylpyridine) Segments in Block Copolymers: Synthesis, Self-Assembly, and Versatility. *Macromolecules* **2019**, *52*, 1354–1370. https://doi.org/10.1021/acs.macromol.8b01661.

(109) Kennemur, J. G. Poly(Vinylpyridine) Segments in Block Copolymers: Synthesis, Self-Assembly, and Versatility. *Macromolecules*. 2019, pp 1354–1370. https://doi.org/10.1021/acs.macromol.8b01661.

(110) Wang, Y.; Yang, H.; Chen, S.; Chen, H.; Chai, Z. Fabrication of Hybrid Polymeric Micelles Containing AuNPs and Metalloporphyrin in the Core. *Polymers (Basel).* **2019**, *11* (3). https://doi.org/10.3390/polym11030390.

(111) Raczkowska, J.; Stetsyshyn, Y.; Awsiuk, K.; Zemła, J.; Kostruba, A.; Harhay, K.; Marzec, M.; Bernasik, A.; Lishchynskyi, O.; Ohar, H.; Budkowski, A. Temperature-Responsive Properties of Poly(4-Vinylpyridine) Coatings: Influence of Temperature on the Wettability, Morphology, and Protein Adsorption. *RSC Adv.* **2016**, *6* (90), 87469–87477. https://doi.org/10.1039/c6ra07223b.

(112) Lee, J.; Mishra, A. K.; Choi, C.; Kim, D.; Kim, E. Y.; Yong, K.; Kim, J. K. Three-Dimensional Nanoporous Metal Structures from Poly(2-Vinylpyridine)-Block -Poly(4-Vinylpyridine) Copolymer Thin Film . *ACS Appl. Mater. Interfaces* **2020**, *12* (13), 15667–15674. https://doi.org/10.1021/acsami.9b23009.

(113) Albadi, J.; Keshavarz, M.; Shirini, F.; Vafaie-Nezhad, M. Copper Iodide Nanoparticles on Poly(4-Vinyl Pyridine): A New and Efficient Catalyst for Multicomponent Click Synthesis of 1,4-Disubstituted-1,2,3-Triazoles in Water. *Catal. Commun.* **2012**, *27*, 17–20. https://doi.org/10.1016/j.catcom.2012.05.023.

(114) Li, Y.; Fan, K.; Ban, H.; Yang, M. Detection of Very Low Humidity Using Polyelectrolyte/Graphene Bilayer Humidity Sensors. *Sensors Actuators, B Chem.* **2016**, *222*, 151–158. https://doi.org/10.1016/j.snb.2015.08.052.

(115) Ozay, O.; Akcali, A.; Otkun, M. T.; Silan, C.; Aktas, N.; Sahiner, N. P(4-VP) Based Nanoparticles and Composites with Dual Action as Antimicrobial Materials. *Colloids Surfaces B Biointerfaces* **2010**, *79* (2), 460–466. https://doi.org/10.1016/j.colsurfb.2010.05.013.

(116) Kalteis, T.; Lüring, C.; Gugler, G.; Zysk, S.; Caro, W.; Handel, M.; Grifka, J.

Akute Gewebetoxizität von PMMA-Knochenzementen. *Z. Orthop. Ihre Grenzgeb.* **2004**, *142* (6), 666–672. https://doi.org/10.1055/s-2004-832317.

(117) Schilling, A. F.; Linhart, W.; Filke, S.; Gebauer, M.; Schinke, T.; Rueger, J. M.; Amling, M. Resorbability of Bone Substitute Biomaterials by Human Osteoclasts. *Biomaterials* **2004**, *25* (18), 3963–3972. https://doi.org/10.1016/j.biomaterials.2003.10.079.

(118) Zheng, W.; Wong, S. C. Electrical Conductivity and Dielectric Properties of PMMA/Expanded Graphite Composites. *Compos. Sci. Technol.* **2003**, *63* (2), 225–235. https://doi.org/10.1016/S0266-3538(02)00201-4.

(119) Philip, B.; Abraham, J. K.; Chandrasekhar, A. Carbon Nanotube / PMMA Composite Thin Films for Gas-Sensing Applications. *935*, 1–6.

(120) Liu, J.; Liu, T.; Kumar, S. Effect of Solvent Solubility Parameter on SWNT Dispersion in PMMA. *Polymer (Guildf).* **2005**, *46* (10), 3419–3424. https://doi.org/10.1016/j.polymer.2005.02.086.

(121) Yoshinaga, K.; Fujiwara, K.; Mouri, E.; Ishii, M.; Nakamura, H. Stepwise Controlled Immobilization of Colloidal Crystals Formed by Polymer-Grafted Silica Particles. *Langmuir* **2005**, *21* (10), 4471–4477. https://doi.org/10.1021/la0467786.

(122) Oultache, A. K.; Prud'homme, R. E. XPS Studies of Ni Deposition on Polymethyl Methacrylate and Poly(Styrene-Co-Acrylonitrile). *Polym. Adv. Technol.* **2000**, *11* (6), 316–323. https://doi.org/10.1002/1099-1581(200006)11:6<316::AID-PAT983>3.0.CO;2-S.

(123) Steiner, G.; Zimmerer, C.; Salzer, R. Characterization of Metal-Supported Poly(Methyl Methacrylate) Microstructures by FTIR Imaging Spectroscopy. *Langmuir* **2006**, *22* (9), 4125–4130. https://doi.org/10.1021/la053221x.

(124) Pawar, P. G.; Xing, R.; Kambale, R. C.; Kumar, A. M.; Liu, S.; Latthe, S. S. Polystyrene Assisted Superhydrophobic Silica Coatings with Surface Protection and Self-Cleaning Approach. *Prog. Org. Coatings* **2017**, *105*, 235–244. https://doi.org/10.1016/j.porgcoat.2017.01.016.

(125) Kim, J.; Jung, H. Y.; Park, M. J. End-Group Chemistry and Junction Chemistry in Polymer Science: Past, Present, and Future. *Macromolecules* **2020**, *53* (3), 746–763. https://doi.org/10.1021/acs.macromol.9b02293.

(126) Maharana, T.; Negi, Y. S.; Mohanty, B. Review Article: Recycling of Polystyrene. *Polym. - Plast. Technol. Eng.* **2007**, *46* (7), 729–736. https://doi.org/10.1080/03602550701273963.

(127) Ibrahim, S.; El-Naggar, M. E.; Youssef, A. M.; Abdel-Aziz, M. S. Functionalization of Polystyrene Nanocomposite with Excellent Antimicrobial Efficiency for Food Packaging Application. *J. Clust. Sci.* **2020**, *31* (6), 1371–1382. https://doi.org/10.1007/s10876-019-01748-9.

(128) Cummins, C.; Weingärtner, T.; Morris, M. A. Enabling Large-Area Selective Deposition on Metal-Dielectric Patterns Using Polymer Brush Deactivation. *J. Phys. Chem. C* **2018**, *122* (26), 14698–14705. https://doi.org/10.1021/acs.jpcc.8b04092.

(129) Oria, L.; Luzuriaga, A. R. De; Alduncin, J. A.; Perez-murano, F. Microelectronic Engineering Polystyrene as a Brush Layer for Directed Self-Assembly of Block Co-Polymers. *Microelectron. Eng.* **2013**, *110*, 234–240. https://doi.org/10.1016/j.mee.2012.12.006.

(130) Klesko, J. P.; Rahman, R.; Dangerfield, A.; Nanayakkara, C. E.; L'Esperance, T.; Moser, D. F.; Fabián Peña, L.; Mattson, E. C.; Dezelah, C. L.; Kanjolia, R. K.; Chabal, Y. J. Selective Atomic Layer Deposition Mechanism for Titanium Dioxide Films with (EtCp)Ti(NMe2)3: Ozone versus Water. *Chem. Mater.* **2018**, *30* (3), 970–981. https://doi.org/10.1021/acs.chemmater.7b04790.

(131) Shimizu, H.; Watanabe, N.; Morikawa, T.; Shima, A.; Iwamuro, N. 1.2 KV Silicon Carbide Schottky Barrier Diode Embedded MOSFETs with Extension Structure and Titanium-Based Single Contact. *Jpn. J. Appl. Phys.* **2020**, *59* (2). https://doi.org/10.7567/1347-4065/ab65a5.

(132) Korzhenko, D. V.; Yurjev, Y. N.; Emlin, D. R.; Plotnikov, S. A.; Vladimirov, A. B.; Romanov, I. Y.; Loginov, B. A.; Loginov, A. B. Comparative Analysis of Properties of the Carbon-Based Coatings Obtained through Various PVD and CVD Deposition Methods. *J. Phys. Conf. Ser.* **2020**, *1443* (1). https://doi.org/10.1088/1742-6596/1443/1/012006.

(133) Smith, R. C.; Ma, T.; Hoilien, N.; Tsung, L. Y.; Bevan, M. J.; Colombo, L.; Roberts, J.; Campbell, S. A.; Gladfelter, W. L. Chemical Vapour Deposition of the Oxides of Titanium, Zirconium and Hafnium for Use as High-k Materials in Microelectronic Devices. A Carbon-Free Precursor for the Synthesis of Hafnium Dioxide. *Adv. Funct. Mater.* **2000**, *10* (3–5), 105–114. https://doi.org/10.1002/1099-0712(200005/10)10:3/5<105::aid-amo402>3.0.co;2-j.

(134) Peter, S.; Ehrler, R.; Seyller, T.; Speck, F. Annealing Effects on A-SiC:H and a-SiCN:H Films Deposited by Plasma CVD Methods. *Vacuum* **2020**, *178* (April), 109410. https://doi.org/10.1016/j.vacuum.2020.109410.

(135) Nowling, G. R.; Babayan, S. E.; Jankovic, V.; Hicks, R. F. Remote Plasma-Enhanced Chemical Vapour Deposition of Silicon Nitride at Atmospheric Pressure. *Plasma Sources Sci. Technol.* **2002**, *11* (1), 97–103. https://doi.org/10.1088/0963-0252/11/1/312.

(136) Farling, C. G.; Stackaruk, M. C.; Pye, C. C.; Brosseau, C. L. Fabrication of High Quality Electrochemical SERS (EC-SERS) Substrates Using Physical Vapour Deposition. *Physical Chemistry Chemical Physics*. 2021. https://doi.org/10.1039/d1cp02416g.

(137) Oviroh, P. O.; Akbarzadeh, R.; Pan, D.; Coetzee, R. A. M.; Jen, T. C. New

Development of Atomic Layer Deposition: Processes, Methods and Applications. *Science and Technology of Advanced Materials*. 2019, pp 465–496. https://doi.org/10.1080/14686996.2019.1599694.

(138) Peng, Q.; Tseng, Y. C.; Darling, S. B.; Elam, J. W. A Route to Nanoscopic Materials via Sequential Infiltration Synthesis on Block Copolymer Templates. *ACS Nano* **2011**, *5* (6), 4600–4606. https://doi.org/10.1021/nn2003234.

(139) Snelgrove, M.; Zehe, C.; Lundy, R.; Yadav, P.; Rueff, J.-P.; O'Connor, R.; Bogan, J.; Hughes, G.; McGlynn, E.; Morris, M.; Mani-Gonzalez, P. G. Surface Characterization of Poly-2-Vinylpyridine—A Polymer for Area Selective Deposition Techniques. *J. Vac. Sci. Technol. A* **2019**, *37* (5), 050601. https://doi.org/10.1116/1.5115769.

(140) Mani-Gonzalez, P. G.; Snelgrove, M.; Rueff, J.-P.; Lundy, R.; Yadav, P.; Bogan, J.; O'Connor, R.; Morris, M.; Hughes, G. Analysis of Al and Cu Salt Infiltration into a Poly 2- Vinylpyridine (P2vP) Polymer Layer for Semiconductor Device Patterning Applications. *J. Phys. D. Appl. Phys.* **2019**, 1–20. https://doi.org/10.1088/1361-6463/ab60e8.

Chapter 2. Optimizing polymer brush coverage to develop highly coherent sub 5 nm oxide film by ion inclusion.

2.1 Abstract:

Area selective deposition is promising technique for positional self-alignment of materials at pre-patterned surfaces. Critical to this is the development of molecular systems that have selective surface binding and can act as a template to material growth. This chapter reports how end functionalized polymers can be used to create oxide films through a grafting method. Here, we detail a facile approach for rapid grafting (in seconds) of polymer brush films with complete coverage over large areas with high uniformity (pinhole free). Subsequent conversion to an oxide (~3-4 nm thickness) is performed via liquid phase metal ion infiltration. Exposing the covalently grafted polymer brush (P2VP-OH) to a metal salt-solvent solution (using the Al^{3+} ion as a model species) swells the polymer, facilitating ion inclusion. Early results suggest a solvent mediated approach to polymer film infiltration can be used to develop inorganic films in a facile process. Whilst data shows inclusion into both large area and patterned films, the mechanism and understanding of these has been limited. In particular, the solution-mediated process described here shows the preparation of nano-metal oxide films of tuneable thickness. Here, a simple process is demonstrated for the fabrication of highly ordered materials enabling them to be transferred from the template polymer brush with precision. A surface deactivation strategy is also realized using a hydroxyl-terminated polystyrene (PS-OH) brush that prevents the deposition of ions. We consider this strategy as means to prevent electro migration of ions as well as the possibility of coating ALD layers.

2.2 Introduction:

The continual aggressive miniaturization of semiconductor devices with critical dimensions approaching 5 nm has led to cost and integration challenges.[1] Novel methods to compliment optical lithography (namely i193 and EUV) include block copolymer [2–8] (BCP) lithography, nanoimprint lithography [9,10] and, more recently, area selective deposition [11] (ASD). These methods are potential candidates for integration into future fabrication and the possibility of selective inclusion of materials *e.g.* metal, metal oxides, dielectrics may afford a direct means of generating material patterns. Thus, these techniques can reduce the number of processing steps by permitting growth of materials in desired wafer regions only. Further, BCP lithography and ASD can be implemented to assist shrinking metal and metal oxide line widths to help alleviate registration and edge placement errors. Methods for producing high quality metal and oxide films are particularly useful as they can deliver potential materials to augment silicon device technologies particularly in monolithic integration. The techniques we discuss here may have significant relevance in this area since they are below the low temperature ceiling (<500 °C) required for CMOS fabrication.[12] Oxide materials can support development of future functional devices with high and low dielectric constant (κ), ferroelectric, magnetic and optical properties.[13] For logic and memory integration, applications can range from the low-κ films that sustain electrical isolation between interconnects through to the high-κ gate oxide. Usage has even been extended to high contrast oxide etch masks during device fabrication.[14,15]

Diverse methods have been studied hitherto in the ASD field encompassing the use of self-assembled monolayers and unreactive polymer layers. These have been combined with atomic layer deposition (ALD) in order to deposit precise metal or dielectric layers. For example, Bent and co-workers have introduced the feasibility of self-assembled monolayers to activate and deactivate patterned copper-silicon line/space[16,17] and other substrate materials[18–22] in conjunction with ALD. Likewise Ritala and Leskelä have implemented

well-defined strategies to pattern self-assembled monolayers to produce features on silicon and copper substrates.[23–25] Further, they have demonstrated the use of patterned polymer films as activation[26,27] and deactivation[28,29] layers for a range of selective ALD processes. Additionally, ALD has been shown by Parsons and co-workers to selectively deposit material on silicon and silicon nitride via surface deactivation with SAMs,[30] using patterned amorphous carbon [31] or by utilizing inherent substrate selectivity.[32–34] The Parsons group has recently demonstrated a viable ASD approach without using organic inhibitors by combining ALD with Atomic layer etching cycles.[35] Kessels and coworkers have established several area selective ALD approaches that exploit: unreactive polymers as inhibitors for ALD precursors,[36] surface activation via reactive plasma micro patterning,[37] catalytic oxygen activation of noble metal surfaces,[38] and by using a three-step ALD cycle comprising a selective organic inhibitor, precursor and reactive plasma process.[39] Kessels and coworkers have even extended the work to resist-free area-selective ALD on graphene surfaces.[40] Work by Cummins and Morris demonstrated how polymer brush layers can be used to selectively activate or deactivate patterned Cu/SiO_2 substrates for ASD of metal and metal oxide films.[41,42]

In this chapter, we focus on developing a rapid technique for grafting polymer brushes via condensation reactions[43,44] with very high coverage and uniformity followed by a subsequent conversion process to aluminum oxide. We describe a robust, facile process to infiltrate hydroxyl-terminated poly-2-vinyl pyridine (P2VP-OH) (**Figure 2.1 (a)**) films via metal ion diffusion to produce ~3.5 nm thick oxide films across large areas. Moreover, we elucidate a deactivation strategy using a hydroxyl-terminated polystyrene (PS-OH) (**Figure 2.1 (b)**) brush that prevents the infiltration of ions and subsequent film formation. The latter strategy suggests a means to prevent electromigration of ions as well as the possibility to coat ALD layers. Polymer selective casting/salt solutions were used to ensure uniform, high quality grafted brush films and to facilitate swelling during the ion inclusion process. We chose the

monoatomic Al^{3+} trication as a model species for liquid phase ion inclusion. The Al^{3+}ion has potent Lewis acidity,[45] forms stable acid-base interactions to pyridine's nitrogen atoms[46,47] and is capable of forming a metal coordination center with multiple pyridine ligands.[48] The infiltration process is also implemented on these two systems combined as poly (styrene)-block-poly (4-vinyl-pyridine) (PS-b-P4VP) (**Figure 2.1 (c)**) to highlight the selectivity of the inclusion process. Finally, the infiltrated polymers were converted to oxide films and nanowires.

Our results highlight the critical parameters required for optimizing polymer brush deposition and coverage, while demonstrating the selective capacity for ion inclusion (P2VP/P4VP) and suitability for surface deactivation (PS). This work provides insight into the ion inclusion/blocking capability of these polymers and may elucidate ways to exploit their ASD potential in future device-processing strategies.

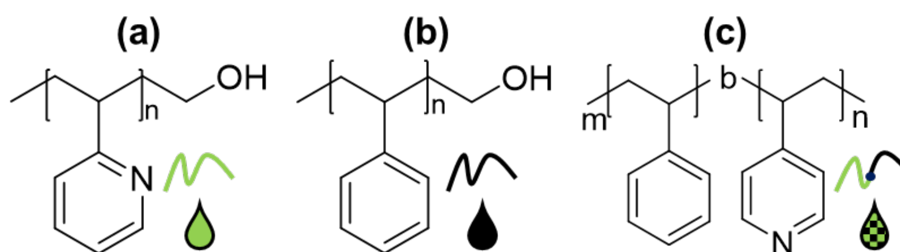

Figure 2.1. (a) Poly-2-(vinyl pyridine) hydroxyl terminated **(b)** Poly-(styrene) hydroxyl terminated **(c)** poly (styrene)-block-poly (4-vinyl pyridine).

2.3 Experimental section:

2.3.1 Materials:

Hydroxy-terminated (PS-OH) (P11116-SOH) (PDI: 1.05), hydroxy-terminated (P2VP-OH) (P7544-2VPOH) (PDI: 1.05), polystyrene (PS) (P9405-S) (PDI: 1.03), poly-2-vinyl pyridine (P2VP) (P41306-2VP) (PDI: 1.04), poly(styrene)-block-poly(4-vinyl-pyridine) (PS-b-P4VP) (P9009-S4VP) (PDI: 1.10) were purchased from Polymer Source (Canada) and used

without further purification. The polymers have glass transition temperatures of T_g = 95°C and 91°C for PS-OH and P2VP-OH respectively. The molecular weight of the functionalized homopolymers is 6 kg $mol.^{-1}$The block molecular weights of the PS-b-P4VP were 24 kg mol^{-1} and 9.5 kg $mol.^{-1}$ The degree of polymerization for PS-b-P4VP was calculated as N=320. Tetrahydrofuran (THF) (inhibitor free), toluene, chloroform, anhydrous ethanol, hydrogen peroxide and sulphuric acid (MERCK, Ireland) were high-performance liquid chromatography (HPLC) grade and used as received. Deionized water (ρ = 18.2 MΩ.cm) was used were necessary. Aluminum nitrate nonahydrate ($Al(NO_3)_3.9H_2O$, 99.997%) was purchased from Merck, Ireland.

2.3.2 Fabrications:

Silicon substrates with native oxide were cleaved into 2 cm^2 pieces and degreased by ultrasonication in THF for 20 min. Substrate surfaces were cleaned and hydroxyl functionalised using an oxygen plasma treatment for 5 min (**Figure 2.2 (a)**) (40 kHz, 50 W, Barrel Asher) (see **Figure S2.7.1** for functionalization data). The P2VP-OH and PS-OH brushes were dissolved in THF and toluene respectively by stirring overnight at room temperature to yield 0.2 wt.% polymer solutions and spin coated at 3000 rpm for 30 seconds (**Figure 2.2 (b)**). Samples were placed on a hotplate and annealed for 1 min between 20-260°C. Following this samples were sonicated in respective solvents for 20 min (2 x 10 min washes). This was carried out to remove physisorbed ungrafted polymer material and produce monolayer coverage (**Figure 2.2 (c)**). It should be noted that the selection of polymer concentration in the casting solution is important for generation of regular polymer films particularly for reactive brushes such as P2VP. This will be discussed in detail in chapter 3. Aluminum nitrate solution (0.5 wt.% in ethanol) was spin coated (3000 rpm/30s) onto the grafted films (**Figure 2.2 (d)**). Conversion to oxide and polymer ashing was performed by exposing to UV/ozone for 3 h. (**Figure 2.2 (e)**) (Novascan PDSP-UV4). A

similar process was carried out for preparation of nanolines and nanodots using PS-b-P4VP with the self-assembly process described in literature.[49–51]

The unfunctionalized P2VP and PS homopolymers were used to fabricate pure PS and P2VP substrates. The powders were dry-pressed into disc-shaped pellets ≈2 mm thick at a pressure of 350 MPa in a 13 mm diameter steel pellet die (Specac, 13 mm evacuable pellet die). The as pressed pellets were exposed to selective solvent vapor (THF for P2VP and Toluene for PS) until a smooth mirror like surface was produced (~5 min.) (See **Figure S2.7.2**).

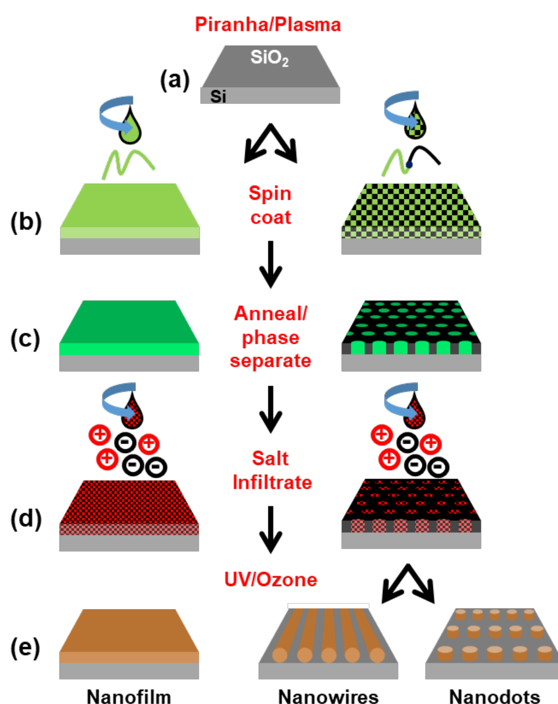

Figure 2.2: Process flow for the preparation of (a)-(c) polymer brush and block copolymer films (d) ion infiltration and (e) polymer ashing and conversion to oxide.

2.3.3 Characterization:

Field emission scanning electron microscopy (FESEM, Carl Zeiss Ultra) was performed using a secondary electron detector (InLens), 1 kV accelerating voltage). Focused ion beam etching (FIB, Helios Nanolab 460) was used for preparing lamella using standard high kV milling and a final low kV final polish, this rendered the lamella electron transparent indicating it is an appropriate thickness for TEM. A platinum capping layer was used.

Transmission electron microscopy (TEM, FEI Osiris) was performed using brightfield and STEM imaging. During STEM detector lengths were 220, 550 and 770 mm. The accelerating voltage was 200 kV. The EDX beam current was 1 nA, acquisition time: 30 min. Atomic force microscopy (AFM, Park Systems XE7) was used with a non-contact cantilever (AC160TS, force constant ~26Nm^{-1}, resonant frequency = ~300 kHz).

X-ray photoelectron spectroscopy (XPS, VG Scientific ESCAlab Mk II) was performed under ultra-high vacuum conditions (<5 x 10^{-10} mbar) using a hemispherical analyzer and Al Kα X-rays (1486.6 eV). The emitted photoelectrons were collected at a take-off angle of 90 ° from the samples surface. The analyzer pass energy was set to 100 eV for survey scans and 40 eV for high-resolution core scans, yielding an overall resolution of 1.5 eV. Photoemission peak positions were corrected to C 1s at a binding energy of 248.8 eV.

Dynamic contact angle (CA) measurments (custom built system) were recorded on five different regions of each sample using a high-speed camera (60 Hz sampling rate) to capture the advancing and receding CAs of three probe liquids (water, diiodomethane and glycerol). Liquids were dispensed with flow rates of 5 nls^{-1} using a 35-gauge needle (Ø135 µm OD) with droplet volumes between 40-100 nl. Surface energy analysis was determined from the advancing CAs of the three probe liquids using the Lifshitz-van der Waals/acid-base approach.[52]

Thermogravimetric analysis (TGA, Pyris 1) was performed on the homopolymers at a temperature range of 25°C - 700°C for 90 min.

2.4 Result:

2.4.1 Polymer brush optimization.

Selective casting solutions were identified based on the polymer-solvent Flory-Huggins interaction parameter χ_{AB}. Systems with a low interaction parameter attain a high miscibility.

Hansen solubility approach was employed to estimate χ_{AB}.[53] With the Hansen approach the Flory-Huggins parameter is given by equation 1 (also see **Table 1** below):

$$\chi_{AB} = \frac{V_S}{4RT}\left[4\left(\delta_{d,A} - \delta_{d,B}\right)^2 + \left(\delta_{p,A} - \delta_{p,B}\right)^2 + \left(\delta_{h,A} - \delta_{h,B}\right)^2\right] \quad [1]$$

where V_S is the molecular volume, R is the gas constant and T is the temperature (K). Material specific solubility parameters for non-specific dispersive (δ_d), specific polar (δ_p) and specific hydrogen bonding (δ_h) interactions for solvents and PS were found from ref .[53,54] Solubility parameters for P2VP were obtained from ref [55] (see section S2.7.2). For P2VP-OH we chose the aprotic, moderately polar solvent THF ($\chi_{2VP\text{-}THF} \approx 0.13$) and the relatively non-polar solvent toluene for PS-OH ($\chi_{PS\text{-}Tol} \approx 0.06$) as highly selective solvents.

Table 1. Polymer-Solvent Flory-Huggins Interaction Parameters Estimated Using Eq. 1 at T = 298 K.

Combination	P2VP/ THF	PS/ Tol	P2VP/ EtOH	PS/ EtOH
χ_{AB}	0.13	0.06	0.38	1.93

Figure 2.3 shows optimization data used for grafting P2VP-OH and PS-OH (Mw = 6 kg mol^{-1}) polymer brush films to silicon substrates. **Figure 2.3 (a)** displays TGA data for PS-OH and P2VP-OH. The polymers undergo thermal degradation (PS-OH ~ 260 °C, P2VP-OH ~ 320 °C) indicating the maximum upper threshold for the grafting process in order to avoid degradation of the polymer brushes. P2VP-OH films were cast and annealed over a temperature range of 20–260 °C and PS-OH between 20–190 °C for 1 min. Advancing water contact angle (WCA) measurements were immediately recorded on the grafted brushes and the pressed polymer pellets (**Figure 2.3 (b)**). The control SiO_2 sample has an average advancing WCA of θ_{SiO2} = 12.1° ± 0.9° with no apparent increase in WCA value observed

for the polymer cast samples at temp <100^0C. Above a value of 100^0, the advancing WCAs for the PS-OH samples rapidly asymptote and saturate with an average advancing WCA of θ_a = 90.3° ± 1.5° at 150 °C, similar to the value obtained for the pressed PS pellet ($\theta_{PS(max)}$ = 90.2° ± 0.5°). The WCAs for the P2VP-OH samples increase at a slower rate, reaching a 76.7° ± 1.1° above 230 °C ($\theta_{P2VP(max)}$ = 76.7° ± 1.7°).

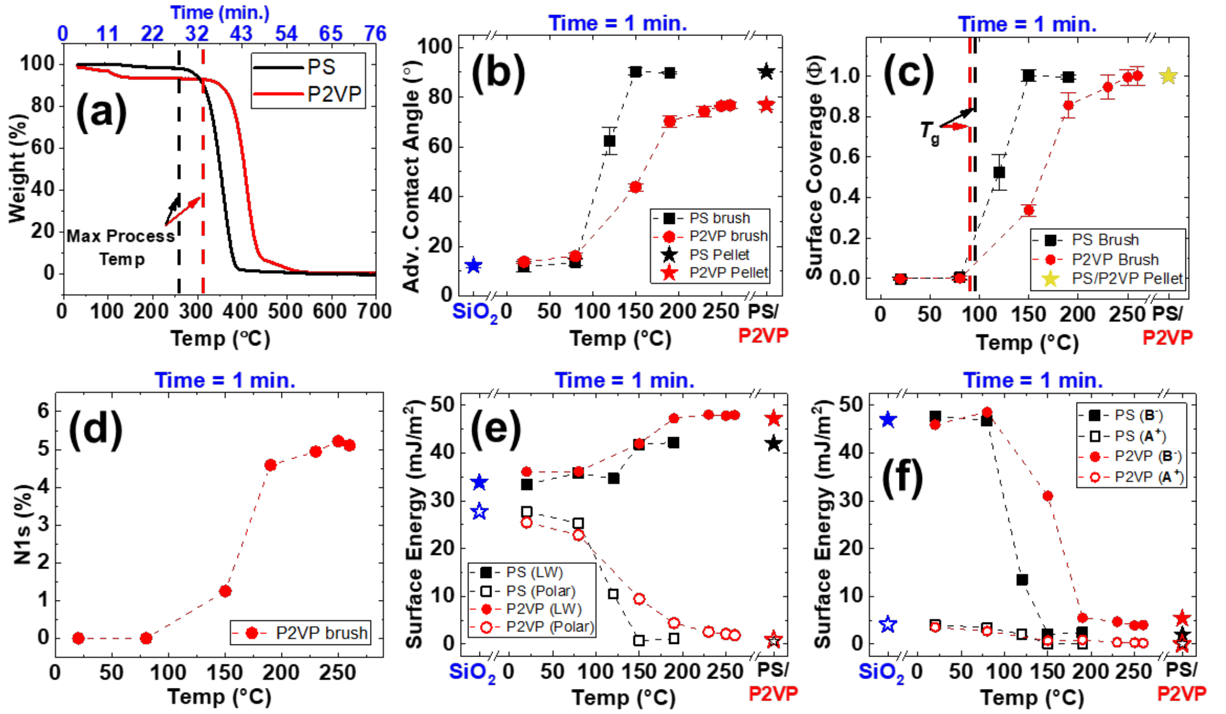

Figure 2.3: (a) Thermogravimetric analysis of the P2VP-OH and PS-OH brushes. (b)Advancing water contact angles of brush samples annealed over the range of the temperatures with corresponding coverages (c). (d) XPS N 1s atomic percentages of P2VP-OH grafted polymer brush as a function of the temperature. (e) apolar (LW) and polar surface energy. (f) Lewis acid (A^+) and Lewis base (B^-) interactions for annealed brush samples. The dashed lines are the guide for the eye.

To correlate the observed θ_a behavior with the surface coverage of the PS-OH and P2VP-OH brushes we used the Cassie-Baxter equation[56,57] under the assumption of surface energy heterogeneity at the molecular scale,[58]

$$\Phi = \left(\frac{\cos\theta_{temp}}{\cos\theta_{SiO_2}} - 1\right) \Big/ \left(\frac{\cos\theta_{max}}{\cos\theta_{SiO_2}} - 1\right) \qquad [2]$$

Where Φ is the apparent surface coverage of the grafted polymer brush, θ_{temp} is θ_a measured at a given temperature and θ_{max} is θ_a of the PS and P2VP pellets ($\theta_{PS(max)}$ and $\theta_{P2VP(max)}$). **Figure 2.3(c)** shows the evolution of surface coverage with annealing temperature for the brush samples, calculated using equation 2. For both PS-OH and P2VP-OH, grafting only occurs above the glass transition temperature (T_g). Even though T_g is similar for both polymers, we attribute the slower rate of grafting for P2VP-OH with strong pyridine-pyridine stacking interactions [59] which would retard chain reptation kinetics. Using XPS, the N 1s signal was tracked for the P2VP-OH samples over the temperature range in **Figure 2.3 (d)**, with a similar evolution profile to **Figure 2.3 (b)** and **(c). Figure 2.3 (e)** shows the Liftshitz-van der Walls (apolar) interactions (LW) and Lewis acid-base interactions (polar) for the PS-OH and P2VP-OH samples. At temperature < 100 °C the surface energy components of the PS-OH and P2VP-OH samples are similar to the values obtained for the SiO_2 control ($LW_{SiO2} \approx 34$ mJ/m^2, $Polar_{SiO2} \approx 28$ mJ/m^2). At increased temperatures, the surface energy components of the samples transition to the values obtained for the PS and P2VP pellets ($LW_{PS} \approx 42$ mJ/m^2, $Polar_{PS} \approx 0$ mJ/m^2 and $LW_{P2VP} \approx 47$ mJ/m^2, $Polar_{P2VP} \approx 1$ mJ/m^2). The large decrease in polar surface energy for samples annealed at optimum grafting temperatures is consistent with very high coverage of the grafted polymer brushes which screen polar interactions from the underlying oxide surface. **Figure 2.3 (f)** displays the Lewis acid (A^+) and Lewis base (B^-) interactions. For samples annealed at temperature < 100 °C, A^+ and B^- resemble the values of the SiO_2 control ($A^+_{SiO2} \approx 4$ mJ/m^2, $B^-_{SiO2} \approx 47$ mJ/m^2). At higher temperatures these components evolve to the values obtained for the PS and P2VP pellets ($A^+_{PS} \approx 0$ mJ/m^2, $B^-_{PS} \approx 0$ mJ/m^2 and $A^+_{P2VP} \approx 0$ mJ/m^2, $B^-_{P2VP} \approx$ 5 mJ/m^2).

We note that casting spin speed had no observable impact on coverage (**Figure S2.7.3**). To capture the grafting process over longer timescales we cast and annealed the polymers at

fixed temperatures (PS-OH = 120 °C, P2VP-OH = 150). At these temperatures, complete grafting took as long as 40 min (**Figure S2.7.4**).

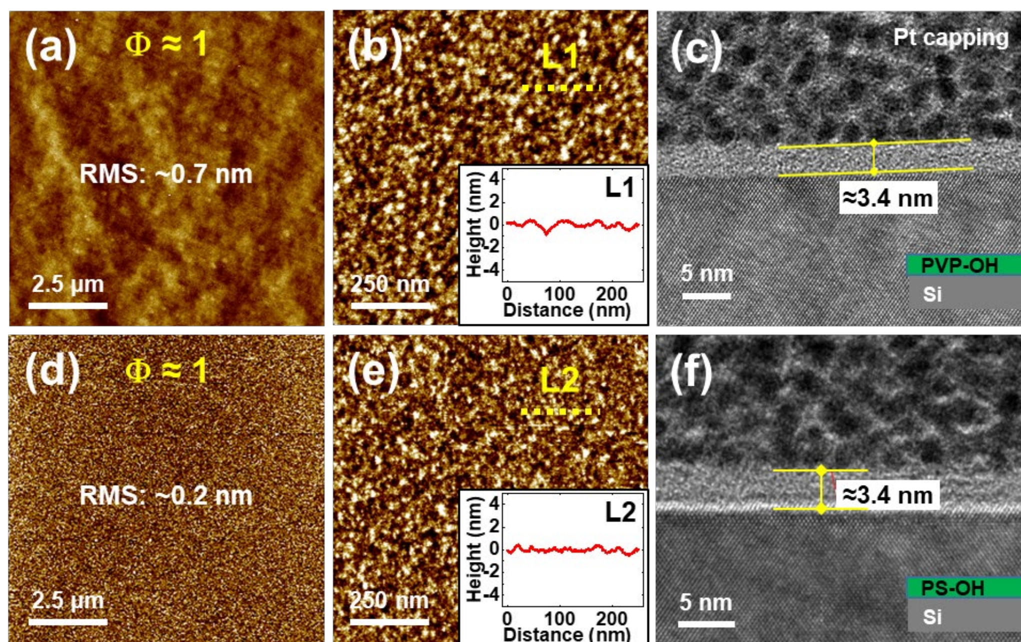

Figure 2.4: (a) and (b) AFM images with roughness profile at L1 (inset), (c) Bright field TEM images of P2VP grafted polymer brush. (d)-(f) are of PS grafted polymer brush.

To covalently grafts a polymer brush, the polymer chains, must reptate until the hydroxyl end groups locate the substrate and overcome the thermodynamic reaction barrier to condensation.[44] The more rapid bonding process is effectively limited by the slower diffusional processes .[60] The Rouse model predicts faster diffusion kinetics with temperature ($D \propto T$), where D is the chain diffusion coefficient.[61] Our results demonstrate complete grafting for both PS-OH (~ 150 °C) and P2VP-OH (~ 230 °C) in 1 min without compromising thermal limitations. Conceivably this is a compelling advantage over self-assembled monolayer (SAM) ASD approaches where deposition times are typically hours to days.

Figure 2.4 (a) – (f) shows AFM and TEM data of optimized grafted polymer brushes. The grafted polymer films are very smooth with the RMS roughness for P2VP-OH ≈ 0.7 nm (**Figure 2.4 (a)**) and PS-OH ≈ 0.2 nm (**Figure 2.4 (d)**) as determined by AFM scans (3

scans). The roughness factor r, defined as the ratio of actual surface area to projected area, was calculated from the height images in Figure **2.4 (a)** and **(d)** to be ≈ 1.04 for P2VP-OH and ≈ 1.003 for PS-OH, low values representing minimal contribution to surface wettability as per the Wenzel equation, $\cos\theta_{apparent} = r\cos\theta$.[62] The grafted brush films are high quality with no pinholes present in the high-res height images in **Figure 2.4 (b)** and **(e)** for P2VP-OH and PS-OH brushes respectively with linescans taken at L1 and L2 (inset). TEM cross-sections of the grafted P2VP-OH **Figure 2.4 (c)** and PS-OH **Figure 2.4 (f)** show the brush films with thickness ≈ 3.5 nm. See **Figure S.2.7.5** and **S2.7.6** for elemental EDX mapping of the films. We note that from AFM scans that P2VP-OH films require more thorough washing compared to the PS-OH films to completely remove physisorbed polymer. This is consistent with the strong pyridine-pyridine stacking due to substantial π-orbital interactions.[59] To ensure all unbound overlayers are more efficiently removed a more selective solvent such as ethyl lactate ($\chi_{2VP\text{-}EL}$ ≈ 0.02) or heating during washing will reduce the χ_{AB} value (see Eq. 1). See **Figure S2.7.7 (a)** for optical microscopy of the grafted P2VP-OH film.

2.4.2 P2VP-OH ion inclusion:

Figure 2.5 shows data from the ion inclusion and ashing process for a P2VP-OH grafted brush. The TEM cross section in **Figure 2.5 (a)** is of the P2VP-OH brush exposed to an aluminum nitrate solution. To assist metal ion insertion, the salt was dissolved in ethanol, a P2VP selective solvent ($\chi_{2VP\text{-}EtOH}$ ≈ 0.38) (Table 1). The grafted P2VP-OH film (≈ 3.5 nm, **Figure 2.4 (c)**) swells following exposure to the salt solution, indicating ion uptake (≈ 4-6 nm, **Figure 2.5 (a)).** Subsequently the UV/ozone exposure reduces thickness (≈ 2-3 nm **Figure 2.5 (b)**), consistent with polymer ashing and film densification. No obvious defects are present in the SEM image (inset). The EDX elemental maps in **Figure 2.5 (c)** show the incorporation of aluminum, see **Figure S2.7.8** for additional EDX data. **Figure 2.5 (d-f)** displays the XPS survey and high-res spectra of the process. The spectra of the N 1s region

for the grafted P2VP-OH film has a peak at ≈ 399 eV associated with C=N-C pyridine bonds.[63] Following salt infiltration this peak attenuates and a nitrate peak appears at ≈ 407 eV [64] along with an Al 2p peak (survey), indicating that both the aluminum and nitrate counter ion infiltrate the P2VP-OH brush layer. Post UV/ozone, the pyridine and nitrate N 1s signals disappear (within the XPS limit of detection) with the high-res Al 2p oxide peak shown at ≈ 74.4 eV .[65]

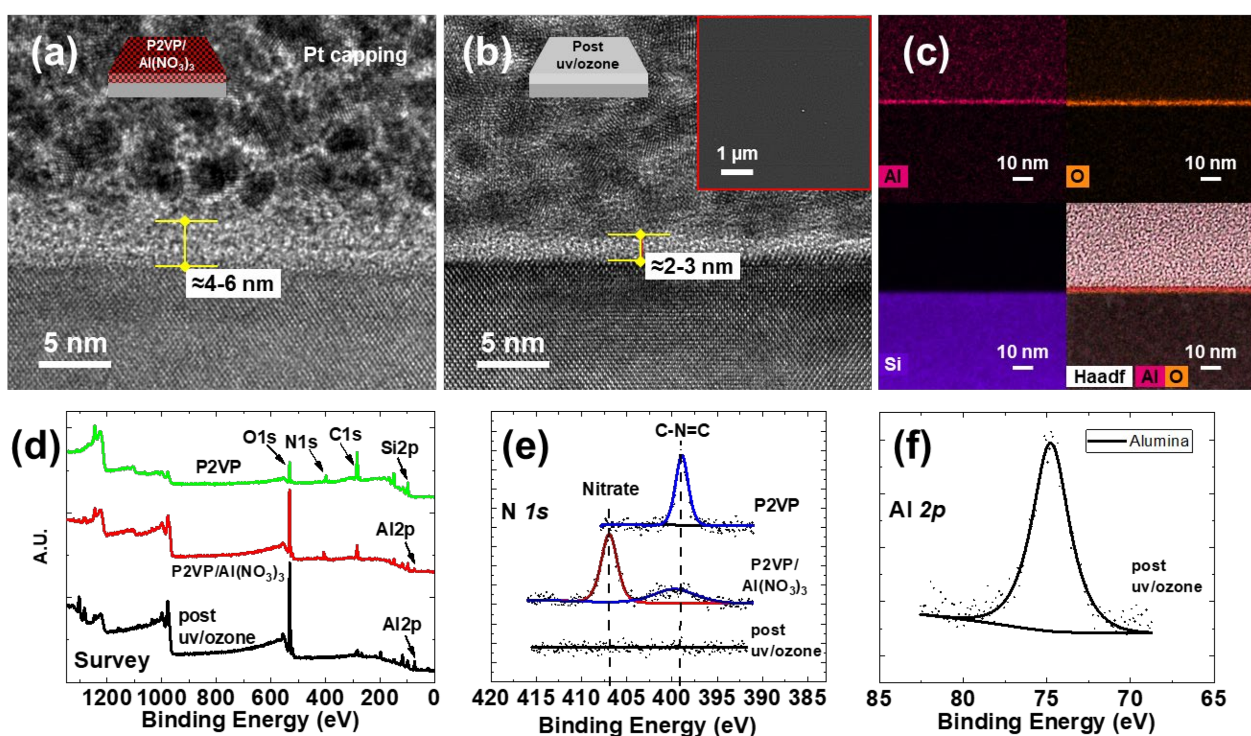

Figure 2.5 Bright-field (a) TEM images of aluminium nitrate infiltrated P2VP grafted polymer, (b) after exposure to UV/Ozone with top down FESEM inset and (c) EDX maps (Al, O, Si) and STEM images (high angle annular dark field images) (HAADF) of the infiltrated film. XPS survey (d) and high-resolution (e) – (f) spectra of the grafted P2VP, infiltrated P2VP and fallowing UV/Ozone exposure.

The scope of metal ion inclusion in to P2VP-OH film is evident and studies in the periodic trends of strong pyridine-metal binding illustrate the potential for incorporation of a multitude of metal ions.[66] However, a note of caution in using a P2VP-OH brush is the increased steric hindrance of the nitrogen lone pair due to the proximity of the pyridinyl nitrogen with the backbone. A recent (2019) and meticulous review by Kennemur [67]

highlights the issue of using larger, more sterically demanding species (e.g. silver and gold cations) for coordinating to the strained geometry of the P2VP repeating unit.

Furthermore, while we have demonstrated an effective UV/ozone process for ashing organics and forming an oxide, the slow nature of the process (3 hr.) is somewhat prohibitive from an integration standpoint. Therefore, efforts must be made to develop more efficient plasma or other reactive oxygen based processes.

2.4.3 PS-OH Surface Deactivation.

Figure 2.6 shows STEM and EDX data for the PS brush exposed to the salt solution. The STEM (HAADF) image in **Figure 2.6 (a)** is a cross-section of the PS brush after casting the aluminum nitrate solution. There is no obvious swelling observed in the salt exposed PS film with a thickness (≈ 3 nm) similar to the as grafted PS brush (**Figure 2.4 (d)),** indicating a lack of solvent and ion uptake. The EDX maps in **Figure 2.6 (b)** confirm that ion infiltration is inhibited by the PS film. After spin casting, the salt solution liquid film quickly recedes ($\chi_{PS\text{-}EtOH} \approx 1.93$, **Table 1**) leaving a dispersion pattern (**Figure S2.7.11**). Discrete salt deposits form on the PS surface as the ethanol evaporates which can be readily removed with a solvent wash (**Figure S2.7.12**).

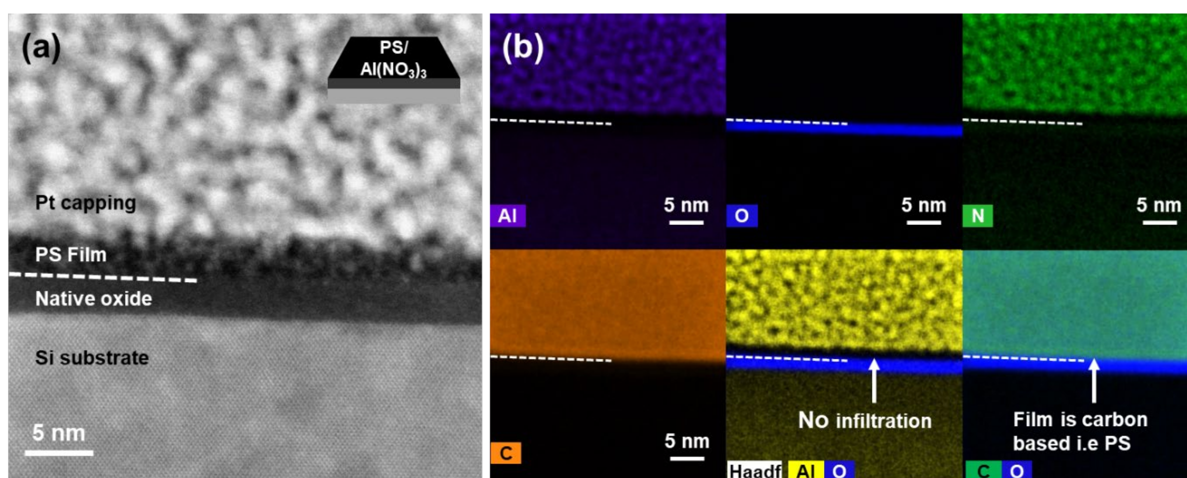

Figure 2.6: STEM images (HAADF) and (b) EDX maps (Al, O, N, C) of the PS grafted polymer after exposure to aluminium nitrate (spin on).

2.5 Conclusions:

The data presented here shows that polymer brushes can be used to develop large scale high quality inorganic films at substrates using brushes that contain metal binding sites. We have demonstrated the selective capacity that a pyridine containing brush has for ion inclusion (P2VP/P4VP) and the potential for developing the process for patterning Al_2O_3, a material of significant importance for patterning. Comparison of PVP with PS proves that the mechanism is via solvent mediated inclusions and takes place through the entire film by a solvent inclusion process. High resolution cross-section TEM shows the swollen polymer film for the first time. The results show that the initial polymer films need very careful control and optimization, if uniform and coherent inorganic films are to be produced. The results presented highlight the parameters required for optimizing polymer brush coverage. The data shows that very high coverage, and films with uniform thickness can be prepared in seconds for even reactive films such as PVP where strong intermolecular forces exists between the molecules. Whilst P2VP is an ideal system for small ions such as Al^{3+}, it would be less favorable for larger ions such as gold because of steric hindrance as discussed herein. The lack of reactivity of PS, where only surface deposition of the salt occurs (due to non-swelling in the salt solution), suggests it could be used to block salt inclusion. Thus, patterning of P2VP and PS by lithography or surface selective end groups on the brush, to deposit only on selected regions of a substrate, could be used to develop various ASD applications. This work provides clear mechanistic insight into the ion inclusion/blocking capability of these polymers and suggests they may rival SAM systems for the development and implementation of ASD related fabrication methods particularly for BEOL technologies. Whilst the methodology is promising, it should be pointed out that, integration into a manufacturing process has several challenges. Further work on a range of metal and dielectric materials is required, particularly, around the development of a reductive process to yield metal materials as the polymer is removed. In summary, we precisely controlled

polymer brushes for activating and deactivating semiconductor surfaces, which is a critical milestone for fulfilling future device scaling and 3D architectures.

2.6 References:

(1) Morris, M. A. Directed Self-Assembly of Block Copolymers for Nanocircuitry Fabrication. *Microelectron. Eng.* **2015**, *132*, 207–217. https://doi.org/10.1016/j.mee.2014.08.009.

(2) Cummins, C.; Mokarian-Tabari, P.; Andreazza, P.; Sinturel, C.; Morris, M. A. Solvothermal Vapor Annealing of Lamellar Poly(Styrene)-Block-Poly(d,l-Lactide) Block Copolymer Thin Films for Directed Self-Assembly Application. *ACS Appl. Mater. Interfaces* **2016**. https://doi.org/10.1021/acsami.6b00765.

(3) Ross, C. a; Berggren, K. K.; Cheng, J. Y.; Jung, Y. S.; Chang, J.-B. Three-Dimensional Nanofabrication by Block Copolymer Self-Assembly. *Adv. Mater.* **2014**, *26* (25), 4386–4396. https://doi.org/10.1002/adma.201400386.

(4) Oh, J.; Suh, H. S.; Ko, Y.; Nah, Y.; Lee, J.-C.; Yeom, B.; Char, K.; Ross, C. A.; Son, J. G. Universal Perpendicular Orientation of Block Copolymer Microdomains Using a Filtered Plasma. *Nat. Commun.* **2019**, *10* (1), 2912. https://doi.org/10.1038/s41467-019-10907-5.

(5) Fernandez, E.; Tu, K. H.; Ho, P.; Ross, C. A. Thermal Stability of L10-FePt Nanodots Patterned by Self-Assembled Block Copolymer Lithography. *Nanotechnology* **2018**, *29* (46), 465301. https://doi.org/10.1088/1361-6528/aade2f.

(6) Tu, K.-H.; Bai, W.; Liontos, G.; Ntetsikas, K.; Avgeropoulos, A.; Ross, C. a. Universal Pattern Transfer Methods for Metal Nanostructures by Block Copolymer Lithography. *Nanotechnology* **2015**, *26* (37), 375301. https://doi.org/10.1088/0957-4484/26/37/375301.

(7) Gotrik, K. W.; Hannon, A. F.; Son, J. G.; Keller, B.; Alexander-katz, A.; Ross, C. A. Morphology Control in Block Copolymer Films Using Mixed Solvent Vapors, 2012.

(8) Cummins, C.; Borah, D.; Rasappa, S.; Senthamaraikannan, R.; Simao, C.; Francone, A.; Kehagias, N.; Sotomayor-Torres, C. M.; Morris, M. A. Self-Assembled Nanofeatures in Complex Three-Dimensional Topographies via Nanoimprint and Block Copolymer Lithography Methods. *ACS Omega* **2017**, *2* (8), 4417–4423. https://doi.org/10.1021/acsomega.7b00781.

(9) Thomas Mårtensson; Patrick Carlberg; Magnus Borgström; Lars Montelius; Werner Seifert, and; Samuelson*, L. Nanowire Arrays Defined by Nanoimprint Lithography. **2004**. https://doi.org/10.1021/NL035100S.

(10) Borah, D.; Cummins, C.; Rasappa, S.; Senthamaraikannan, R.; Salaun, M.; Zelsmann, M.; Liontos, G.; Ntetsikas, K.; Avgeropoulos, A.; Morris, M.; Borah, D.; Cummins, C.; Rasappa, S.; Senthamaraikannan, R.; Salaun, M.; Zelsmann, M.; Liontos, G.; Ntetsikas, K.; Avgeropoulos, A.; Morris, M. A. Nanopatterning via Self-Assembly of a Lamellar-Forming Polystyrene-Block-Poly(Dimethylsiloxane) Diblock Copolymer on Topographical Substrates Fabricated by Nanoimprint Lithography. *Nanomaterials* **2018**, *8* (1), 32. https://doi.org/10.3390/nano8010032.

(11) Prasittichai, C.; Pickrahn, K. L.; Sadat, F.; Hashemi, M.; Bergsman, D. S.; Bent, S. F. Improving Area-Selective Molecular Layer Deposition by Selective. **2014**. https://doi.org/10.1021/am504441e.

(12) IEEE International Interconnect Technology Conference/Advanced Metallization Conference (IITC/AMC); 2016; pp 133–135.

(13) Nagata, T. *Material Design of Metal/Oxide Interfaces for Nanoelectronics Applications*, 1st ed.; Springer Japan, 2020.

(14) Cummins, C.; Morris, M. A. Using Block Copolymers as Infiltration Sites for Development

of Future Nanoelectronic Devices: Achievements, Barriers, and Opportunities. *Microelectron. Eng.* **2018**, *195*, 74–85. https://doi.org/10.1016/J.MEE.2018.04.005.

(15) Lundy, R.; Cummins, C.; Flynn, S. P.; Ghosh, A.; Collins, M. N.; Dalton, E.; Kelleher, S. M.; Daniels, S.; Morris, M.; Enright, R. Block Copolymer Enabled Nanoporous Membrane Fabrication for High Heat Flux Dissipation Applications. In *Poster Presentation at EMRS Spring Meeting; Lille, France*; 2015.

(16) Sadat, F.; Hashemi, M.; Prasittichai, C.; Bent, S. F.; Science, M.; Engineering, C.; Present, U. S. Self-Correcting Process for High Quality Patterning by Atomic Layer Deposition. **2015**, No. 9, 8710–8717. https://doi.org/10.1021/acsnano.5b03125.

(17) Sadat, F.; Hashemi, M.; Birchansky, B. R.; Bent, S. F. Selective Deposition of Dielectrics: Limits and Advantages of Alkanethiol Blocking Agents on Metal − Dielectric Patterns. **2016**. https://doi.org/10.1021/acsami.6b09960.

(18) Chen, R.; Kim, H.; McIntyre, P. C.; Bent, S. F. Self-Assembled Monolayer Resist for Atomic Layer Deposition of HfO2 and ZrO2 High-κ Gate Dielectrics. *Appl. Phys. Lett.* **2004**, *84* (20), 4017–4019. https://doi.org/10.1063/1.1751211.

(19) Rong Chen, †; Hyoungsub Kim, ‡; Paul C. McIntyre, ‡ and; Stacey F. Bent*, §. Investigation of Self-Assembled Monolayer Resists for Hafnium Dioxide Atomic Layer Deposition. **2005**. https://doi.org/10.1021/CM0486666.

(20) Junsic Hong, †; David W. Porter, †; Raghavasimhan Sreenivasan, ‡; Paul C. McIntyre, ‡ and; Stacey F. Bent*, †. ALD Resist Formed by Vapor-Deposited Self-Assembled Monolayers. **2006**. https://doi.org/10.1021/LA0606401.

(21) Jiang, X.; Bent, S. F. Area-Selective ALD with Soft Lithographic Methods: Using Self-Assembled Monolayers to Direct Film Deposition. https://doi.org/10.1021/jp905317n.

(22) Bobb-semple, D.; Nardi, K. L.; Draeger, N.; Hausmann, D. M.; Bent, S. F. Area-Selective Atomic Layer Deposition Assisted by Self-Assembled Monolayers: A Comparison of Cu, Co, W, and Ru. **2019**. https://doi.org/10.1021/acs.chemmater.8b04926.

(23) Färm, E.; Kemell, M.; Ritala, M.; Leskelä, M. Self-Assembled Octadecyltrimethoxysilane Monolayers Enabling Selective-Area Atomic Layer Deposition of Iridium. *Chem. Vap. Depos.* **2006**, *12* (7), 415–417. https://doi.org/10.1002/cvde.200604219.

(24) Färm, E.; Kemell, M.; Ritala, M.; Leskelä, M. Selective-Area Atomic Layer Deposition with Microcontact Printed Self-Assembled Octadecyltrichlorosilane Monolayers as Mask Layers. *Thin Solid Films* **2008**, *517* (2), 972–975. https://doi.org/10.1016/J.TSF.2008.08.191.

(25) Färm, E.; Vehkamäki, M.; Ritala, M.; Leskelä, M. Passivation of Copper Surfaces for Selective-Area ALD Using a Thiol Self-Assembled Monolayer. *Semicond. Sci. Technol.* **2012**, *27* (7), 074004. https://doi.org/10.1088/0268-1242/27/7/074004.

(26) Färm, E.; Lindroos, S.; Ritala, M.; Markku, L. Microcontact Printed Films as an Activation Layer for Selective Atomic Layer Deposition, July 2011.

(27) Färm, E.; Lindroos, S.; Ritala, M.; Leskelä, M. Microcontact Printed RuO x Film as an Activation Layer for Selective-Area Atomic Layer Deposition of Ruthenium. *Chem. Mater.* **2012**, *24* (2), 275–278. https://doi.org/10.1021/cm202468s.

(28) Färm, E.; Kemell, M.; Ritala, M.; Leskelä, M. Selective-Area Atomic Layer Deposition Using Poly(Methyl Methacrylate) Films as Mask Layers. *J. Phys. Chem. C* **2008**, *112* (40), 15791–15795. https://doi.org/10.1021/jp803872s.

(29) Färm, E.; Kemell, M.; Santala, E.; Ritala, M.; Leskelä, M. Selective-Area Atomic Layer

Deposition Using Poly(Vinyl Pyrrolidone) as a Passivation Layer. *J. Electrochem. Soc.* **2010**, *157* (1), K10. https://doi.org/10.1149/1.3250936.

(30) Park, K. J.; Doub, J. M.; Gougousi, T.; Parsons, G. N. Microcontact Patterning of Ruthenium Gate Electrodes by Selective Area Atomic Layer Deposition. *Appl. Phys. Lett.* **2005**, *86* (5), 051903. https://doi.org/10.1063/1.1852079.

(31) Stevens, E.; Tomczak, Y.; Chan, B. T.; Altamirano Sanchez, E.; Parsons, G. N.; Delabie, A. Area-Selective Atomic Layer Deposition of TiN, TiO_2 , and HfO_2 on Silicon Nitride with Inhibition on Amorphous Carbon. *Chem. Mater.* **2018**, *30* (10), 3223–3232. https://doi.org/10.1021/acs.chemmater.8b00017.

(32) Atanasov, S. E.; Kalanyan, B.; Parsons, G. N. Inherent Substrate-Dependent Growth Initiation and Selective-Area Atomic Layer Deposition of TiO_2 Using "Water-Free" Metal-Halide/Metal Alkoxide Reactants. *J. Vac. Sci. Technol. A Vacuum, Surfaces, Film.* **2016**, *34* (1), 01A148. https://doi.org/10.1116/1.4938481.

(33) Parsons, G. N.; Kalanyan, B.; Atanasov, S. E.; Lemaire, P.; Oldham, C. (Invited) Using Inherent Substrate-Dependent Nucleation to Promote Metal and Metal Oxide Selective-Area Atomic Layer Deposition. *ECS Trans.* **2016**, *75* (6), 77–83. https://doi.org/10.1149/07506.0077ecst.

(34) Parsons, G. N. Functional Model for Analysis of ALD Nucleation and Quantification of Area-Selective Deposition. *J. Vac. Sci. Technol. A* **2019**, *37* (2), 020911. https://doi.org/10.1116/1.5054285.

(35) Song, S. K.; Saare, H.; Parsons, G. N. Integrated Isothermal Atomic Layer Deposition/Atomic Layer Etching Supercycles for Area-Selective Deposition of TiO2. *Chem. Mater.* **2019**, *31*, 4793–4804. https://doi.org/10.1021/acs.chemmater.9b01143.

(36) Vervuurt, R. H. J.; Sharma, A.; Jiao, Y.; Kessels, W. (Erwin) M. M.; Bol, A. A. Area-Selective Atomic Layer Deposition of Platinum Using Photosensitive Polyimide. *Nanotechnology* **2016**, *27* (40), 405302. https://doi.org/10.1088/0957-4484/27/40/405302.

(37) Mameli, A.; Kuang, Y.; Aghaee, M.; Ande, C. K.; Karasulu, B.; Creatore, M.; Mackus, A. J. M.; Kessels, W. M. M.; Roozeboom, F. Area-Selective Atomic Layer Deposition of In_2O_3:H Using a μ-Plasma Printer for Local Area Activation. *Chem. Mater.* **2017**, *29* (3), 921–925. https://doi.org/10.1021/acs.chemmater.6b04469.

(38) Singh, J. A.; Thissen, N. F. W.; Kim, W.-H.; Johnson, H.; Kessels, W. (Erwin) M. .; Bol, A. A.; Bent, S. F.; Mackus, A. J. M. Area-Selective Atomic Layer Deposition of Metal Oxides on Noble Metals through Catalytic Oxygen Activation. *Chem. Mater.* **2017**, acs.chemmater.7b03818. https://doi.org/10.1021/acs.chemmater.7b03818.

(39) Mameli, A.; Merkx, M. J. M.; Karasulu, B.; Roozeboom, F.; Kessels, W. E. M. M.; Mackus, A. J. M. Area-Selective Atomic Layer Deposition of SiO 2 Using Acetylacetone as a Chemoselective Inhibitor in an ABC-Type Cycle. **2017**. https://doi.org/10.1021/acsnano.7b04701.

(40) Thissen, N. F. W.; Vervuurt, R. H. J.; Mackus, A. J. M.; Mulders, J. J. L.; Weber, J.-W.; Kessels, W. M. M.; Bol, A. A. Graphene Devices with Bottom-up Contacts by Area-Selective Atomic Layer Deposition. *2D Mater.* **2017**, *4* (2), 025046. https://doi.org/10.1088/2053-1583/aa636a.

(41) Cummins, C.; Shaw, M. T.; Morris, M. A. Area Selective Polymer Brush Deposition. **2017**, *1700252*, 1–6. https://doi.org/10.1002/marc.201700252.

(42) Cummins, C.; Weingärtner, T.; Morris, M. A. Enabling Large-Area Selective Deposition on

Metal-Dielectric Patterns Using Polymer Brush Deactivation. *J. Phys. Chem. C* **2018**, *122* (26), 14698–14705. https://doi.org/10.1021/acs.jpcc.8b04092.

(43) Brinker, C. J. *HYDROLYSIS AND CONDENSATION OF SILICATES: EFFECTS ON STRUCTURE*; 1988; Vol. 100.

(44) Lebrun, J. J.; Porte, H. Polysiloxanes. *Compr. Polym. Sci. Suppl.* **1989**, 593–609. https://doi.org/10.1016/B978-0-08-096701-1.00175-0.

(45) Haynes, W. M. *CRC Handbook of Chemistry and Physics*, 91st ed.; CRC: Boca Raton, Fl, 2010.

(46) Kundu, A.; Pitchaimani, J.; Madhu, V.; Sakthivel, P.; Ganesamoorthy, R.; Anthony, S. P. Bay Functionalized Perylenediimide with Pyridine Positional Isomers: NIR Absorption and Selective Colorimetric/Fluorescent Sensing of Fe3+ and Al3+ Ions. *J. Fluoresc.* **2017**, *27* (2), 491–500. https://doi.org/10.1007/s10895-016-1976-z.

(47) Thompson, E. J.; Myers, T. W.; Berben, L. A.; Thompson, E. J.; Myers, T. W.; Berben, L. A. Coordination Complexes Synthesis of Square-Planar Aluminum(III) Complexes**. *Angew. Chem. Int. Ed* **2014**, *53*, 14132–14134. https://doi.org/10.1002/anie.201407098.

(48) Bhuvanesh, N.; Suresh, S.; Kannan, K.; Rajesh Kannan, V.; Maroli, N.; Kolandaivel, P.; Nandhakumar, R. Bis-Anthracene Derived Bis-Pyridine: Selective Fluorescence Sensing of Al^{3+} Ions. *New J. Chem.* **2019**, *43* (6), 2519–2528. https://doi.org/10.1039/C8NJ04789H.

(49) Cummins, C.; Borah, D.; Rasappa, S.; Chaudhari, a; Ghoshal, T.; O'Driscoll, B. M. D.; Carolan, P.; Petkov, N.; Holmes, J. D.; Morris, M. a. Self-Assembly of Polystyrene-Block-Poly(4-Vinylpyridine) Block Copolymer on Molecularly Functionalized Silicon Substrates: Fabrication of Inorganic Nanostructured Etchmask for Lithographic Use. *J. Mater. Chem. C* **2013**, *1* (47), 7941–7951. https://doi.org/Doi 10.1039/C3tc31498g.

(50) Cummins, C.; Gangnaik, A.; Kelly, R. A.; Borah, D.; O'Connell, J.; Petkov, N.; Georgiev, Y. M.; Holmes, J. D.; Morris, M. A. Aligned Silicon Nanofins *via* the Directed Self-Assembly of PS- *b* -P4VP Block Copolymer and Metal Oxide Enhanced Pattern Transfer. *Nanoscale* **2015**, *7* (15), 6712–6721. https://doi.org/10.1039/C4NR07679F.

(51) Lundy, R.; Flynn, S. P.; Cummins, C.; Kelleher, S. M.; Collins, M. N.; Dalton, E.; Daniels, S.; Morris, M. A.; Enright, R. Controlled Solvent Vapor Annealing of a High χ Block Copolymer Thin Film. *Phys. Chem. Chem. Phys.* **2017**, *19* (4), 2805–2815. https://doi.org/10.1039/C6CP07633E.

(52) Ma, K.-X.; Ho, C.-H.; Zhu, F.; Chung, T.-S. Investigation of Surface Energy for Organic Light Emitting Polymers and Indium Tin Oxide. *Thin Solid Films* **2000**, *371* (1–2), 140–147. https://doi.org/10.1016/S0040-6090(00)00994-9.

(53) Hansen, C. M. *Hansen Solubility Parameters: A User's Handbook*; CRC press, 2007.

(54) Starý, Z. Thermodynamics and Morphology and Compatibilization of Polymer Blends. In *Characterization of Polymer Blends*; Wiley-VCH Verlag GmbH & Co. KGaA, 2014; pp 93–132.

(55) Arras, M. M. L.; He, B.; Jandt, K. D. High Molar Mass Amphiphilic Block Copolymer Enables Alignment and Dispersion of Unfunctionalized Carbon Nanotubes in Melt-Drawn Thin-Films. *Polymer (Guildf).* **2017**, *127*, 15–27. https://doi.org/10.1016/j.polymer.2017.08.030.

(56) Cassie, A. B. D.; Baxter, S. Wettability of Porous Surfaces. *Trans. Faraday Soc.* **1944**, *40*, 546–551.

(57) Lundy, R.; Byrne, C.; Bogan, J.; Nolan, K.; Collins, M. N.; Dalton, E.; Enright, R. Exploring the Role of Adsorption and Surface State on the Hydrophobicity of Rare Earth Oxides. *ACS Appl. Mater. Interfaces* **2017**, *9* (15), 13751–13760. https://doi.org/10.1021/acsami.7b01515.

(58) Laibinis, P. E.; Whitesides, G. M. ω-Terminated Alkanethiolate Monolayers on Surfaces of Copper, Silver, and Gold Have Similar Wettabilities. *J. Am. Chem. Soc.* **1992**, *114* (6), 1990–1995. https://doi.org/10.1021/ja00032a009.

(59) Sierański, T. Discovering the Stacking Landscape of a Pyridine-Pyridine System. *J. Mol. Model.* **2017**, *23* (12). https://doi.org/10.1007/s00894-017-3496-4.

(60) Secor, R. M. The Kinetics of Condensation Polymerization. *AIChE J.* **1969**, *15* (6), 861–865. https://doi.org/10.1002/aic.690150612.

(61) Gennes, P.-G. de. *Scaling Concepts in Polymer Physics*; Cornell University Press, 1979.

(62) Wenzel, R. Resistance of Solid Surfaces to Wetting by Water. *Ind. Eng. Chem.* **1936**, *28* (8), 988–994.

(63) Si, W.; Lei, W.; Hao, Q.; Xia, X.; Zhang, H.; Li, J.; Li, Q.; Cong, R. Facile Synthesis of Nitrogen-Doped Graphene Derived from Graphene Oxide and Vitamin B3 as High-Performance Sensor for Imidacloprid Determination. *Electrochim. Acta* **2016**, *212*, 784–790. https://doi.org/10.1016/j.electacta.2016.07.063.

(64) Hantsche, H. High Resolution XPS of Organic Polymers, the Scienta ESCA300 Database. By G. Beamson and D. Briggs, Wiley, Chichester 1992, 295 Pp., Hardcover, £ 65.00, ISBN 0-471-93592-1. *Adv. Mater.* **2005**, *5* (10), 778–778. https://doi.org/10.1002/adma.19930051035.

(65) Bolt, P. H.; ten Grotenhuis, E.; Geus, J. W.; Habraken, F. H. P. M. The Interaction of Thin NiO Layers with Single Crystalline α-Al2O3(112̅0) Substrates. *Surf. Sci.* **1995**, *329* (3), 227–240. https://doi.org/10.1016/0039-6028(95)00063-1.

(66) M. T. Rodgers, *; J. R. Stanley, and; Amunugama, R. Periodic Trends in the Binding of Metal Ions to Pyridine Studied by Threshold Collision-Induced Dissociation and Density Functional Theory. **2000**. https://doi.org/10.1021/JA0027923.

(67) Kennemur, J. G. Poly(Vinylpyridine) Segments in Block Copolymers: Synthesis, Self-Assembly, and Versatility. *Macromolecules* **2019**, *52*, 1354–1370. https://doi.org/10.1021/acs.macromol.8b01661.

2.7 Appendix

Optimizing polymer brush coverage to develop highly coherent sub-5nm oxide films by ion inclusion

Section S2.7.1 – Surface cleaning/functionalization and polymer pellet fabrication. Good coverage achieved in very short plasma cleaning times (Figure S2.7.1). Oxygen plasma produced a clean, functionalized hydrophilic surface. A very smooth PS monolayer was obtained following the grafting process. The plasma functionalization step is necessary for removal of adventitious carbon/organics. Silica surfaces can natively contain -OH groups.

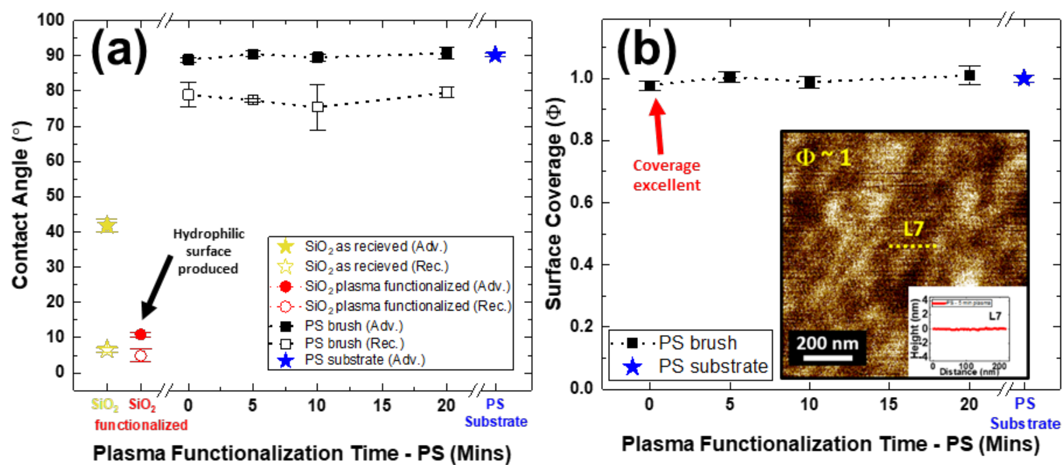

Figure S2.7.1 (a): Contact angle data for the cleaned silicon substrate and grafted PS-OH. A few minutes plasma cleaning is sufficient to clean the substrates. (b) PS-OH brush coverage as the function of plasma cleaning time.

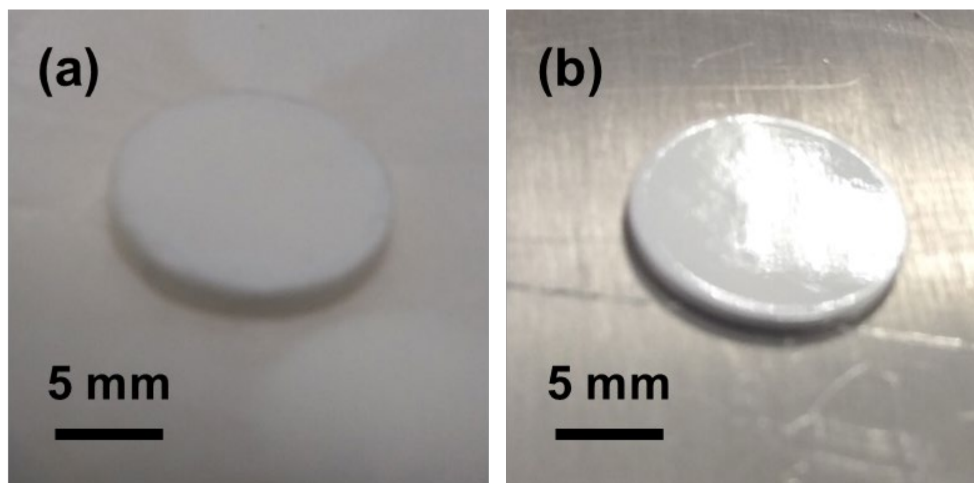

Figure 2.7.2 (a): A pressed polymer pellet using a hydraulic press and (b) a pressed pellet exposed to selective solvent vapour (THF for P2VP and toluene for PS) until smooth mirror like surface was obtained. The smooth surface is required to minimize roughness contribution for surface wettability.

Section S2.7.2 – Hansen Solubility Parameters

Table S1 tabulates the solubility parameters used to estimate (using **Eq. 1**) the χ values.

Table S1 System molecular volumes and Hansen solubility parameters

Species	V_m (µm³/mol)	δ_d (MPa$^{0.5}$)	δ_p (MPa$^{0.5}$)	δ_h (MPa$^{0.5}$)
2-vinylpyridine	108.0	16.3	7.1	11.6
Styrene	115.0	18.6	1.0	4.1
Tetrahydrofuran	81.7	16.8	5.7	8.0
Toluene	106.8	18.0	1.4	2.0
Ethyl lactate	115.0	16.0	7.6	12.5
PGMEA	137.1	15.6	5.6	9.8

We note that the biodegradable "green solvent" ethyl lactate ($\chi_{2VP-EL} \approx 0.02$) and the commonly used solvent in the semiconductor industry, propylene glycol methyl ether acetate ($\chi_{2VP-PGMEA} \approx 0.10$) are also ideal and have been used here yielding good results.

Section S2.7.3 – Brush Optimization: Spin Speed and Grafting Kinetics

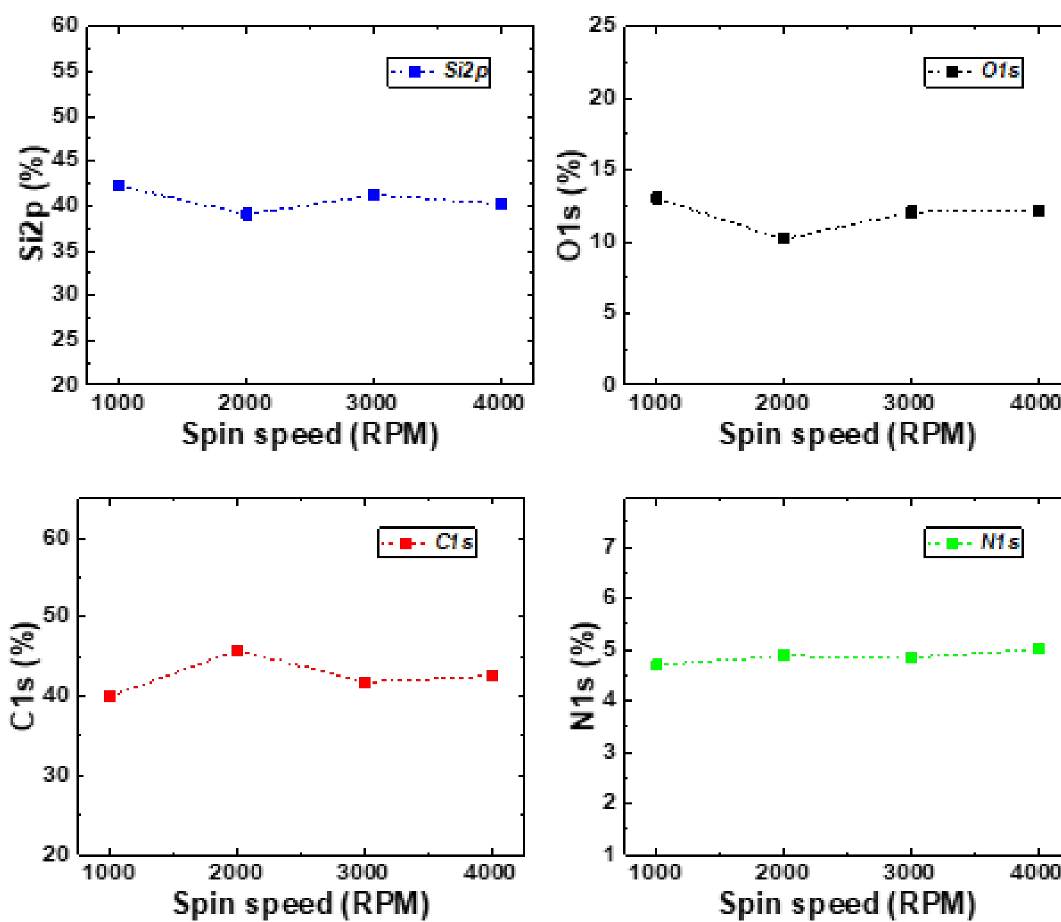

Figure 2.7.3: XPS atomic percentage (Si, O, C, N) of P2VP-OH grafted brush annealed using a range of spin speeds. Spin speed has negligible impact on the coverage of grafted P2VP.

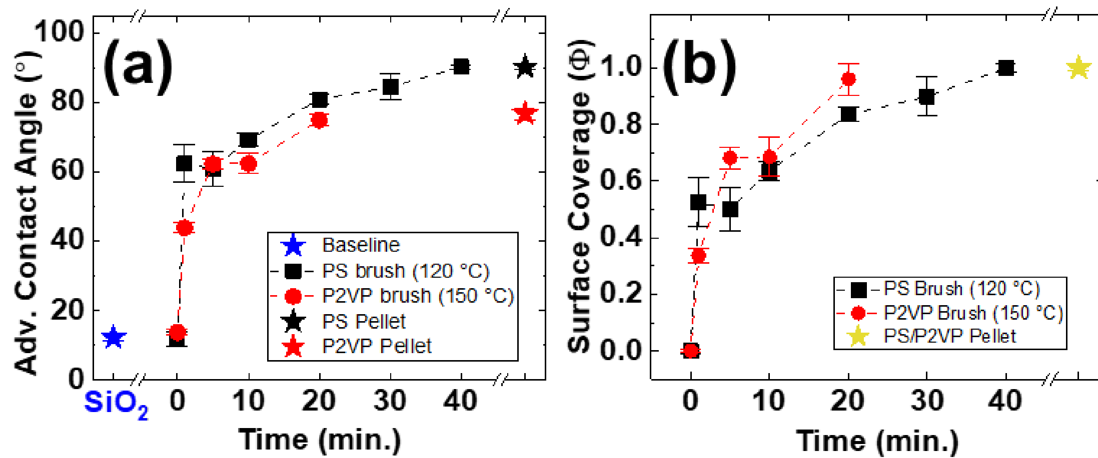

Figure S 2.7.4: Grafting process over a 40 minute period for fix temperature (PS-OH= 120 ^{0}C, P2VP-OH= 150 ^{0}C).

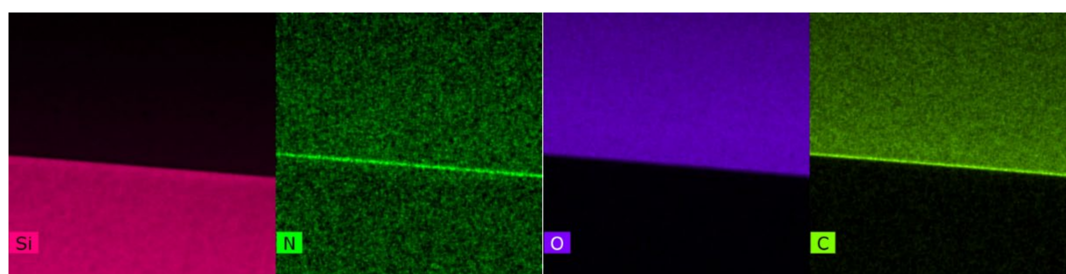

Figure S2.7.5: Energy dispersive x-ray (EDX maps) (Si, N, O, C) of P2VP-OH grafted brush.

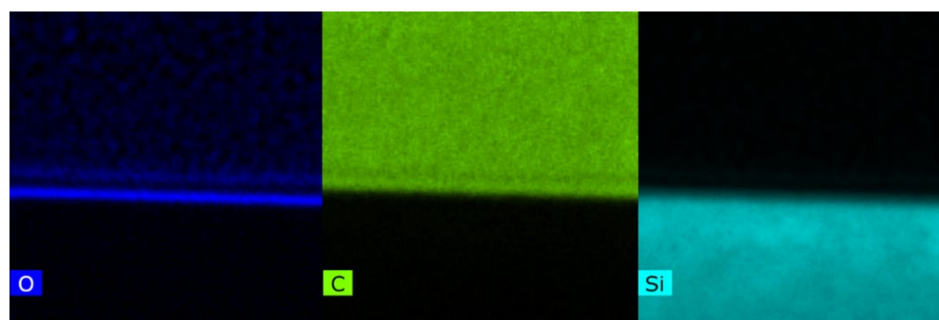

Figure 2.7.6: EDX maps (O, C, Si,) of the PS-OH grafted brush.

Section S2.7.4 – Ion Infiltration with a *P2VP* grafted Polymer Brush Monolayer.

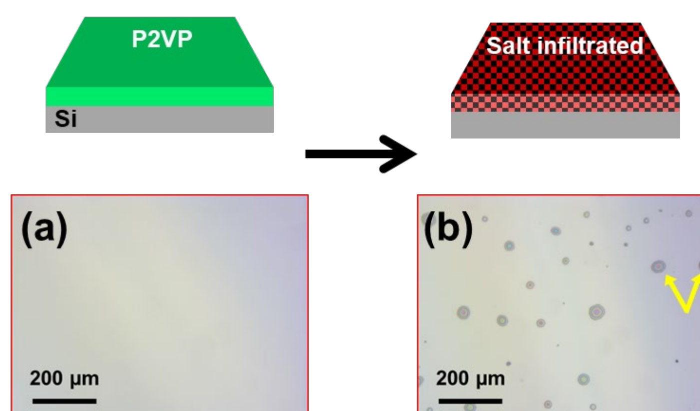

Figure 2.7.7: Optical microscopy of grafted P2VP-OH monolayer before (a) and after (b) salt infiltration. Pre infiltration the P2VP coverage appears free of agglomerations (see Figure 2.5 (b) for high-res SEM and TEM). Post infiltration, newton ring structures become present (yellow arrows) resulting from excess salt deposits from solution. Removal of deposit can achieved by washing in a suitable solvent.

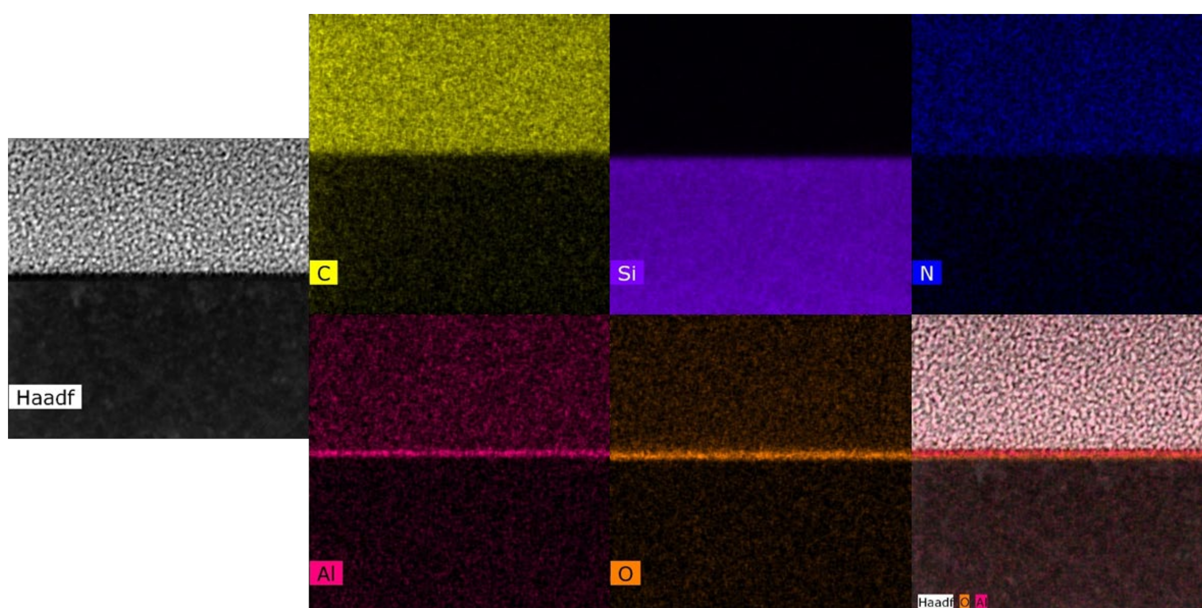

Figure S2.7.8: High-angle annular dark field image (HAADF) with EDX maps (C, Si, N, Al, O and over layered HAADF / O / Al).

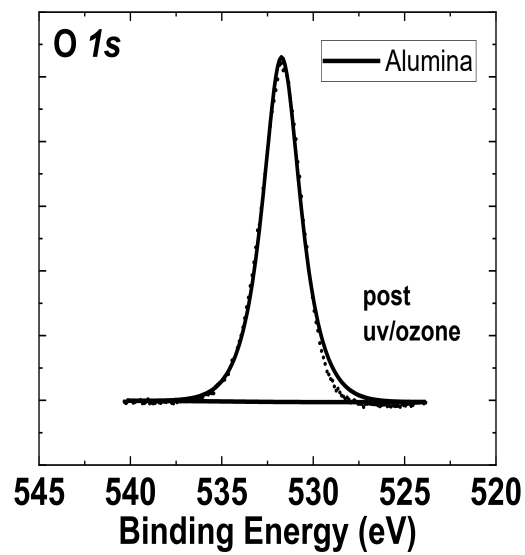

Figure S2.7.9: XPS high-res O 1s spectra of the aluminium nitrate infiltrated brush after UV/Ozone treatment see Figure 2.5 (d)-(f) of chapter for complete XPS spectra of the pre to post infiltrated P2VP polymer brush.

Section S2.6.5 – Ion Blocking with a *PS* grafted Polymer Brush Monolayer.

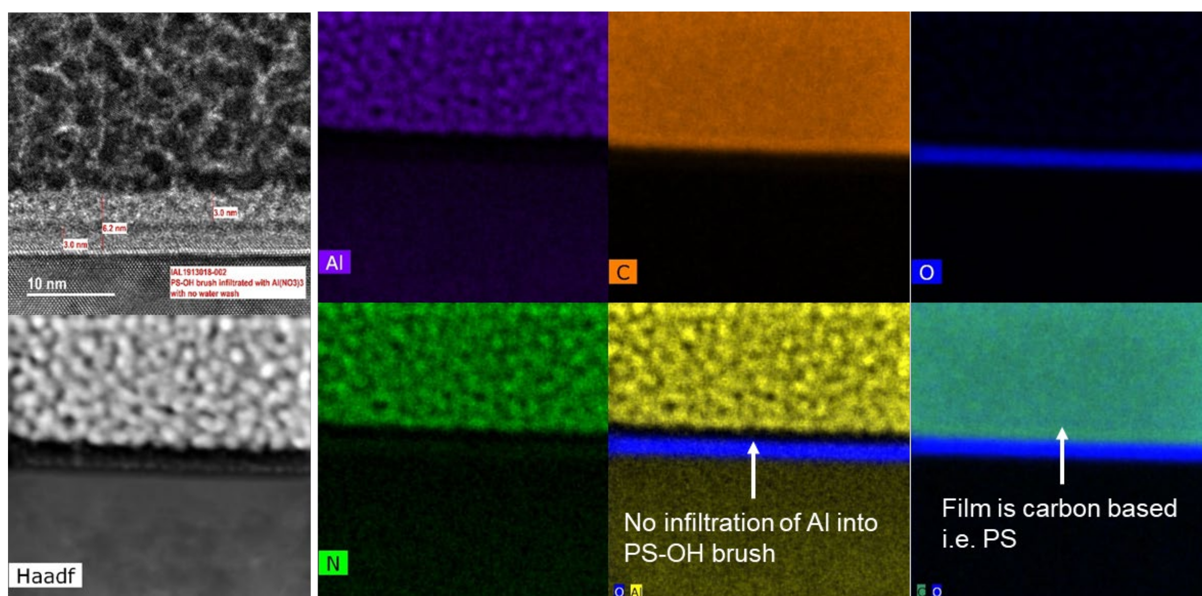

Figure S2.7.10: TEM and HAADF images with EDX maps (Al, C, O, N, overlayered HAADF/O/Al and overlayered C/O). There is no Al detected in the PS film see Figure 2.4 for high-res STEM and EDX maps.

Figure S 2.7.11: Optical microscopy images (a) and (b) and secondary electron SEM micrographs (c) of aluminium nitrate in ethanol solution spun cast onto a PS grafted monolayer. Upon spin casting, the salt solution liquid film immediately recedes with the resulting dispersion pattern seen in (a) and (b). These discrete salt deposits from on the PS surface as the ethanol evaporates.

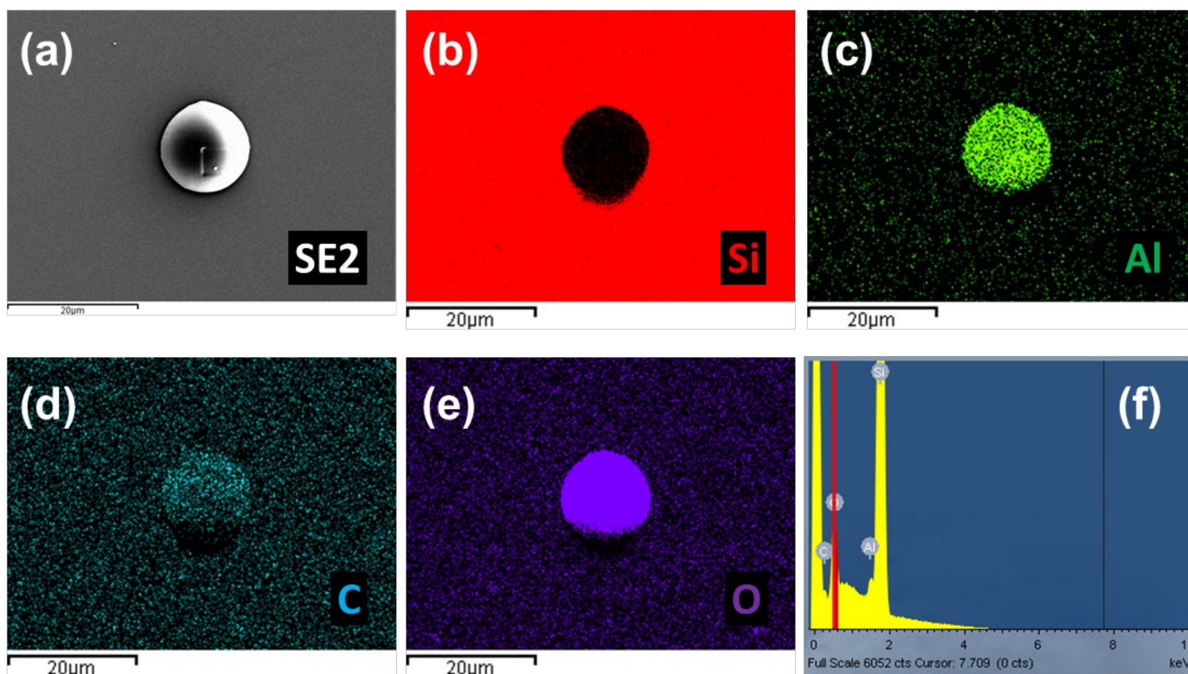

Figure S2.7.12 (a): secondary electron SEM images, (b)-(e) EDX maps and (f) EDX spectra of the aluminium nitrate on the PS brush. The data indicates that the deposits that form is aggregations of the salt. The deposits are readily removed by dipping in water or other suitable solvents.

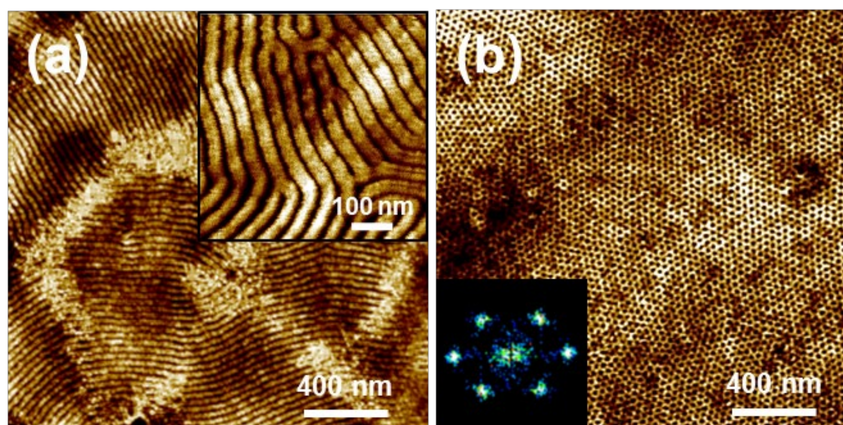

Figure S2.7.13: AFM images of the PS-b-P4VP (a) nanowire template and its conversion to aluminium oxide nanowires (inset) and (b) nanodot template with FFT (inset).

The salt infiltration and ashing process was performed on the PS and a PVP system combined (phase segregated PS-b-P4VP) to highlight the contrasting selectivity each system has with the inclusion process and to demonstrate direct writing of oxide device nanopatterns. **Figure S2.7.13 (a)** shows an AFM topographic image of a PS-b-P4VP nanowire template. The template is infiltrated with aluminum nitrate and subsequently converted to oxide nanowires (inset) with ≈ 25 nm wire diameters. **Figure S2.7.13 (b)** shows a well-ordered nanodot template of the same system with FFT (inset).

Chapter 3. Precise definition of monolayer point in polymer brush films for fabricating highly coherent TiO_2 thin films by vapour phase infiltration.

3.1 Abstract:

We describe a versatile bottom-up approach to covalently and rapidly graft hydroxyl terminated poly-2-(vinyl pyridine) (P2VP-OH) polymers in 60 seconds that can subsequently be used to fabricate high quality titania (TiO_2) films on silicon substrates. A facile strategy based upon room temperature titanium vapor phase infiltration of the grafted P2VP-OH polymer brushes to produces TiO_2 nanofilms of 2-4 nm thickness. To fabricate coherent inorganic films with precise thickness control, it is critical to generate a complete polymer brush monolayer. Grafting monolayers is straightforward for polymers that are weakly interacting with one another but more challenging for reactive systems. Crucial parameters are explored including molecular weight and solution concentration for grafting dense P2VP-OH monolayers from the liquid phase with high coverage and uniformity across wafer scale areas (> 2 cm^2). Additionally, we compare the P2VP-OH polymer systems with another reactive polymer, poly (methyl methacrylate)-OH (PMMA-OH) and a relatively non-reactive polymer, poly (styrene)-OH (PS-OH). Furthermore, we prove the latter to be effective for surface blocking and deactivation. Our methodology provides new insight into the rapid grafting of polymer brushes and their ability to form TiO_2 films. We believe the results described herein are important for further expanding the use of reactive and unreactive polymers for fields including area selective deposition, solar cells absorber layers, and antimicrobial surface coating layers.

3.2 Introduction:

Continued miniaturization of semiconductor devices has led to cost and integration issues[1] which challenge the manufacture of a 3 nm node as envisaged by Samsung and TSMC foundries for 2023.[2,3] Gate voltage scaling at these dimensions necessitates state-of-the-art architectures beyond FinFETs such as gate-all-around FET technology, leading to further integration complexity.[4] Approaches complimenting photolithography include nanoimprint lithography,[5,6] block copolymer lithography[7–14] and, recently, area selective deposition (ASD).[15–17] Such methods are favorable in enabling future device integration and help alleviate fabrication demands, e.g., litho-etch-litho-etch.

In particular, the ability of ASD to selectively include many materials sets such as oxides, dielectrics and metals provides a route to produce material patterns and reduce the number of processing steps. The capacity of ASD to produce uniform metal and oxide layers can assist development of silicon device technologies[18] and ASD is promising for implementation and cost reduction in fields beyond CMOS processing, where stacked or patterned layers are required e.g. energy harvesting surfaces[19] and advances in catalysis.[20]

Various innovative ASD approaches have been reported, and are typically based on self-assembled monolayers (SAMs) and atomic layer deposition (ALD) or molecular layer deposition. Others have examined unreactive polymeric resist layers combined with ALD of metal and dielectric films. For example, Leskelä *et al.* designed an approach using patterned SAMs to generate features on copper and silicon substrates[21–23] as well as patterned organic films for activation[24,25] and deactivation[26,27] layers with various ALD depositions (Ru, Ir, Pt, Al_2O_3 and TiO_2). Bent *et al.* have championed SAM use to mask and pattern copper lines on silicon[28,29] and several other substrate materials[30–34] together with ALD metallization.

Furthermore, the Bent group has demonstrated a process for topographic selective anisotropic deposition of platinum via ALD by deactivating horizontal regions (ion implanted) with fluorocarbons.[35] More recent ASD research has used ASD solely to fabricate

defined materials at site specific areas. For instance, Kessels and co-workers have incorporated area selective ALD approaches that use organic inhibitors with ALD precursors,[36] surface activation via reactive plasma micro patterning,[37] and tuning the oxygen ALD cycle exposure to selectively nucleate platinum on wafer regions.[38] The research has been extended to area-selective ALD on graphene surfaces (resist free),[39] and ASD of ZnO by area activation using electron beam-induced deposition.[40] Kessels and co-workers have used ALD with catalytic oxygen activation of noble metal surfaces,[41] using a triple step ALD cycle with a selective organic inhibitor, precursor and reactive plasma.[42] The group have also demonstrated selective deposition of ruthenium on Pt/SiO_2 line space using ALD and atomic layer etching (ALE) cycles.[43] Parsons *et al.* have demonstrated selective deposition of diverse material sets (*e.g.* Ru, TiN, TiO_2 and HfO_2) via ALD on silicon nitride and silicon substrates by deactivating wafer areas with SAMs,[44] using patterned amorphous carbon,[45] and by exploiting inherent substrate selectivity.[46–48] The group also developed a TiO_2 ASD approach using ALD/ALE cycles.[49] More recently, Bates *et al.* introduced precise design rules for a new ASD technique known as 'spin dewetting' that exploits modification of surface energies of line-space patterns.[50,51] Selectivity is induced by tuning polymer design to promote preferential dewetting from one substrate material and uniform wetting on the other.

Our previous work demonstrated the feasibility of using polymer brush (note that a brush in this sense is a film of polymer which is covalently attached to the film surface through a reactive terminal group) films to selectively deactivate patterned Cu/SiO_2 line space for ASD of metal layers.[52] The brush was selectively grafted using end groups that bind to site-specific wafer regions. Further, we demonstrated a simple approach for rapid grafting (in seconds) of end functionalized reactive polymer brush films with complete coverage and subsequent conversion to various oxides (Al_2O_3,[53] Co_3O_4,[54] CuO,[55,56]) via liquid phase metal

ion insertion. Surface deactivation was also achieved using a PS-OH brush that prevents the deposition of ions.

Liquid phase deposition of metal ions on grafted brushes has many benefits due to the multitude of readily available, low cost and easily prepared (water soluble) salt precursors. However, developing a vapor phase brush infiltration approach can be beneficial for a wide array of applications, both ASD and blanket layers in the semiconductor industry. Moreover, achieving dense inorganic films in a simple one-step inclusion method at low temperatures is very appealing for industrial demands. Significantly, a vapor phase inclusion technique can deposit uniform ultra-thin films of high quality. Evaporation and CVD-based techniques has been recognized as reliable root for the fabrications of high quality 2D metal oxide films with precise thickness control over large areas (300 mm).[57] Titanium is an attractive model species for vapor phase brush infiltration given its use in a variety of far reaching applications *e.g.* TiO_2 films are routinely fabricated by sol-gel,[58] pulsed laser deposition,[59] chemical vapor deposition,[60] and ALD.[61,62] TiO_2 coatings are widely used in self-cleaning technologies,[63] as an electrode support,[64] as a dielectric medium,[65] and in photocatalysis.[66] ALD grown TiO_2 nanofilms have been used in many applications: corrosion protection layers on copper,[67] in high-κ dielectrics, solar cells (perovskite),[68] carbon nanotubes,[69] and composite nanostructures for water splitting to name a few.[70]

In this chapter, a proof-of-concept technique for vapor phase infiltration of covalently grafted polymer brushes to produce wafer-scale (> 2 cm^2) TiO_2 films with high uniformity is demonstrated on Si substrates. To fabricate coherent inorganic films with precise thickness control, it is critical to generate high-quality polymer brush films i.e. a complete monolayer. Definition of a polymer monolayer with complete coverage can be achieved and is straightforward for polymers which are weakly interacting with one another and the substrate (apart from the reactive terminal group used for grafting). Creating a complete monolayer is considerably more challenging for reactive systems with metal binding sites like poly-2-

vinyl pyridine, hydroxy-terminated (P2VP-OH). The crucial parameters necessary for grafting P2VP monolayers from the liquid phase with very high coverage and uniformity are explored. Factors such as polymer molecular weight (4 - 16 kg mol^{-1}), concentration of casting solution (0.01 – 6 wt. %) and quantity of end groups (mono/di hydroxy terminated) are examined (see **Table 1**). Finally, the potential of a Polystyrene, hydroxy-terminated (PS-OH) brush for substrate deactivation by limiting TTIP infiltration is highlighted. Precisely

Controlling polymer brushes for activating (P2VP-OH) and deactivating (PS-OH) semiconductor surfaces is a critical milestone for fulfilling future device scaling and 3D architectures. The techniques discussed herein can have considerable importance due to the low process temperature (<500 °C) needed for CMOS fabrication.[71] The fundamental insights obtained can illuminate ways to utilize polymer brush films for vapor phase film and ASD device-fabrication strategies.

Table 1 Polymer properties and annealing condition.

Polymer	Mn (kg mol^{-1})	End group (-OH)	Anneal Conditions
P2VP-OH	4.0	mono/di	60 s (230 °C)
	6.2	mono	60 s (230 °C)
	10.0	mono	60 s (230 °C)
	16.0	mono	60 s (230 °C)
PS-OH	6.0	mono	60 s (150 °C)
	10.0	mono	60 s (150 °C)
	16.0	mono	60 s (150 °C)
PMMA-OH	6.3	mono	90 s (190 °C)

3.3 Experiment section:

3.3.1 Materials.

Functionalized polymers: Poly-2-vinyl pyridine, hydroxy-terminated (P2VP-OH): 4 kg mol^{-1} (P18796-2VPOH) (PDI: 1.06), 6.2 kg mol^{-1} (P7544-2VPOH) (PDI: 1.05), 9.6 kg mol^{-1}

(P19125-2VPOH) (PDI: 1.07), 16 kg mol^{-1} (P19128-2VPOH) (PDI: 1.11), di-hydroxy-terminated P2VP: 4 kg mol^{-1} (P18798-2VPOH) (PDI: 1.06). Poly(methyl methacrylate), hydroxy-terminated (PMMA-OH): 6.3 kg mol^{-1} (P1763-MMAOH) (PDI: 1.06). Polystyrene, hydroxy-terminated (PS-OH): 6 kg mol^{-1} (P11116-SOH) (PDI: 1.05), 10 kg mol^{-1} (P18787-SOH) (PDI: 1.09), 16 kg mol^{-1} (P13135-SOH) (PDI: 1.09). The polymers have glass transition temperatures of T_g = 95 °C, 91 °C and 85 °C for PS-OH, P2VP-OH and PMMA-OH respectively.

Homopolymers: Poly-2-vinyl pyridine (P41306-2VP) (PDI: 1.04), Polystyrene (P9405-S) (PDI: 1.03). All polymers were purchased from Polymer Source (Canada) and used without further purification.

Solvents: Tetrahydrofuran (THF) (inhibitor free), toluene, (MERCK, Ireland) were high-performance liquid chromatography (HPLC) grade and deionized water (ρ = 18.2 MΩ.cm) used as received.

Precursor: Titanium tetraisopropoxide (TTIP) (99.999%) (MERCK, Ireland) was used as received.

Pure P2VP, PS ,PMMA and SiO_2 Reference Substrates. Unfunctionalized P2VP, PS and PMMA homopolymers were used to fabricate reference substrates. The powders were each dry-pressed into disc-shaped pellets (≈ 2 mm thick) at 350 MPa in a 13 mm diameter steel pellet die (Specac, 13 mm evacuable pellet die). The pellets were exposed to solvent vapors (THF for P2VP and toluene for PS and PMMA) until a smooth mirror like surface was produced, similar to our previous work.[53] These fabricated substrates were used to determine the baseline contact angles for pure polymer surfaces to infer brush coverage on Si substrates. Plasma cleaned SiO_2 was used as a reference (60 s, 40 kHz, 50 W, Barrel Asher).

3.3.2 Polymer brush grafting

Silicon substrates (with native oxide) were cleaned and hydroxyl functionalized using an oxygen plasma treatment for 60 s (40 kHz, 50 W, Barrel Asher). P2VP-OH was dissolved in

THF, PMMA-OH and PS-OH were dissolved in toluene by stirring at room temperature (12 hr.). Polymer-solvent casting solutions were prepared at concentrations ranging from 0.01 – 6 wt. % and spin coated at 3000 rpm for 30 s. Samples were placed on a hotplate and annealed at: 150 °C for 60 s (PS-OH), 190 °C for 90 s (PMMA-OH) and 230 °C for 60 s (P2VP-OH) for covalent grafting on SiO_2 via condensation reactions.[72,73] See **Figure S3.7.1** for thermogravimetric analysis (TGA) showing max process temperatures for each polymer. Following baking periods, samples were sonicated in respective solvents for 20 min (2 x 10 min washes) to remove physisorbed, ungrafted polymer material.

3.3.3 Titanium Dioxide Fabrication

For the TTIP infiltration process, grafted monolayer films of 0.2 wt. % P2VP (4 and 6 kg mol^{-1}) and 0.2 wt. % PS were used (6 kg mol^{-1}). Samples were place upside-down in a sealed glass chamber (height: 50 mm, diameter: 24 mm) containing ≈ 1 ml TTIP for 2 hr. at 20 °C (partial pressure ≈ 53 Pa).[74] Polymer ashing and conversion to titanium dioxide was achieved by UV/ozone exposure (3 hr.) (Novascan PDSP-UV4).

3.3.4 Characterization

Field emission scanning electron microscopy (FESEM, Carl Zeiss Ultra) was performed using a secondary electron detector (InLens) with an accelerating voltage 1 - 2 kV. Focused ion beam etching (FIB, Helios Nanolab 460) was used for preparing lamella specimen using standard high kV milling and a low kV final polish, this rendered the lamella electron transparent indicating an appropriate thickness for TEM. A capping layer of e-beam platinum (~ 100 nm) and ion-beam Pt (~2 micron) was used for FIB lamella. Transmission electron microscopy (TEM, FEI Osiris) was performed using brightfield and STEM imaging. During STEM detector lengths were 220, 550 and 770 mm. The accelerating voltage was 200 kV. The EDX beam current was 1 nA, acquisition time: 30 min. Atomic force microscopy (AFM, Park Systems XE7) was used with a non-contact cantilever (AC160TS, force constant ≈26 Nm^{-1}, resonant frequency ≈ 300 kHz).

X-ray photoelectron spectroscopy (XPS, VG Scientific ESCAlab Mk II) was performed under ultra-high vacuum conditions (<5 x 10^{-10} mbar) using a hemispherical analyzer and Al Kα X-rays (1486.7 eV). The emitted photoelectrons were collected at a take-off angle of 90 ° from the samples surface. The analyzer pass energy was set to 100 eV for survey scans and 20 – 40 eV for high-resolution core scans, yielding an overall resolution of 1.5 eV. Photoemission peak positions were corrected to C 1s at a binding energy of 284.8 eV.[75]

Dynamic contact angle (CA) measurments (custom built system) were recorded on five different regions of each sample using a high-speed camera (60 Hz sampling rate) to capture the advancing and receding CAs of three probe liquids (water, diiodomethane and glycerol). Liquids were dispensed with flow rates of 5 nls^{-1} using a 35-gauge needle (Ø135 μm OD) with droplet volumes between 40-100 nl. Surface energy analysis was determined from the advancing CAs of the three probe liquids using the Lifshitz-van der Waals/acid-base approach.[76]

Dynamic Light Scattering (DLS, Malvern Zetasizer Nano ZSP) was performed on the polymer casting solutions.

(TGA, Pyris 1) was performed on the functionalized polymers at a temperature range of 25°C - 700°C for 90 min.

3.4 Results and discussions:

3.4.1 Monolayer point of a grafted polymer brush:

We chose (P2VP-OH) (**Figure 3.1 (a)**) due to the strong metal-pyridine binding interactions observed for a myriad of metal ions including Ti.[77,78] We compare grafting parameters to another reactive polymer PMMA-OH (**Figure 3.1 (b)**) and a relatively non-reactive polymer PS-OH (**Figure 3.1 (c)**). The high-quality grafted P2VP brushes were exposed to vapor phase titanium tetraisopropoxide (TTIP) (**Figure 3.1 (d)**). Conversion to TiO_2 is performed using UV/ozone processing. Control over the final oxide thickness (≈ 2-4 nm) is demonstrated by adjusting the polymer molecular weight. This organometallic precursor (and component of

the Sharpless epoxidation) was chosen for its ability to selectively deposit Ti^{4+} cations within the hydrophilic domains of self-assembled block copolymers in our previous work.[79]

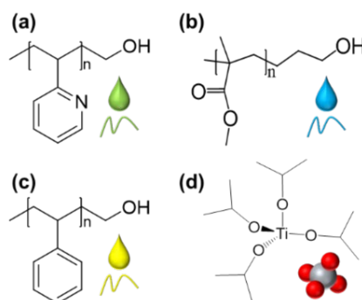

Figure 3.1: Hydroxy terminated (a) Poly-(2-vinyl pyridine), (b) Poly-(methyl methacrylate), (c) Poly-(styrene) (d) titanium tetraisoprpoxide.

The Hansen approach was used to identify selective polymer-solvent casting solutions (P2VP/THF and PS/toluene respectively) and is described in detail elsewhere.[53] **Figure 3.2** shows examples of the 6 kg mol^{-1} P2VP-OH grafted from solutions of solvents above and below the critical agglomerate concentration (CAC) to silicon substrates. The SEM image in **Figure 3.2 (a)** is characteristic of a well grafted brush monolayer, cast from a 0.2 wt. % solution. (see **Figure S3.7.2**) for higher magnification SEM images. The TEM image in **Figure 3.2 (a)** (inset) shows the brush film has high uniformity and a thickness ≈ 4 nm (see (**Figure S3.7.3**) for TEM of the 4 kg mol^{-1}grafted monolayer ≈ 3.4 nm). By contrast, the SEM image in **Figure 3.2 (b**) cast from a 2.0 wt. % solution is an example of a poorly grafted P2VP-OH film with a molecular weight of 6.2 kg mol^{-1}. Polymer coverage is uneven and shown in more detail in (**Figure S3.7.4**). The nature of P2VP-OH material displayed in **Figure 3.2 (b)** suggests that ideal conditions are not satisfied to define the observed structure as a brush film.

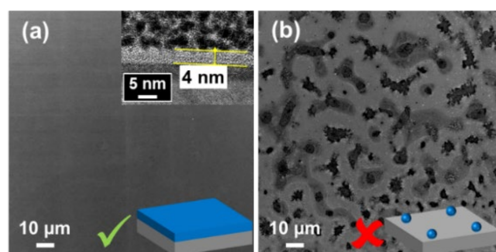

Figure 3.2: SEM images of a grafted P2VP-OH (M_n= 6 kg mol^{-1}) cast (a) below the CAC (with TEM images inset) showing a uniform monolayer and (b) above the CAC with uneven coverage.

Di-hydroxy terminated P2VP (Mn = 4 kg mol^{-1}) was end-grafted but uniform monolayer coverage was not achieved (see **Figure S3.7.5 (a)**). Large agglomerates are present throughout the film, consistent with hydroxy end groups grafting to adjacent polymer end groups during annealing. We also note that P2VP-OH polymer with molecular weights of 10 and 16 kg mol^{-1} did not form uniform monolayers (**Figure S3.7.5 (b)** and **(c)**). DLS studies were performed on the casting solutions to elucidate the impact of concentration and molecular weight on the grafting mechanism. DLS of P2VP-OH (Mn = 6 kg mol^{-1}) casting solutions show an increase in agglomerate size with concentration (**Figure S3.7.6 (a)** and **(b)**). **Figure S3.7.6 (c)** shows an increase in agglomerate size with molecular weight at fixed concentration (0.2 wt. %). The increase in agglomerate size in the casting solutions with concentration or molecular weight is consistent with the particularly strong pyridine-pyridine stacking interactions of the P2VP molecular system.[80] **Figure 3.3** displays a schematic of the proposed grafting mechanism above and below the CAC. As the casting solution concentration or polymer molecular weight increases, larger sized agglomerates deposit on the substrate following spin-coating. Above the CAC the agglomerates are sufficiently large that steric repulsion effects begin to prevent formation of a uniform coating *i.e.* gaps develop between agglomerates. Upon annealing, the chains near the substrate reptate and successfully locate the surface to overcome the thermodynamic reaction barrier to condensation. The physisorbed overlayers are removed during the solvent wash to reveal

an uneven coating. Below the CAC, a uniform brush monolayer can be prepared for TTIP vapor infiltration.

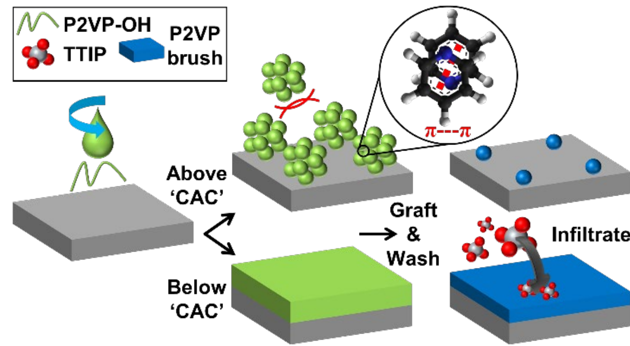

Figure 3.3: Schematic representation of the grafting process above and below the CAC for P2VP-OH (molecular weight=6 kg mol^{-1}). Poor coverage occurs above CAC due to strong pyridine-pyridine stacking interactions. The P2VP monolayer brush can be infiltrated with TTIP converted to TiO_2 using UV/Ozone.

Figure 3.4 shows optimization data used to determine the monolayer point for grafting 4 and 6 kg mol^{-1} P2VP-OH to silicon substrates. Solutions (0.01 – 6 wt. %) were cast, grafted via baking and advancing water contact angle (WCA) measurements were immediately recorded, shown in **Figure 3.4 (a)**. The control reference SiO_2 sample has an average advancing WCA of $\theta_{SiO2} = 4.0° \pm 0.4°$. At 0.01 wt. %, the average advancing WCA increases to $\theta_{P2VP(\mathbf{4k})} = 47.4° \pm 0.8°$ and $\theta_{P2VP(\mathbf{6k})} = 57.1° \pm 2.6°$ respectively. Above 0.05 wt. %, the advancing WCAs rapidly asymptote and saturate with an average advancing WCA of $\theta_a \approx 77°$, similar to the value obtained for the pressed P2VP pellet ($\theta_{P2VP(max)} = 76.7° \pm 1.6°$). This trend holds for the 4 kg mol^{-1} polymer, however above a concentration of $\approx$ 1 wt. % the 6 kg mol^{-1} P2VP-OH rapidly transitions to a highly wetting surface ($\theta_{P2VP(\mathbf{6k})} < 10°$) consistent with very low grafting density.

The observed θ_a behavior of the P2VP-OH brush surfaces is correlated to surface coverage using the Cassie-Baxter equation[81,82] with the assumption of surface energy heterogeneity at the molecular scale,[83]

$$\Phi = \left(\frac{\cos\theta_A}{\cos\theta_{SiO2}} - 1\right) / \left(\frac{\cos\theta_{max}}{\cos\theta_{SiO2}} - 1\right) \text{----1}$$

Where Φ is the apparent surface coverage of the grafted polymer brush, θ_{conc} is θ_a measured at a given grafting concentration and $\theta_{P2VP(max)}$ is θ_a of the pure P2VP pellet. **Figure 3.4 (b)** shows the change of surface coverage with solution concentration for the brush samples, calculated from equation 1. The increased Φ at the low dilution limit (0.01 wt. %) for the 6 kg mol^{-1} vs 4 kg mol^{-1} P2VP-OH brush is consistent with a longer chain length *i.e.* more surface coverage for equivalent condensation reactions. Additionally, we used X-ray photoelectron spectroscopy in order to provide further confirmation of the grafting behavior of the 4 kg mol^{-1} and 6 kg mol^{-1} P2VP-OH systems. The N *1s* signal (~ 401 eV) from grafted brushes was tracked over the concentration range in **Figure 3.4 (c)**. A strikingly similar evolution profile to **Figure 3.4 (a)** and **(b)** is observed from the N *1s* data, consistent with the coverage level determined by WCA and Cassie-Baxter equation. **Figure 3.4 (d) – (f)** are AFM images of the 4 kg mol^{-1} P2VP-OH grafted brush (0.2 wt. %, 2.0 wt. %, 6.0 wt. %). The films are very smooth with high coverage, RMS roughness ≈ 0.6 nm (average of 3 AFM scans). The roughness factor r, defined as the ratio of actual surface area to projected area, was calculated from the height images < 1.04, representing minimal contribution to surface wettability as per the Wenzel equation, $\cos\theta_{apparent} = r\cos\theta$.[84] For the 6 kg mol^{-1} brush (**Figure 3.4 (g) – (i)**) only the 0.2 wt. % shows good uniformity and coverage. See (**Figure S3.7.7**) for detailed surface energy analysis of the grafted brushes. At high coverage the dispersive and polar components match that of the pure polymer pellet, and the silicon control at low coverage (**Figure S3.7.7 (a)**). The same trend is observed for the Lewis acid and Lewis base interactions (**Figure S3.7.7 (b)**).

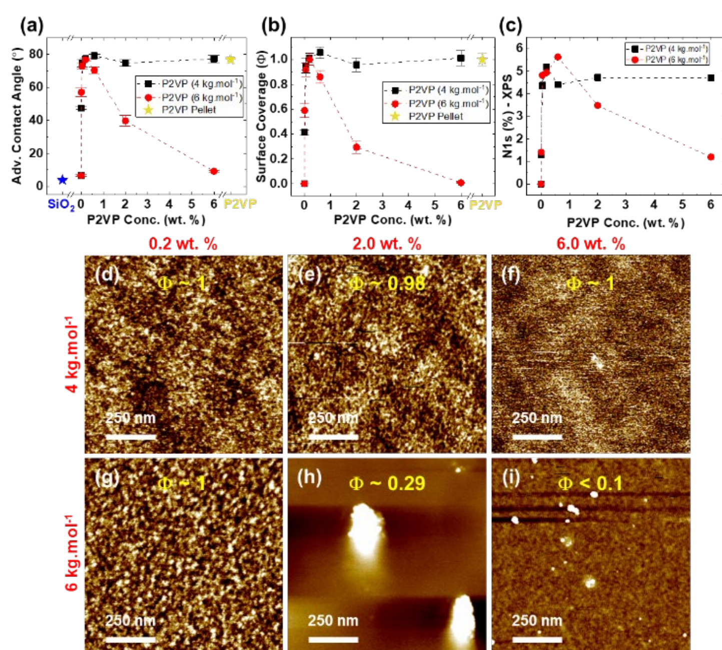

Figure 3.4 (a): Advancing WCAs of the 4 and 6 kg mol^{-1} P2VP brush samples grafted on silicon substrates over the range of concentrations with corresponding coverage (b). (c) XPS nitrogen (N 1s) atomic percentage of the grafted polymers as the function of concentrations. AFM topography images of the P2VP brushes grafted from 0.2 to 6 wt. % solutions for (d)-(f) 4 kg mol^{-1} and (g)-(h) 6 kg mol^{-1} P2VP-OH.

The grafting process was tested with PS-OH (Mn = 6.0 – 16.0 kg mol^{-1}), as shown in Section **S3.7.2**. Grafting high quality uniform monolayers was achievable at all molecular weights and concentrations (> 0.01 wt. %). PMMA-OH (Mn = 6.3 kg mol^{-1}) was tested (Section **S3.7.3**) with high-quality monolayers observed even for 6.0 wt. % grafting solutions. These less reactive brushes can graft monolayers at higher molecular weight and concentration compared with PVP where stronger intermolecular forces exist between the molecules due to substantial π-orbital interactions.[80] Casting at elevated temperature, or using a more selective solvent, is also a possible route to high molecular weight PVP based monolayer films.

3.4.2 Polymer Brush Exposure/Infiltration to Titanium Isopropoxide.

The optimized 4 and 6 kg mol^{-1} P2VP-OH brush monolayers were exposed to TTIP vapors and converted to TiO_2 films (see experimental for TTIP infiltration conditions). The Ti 2p XPS spectra in **Figure 3.5 (a)** shows the TTIP infiltrated brushes and its conversion to TiO_2. Both brushes were treated under the same TTIP processing conditions, however ≈ 50 % more precursor uptake is measured in the 6 kg mol^{-1} brush. See **Figure S3.7.15** for the corresponding survey spectra showing an increase in the Ti signal from 6.2 % to 9.0%. TiO_2 is formed after UV/Ozone exposure with the Ti $2p_{3/2}$ and Ti $2p_{1/2}$ peaks at ≈ 458 and 464 eV respectively.[85] A slight reduction in the Ti signal occurs following ashing due to partial removal of TTIP precursor. The O 1s spectra in **Figure 3.5 (b)** displays the TTIP infiltrated P2VP-OH brush (Mn = 6.2) before and after UV/ozone exposure. Before UV/ozone, the Ti^{4+}, SiO_2 and isopropoxide peaks are observed at ≈ 529.7 eV (Ti-O bonds), ≈ 531.7 eV (Si-O bonds) and ≈ 532.5 eV (C-O bonds) respectively.[79,85] Post UV/ozone, we observe the absence of the isopropoxide peak and partial loss of the Ti^{4+} peak is observed. There is an increase in the SiO_2 peak due to reduced attenuation of the substrate signal. Before UV/ozone, the N 1s region **(Figure 3.5 (c)** has a peak at ≈ 399 eV associated with C=N-C pyridine bonds[86,87] while after UV/ozone, the pyridine signal is absent (within XPS detection limits) indicating total removal/conversion of brush material.

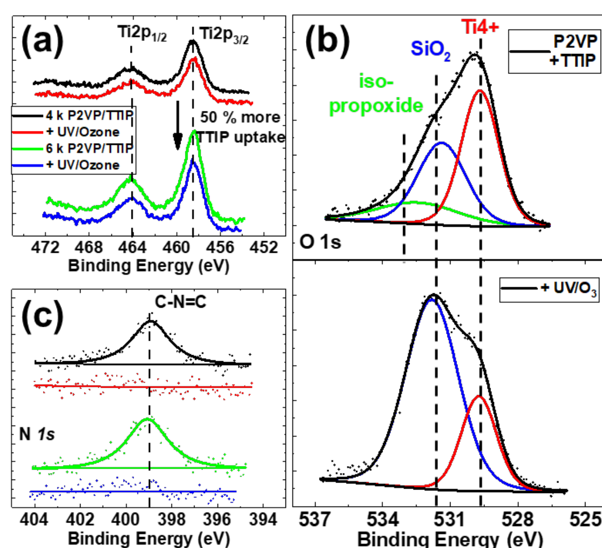

Figure 3.5 XPS: high-res spectra (raw counts) of grafted 4 and 6 kg mol^{-1} P2VP-OH brushes exposed to TTIP and fallowing uv/ozone for (a) Titanium 2p (b) oxygen 1s and (c) nitrogen 1s.

EDX elemental maps in **Figure 3.6 (b)** show the film with titanium and oxygen signals present. **Figure S3.7.16** shows the film before UV/ozone and Figure **S3.7.17 – S3.7.18** are of the process applied to the 4 kg mol^{-1} P2VP-OH brush. Moreover, a thinner TiO_2 film (≈ 2 nm) is fabricated using the 4 kg mol^{-1} brush showing that our process can be used to tune TiO_2 films with nanometer control. For comparison, the TTIP infiltration process was applied to the 6 kg mol^{-1} PS-OH grafted brush (**Figure S3.7.19**). PS-OH grafted brushes exhibit excellent potential for blocking TTIP infiltration with EDX maps confirming that the precursor is inhibited by the PS brush with no Ti present at the substrate interface.

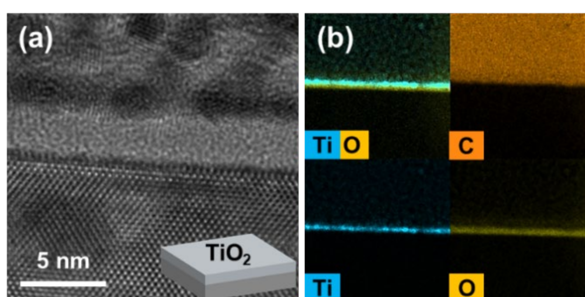

Figure 3.6 (a): Bright-field TEM images of the TiO_2 film (after uv/ozone) and (b) the corresponding EDX maps (Ti, C, O) fallowing TTIP treatment of a uniform P2VP-OH film (M_n = 6 kg mol^{-1}).

3.5 Conclusions

High quality TiO_2 films were fabricated using simple apparatus that allowed definition of precise polymer films for hosting titanium precursors using a facile vapor phase infiltration technique. It was shown that high coverage, pin hole free, homogeneous TiO_2 films with tunable thickness could be produced as confirmed by extensive SEM and TEM analysis. This article discussed the precise parameters required for end-grafting monolayer P2VP-OH polymer brushes (polymer molecular weight, casting solution concentration and terminal group density). The brush layer deposition/attachment requires careful optimization to allow monolayer formation. This subsequently facilitates the regularity of the inorganic film. As the P2VP brushes contain active groups that bind to metal, there is a propensity for coordination of the polymer to form aggregates in solution and 3D films that mitigate against precise monolayer formation. This work shows that process conditions and treatments can be created to mitigate these difficulties. Brushes such as PMMA may be more suitable for fabricating thick inorganic films and studies are currently underway. In parallel, we have shown that PS brushes demonstrate excellent potential for surface deactivation where TTIP deposition was completely prevented from reaching the substrate. In summary, we precisely controlled polymer brushes for activating (P2VP-OH) and deactivating (PS-OH) semiconductor surfaces, which is a first achievement of this critical milestone for fulfilling future device scaling and 3D architectures. We envisage that our deposition and brush process could also find use in other sectors that rely on uniform nanometer inorganic films e.g. glass coating technologies (self-cleaning, anti-condensation, low emissivity etc.), digital display (electrode, conductive and emissive LCD/LED/OLED layers).

3.6 References:

(1) Morris, M. A. Directed Self-Assembly of Block Copolymers for Nanocircuitry Fabrication. *Microelectron. Eng.* **2015**, *132*, 207–217. https://doi.org/10.1016/j.mee.2014.08.009.

(2) Samsung Electronics' Leadership in Advanced Foundry Technology Showcased with Latest Silicon Innovations and Ecosystem Platform.

(3) TSMC starts work on US$19.6 Billion 3nm fab i... | Taiwan News.

(4) Bae, G.; Bae, D. I.; Kang, M.; Hwang, S. M.; Kim, S. S.; Seo, B.; Kwon, T. Y.; Lee, T. J.; Moon, C.; Choi, Y. M.; Oikawa, K.; Masuoka, S.; Chun, K. Y.; Park, S. H.; Shin, H. J.; Kim, J. C.; Bhuwalka, K. K.; Kim, D. H.; Kim, W. J.; Yoo, J.; Jeon, H. Y.; Yang, M. S.; Chung, S. J.; Kim, D.; Ham, B. H.; Park, K. J.; Kim, W. D.; Park, S. H.; Song, G.; Kim, Y. H.; Kang, M. S.; Hwang, K. H.; Park, C. H.; Lee, J. H.; Kim, D. W.; Jung, S. M.; Kang, H. K. 3nm GAA Technology Featuring Multi-Bridge-Channel FET for Low Power and High Performance Applications. In *Technical Digest - International Electron Devices Meeting, IEDM*; Institute of Electrical and Electronics Engineers Inc., 2019; Vol. 2018-Decem, pp 28.7.1-28.7.4. https://doi.org/10.1109/IEDM.2018.8614629.

(5) Thomas Mårtensson; Patrick Carlberg; Magnus Borgström; Lars Montelius; Werner Seifert, and; Samuelson*, L. Nanowire Arrays Defined by Nanoimprint Lithography. **2004**. https://doi.org/10.1021/NL035100S.

(6) Borah, D.; Cummins, C.; Rasappa, S.; Senthamaraikannan, R.; Salaun, M.; Zelsmann, M.; Liontos, G.; Ntetsikas, K.; Avgeropoulos, A.; Morris, M.; Borah, D.; Cummins, C.; Rasappa, S.; Senthamaraikannan, R.; Salaun, M.; Zelsmann, M.; Liontos, G.; Ntetsikas, K.; Avgeropoulos, A.; Morris, M. A. Nanopatterning via Self-Assembly of a Lamellar-Forming Polystyrene-Block-Poly(Dimethylsiloxane) Diblock Copolymer on Topographical Substrates Fabricated by Nanoimprint Lithography. *Nanomaterials* **2018**, *8* (1), 32. https://doi.org/10.3390/nano8010032.

(7) Cummins, C.; Mokarian-Tabari, P.; Andreazza, P.; Sinturel, C.; Morris, M. A. Solvothermal Vapor Annealing of Lamellar Poly(Styrene)-Block-Poly(d,l-Lactide) Block Copolymer Thin Films for Directed Self-Assembly Application. *ACS Appl. Mater. Interfaces* **2016**. https://doi.org/10.1021/acsami.6b00765.

(8) Ross, C. a; Berggren, K. K.; Cheng, J. Y.; Jung, Y. S.; Chang, J.-B. Three-Dimensional Nanofabrication by Block Copolymer Self-Assembly. *Adv. Mater.* **2014**, *26* (25), 4386–4396. https://doi.org/10.1002/adma.201400386.

(9) Oh, J.; Suh, H. S.; Ko, Y.; Nah, Y.; Lee, J.-C.; Yeom, B.; Char, K.; Ross, C. A.; Son, J. G. Universal Perpendicular Orientation of Block Copolymer Microdomains Using a Filtered Plasma. *Nat. Commun.* **2019**, *10* (1), 2912. https://doi.org/10.1038/s41467-019-10907-5.

(10) Fernandez, E.; Tu, K. H.; Ho, P.; Ross, C. A. Thermal Stability of L10-FePt Nanodots Patterned by Self-Assembled Block Copolymer Lithography. *Nanotechnology* **2018**, *29* (46), 465301. https://doi.org/10.1088/1361-6528/aade2f.

(11) Tu, K.-H.; Bai, W.; Liontos, G.; Ntetsikas, K.; Avgeropoulos, A.; Ross, C. a. Universal Pattern Transfer Methods for Metal Nanostructures by Block Copolymer Lithography. *Nanotechnology* **2015**, *26* (37), 375301. https://doi.org/10.1088/0957-4484/26/37/375301.

(12) Gotrik, K. W.; Hannon, A. F.; Son, J. G.; Keller, B.; Alexander-katz, A.; Ross, C. A. Morphology Control in Block Copolymer Films Using Mixed Solvent Vapors, 2012.

(13) Lundy, R.; Flynn, S. P.; Cummins, C.; Kelleher, S. M.; Collins, M. N.; Dalton, E.; Daniels, S.; Morris, M. A.; Enright, R. Controlled Solvent Vapor Annealing of a High χ Block Copolymer Thin Film. *Phys. Chem. Chem. Phys.* **2017**, *19* (4), 2805–2815. https://doi.org/10.1039/C6CP07633E.

(14) Lundy, R.; Flynn, S. P.; Cummins, C.; Kelleher, S. M.; Collins, M. N.; Dalton, E.; Daniels, S.; Morris, M.; Enright, R. Nanoporous Membrane Production via Block Copolymer Lithography for High Heat Dissipation Systems. In *2016 15th IEEE Intersociety Conference on Thermal and Thermomechanical Phenomena in Electronic Systems (ITherm)*; IEEE, 2016; pp 1267–1272.

(15) Mackus, A. J. M.; Merkx, M. J. M.; Kessels, W. M. M. From the Bottom-Up: Toward Area-Selective Atomic Layer Deposition with High Selectivity †. *Chem. Mater.* **2019**, *31* (1), 2–12. https://doi.org/10.1021/acs.chemmater.8b03454.

(16) Seo, S.; Oh, I.-K.; Yeo, B. C.; Han, S. S.; Yoon, C. M.; Yang, J. Y.; Yoon, J.; Yoo, C.; Kim, H.; Lee, Y.; Lee, S. J.; Myoung, J.-M.; Lee, H.-B.-R.; Kim, W.-H.; Kim, H. Reaction Mechanism of Area-Selective Atomic Layer Deposition for Al2O3 Nanopatterns. *ACS Appl. Mater. Interfaces* **2017**, acsami.7b13365. https://doi.org/10.1021/acsami.7b13365.

(17) Prasittichai, C.; Pickrahn, K. L.; Minaye Hashemi, F. S.; Bergsman, D. S.; Bent, S. F. Improving Area-Selective Molecular Layer Deposition by Selective SAM Removal. *ACS Appl. Mater. Interfaces* **2014**, *6* (20), 17831–17836. https://doi.org/10.1021/am504441e.

(18) Nagata, T. *Material Design of Metal/Oxide Interfaces for Nanoelectronics Applications*, 1st ed.; Springer Japan, 2020.

(19) Li, R.; Zhang, F.; Wang, D.; Yang, J.; Li, M.; Zhu, J.; Zhou, X.; Han, H.; Li, C. Spatial Separation of Photogenerated Electrons and Holes among {010} and {110} Crystal Facets of BiVO 4. *Nat. Commun.* **2013**, *4*. https://doi.org/10.1038/ncomms2401.

(20) Xie, J.; Yang, X.; Han, B.; Shao-Horn, Y.; Wang, D. Site-Selective Deposition of Twinned Platinum Nanoparticles on $TiSi_2$ Nanonets by Atomic Layer Deposition and Their Oxygen Reduction Activities. *ACS Nano* **2013**, *7* (7), 6337–6345. https://doi.org/10.1021/nn402385f.

(21) Färm, E.; Kemell, M.; Ritala, M.; Leskelä, M. Self-Assembled Octadecyltrimethoxysilane Monolayers Enabling Selective-Area Atomic Layer Deposition of Iridium. *Chem. Vap. Depos.* **2006**, *12* (7), 415–417. https://doi.org/10.1002/cvde.200604219.

(22) Färm, E.; Kemell, M.; Ritala, M.; Leskelä, M. Selective-Area Atomic Layer Deposition with Microcontact Printed Self-Assembled Octadecyltrichlorosilane Monolayers as Mask Layers. *Thin Solid Films* **2008**, *517* (2), 972–975. https://doi.org/10.1016/J.TSF.2008.08.191.

(23) Färm, E.; Vehkamäki, M.; Ritala, M.; Leskelä, M. Passivation of Copper Surfaces for Selective-Area ALD Using a Thiol Self-Assembled Monolayer. *Semicond. Sci. Technol.* **2012**, *27* (7), 074004. https://doi.org/10.1088/0268-1242/27/7/074004.

(24) Färm, E.; Lindroos, S.; Ritala, M.; Markku, L. Microcontact Printed Films as an Activation Layer for Selective Atomic Layer Deposition, July 2011.

(25) Färm, E.; Lindroos, S.; Ritala, M.; Leskelä, M. Microcontact Printed RuO x Film as an Activation Layer for Selective-Area Atomic Layer Deposition of Ruthenium. *Chem. Mater.* **2012**, *24* (2), 275–278. https://doi.org/10.1021/cm202468s.

(26) Färm, E.; Kemell, M.; Ritala, M.; Leskelä, M. Selective-Area Atomic Layer Deposition Using Poly(Methyl Methacrylate) Films as Mask Layers. *J. Phys. Chem. C* **2008**, *112* (40), 15791–15795. https://doi.org/10.1021/jp803872s.

(27) Färm, E.; Kemell, M.; Santala, E.; Ritala, M.; Leskelä, M. Selective-Area Atomic Layer Deposition Using Poly(Vinyl Pyrrolidone) as a Passivation Layer. *J. Electrochem. Soc.* **2010**, *157* (1), K10. https://doi.org/10.1149/1.3250936.

(28) Minaye Hashemi, F. S.; Prasittichai, C.; Bent, S. F. Self-Correcting Process for High Quality Patterning by Atomic Layer Deposition. *ACS Nano* **2015**, *9* (9), 8710–8717. https://doi.org/10.1021/acsnano.5b03125.

(29) Minaye Hashemi, F. S.; Birchansky, B. R.; Bent, S. F. Selective Deposition of Dielectrics:

Limits and Advantages of Alkanethiol Blocking Agents on Metal-Dielectric Patterns. *ACS Appl. Mater. Interfaces* **2016**, *8* (48), 33264–33272. https://doi.org/10.1021/acsami.6b09960.

(30) Chen, R.; Kim, H.; McIntyre, P. C.; Bent, S. F. Self-Assembled Monolayer Resist for Atomic Layer Deposition of HfO2 and ZrO2 High-κ Gate Dielectrics. *Appl. Phys. Lett.* **2004**, *84* (20), 4017–4019. https://doi.org/10.1063/1.1751211.

(31) Rong Chen, †; Hyoungsub Kim, ‡; Paul C. McIntyre, ‡ and; Stacey F. Bent*, §. Investigation of Self-Assembled Monolayer Resists for Hafnium Dioxide Atomic Layer Deposition. **2005**. https://doi.org/10.1021/CM0486666.

(32) Junsic Hong, †; David W. Porter, †; Raghavasimhan Sreenivasan, ‡; Paul C. McIntyre, ‡ and; Stacey F. Bent*, †. ALD Resist Formed by Vapor-Deposited Self-Assembled Monolayers. **2006**. https://doi.org/10.1021/LA0606401.

(33) Jiang, X.; Bent, S. F. Area-Selective ALD with Soft Lithographic Methods: Using Self-Assembled Monolayers to Direct Film Deposition. https://doi.org/10.1021/jp905317n.

(34) Bobb-semple, D.; Nardi, K. L.; Draeger, N.; Hausmann, D. M.; Bent, S. F. Area-Selective Atomic Layer Deposition Assisted by Self-Assembled Monolayers: A Comparison of Cu, Co, W, and Ru. **2019**. https://doi.org/10.1021/acs.chemmater.8b04926.

(35) Kim, W. H.; Minaye Hashemi, F. S.; Mackus, A. J. M.; Singh, J.; Kim, Y.; Bobb-Semple, D.; Fan, Y.; Kaufman-Osborn, T.; Godet, L.; Bent, S. F. A Process for Topographically Selective Deposition on 3D Nanostructures by Ion Implantation. *ACS Nano* **2016**, *10* (4), 4451–4458. https://doi.org/10.1021/acsnano.6b00094.

(36) Vervuurt, R. H. J.; Sharma, A.; Jiao, Y.; Kessels, W. (Erwin) M. M.; Bol, A. A. Area-Selective Atomic Layer Deposition of Platinum Using Photosensitive Polyimide. *Nanotechnology* **2016**, *27* (40), 405302. https://doi.org/10.1088/0957-4484/27/40/405302.

(37) Mameli, A.; Kuang, Y.; Aghaee, M.; Ande, C. K.; Karasulu, B.; Creatore, M.; Mackus, A. J. M.; Kessels, W. M. M.; Roozeboom, F. Area-Selective Atomic Layer Deposition of In_2O_3:H Using a μ-Plasma Printer for Local Area Activation. *Chem. Mater.* **2017**, *29* (3), 921–925. https://doi.org/10.1021/acs.chemmater.6b04469.

(38) MacKus, A. J. M.; Verheijen, M. A.; Leick, N.; Bol, A. A.; Kessels, W. M. M. Influence of Oxygen Exposure on the Nucleation of Platinum Atomic Layer Deposition: Consequences for Film Growth, Nanopatterning, and Nanoparticle Synthesis. *Chem. Mater.* **2013**, *25* (9), 1905–1911. https://doi.org/10.1021/cm400562u.

(39) Thissen, N. F. W.; Vervuurt, R. H. J.; Mackus, A. J. M.; Mulders, J. J. L.; Weber, J.-W.; Kessels, W. M. M.; Bol, A. A. Graphene Devices with Bottom-up Contacts by Area-Selective Atomic Layer Deposition. *2D Mater.* **2017**, *4* (2), 025046. https://doi.org/10.1088/2053-1583/aa636a.

(40) Mameli, A.; Karasulu, B.; Verheijen, M. A.; Barcones, B.; Macco, B.; Mackus, A. J. M.; Kessels, W. M. M. E.; Roozeboom, F. Area-Selective Atomic Layer Deposition of ZnO by Area Activation Using Electron Beam-Induced Deposition. *Chem. Mater.* **2019**, *31* (4), 1250–1257. https://doi.org/10.1021/acs.chemmater.8b03165.

(41) Singh, J. A.; Thissen, N. F. W.; Kim, W.-H.; Johnson, H.; Kessels, W. (Erwin) M. .; Bol, A. A.; Bent, S. F.; Mackus, A. J. M. Area-Selective Atomic Layer Deposition of Metal Oxides on Noble Metals through Catalytic Oxygen Activation. *Chem. Mater.* **2017**, acs.chemmater.7b03818. https://doi.org/10.1021/acs.chemmater.7b03818.

(42) Mameli, A.; Merkx, M. J. M.; Karasulu, B.; Roozeboom, F.; Kessels, W. E. M. M.; Mackus, A. J. M. Area-Selective Atomic Layer Deposition of SiO_2 Using Acetylacetone as a Chemoselective Inhibitor in an ABC-Type Cycle. **2017**. https://doi.org/10.1021/acsnano.7b04701.

(43) Vos, M. F. J.; Chopra, S. N.; Verheijen, M. A.; Ekerdt, J. G.; Agarwal, S.; Kessels, W. M.

M.; Mackus, A. J. M. Area-Selective Deposition of Ruthenium by Combining Atomic Layer Deposition and Selective Etching. *Chem. Mater.* **2019**, *31*, 3878–3882. https://doi.org/10.1021/acs.chemmater.9b00193.

(44) Park, K. J.; Doub, J. M.; Gougousi, T.; Parsons, G. N. Microcontact Patterning of Ruthenium Gate Electrodes by Selective Area Atomic Layer Deposition. *Appl. Phys. Lett.* **2005**, *86* (5), 051903. https://doi.org/10.1063/1.1852079.

(45) Stevens, E.; Tomczak, Y.; Chan, B. T.; Altamirano Sanchez, E.; Parsons, G. N.; Delabie, A. Area-Selective Atomic Layer Deposition of TiN, TiO_2, and HfO_2 on Silicon Nitride with Inhibition on Amorphous Carbon. *Chem. Mater.* **2018**, *30* (10), 3223–3232. https://doi.org/10.1021/acs.chemmater.8b00017.

(46) Atanasov, S. E.; Kalanyan, B.; Parsons, G. N. Inherent Substrate-Dependent Growth Initiation and Selective-Area Atomic Layer Deposition of TiO_2 Using “Water-Free” Metal-Halide/Metal Alkoxide Reactants. *J. Vac. Sci. Technol. A Vacuum, Surfaces, Film.* **2016**, *34* (1), 01A148. https://doi.org/10.1116/1.4938481.

(47) Parsons, G. N.; Kalanyan, B.; Atanasov, S. E.; Lemaire, P.; Oldham, C. (Invited) Using Inherent Substrate-Dependent Nucleation to Promote Metal and Metal Oxide Selective-Area Atomic Layer Deposition. *ECS Trans.* **2016**, *75* (6), 77–83. https://doi.org/10.1149/07506.0077ecst.

(48) Parsons, G. N. Functional Model for Analysis of ALD Nucleation and Quantification of Area-Selective Deposition. *J. Vac. Sci. Technol. A* **2019**, *37* (2), 020911. https://doi.org/10.1116/1.5054285.

(49) Song, S. K.; Saare, H.; Parsons, G. N. Integrated Isothermal Atomic Layer Deposition/Atomic Layer Etching Supercycles for Area-Selective Deposition of TiO2. *Chem. Mater.* **2019**, *31*, 4793–4804. https://doi.org/10.1021/acs.chemmater.9b01143.

(50) Zhang, Y.; Discekici, E. H.; Burns, R. L.; Somervell, M.; Hawker, C. J.; Bates, C. M. A Single-Step, Spin-on Process for High Fidelity and Selective Polymer Deposition. *ACS Appl. Polym. Mater.* **2019**, acsapm.9b00914. https://doi.org/10.1021/acsapm.9b00914.

(51) Zhang, Y.; D’Ambra, C. A.; Katsumata, R.; Burns, R. L.; Somervell, M. H.; Segalman, R. A.; Hawker, C. J.; Bates, C. M. Rapid and Selective Deposition of Patterned Thin Films on Heterogeneous Substrates via Spin Coating. *ACS Appl. Mater. Interfaces* **2019**, *11* (23), 21177–21183. https://doi.org/10.1021/acsami.9b05190.

(52) Cummins, C.; Weingärtner, T.; Morris, M. A. Enabling Large-Area Selective Deposition on Metal-Dielectric Patterns Using Polymer Brush Deactivation. *J. Phys. Chem. C* **2018**, *122* (26), 14698–14705. https://doi.org/10.1021/acs.jpcc.8b04092.

(53) Lundy, R.; Yadav, P.; Selkirk, A.; Mullen, E.; Ghoshal, T.; Cummins, C.; Morris, M. A. Optimizing Polymer Brush Coverage to Develop Highly Coherent Sub-5nm Oxide Films by Ion Inclusion. *Chem. Mater.* **2019**. https://doi.org/10.1021/acs.chemmater.9b02856.

(54) Cummins, C.; Shaw, M. T.; Morris, M. A. Area Selective Polymer Brush Deposition. **2017**, *1700252*, 1–6. https://doi.org/10.1002/marc.201700252.

(55) Snelgrove, M.; Mani-Gonzalez, P. G.; Bogan, J.; Lundy, R.; Rueff, J. P.; Hughes, G.; Yadav, P.; McGlynn, E.; Morris, M.; O’Connor, R. Hard X-Ray Photoelectron Spectroscopy Study of Copper Formation by Metal Salt Inclusion in a Polymer Film. *J. Phys. D. Appl. Phys.* **2019**, *52* (43). https://doi.org/10.1088/1361-6463/ab35b2.

(56) Mani-Gonzalez, P. G.; Snelgrove, M.; Rueff, J.-P.; Lundy, R.; Yadav, P.; Bogan, J.; O’Connor, R.; Morris, M.; Hughes, G. Analysis of Al and Cu Salt Infiltration into a Poly 2-Vinylpyridine (P2vP) Polymer Layer for Semiconductor Device Patterning Applications. *J. Phys. D. Appl. Phys.* **2019**, 1–20. https://doi.org/10.1088/1361-6463/ab60e8.

(57) Walia, S. *Low Power Semiconductor Devices and Processes for Emerging Applications in*

Communications, Computing, and Sensing; CRC Press, 2018. https://doi.org/10.1201/9780429503634.

(58) Wang, C. C.; Ying, J. Y. Sol-Gel Synthesis and Hydrothermal Processing of Anatase and Rutile Titania Nanocrystals. *Chem. Mater.* **1999**, *11* (11), 3113–3120. https://doi.org/10.1021/cm990180f.

(59) Major, B.; Ebner, R.; Zięba, P.; Wolczyǹski, W. Titanium-Based Films Deposited Using a Nd:YAG Pulsed Laser. *Appl. Phys. A Mater. Sci. Process.* **1999**, *69* (7). https://doi.org/10.1007/s003390051559.

(60) Shi, J.; Wang, X. Growth of Rutile Titanium Dioxide Nanowires by Pulsed Chemical Vapor Deposition. *Cryst. Growth Des.* **2011**, *11* (4), 949–954. https://doi.org/10.1021/cg200140k.

(61) Klesko, J. P.; Rahman, R.; Dangerfield, A.; Nanayakkara, C. E.; L'Esperance, T.; Moser, D. F.; Fabián Peña, L.; Mattson, E. C.; Dezelah, C. L.; Kanjolia, R. K.; Chabal, Y. J. Selective Atomic Layer Deposition Mechanism for Titanium Dioxide Films with (EtCp)Ti(NMe2)3: Ozone versus Water. *Chem. Mater.* **2018**, *30* (3), 970–981. https://doi.org/10.1021/acs.chemmater.7b04790.

(62) Ritala, M.; Leskela, M.; Niinisto, L.; Haussalo, P. Titanium Isopropoxide as a Precursor in Atomic Layer Epitaxy of Titanium Dioxide Thin Films. *Chem. Mater.* **1993**, *5* (8), 1174–1181. https://doi.org/10.1021/cm00032a023.

(63) Ganesh, V. A.; Raut, H. K.; Nair, A. S.; Ramakrishna, S. A Review on Self-Cleaning Coatings. *Journal of Materials Chemistry*. November 2011, pp 16304–16322. https://doi.org/10.1039/c1jm12523k.

(64) Usai, S.; Walsh, J. J. Facile Assembly of Polyoxometalate-Polyelectrolyte Films on Nano-MO2(M = Sn, Ti) for Optical Applications. *J. Electroanal. Chem.* **2018**, *815* (March), 86–89. https://doi.org/10.1016/j.jelechem.2018.03.007.

(65) Busani, T.; Devine, R. A. B. Dielectric and Infrared Properties of TiO_2 Films Containing Anatase and Rutile. *Semicond. Sci. Technol.* **2005**, *20* (8), 870–875. https://doi.org/10.1088/0268-1242/20/8/043.

(66) Rahimi, N.; Pax, R. A.; Gray, E. M. A. Review of Functional Titanium Oxides. I: TiO2and Its Modifications. *Prog. Solid State Chem.* **2016**, *44* (3), 86–105. https://doi.org/10.1016/j.progsolidstchem.2016.07.002.

(67) Daubert, J. S.; Hill, G. T.; Gotsch, H. N.; Gremaud, A. P.; Ovental, J. S.; Williams, P. S.; Oldham, C. J.; Parsons, G. N. Corrosion Protection of Copper Using Al_2O_3, TiO_2, ZnO, HfO_2, and ZrO_2 Atomic Layer Deposition. *ACS Appl. Mater. Interfaces* **2017**, *9* (4), 4192–4201. https://doi.org/10.1021/acsami.6b13571.

(68) Zardetto, V.; Williams, B. L.; Perrotta, A.; Di Giacomo, F.; Verheijen, M. A.; Andriessen, R.; Kessels, W. M. M.; Creatore, M. Atomic Layer Deposition for Perovskite Solar Cells: Research Status, Opportunities and Challenges. *Sustainable Energy and Fuels*. Royal Society of Chemistry 2017, pp 30–55. https://doi.org/10.1039/c6se00076b.

(69) Liao, S. Y.; Yang, Y. C.; Huang, S. H.; Gan, J. Y. Synthesis of Pt@TiO2@CNTs Hierarchical Structure Catalyst by Atomic Layer Deposition and Their Photocatalytic and Photoelectrochemical Activity. *Nanomaterials* **2017**, *7* (5). https://doi.org/10.3390/nano7050097.

(70) Kulmas, M.; Paterson, L.; Höflich, K.; Bashouti, M. Y.; Wu, Y.; Göbelt, M.; Ristein, J.; Bachmann, J.; Meyer, B.; Christiansen, S. Composite Nanostructures of TiO_2 and ZnO for Water Splitting Application: Atomic Layer Deposition Growth and Density Functional Theory Investigation. *Adv. Funct. Mater.* **2016**, *26* (27), 4882–4889. https://doi.org/10.1002/adfm.201505524.

(71) IEEE International Interconnect Technology Conference/Advanced Metallization

Conference (IITC/AMC); 2016; pp 133–135.

(72) Brinker, C. J. *HYDROLYSIS AND CONDENSATION OF SILICATES: EFFECTS ON STRUCTURE*; 1988; Vol. 100.

(73) Lebrun, J. J.; Porte, H. Polysiloxanes. *Compr. Polym. Sci. Suppl.* **1989**, 593–609. https://doi.org/10.1016/B978-0-08-096701-1.00175-0.

(74) Siefering, K. L.; Griffin, G. L. Growth Kinetics of CVD TiO2: Influence of Carrier Gas. *J. Electrochem. Soc.* **1990**, *137* (4), 1206–1208. https://doi.org/10.1149/1.2086632.

(75) Barr, T. L.; Seal, S. Nature of the Use of Adventitious Carbon as a Binding Energy Standard. *J. Vac. Sci. Technol. A Vacuum, Surfaces, Film.* **1995**, *13* (3), 1239–1246. https://doi.org/10.1116/1.579868.

(76) Ma, K.-X.; Ho, C.-H.; Zhu, F.; Chung, T.-S. Investigation of Surface Energy for Organic Light Emitting Polymers and Indium Tin Oxide. *Thin Solid Films* **2000**, *371* (1–2), 140–147. https://doi.org/10.1016/S0040-6090(00)00994-9.

(77) M. T. Rodgers, *; J. R. Stanley, and; Amunugama, R. Periodic Trends in the Binding of Metal Ions to Pyridine Studied by Threshold Collision-Induced Dissociation and Density Functional Theory. **2000**. https://doi.org/10.1021/JA0027923.

(78) Kennemur, J. G. Poly(Vinylpyridine) Segments in Block Copolymers: Synthesis, Self-Assembly, and Versatility. *Macromolecules* **2019**, *52*, 1354–1370. https://doi.org/10.1021/acs.macromol.8b01661.

(79) Giraud, E. C.; Mokarian-Tabari, P.; Toolan, D. T. W.; Arnold, T.; Smith, A. J.; Howse, J. R.; Topham, P. D.; Morris, M. A. Highly Ordered Titanium Dioxide Nanostructures via a Simple One-Step Vapor-Inclusion Method in Block Copolymer Films. *ACS Appl. Nano Mater.* **2018**, *1* (7), 3426–3434. https://doi.org/10.1021/acsanm.8b00632.

(80) Sierański, T. Discovering the Stacking Landscape of a Pyridine-Pyridine System. *J. Mol. Model.* **2017**, *23* (12). https://doi.org/10.1007/s00894-017-3496-4.

(81) Cassie, A. B. D.; Baxter, S. Wettability of Porous Surfaces. *Trans. Faraday Soc.* **1944**, *40*, 546–551.

(82) Lundy, R.; Byrne, C.; Bogan, J.; Nolan, K.; Collins, M. N.; Dalton, E.; Enright, R. Exploring the Role of Adsorption and Surface State on the Hydrophobicity of Rare Earth Oxides. *ACS Appl. Mater. Interfaces* **2017**, *9* (15), 13751–13760. https://doi.org/10.1021/acsami.7b01515.

(83) Laibinis, P. E.; Whitesides, G. M. ω-Terminated Alkanethiolate Monolayers on Surfaces of Copper, Silver, and Gold Have Similar Wettabilities. *J. Am. Chem. Soc.* **1992**, *114* (6), 1990–1995. https://doi.org/10.1021/ja00032a009.

(84) Wenzel, R. Resistance of Solid Surfaces to Wetting by Water. *Ind. Eng. Chem.* **1936**, *28* (8), 988–994.

(85) Liu, F. M.; Wang, T. M. Surface and Optical Properties of Nanocrystalline Anatase Titania Films Grown by Radio Frequency Reactive Magnetron Sputtering. *Appl. Surf. Sci.* **2002**, *195* (1–4), 284–290. https://doi.org/10.1016/S0169-4332(02)00569-X.

(86) Snelgrove, M.; Zehe, C.; Lundy, R.; Yadav, P.; Rueff, J.-P.; O'Connor, R.; Bogan, J.; Hughes, G.; McGlynn, E.; Morris, M.; Mani-Gonzalez, P. G. Surface Characterization of Poly-2-Vinylpyridine—A Polymer for Area Selective Deposition Techniques. *J. Vac. Sci. Technol. A* **2019**, *37* (5), 050601. https://doi.org/10.1116/1.5115769.

(87) Si, W.; Lei, W.; Hao, Q.; Xia, X.; Zhang, H.; Li, J.; Li, Q.; Cong, R. Facile Synthesis of Nitrogen-Doped Graphene Derived from Graphene Oxide and Vitamin B3 as High-Performance Sensor for Imidacloprid Determination. *Electrochim. Acta* **2016**, *212*, 784–790. https://doi.org/10.1016/j.electacta.2016.07.063.

3.7 Appendix

Precise definition of a ‘monolayer point’ in polymer brush films for fabricating highly coherent tiO2 thin films by vapor phase infiltration.

Section S3.7.2 – P2VP brush monolayer formation

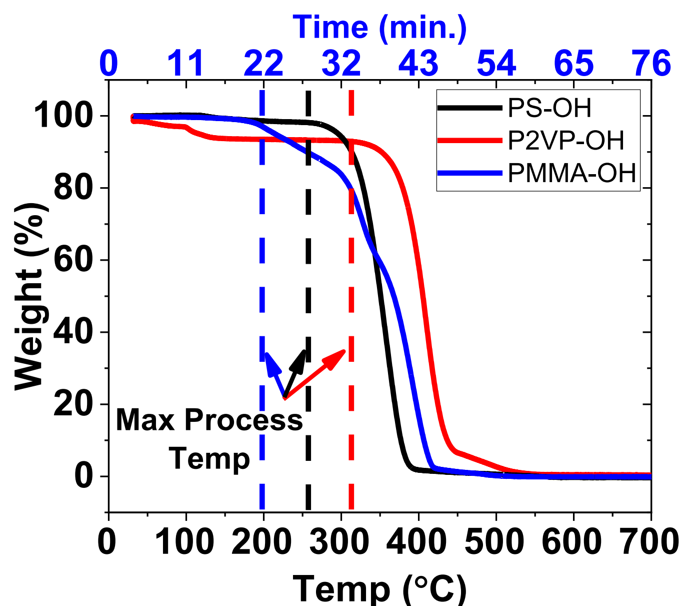

Figure S 3.7.1: Thermogravimetric analysis was performed on the 6 kg mol^{-1}funtionalised polymers at the temperature range of the 25 $^{\circ}$C- 700 °C for 90 min. The polymers undergo thermal degradation (PMMA-OH ~ 195 °C, PS-OH 260 °C and P2VP ~ 320 °C) indicating maximum upper threshold for the grafting process. Note that water loss occurs up to 120/130 °C.

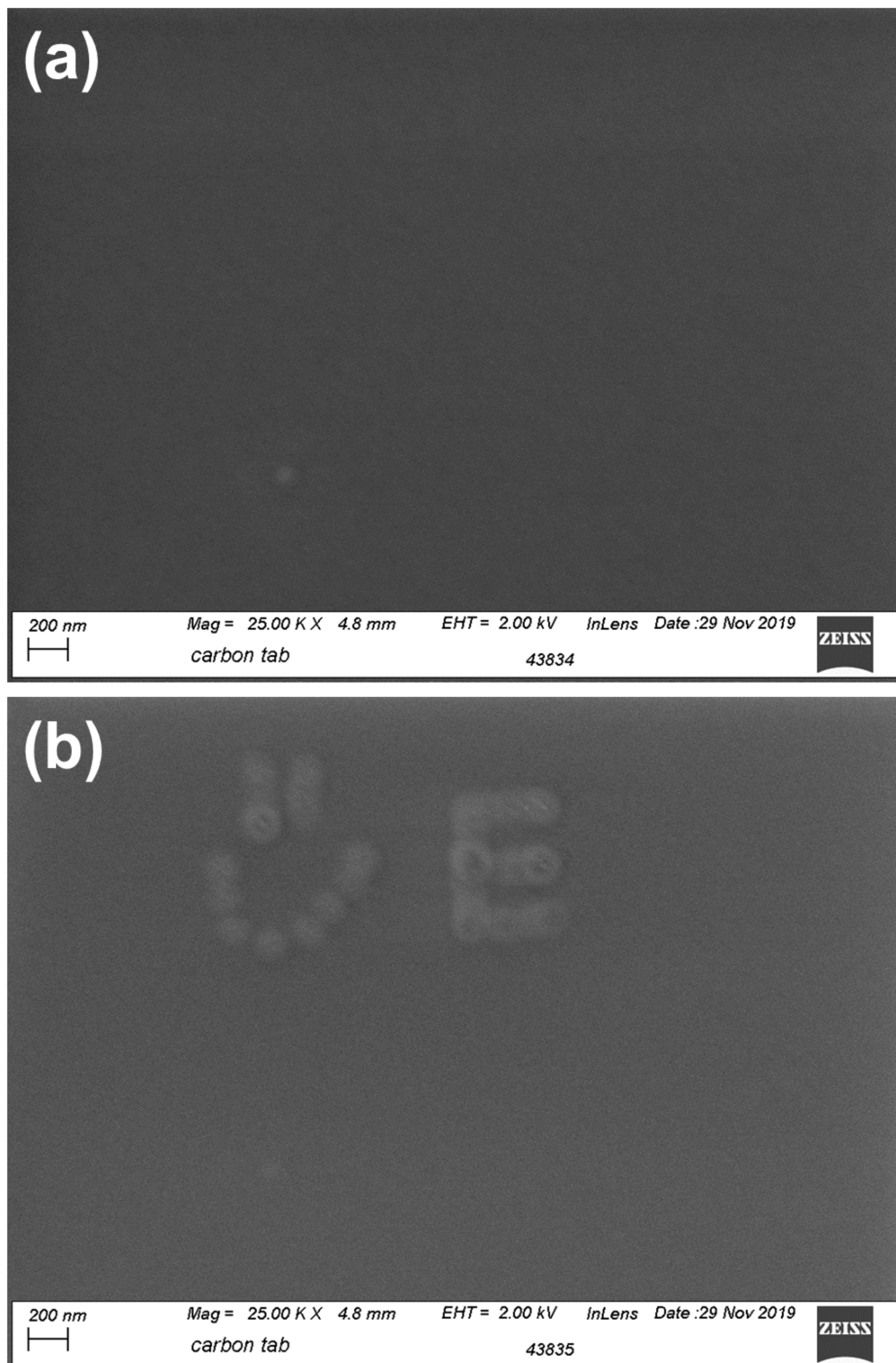

Figure S3.7.2: SEM images (a) and (b) of 6 kg $mol^{-1}$of P2VP-OH (0.2 wt.%) deposited polymer-brush.

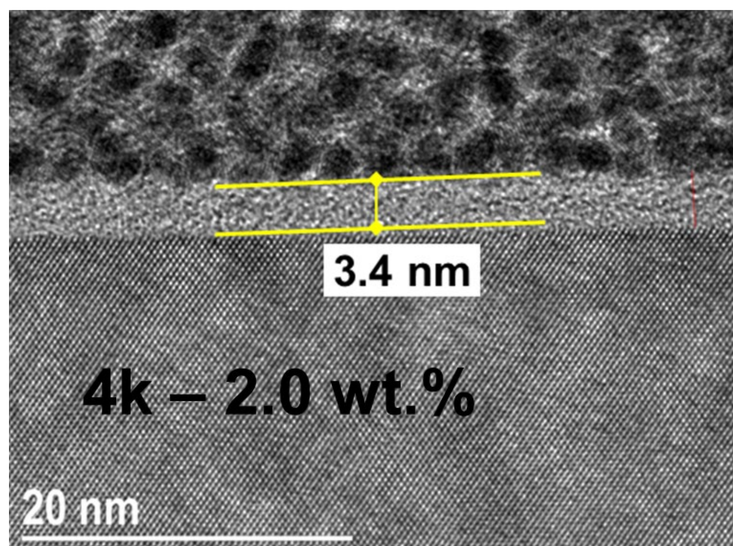

Figure S 3.7.3: Bright-field TEM images of the 4 kg mol^{-1} P2VP-OH grafted from a 0.2 wt.% casting solution.

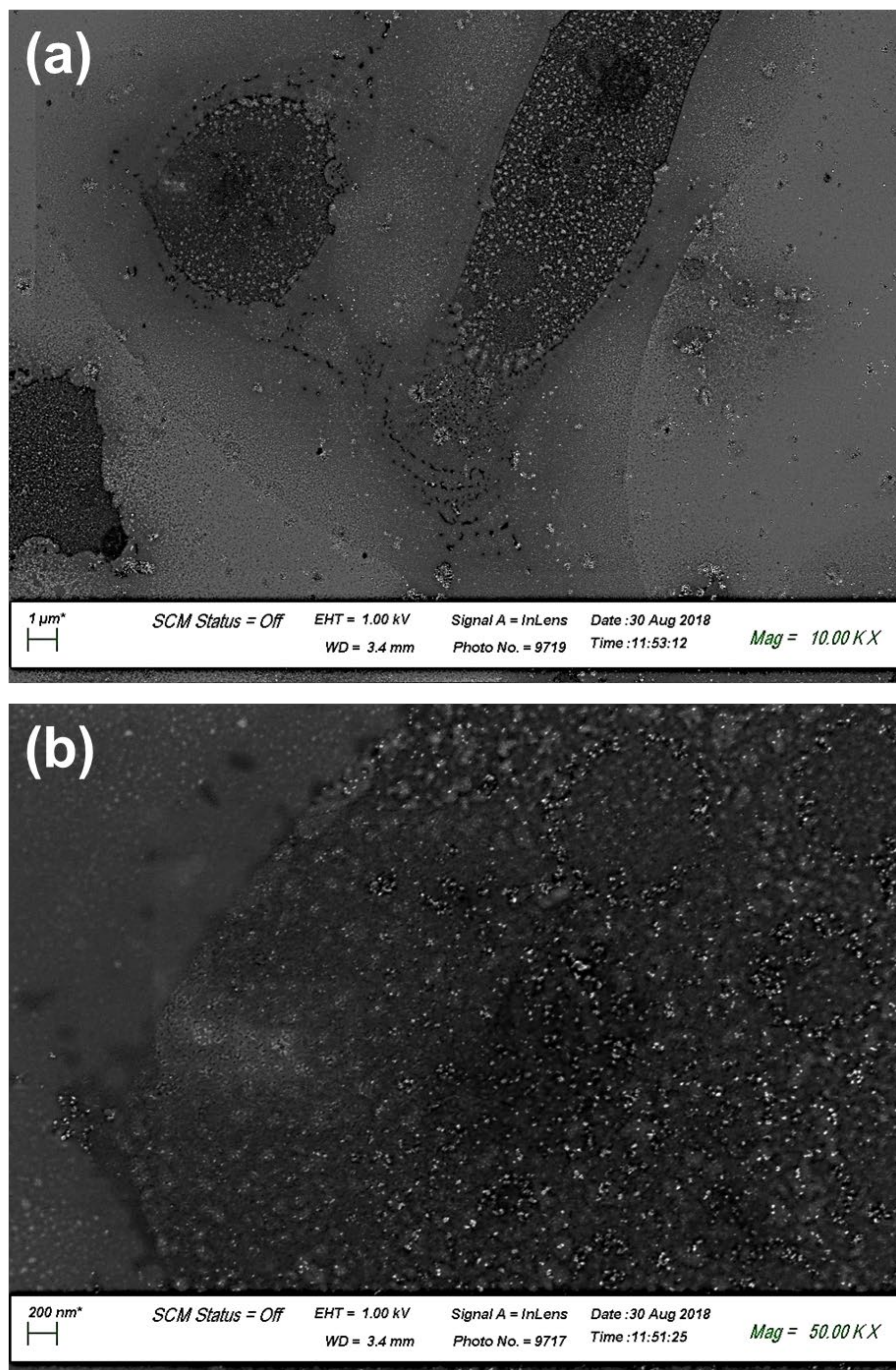

Figure 3.7.4: SEM images (a) and (b) of a 6 kg mol^{-1} P2VP-OH cast from 2.0 wt.% solution. At this concentration uneven coverage is formed.

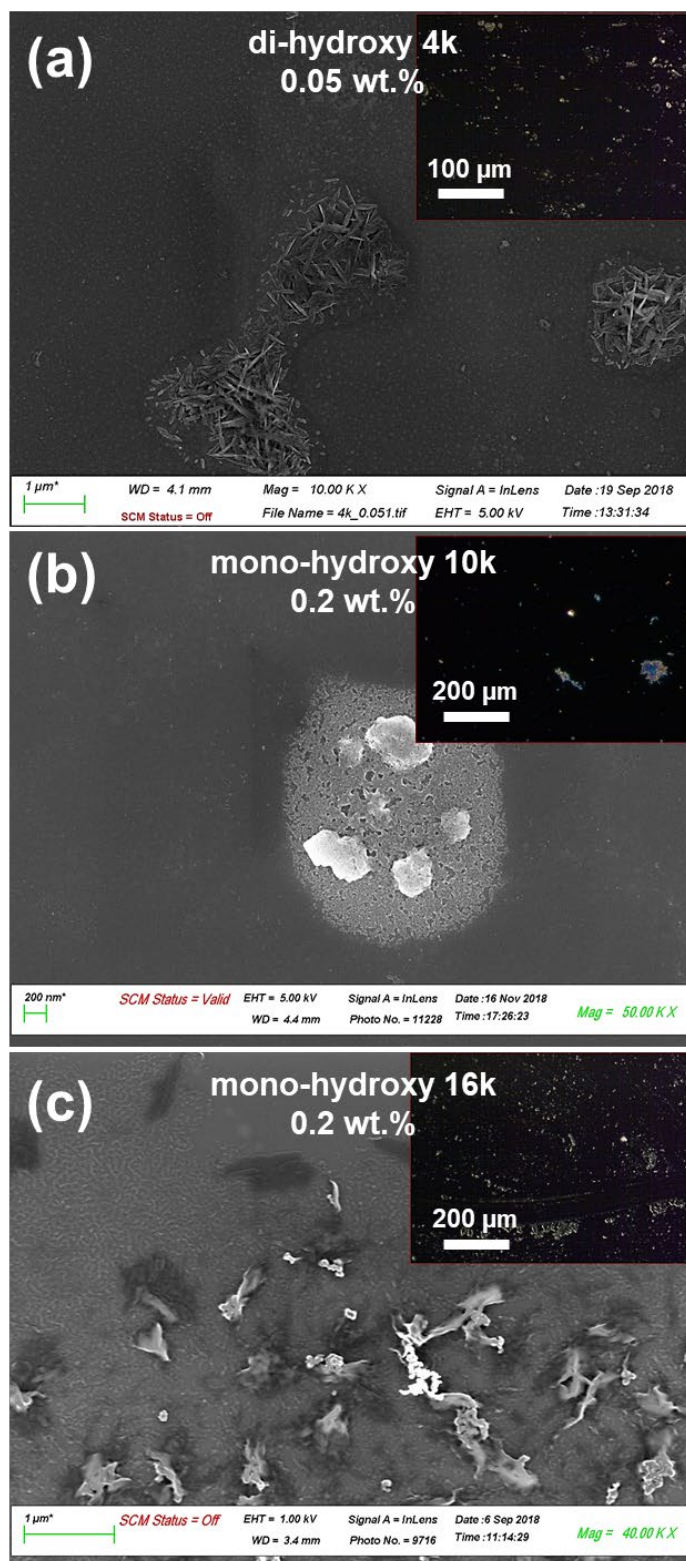

Figure S 3.7.5: SEM images with dark-field microscopy (inset) for P2VP-OH cast and grafted from (a) dihydroxy terminated 4 kg mol^{-1} (b) mono hydroxyl terminated 10 kg mol^{-1}and (c) monohydroxy terminated 16 kg mol^{-1}

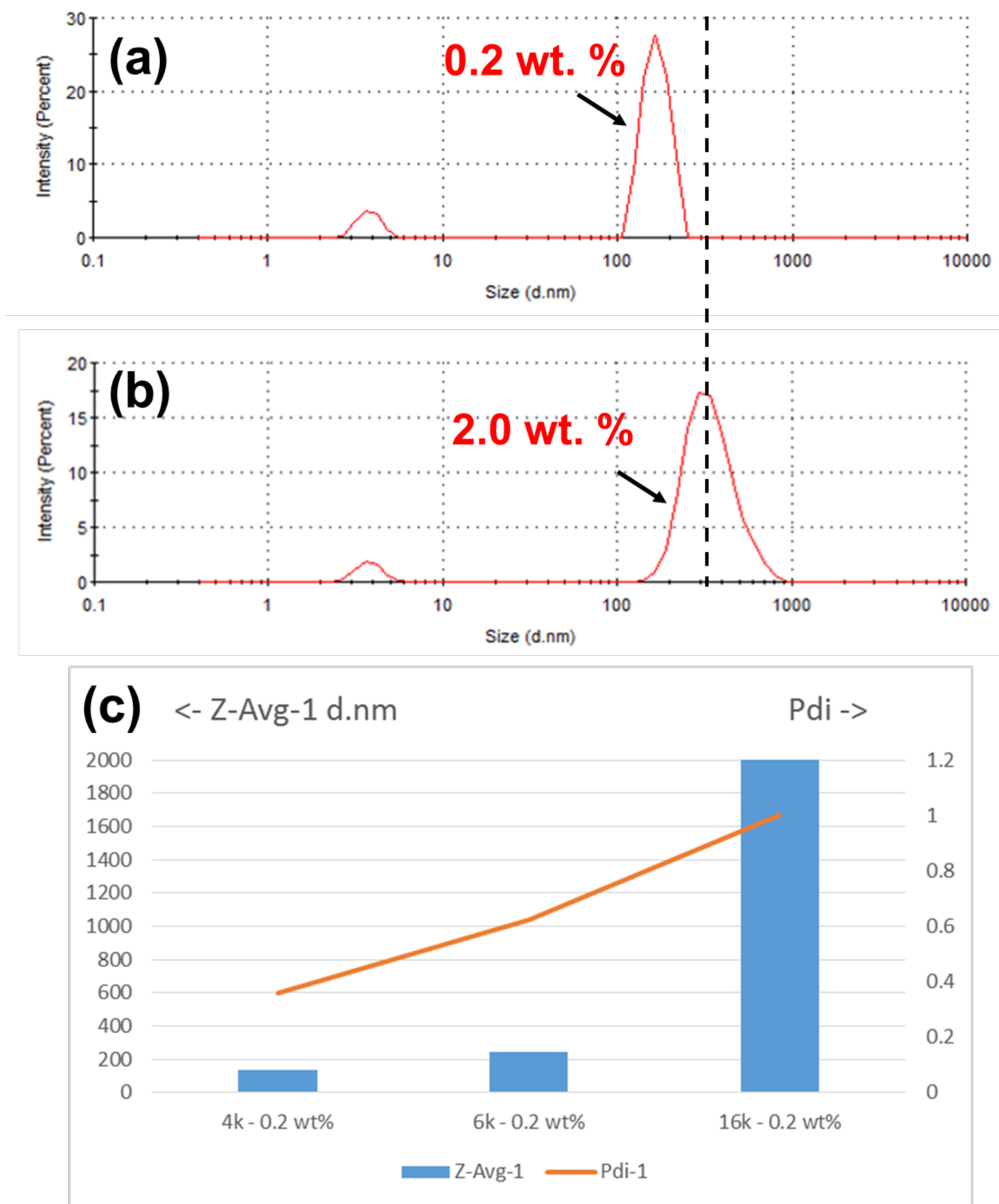

Figure S 3.7.6: Dynamic light scattering data of P2VP casting solution for (a) 0.2 wt.% 6 kg mol^{-1} (b) 2.0 wt.% (6 kg mol^{-1} showing the effect of concentration on agglomeration size.(c) average agglomeration size as a function of molecular weight (4-16 kg mol^{-1} at fixed concentrations (0.2 wt.%).

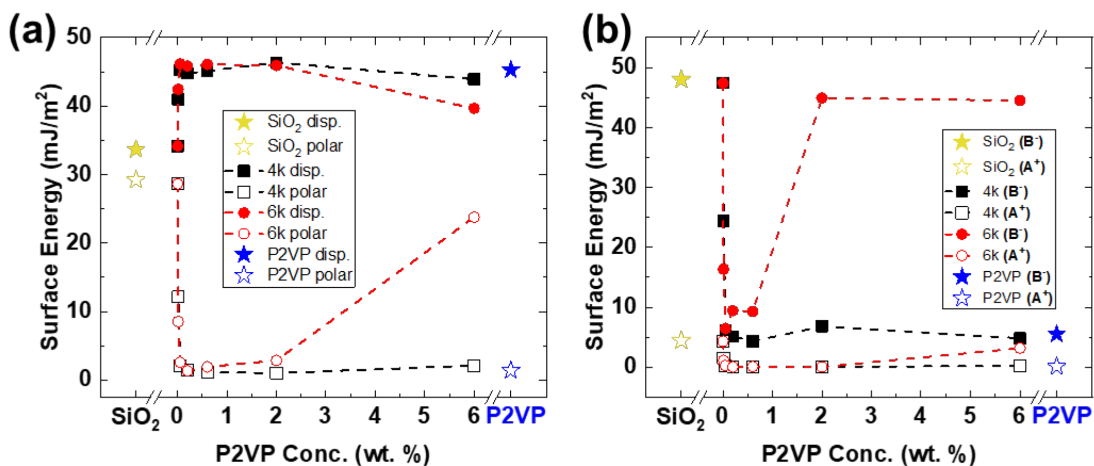

Figure 3.7.7 (a) Apolar (dispersive) and polar surface energy and (b) Lewis acid (A^+) and Lewis base (b^-) interactions for annealed brush samples over a range of the concentrations (0.01-6 wt.%). The dashed line are the guide for the eye.

Section S3.7.2 – PS Brush Monolayer Formation

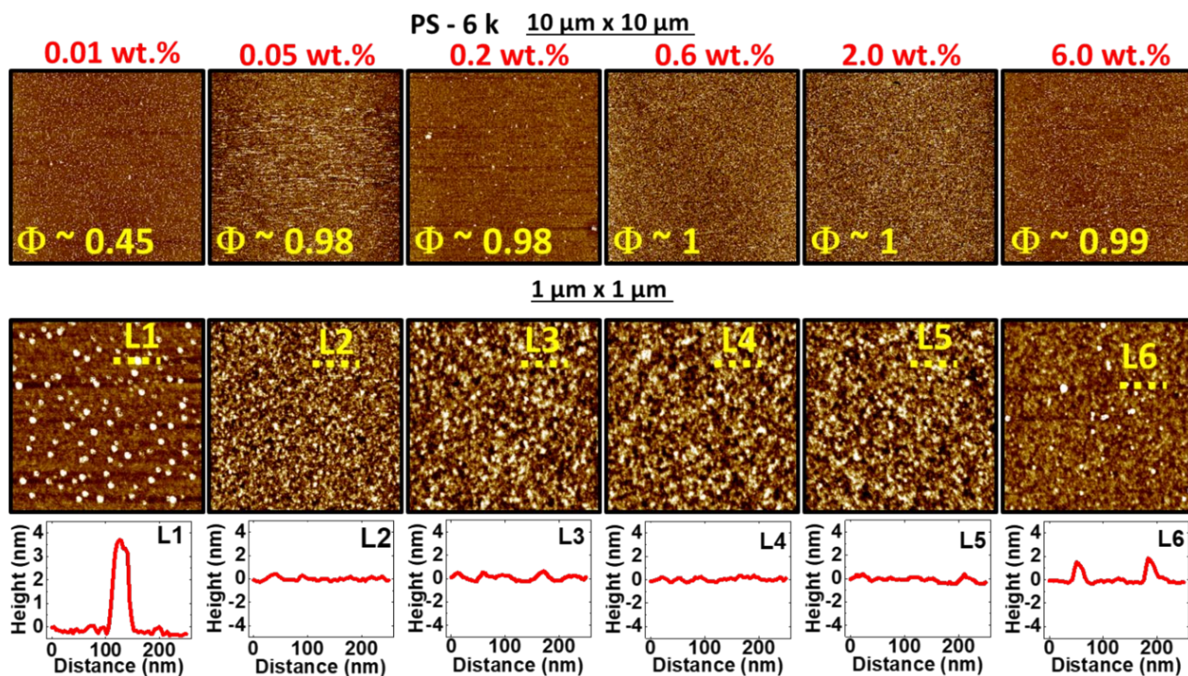

Figure S 3.7.8: AFM images with roughness profile at L1-L6 for 6 kg mol^{-1} PS-OH grafted at various concentration (0.01-6 wt.%). high coverage monolayer formation is evident at very high casting concentration.

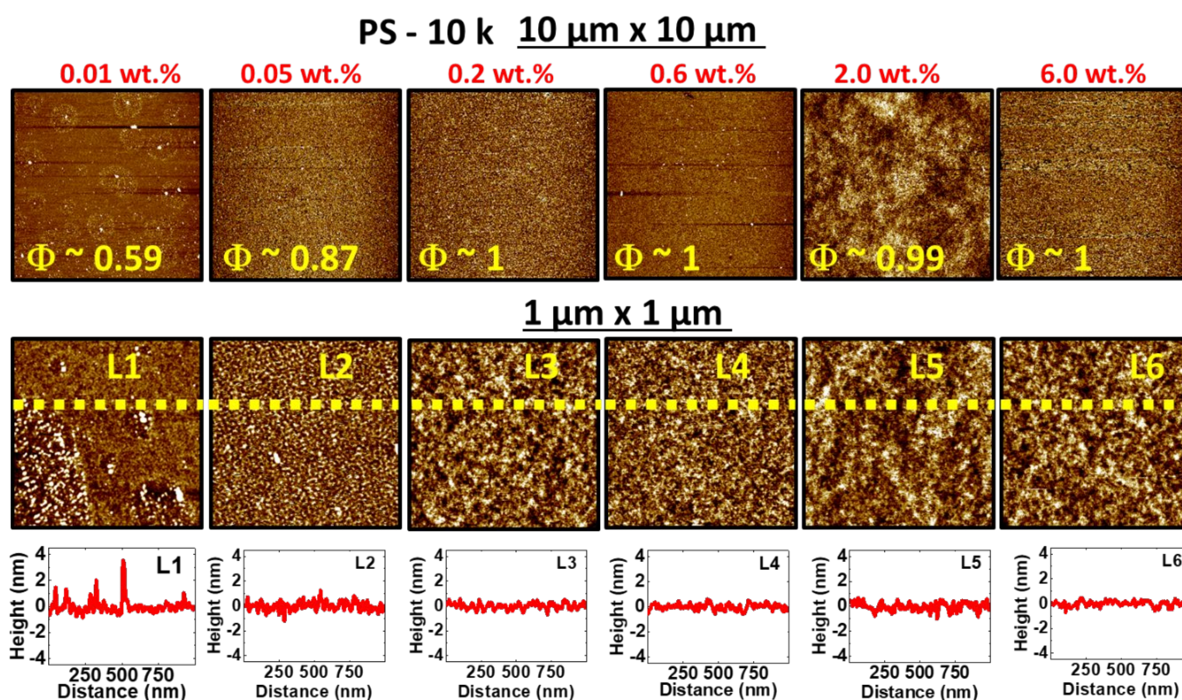

Figure 3.7.9: AFM images with roughness profile at L1-L6 for the 10 kg mol^{-1} PS-OH grafted at various concentration (0.01- 6.0 wt.%.) High coverage monolayer formation is evident at higher concentration.

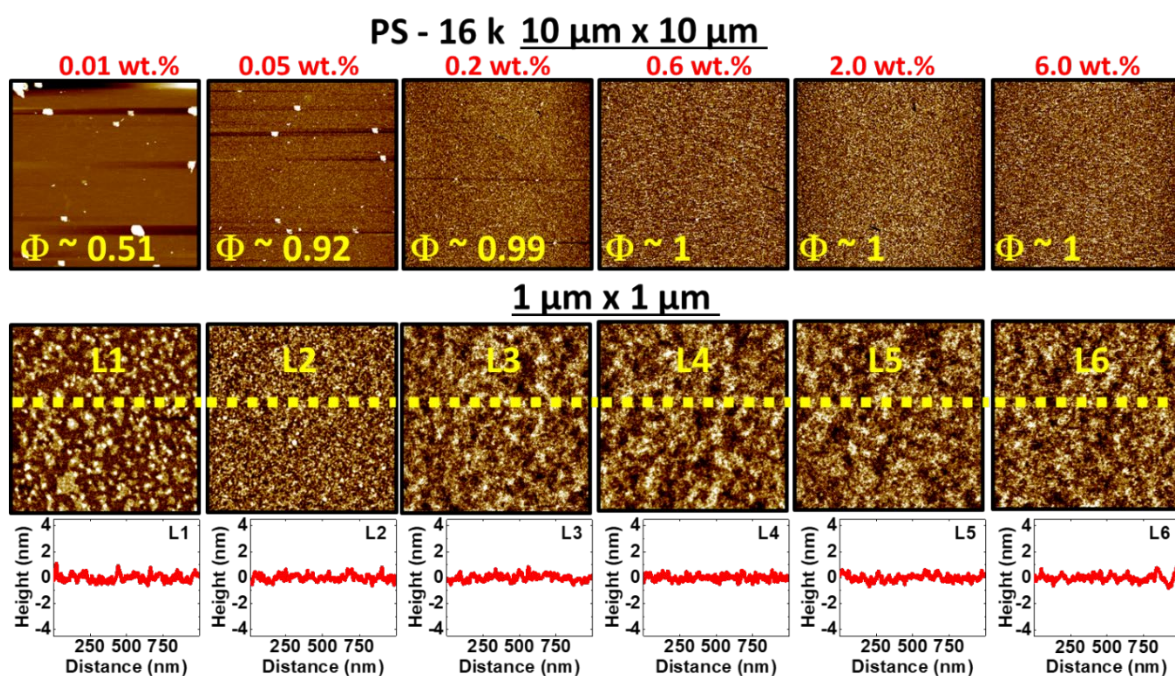

Figure 3.7.10: AFM images with roughness profile at L1-L6 for 16 kg mol^{-1} PS-OH grafted at various concentration (0.01-6 wt.%). High coverage monolayer formation is evident at higher concentration.

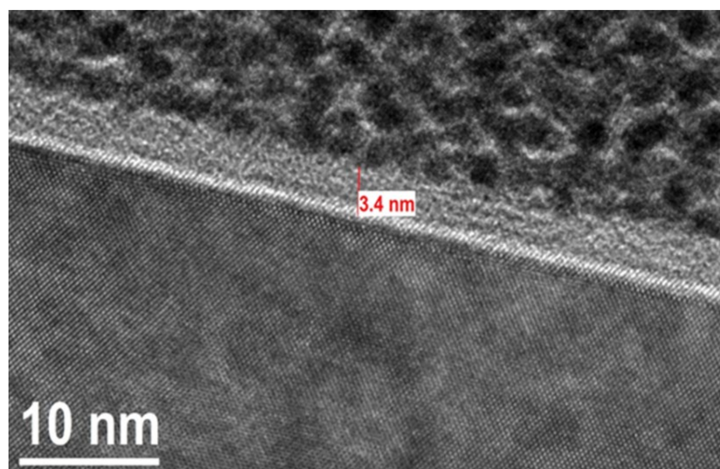

Figure S 3.7.11: Bright-field TEM images of grated PS-OH 6 kg mol^{-1}

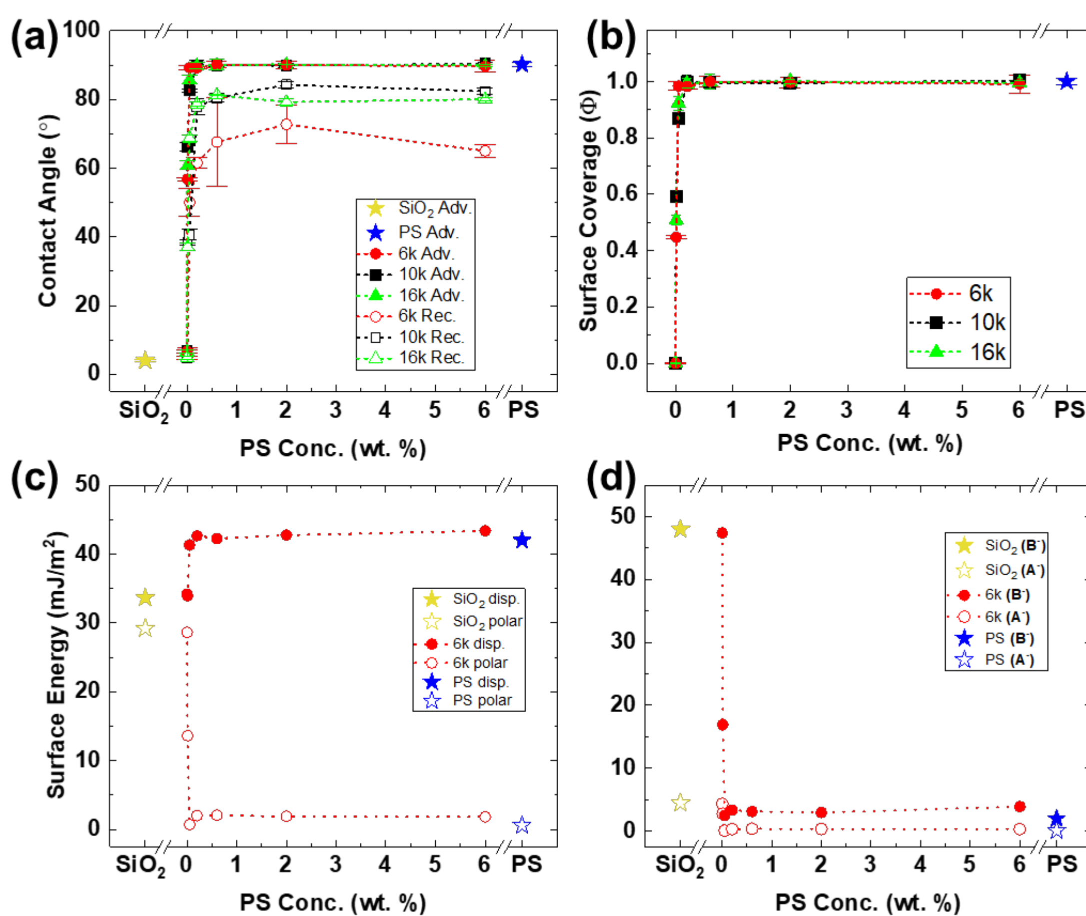

Figure S 3.7.12: Water contact angle of the PS-OH brush annealed over the range of the concentrations (0.01 wt. %- 6 wt.%) with corresponding coverage (b). (c) Apolar (dispersive) and polar surface energy Lewis acid (A^{+}) and Lewis base (B^{-}) for interactions the 6 kg $mole^{-1}$ annealed brush. The dashed lines are the guide for the eye.

Section S3.7.3 – PMMA Brush Monolayer Formation

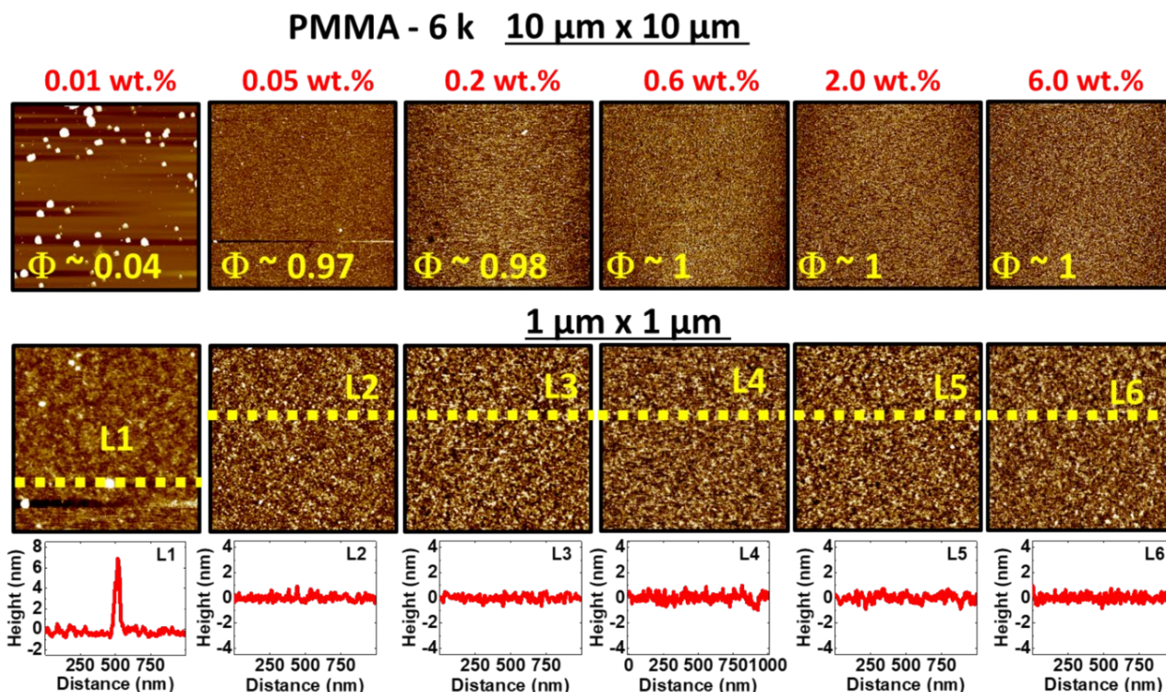

Figure S3.7.13: AFM images with the roughness profile at L1-L6 for the 6 kg mol^{-1}PMMA-OH brush grafted at various concentration (0.01 wt.%-6 wt.%). High coverage of the brush is evident even at higher concentrations.

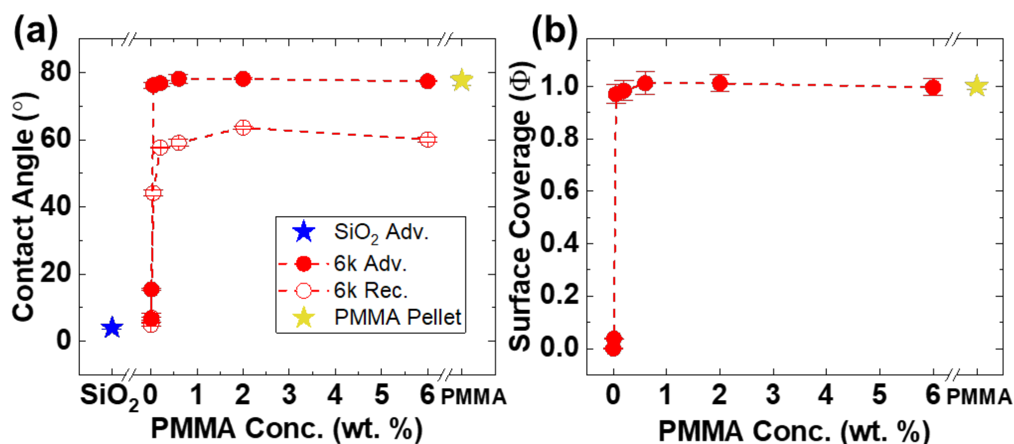

Figure S3.7.14: (a) Water contact angle of the PS-OH brush samples (6-16 kg mol^{-1}) annealed over the range of the concentrations (0.01-6.0 wt.%) with corresponding coverage(b).

Section S3.7.4 – Brush Exposure to Titanium Isopropoxide

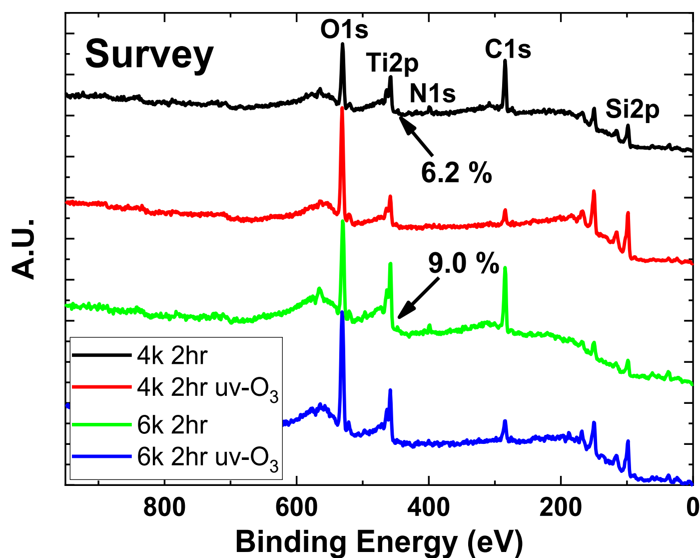

Figure S 3.7.15: XPS survey spectrum of grated 4 and 6 kg mol^{-1} P2VP exposed to TTIP and fallowing UV/ozone. The total Ti signal (atomic %) in the infiltrated 4 kg mol^{-1} is 6.2% and 9.0% in the infiltrated 6 kg mol^{-1} P2VP.

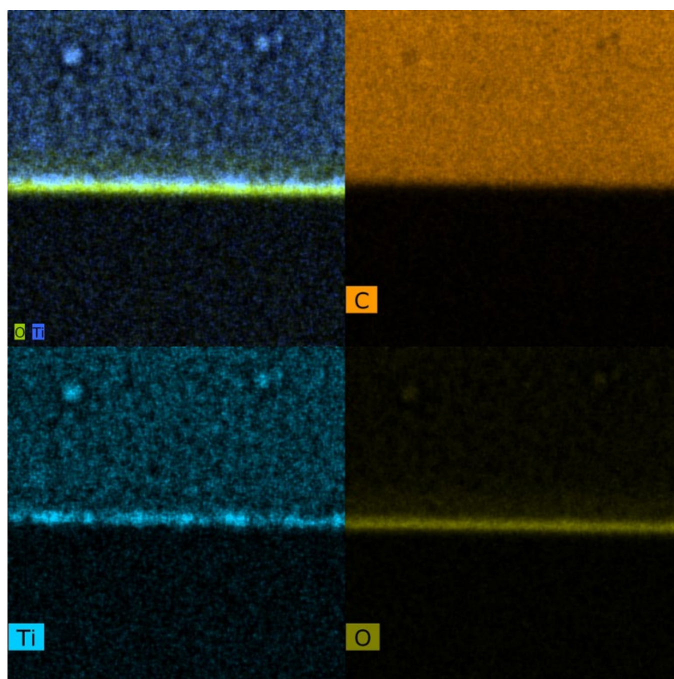

Figure S3.7.16: EDX map (C, Ti, O) of the 6 kg mol^{-1} exposted to TTIP before UV/Ozone.

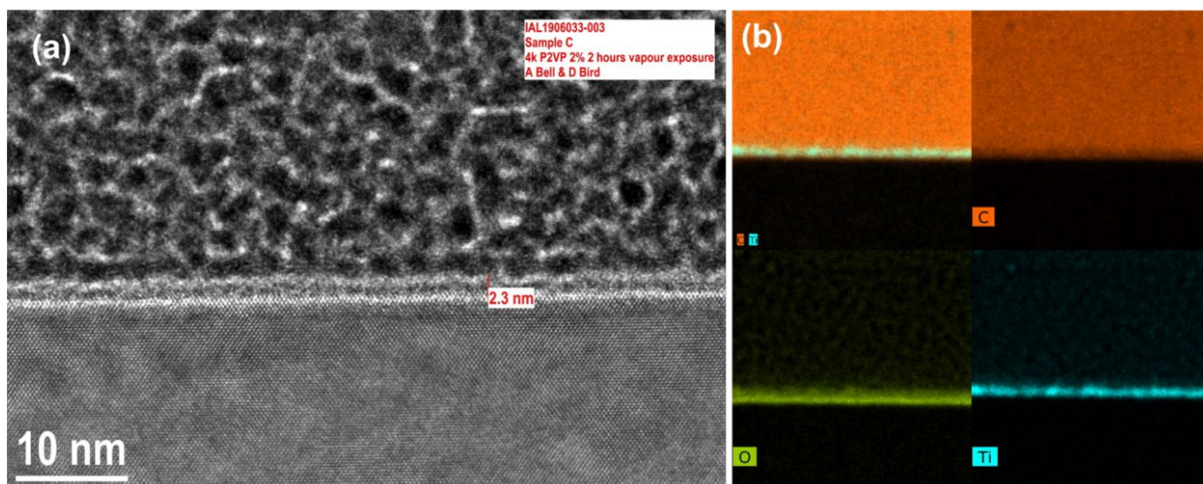

Figure 3.7.17 (a): Bright-field TEM images of the 4 kg mol^{-1} P2VP brush exposed to TTIP (before uv/ozone) and (b) corresponding EDX maps (C, O, and Ti)

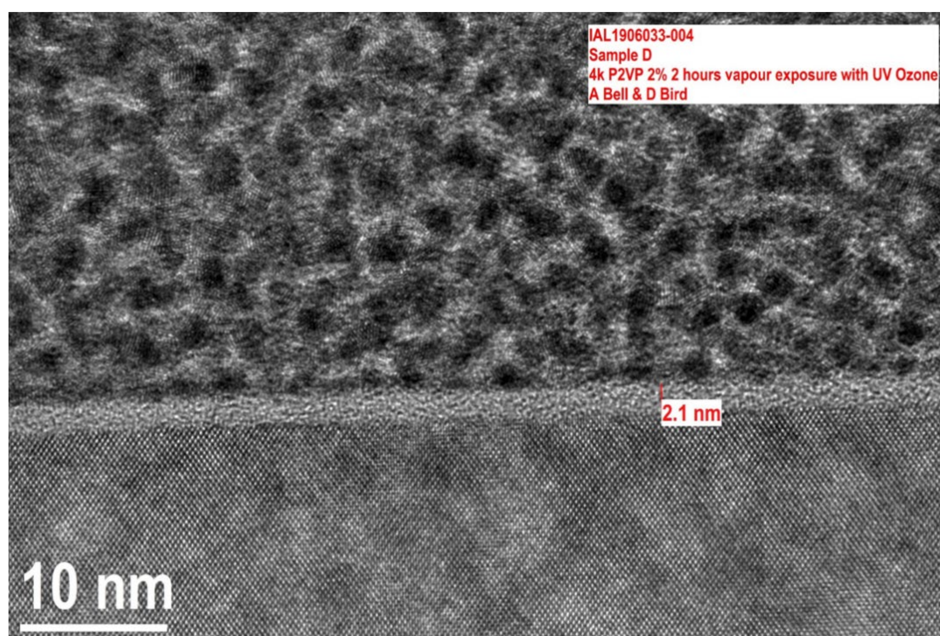

Figure S3.7.18: Bright-field TEM images of the titanium dioxide film formed from the 4 kg mol-^{1} P2VP brush (after uv/ozone).

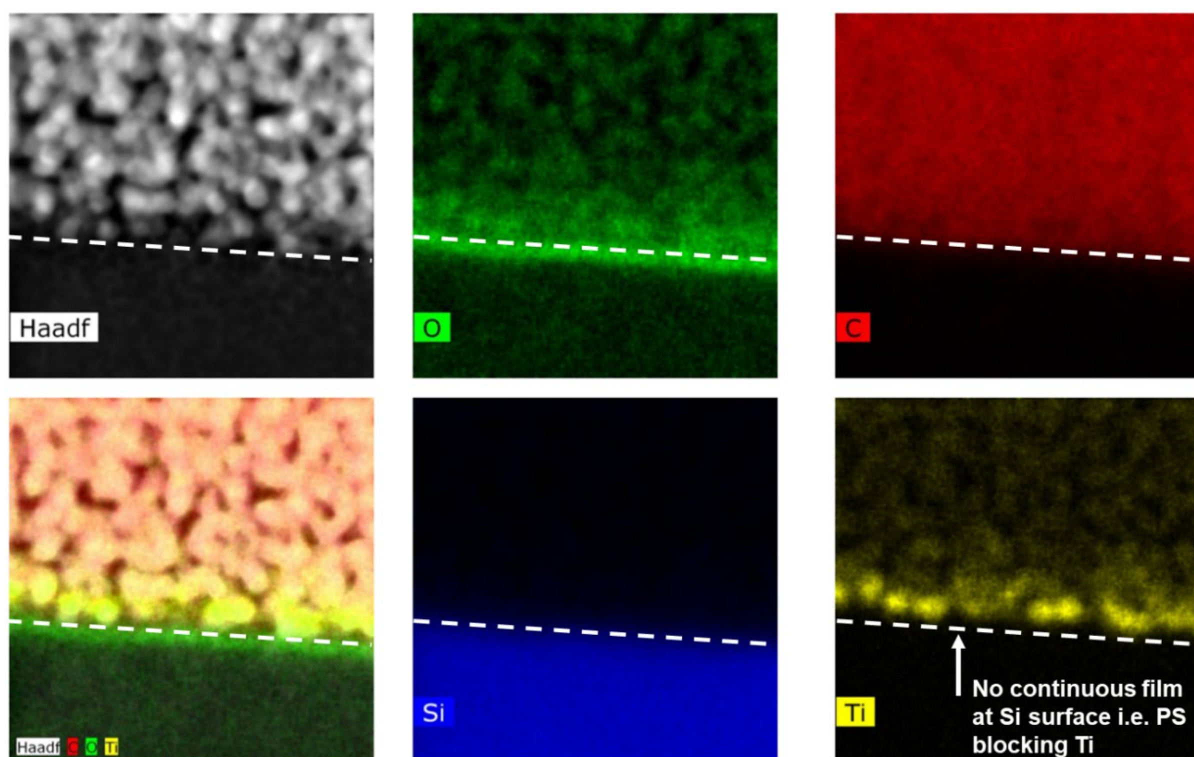

Figure S 3.7.19: STEM images (HAADF) and EDX maps (O, C, Si, and Ti) of 6 kg mol^{-1} PS grafted polymer after exposure to TTIP.

Chapter 4. Fabrication of high-k dielectric metal oxide films on patterned substrates: polymer brush assisted depositions for modern device architectures.

4.1 Abstract:

Fabrication of ultrathin films of high-κ dielectric materials has significant importance in many advanced technological applications including hard protective coatings, sensors, and next-generation logic devices. Current state of the art in fabricating these thin films is photolithography. Device miniaturization and packing density has resulted in cost and integration challenges using established fabrication techniques. Here, we show a polymer brush template assisted deposition of ultrathin (sub-5 nm) high-κ dielectric metal oxide films (hafnium oxide and zirconium oxide) on topographically patterned silicon nitride substrates. This technique, using hydroxyl terminated poly-4-vinyl pyridine (P4VP-OH) as the polymer brush, allows for conformal deposition with uniform thickness along the trenches and sidewalls. A metal salt ethanolic solution is deposited and infiltrates into the grafted monolayer polymer brush films. Tailoring specific polymer interfacial chemistries as a template for ion infiltration combined with subsequent oxygen plasma treatment enabled the fabrication of high quality sub 5 nm conformal metal oxide films.

4.2 Introduction:

Miniaturisation of the on-chip electronic components has driven the development of the semiconductor industry for the past half century. These advances have been enabled through top-down approaches by the clever use of the deep UV (DUV) (193 nm) immersion technology combined with multiple patterning techniques like litho-etch-litho-etch (LELE).[1–3] Continued miniaturization below the 7 nm node has however resulted in cost and integration difficulties.[4,5] Novel processing methods to replace conventional top-down optical lithography encompass block copolymer (BCP) lithography,[6–13] nanoimprint lithography,[14,15] and lately area selective deposition (ASD).[16–18] They allow fabrication of nanoscale material patterns at significantly lower cost and most importantly shorter processing times, compared to top-down lithography techniques.[19,20]

ASD is a bottom-up patterning technique with excellent potential to complement existing optical lithography (DUV and EUV).[16,21] ASD facilitates material deposition in a very controlled manner across specific regions of a substrate. The ability of the ASD approach to deposit highly ordered metal and oxide films is advantageous because it can provide routes to produce material patterns to complement silicon device technology, especially in monolithic integration.[22] Several cutting edge ASD technologies have been developed using chemical modification of substrate surface with self-assembled monolayers (SAMs)[16,23] and unreactive polymers to include material on the region of interest using atomic layer deposition (ALD)[21,24–29] or molecular layer depositions (MLD).[23,30,31] A big advantage of the polymer brush technique over SAM's depositions is the fast processing speed (a few minutes for polymer brush grafting vs hours to day for SAM's monolayer coating). Furthermore, polymer brush assisted deposition process overcomes the issues that ALD technique poses such as high cost of instrumentations.[32]

In earlier research work, we described the use of a polymer brush film to selectively pattern material onto Cu/SiO_2 line area for ASD of copper (Cu) metal layers.[33,34] We developed simple methods for rapid grafting of end terminated polymer brush films with complete coverage and subsequent conversion to numerous oxides (Al_2O_3, Co_3O_4) *via* liquid phase metal salt infiltration,[34,35] Further, we studied the precise parameters that control the monolayer formation of the polymer brush film. Polymer brush layer deposition requires accurate optimization of polymer molecular weight, casting solution concentration, and reactive terminal group density in the formation of pinhole free high coverage monolayers. A vapour phase volatile organometallic titanium (IV) isopropoxide precursor infiltraion of monolayer brush film was studied using a simple apparatus.[36] In addition to this, a surface deactivation strategy using unreactive hydroxyl terminated polystyrene (PS-OH) brush to prevent metal ion inclusion was demonstrated.[37]

So far, the polymer brush technique has been shown to facilitate the deposition of metal oxide films uniformly across relatively smooth substrate surfaces. The application of this technique throughout the trenches and pitches of a topographically patterned substrate would dramatically widen the use case scenarios and allow additional device integration. High-κ dielectric materials such as HfO_2 and ZrO_2 offers low gate leakage current and their usefulness in preventing power dissipation are making them promising material to integrate in advanced CMOS technology.[38] Furthermore, HfO_2 and ZrO_2 are the potential ferroelectric materials that could be effective in the fabrication of sub 7 nm FeFET device architecture.[39]

In this work, we demonstrate a straightforward robust approach for liquid phase infiltration of zirconium oxynitrate and hafnium chloride onto the silicon nitride trenches using P4VP-OH grafted brushes. In order to deposit thin metal oxide films, it is critical to form a high coverage polymer brush template such as hydroxyl terminated P4VP to facilitate inorganic precursor uptake. Furthermore, other reactive polymers such as P2VP and PMMA were infiltrated with the metal precursors to compare the results. Applicability of the reactive

polymer system and favourable interactions with the metal cations on native oxide silicon substrates have been discussed in the literature.[9,47] This study demonstrates the polymer deposition across the trenches for realising conformal coating of ZrO_2 and HfO_2. In addition to this, a surface deactivation strategy using unreactive PS-OH brush to prevent metal ion inclusion is shown.[48,49]

This research work exhibits the deposition of HfO_2 and ZrO_2 thin films at moderate temperatures (200-250 ^{0}C) which is significant due to low process temperature required (<400 ^{0}C) for front end of line (FEOL) fabrication.[50] The obtained fundamental insights showcase the ways to implement polymer brush lithography for the fabrication of high-κ metal oxides such as HfO_2 and ZrO_2. This method could be further used in the fabrication of next generation logic gate devices or ferroelectric devices such as ferroelectric random access memory and field effect transistors.

4.3 Experimental section:

4.3.1 Materials:

Silicon nitride coated substrates were prepared using a low pressure chemical vapour deposition (LPCVD) on p-type silicon substrate with ~7nm thick SiO_2 layer. The topographically patterned Si_3N_4 coated substrate was fabricated using 193 nm photolithography and processed with photoresist and dry etch technique with pitches ranging from 75 nm to 1µ and a trench depth of 40 nm.

Functionalised Polymers**:** hydroxyl terminated poly-4-vinyl pyridine (P4VP-OH) 5 $kmol^{-1}$, (PDI: 1.28), poly-2-vinyl pyridine (P2VP-OH) 6.2 $kmol^{-1}$ (PDI:1.05), poly(methyl methacrylate) (PMMA-OH) 6.3 $kmol^{-1}$ (PDI:1.03), and polystyrene (PS-OH) 6 $kmol^{-1}$, (PDI:1.05), were purchased from Polymer Source (Canada) and used without further purification.

Solvents: High performance liquid chromatography (HPLC) grade acetone, tetrahydrofuran (THF), ethanol, isopropyl alcohol (IPA) and toluene were purchased from Merck Ireland and used without further purification.

Metal Precursor: Hafnium (IV) chloride and zirconium (IV) oxynitrate hydrate were purchased from Sigma-Aldrich and used as received.

4.3.2 Fabrication:

Topographically patterned silicon nitride substrates were cleaved into 2 by 2 cm^2 coupons and ultrasonically washed in IPA and acetone for 10 minutes each. **Figure 4.1 (a)** indicates the degreasing and hydroxyl functionalisation of the substrate surface using oxygen plasma treatments for 2 min (40 kHz, 50 W, Diener PICO Barrel Asher). Polymers were dissolved in their respective solvent (based on Hansen solubility parameters)[52,53] and stirred overnight at 500 rpm to obtain a homogeneous 0.2 wt.% solution, which was then spin deposited to

the substrate at 3200 rpm for 30 sec. Thereafter samples were placed on a hotplate at 230 ^{0}C for 2 min to form strong covalent bonding between the end hydroxyl group of the polymer and the complementary functional group present on the substrate through a condensation reaction (see **Figure 4.1 (b)**).[35,36] The samples were then ultra-sonicated in the corresponding solvent in order to eliminate any physiosorbed polymer and yield chemically grafted monolayer polymer films (see **Figure 4.1 (c)**). A monolayer polymer film was then infiltrated with 0.5 wt.% ethanolic solution of either hafnium(IV) chloride or zirconium(IV) oxynitrate and subsequently underwent oxygen plasma treatment for 20 min at 30 W to oxidize the metal precursor and eliminate the polymer brush layer (see **Figure 4.1 (d)**), thus forming high-quality metal oxide films.

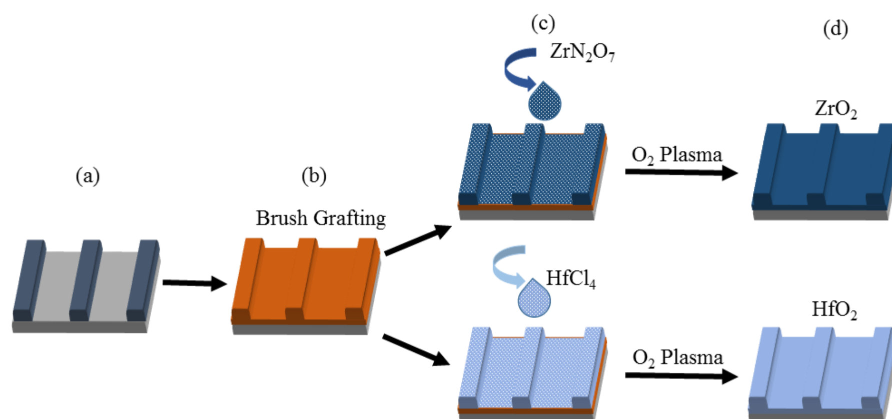

Figure 4.1: Schematic process flow of the sub-5 nm metal oxide film fabrication process. (a - b) monolayer polymer brush film grafting on topographically patterned substrate (c) inorganic ion infiltration, and (d) oxidation of inorganic precursor and elimination of polymer.

4.3.3 Characterization:

Angled (90°) SEM images were obtained by field emission scanning electron microscopy (Zeiss Ultra) using secondary electron detector (in lens) with 1-5 kV accelerating voltage. Focused ion beam etching (FIB Helios nano lab 460) utilising a capping layer of e-beam Pt (100 nm) and ion beam Pt (2 µm) was used to prepare lamellae using standard high kV miling and low kV polish which rendered the lamellae electron transparent indicating an

appropiate thickness for TEM. TEM (FEI Orisis) was performed using bright field and STEM imaging. During STEMs the detector lengths were 220, 550 and 770 mm. The accelerating voltage was 200 kV. The EDX beam current was 1 nA with an acquisition time of 30 min. Atomic force microscopy (AFM Park System XE7) was used with non contact cantilever (AC160TS, force constant ~26 $N.m^{-1}$) resonant frequency ~300 kHz.

XPS data was obtained using a thermofischer-VG instrument equipped with an Al Kα (hν=1486.7 eV) X ray source and a 3 channeltron hemispherical electron analyser under ultrahigh vacuum condition (base pressure; 1 X 10^{-9} mbar). XPS data analysis was performed using Casa XPS software. The binding energy scale was referenced to the C 1s peak of adventitious carbon at 284.8eV.[54] For survey scans, an analyser pass energy of 200 eV was used while a pass energy of 20 eV was used to obtain high resolution spectra of characteristic core levels. The oxygen plasma process was performed in a purpose built chamber with a custom made plasma source coupled with the XPS analysis chamber, to assure sample did not break vacuum after the polymer ashing process. The plasma process took place in pressure of 1 x 10^{-2} mbar of oxygen at 30W for 20 min with an oxgen flow of 100 sccm. Dynamic contact angle (CA) measurements were taken at three representative regions of each sample using high speed camera (60 Hz) sampling rate to capture advancing and receding water contact angle. Flow rates of 5 nls^{-1} were used to dispense liquids through a 35 guage needle (135 µm OD) with droplet volume ranging from 40 nl to 80 nl. Polymer brush coverage was determined using Cassie Baxter equation from the water contact angle.

Thermogravimetric analysis (TGA) was performed using perkin elmer TGA on the homopolymer powder (P4VP-OH) in the temprature range of 30 -600 ºC for 60 min (**see Figure S4.7.1**).

4.4 Results and discussion:

In order to prepare a uniform thin film of metal oxides (HfO_2 and ZrO_2), a polymer template approach was developed that facilitates a controlled inclusion of the metal ions. We chose a P4VP-OH brush as the template for the metal oxide deposition, because this polymer in its neutral form, co-ordinates with the metal ions by donating the loan pair electrons of its nitrogen atom. The Hansen approach is used to find the optimum solvent combination to solubilize the P4VP-OH polymer. The P4VP-OH (0.2 wt. %) dissolved in a 60:40 THF: IPA mixture is then spin casted onto topographically patterned and plane substrates. A polymer grafting temperature of 230 ^{0}C is selected based on our previously published results.[35,36] The Supplementary **Figure S4.7.1** represents the TGA graph, showing the thermal degradation temperature of P4VP-OH (250^{0}C). **Figure 4.2** shows the molecular structure of P4VP-OH and the metal precursors.

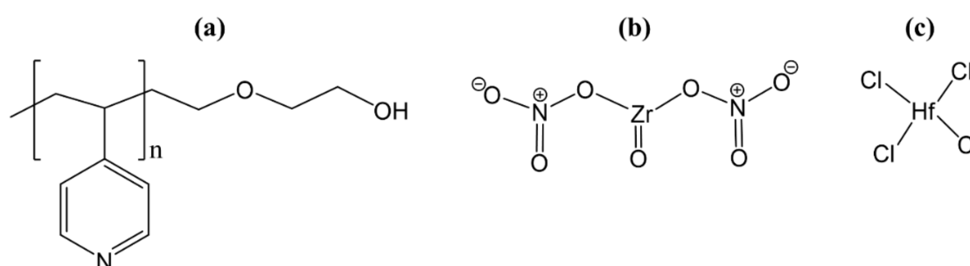

Figure 4.2: Hydroxyl end terminated (a) poly-4-vinyl pyridine, (b) zirconium oxynitrate (c) hafnium tetrachloride.

The heat treatment enabled the uncoiling of the polymer chain, diffusion of the polymer OH moieties to the substrate surface and subsequent condensation with the substrate OH groups to form covalently bonded polymer films. A complete surface coverage of the polymer brush template is critical in delivering conformal deposition of the high-κ dielectric thin films of controlled thickness. Therefore, a broad area of investigation is performed using contact angle measurements to examine the thin film deposition of the polymer brush over the entire

area of the substrate surface. The water contact angle images recorded from three representative positions of each film is used to calculate the polymer brush coverage on substrates (**see Figure S4.7.2**). The Cassie Baxter equation (**1**) with the hypothesis of surface energy homogeneity is used to calculate the surface coverage.

$$\Phi = \left(\frac{\cos\theta_{P4VP}}{\cos\theta_{SiO2}} - 1\right) \Big/ \left(\frac{\cos\theta_{pellet}}{\cos\theta_{SiO2}} - 1\right), (\mathbf{1})$$

Where Φ is the polymer brush surface coverage, θ_{P4VP} is water contact angle of the deposited P4VP, θ_{SiO2} is the advancing water contact angle (θ_a) observed for the plasma treated SiO_2 sample, and θ_{pellet} is the θ_a of a pure P4VP homopolymer pellet. The control, oxygen plasma treated silicon and the silicon surface from the trench-patterned samples, have given θ_a values of 5°± 0.5°. The grafted P4VP polymer on flat region of the patterned substrate and thick spin coated P4VP films show a similar θ_a of 65°. Pelletized P4VP homopolymer θ_a value varies from 65° to 73°owing to the pressure dependent transition of the P4VP motifs.[55] The contact angle images and the data derived by solving the Cassie Baxter equation using the θ_a values confirmed a complete P4VP-OH polymer grafting on the substrates (see **Figure S4.7.2**).

Metal deposition was achieved by spin coating ethanolic solutions of metal salts on the P4VP-OH monolayer films. Subsequently, the continuous metal oxide films were produced by treating the samples under oxygen plasma for 20 min. The plasma treatment enabled the rapid oxidative removal of the polymer brush and conversion of metal precursor to respective metal oxide.

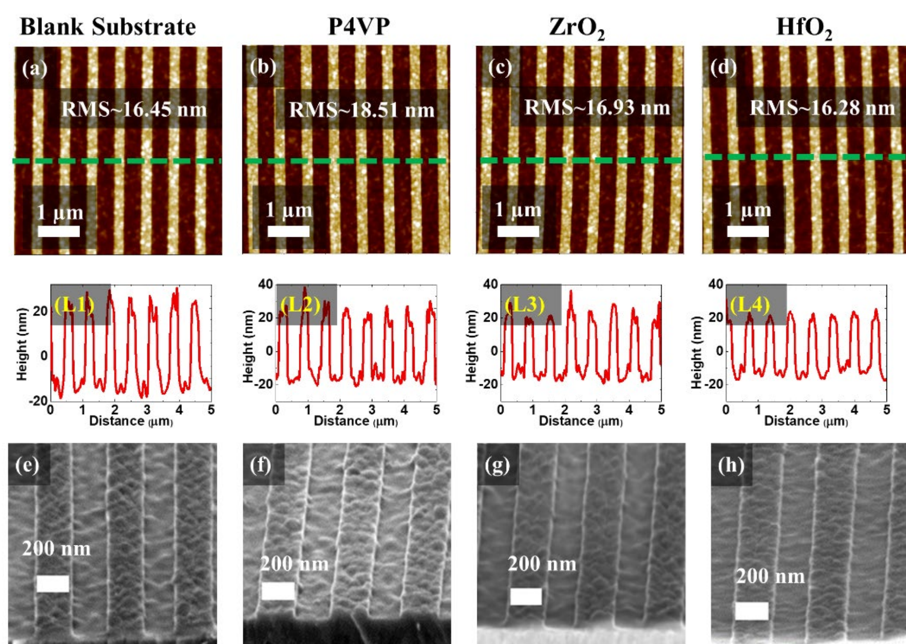

Figure 4.2: AFM images (a-d) with line profile plotted (L1-L4) and angled SEM images (e-h) for blank substrate (a, L1, e), P4VP grafted brush (b, L2, f), ZrO_2 (c, L3, g) and HfO_2 (d, L4, h) films.

AFM was used to examine and compare the roughness and homogeneity of the uncoated patterned substrates, the grafted P4VP-OH films and the final ZrO_2 and HfO_2 films. All four stages provided similar RMS values (L1 to L4 in **Figure 4.3**). The uncoated patterned silicon substrate provided RMS value of 16.45 nm. The P4VP grafting showed a slightly increased RMS value of 18.51 nm. The metal oxide films showed a reduced RMS (16.93 for ZrO_2 nm and 16.28 nm for HfO_2) roughness, similar to that of the uncoated substrate. We have compared the roughness values of plane silicon substrate to that of the metal oxide films prepared on plane silicon substrates using the P4VP-OH template assisted depositions. We observed ultra-smooth, uniform films with roughness values in the range of 0.4 to 0.8 nm (see **Figure S4.7.3**).

The high resolution angled SEM images presented in **Figure 4.3 (e,f)** represents the as received topographically patterned substrate and conformally grafted P4VP films. Zirconium oxide and hafnium oxide films were developed by infiltrating ethanolic solution of the precursors (0.4 wt.%). The interaction between ionic ethanol and P4VP segments is

favourable for the optimum reaction.[56] **Figure 4.3 (g,h)** exhibits SEM image of the P4VP assisted continuous zirconium oxide and hafnium oxide films across the trenches. No obvious defects or roughness was observed for the deposited films. The SEM images recorded from plane substrates, presented in Supplementary **Figure S4.7.3**, also shows the formation of highly uniform films with no significant roughness.

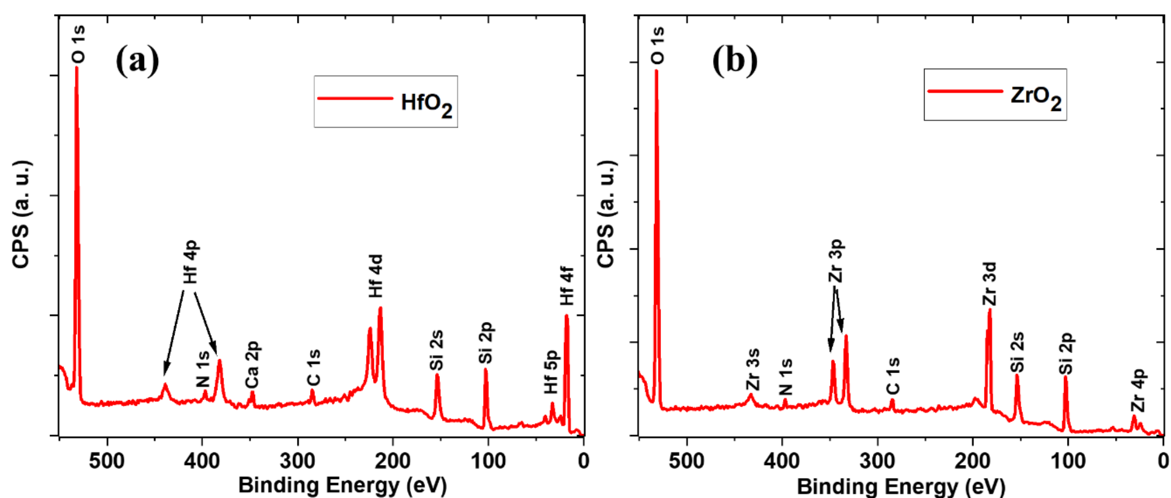

Figure 4.3: XPS survey spectra for (a) HfO_2 and (b) ZrO_2.

XPS survey spectra of the ZrO_2 **Figure 4.4 (a)** and HfO_2 **Figure 4.4 (b)** films clearly show that the respective metal is present on the surface. The HfO_2 sample has peaks that can be assigned to Si, O, C, N and Hf. A small amount of Ca is present, which is most likely due to contamination. The ZrO_2 sample has peaks from Si, O, C, N and Zr. In both cases, the C contribution was <5%, which shows the benefit of being able to measure the XPS directly after plasma processing, without exposing the samples to atmospheric conditions.

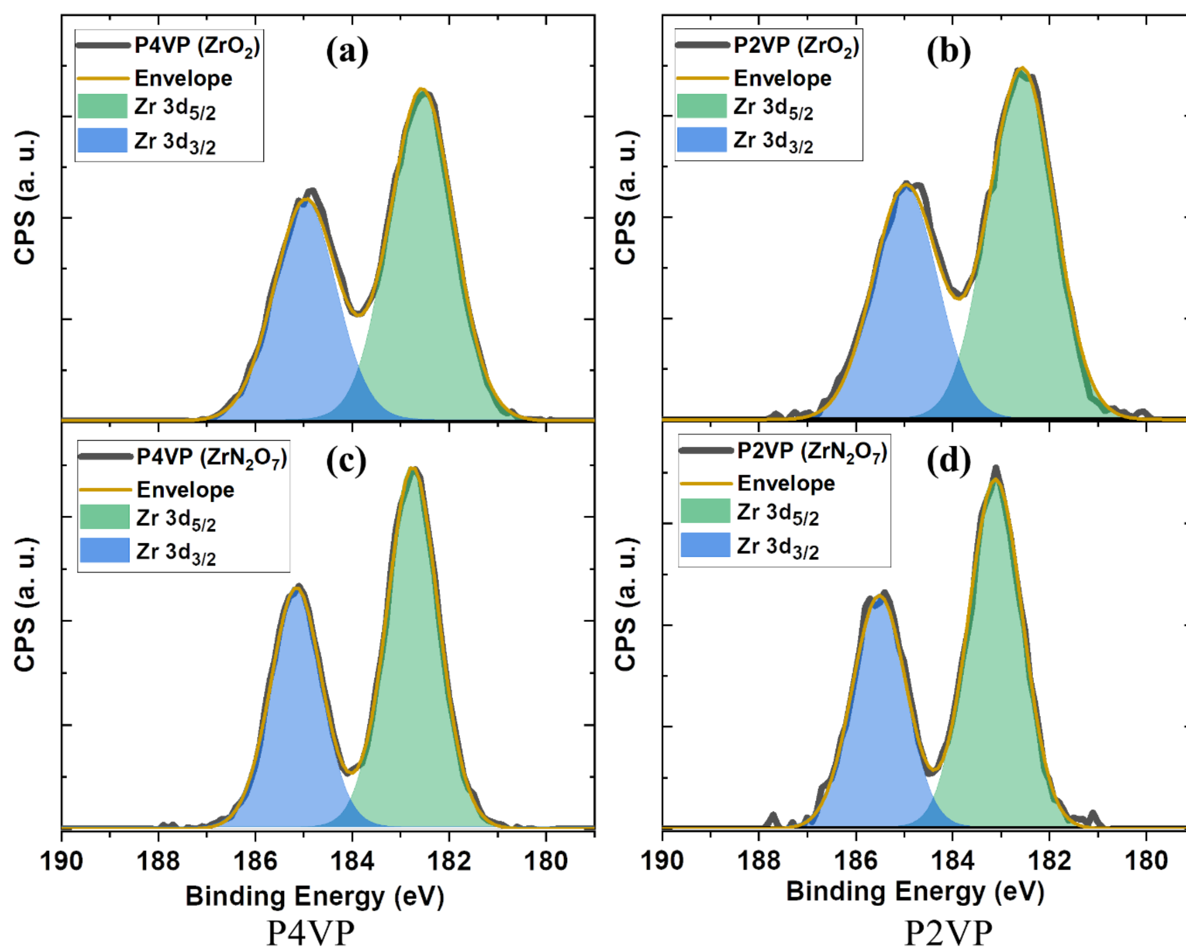

Figure 4.4: High-resolution XPS spectra of the Zr3d region pre (bottom) and post (top) O_2 plasma treatment for P4VP (a) and P2VP (b).

The effect of polymer was investigated by inspecting the high-resolution scans of the Zr 3d region before and after O_2 plasma processing. Using either P4VP (**Figure 4.5 (a)**) or P2VP (**Figure 4.5 (b)**) shows that the position of the nitrogen does not affect the chemical environment of the Zr. The only measurable difference is the amount of metal uptake (higher in P4VP), which suggests that steric hindrance may be a limiting factor.

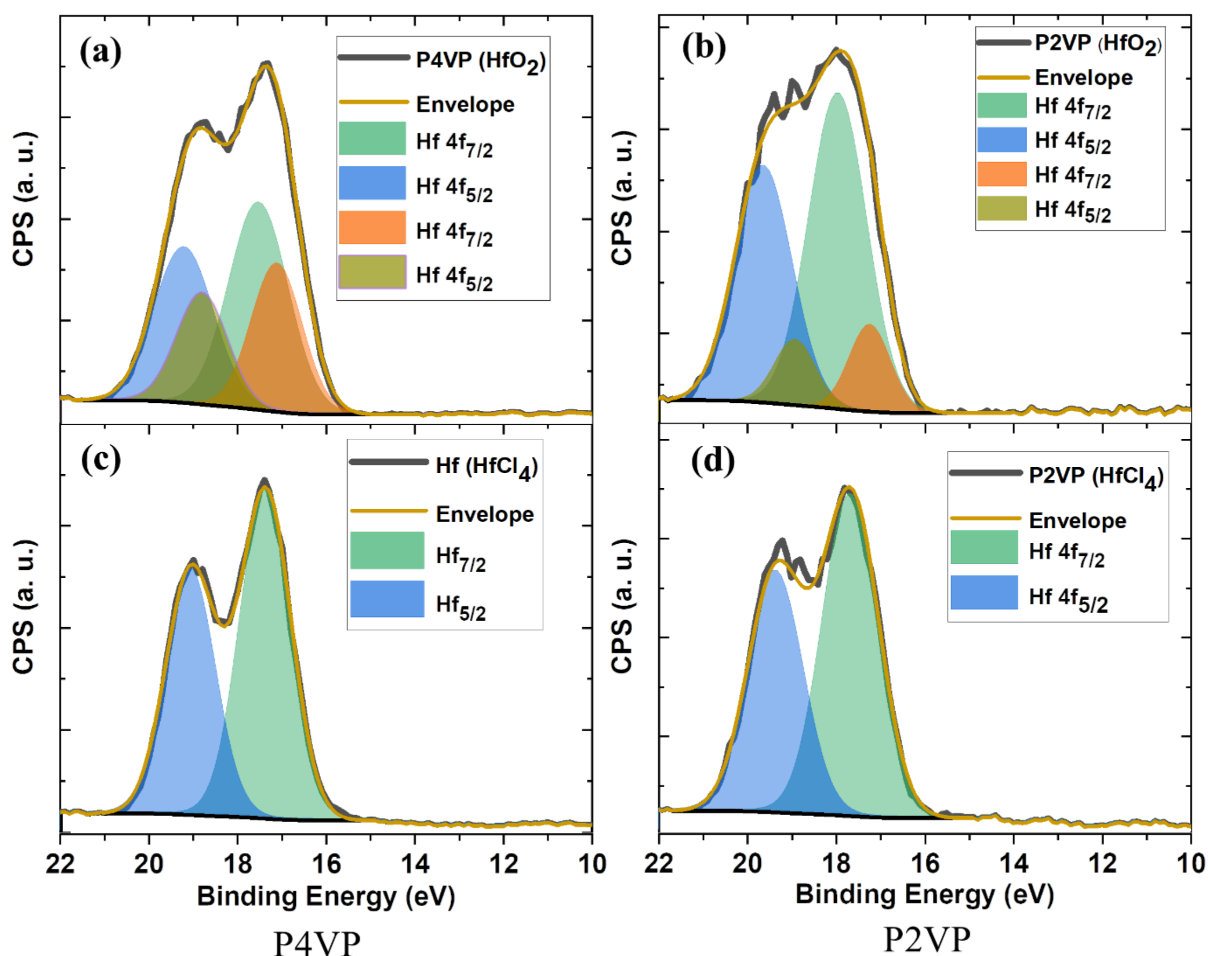

Figure 4.5*:* *High-resolution* XPS spectra of the Hf 4f region pre (bottom) and post (top) O_2 plasma treatment for P4VP (a) and P2VP (b).

The Hf 5f high-resolution scans are well fitted with a doublet showing HfO_2 before being exposed to O_2 plasma (**Figure 4.6,** lower plots). After plasma treatment, two distinct chemical environments are revealed. As seen in the top plots in **Figure 4.6**, the HFO_2 peak is the majority component at 17.5 eV.[57,58] A second peak is evident at 0.5 eV lower binding energy. This is most likely a sub-oxide species.

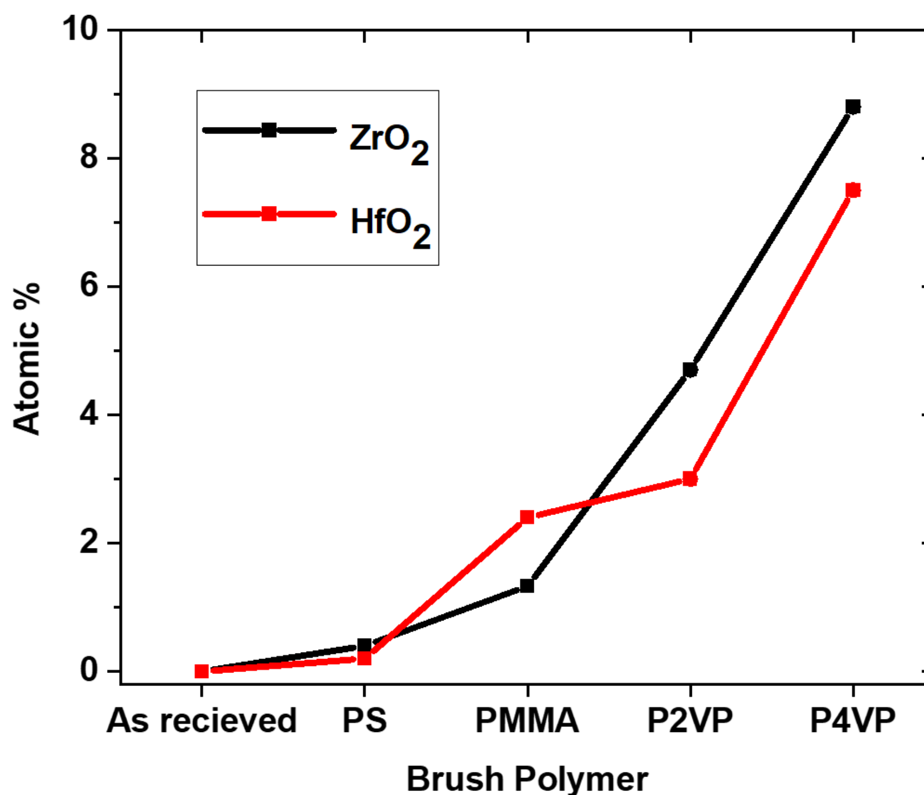

Figure *4*.6: XPS plot of atomic percentage of metal for various polymer systems

The atomic percentage of Zr and Hf were extracted from XPS survey spectra of the thin films formed when using different brush polymers. If polystyrene or no polymer was used, there was no corresponding metal oxide film present, as expected since polystyrene is a saturated molecule, and there is no chemical interaction between the polymer and the metal salt. PMMA results in 1.3% Zr and 2.4% Hf, this is likely due to the weak interaction between the metal cation and C=Ö site on the PMMA matrix. P2VP shows around 3.5%, limited by steric hindrance. P4VP is the polymer which displays the greatest amount of metal uptake, with around 8%.

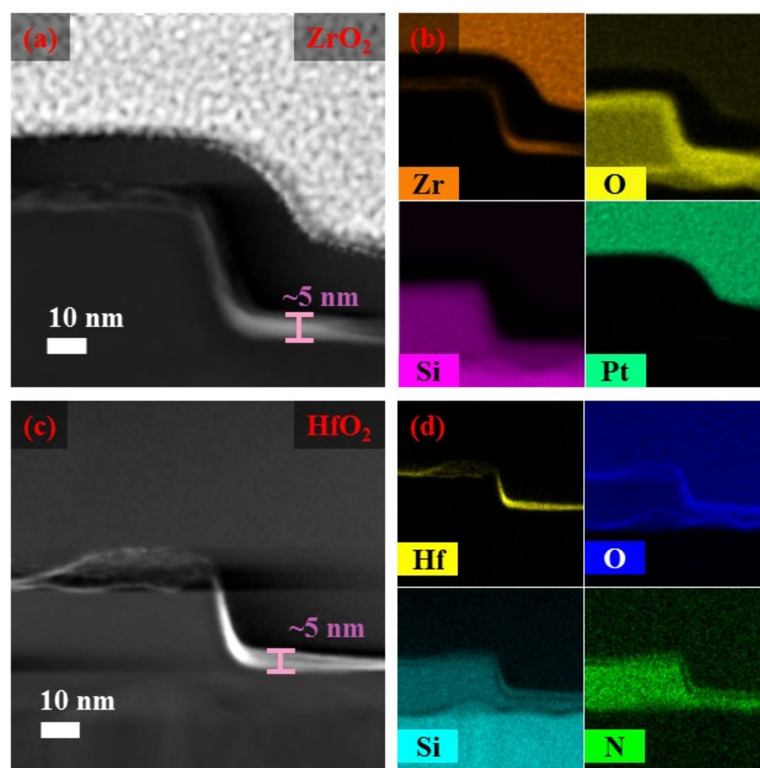

Figure 4.7: HAADF-STEM images of ZrO_2 and HfO_2 coated patterned substrates (a and c) and elemental EDX mapping images of the respective films (b and d).

Scanning tunnelling electron microscope (STEM) high-angle annular dark-field imaging (HAADF) was carried out to examine the metal oxide deposition on the trenches and pitches of the substrate following polymer plasma ashing and oxide conversion. The representative HAADF-STEM cross section images (**Figure 4.7 (a) and (c)**) show a uniformly deposited ZrO_2 and HfO_2 films on a patterned trenches. Deposited ZrO_2 and HfO_2 films are found to be highly regular across the top, bottom and sidewall of the trenches. TEM cross-section of the coated ZrO_2 and HfO_2 (**Figure 4.7(a) and (c)**) showed that the nano metal oxide films of thickness ~ 5 nm were developed. Interestingly, HfO_2 and ZrO_2 deposition across the trenches establish the capability of the P4VP to grow ordered nano metal oxide films. The EDX mapping images (**Fig. 4.7 (b) and (d)**) confirm the presence of Zr and Hf. The presence of the nitrogen signal in the EDX mapping is due to native silicon nitride.

Scope for the fabrications of thin metal oxide film by adjusting the molecular weight of the P4VP polymer could be envisaged. A myriad of metal interactions including sterically demanding species (e.g. silver and gold) with P4VP is highlighted in the literature[59] and using our approach, these metal oxide films can also be fabricated.

4.5 Conclusion:

A polymer brush template approach that facilitates a controlled inclusion of the metal ions to fabricate uniform sub-5 nm films of metal oxides (HfO_2 and ZrO_2) is reported on topographically patterned silicon nitride substrates. The SEM, TEM-HAADF, AFM and contact angle data show that high-quality pinhole-free films are uniformly and conformally deposited across the trenches and pitches of patterned substrates. The P4VP-OH brush coating is demonstrated to be optimal for a controlled conformal deposition of ultrathin films on to the trenches and pitches of the substrates, as the polymer in its neutral form coordinates with the metal ions by donating the loan pair electrons of its nitrogen atom with less steric hindrance. Further work is required to understand the feature size limitation of conformal topographic coating. Passivation of the substrate surface against metal inclusion has also been demonstrated using unreactive polystyrene brush showing the potential for selective masking. It is anticipated that this simple templating technique could allow infiltration of a wide range of materials using liquid and vapour phase techniques on to a wide range of complex topographically patterned substrates.

4.6 References:

(1) Stehlin, F.; Bourgin, Y.; Spangenberg, A.; Jourlin, Y.; Parriaux, O.; Reynaud, S.; Wieder, F.; Soppera, O. Direct Nanopatterning of 100 Nm Metal Oxide Periodic Structures by Deep-UV Immersion Lithography. *Opt. Lett.* **2012**, *37* (22), 4651. https://doi.org/10.1364/ol.37.004651.

(2) Englard, I.; Stegen, R.; Vanoppen, P.; Minnaert-Janssen, I.; der Kinderen, T.; van Brederode, E.; Duray, F.; Linders, J.; Ovchinnikov, D.; Piech, R.; et al. Novel Approach for Immersion Lithography Defectivity Control to Increase Productivity. *Metrol. Insp. Process Control Microlithogr. XXII* **2008**, *6922*, 69223U. https://doi.org/10.1117/12.776085.

(3) Hasan, R. M. M.; Luo, X. Promising Lithography Techniques for Next-Generation Logic Devices. *Nanomanufacturing Metrol.* **2018**, *1* (2), 67–81. https://doi.org/10.1007/s41871-018-0016-9.

(4) Keyes, R. W. Miniaturization of Electronics and Its Limits. *IBM J. Res. Dev.* **1988**, *32* (1), 24–28. https://doi.org/10.1147/rd.321.0024.

(5) Ratnesh, R. K.; Goel, A.; Kaushik, G.; Garg, H.; Chandan; Singh, M.; Prasad, B. Advancement and Challenges in MOSFET Scaling. *Materials Science in Semiconductor Processing*. 2021, p 106002. https://doi.org/10.1016/j.mssp.2021.106002.

(6) Lundy, R.; Flynn, S. P.; Cummins, C.; Kelleher, S. M.; Collins, M. N.; Dalton, E.; Daniels, S.; Morris, M. A.; Enright, R. Controlled Solvent Vapor Annealing of a High χ Block Copolymer Thin Film. *Phys. Chem. Chem. Phys.* **2017**, *19* (4), 2805–2815. https://doi.org/10.1039/C6CP07633E.

(7) Ross, C. a; Berggren, K. K.; Cheng, J. Y.; Jung, Y. S.; Chang, J.-B. Three-Dimensional Nanofabrication by Block Copolymer Self-Assembly. *Adv. Mater.* **2014**, *26* (25), 4386–4396. https://doi.org/10.1002/adma.201400386.

(8) Fernandez, E.; Tu, K. H.; Ho, P.; Ross, C. A. Thermal Stability of L10-FePt Nanodots Patterned by Self-Assembled Block Copolymer Lithography. *Nanotechnology* **2018**, *29* (46), 465301. https://doi.org/10.1088/1361-6528/aade2f.

(9) Mokarian-Tabari, P.; Senthamaraikannan, R.; Glynn, C.; Collins, T. W.; Cummins, C.; Nugent, D.; O'Dwyer, C.; Morris, M. A. Large Block Copolymer Self-Assembly for Fabrication of Subwavelength Nanostructures for Applications in Optics. *Nano Lett.* **2017**, *17* (5), 2973–2978. https://doi.org/10.1021/acs.nanolett.7b00226.

(10) Cummins, C.; Borah, D.; Rasappa, S.; Senthamaraikannan, R.; Simao, C.; Francone, A.; Kehagias, N.; Sotomayor-Torres, C. M.; Morris, M. A. Self-Assembled Nanofeatures in Complex Three-Dimensional Topographies via Nanoimprint and Block Copolymer

Lithography Methods. *ACS Omega* **2017**, *2* (8), 4417–4423. https://doi.org/10.1021/acsomega.7b00781.

(11) Lundy, R.; Flynn, S. P.; Cummins, C.; Kelleher, S. M.; Collins, M. N.; Dalton, E.; Daniels, S.; Morris, M.; Enright, R. Nanoporous Membrane Production via Block Copolymer Lithography for High Heat Dissipation Systems. In *2016 15th IEEE Intersociety Conference on Thermal and Thermomechanical Phenomena in Electronic Systems (ITherm)*; IEEE, 2016; pp 1267–1272.

(12) Yang, X. M.; Wan, L.; Xiao, S.; Xu, Y.; Weller, D. K. Directed Block Copolymer Assembly versus Electron Beam Lithography for Bit-Patterned Media with Areal Density of 1 Terabit/Inch2 and Beyond. *ACS Nano* **2009**, *3* (7), 1844–1858. https://doi.org/10.1021/nn900073r.

(13) Gu, X.; Gunkel, I.; Russell, T. P.; Russell, T. P. Pattern Transfer Using Block Copolymers Subject Areas : Author for Correspondence : *Philos. Trans. R. Soc.* **2013**.

(14) Thomas Mårtensson; Patrick Carlberg; Magnus Borgström; Lars Montelius; Werner Seifert, and; Samuelson*, L. Nanowire Arrays Defined by Nanoimprint Lithography. **2004**. https://doi.org/10.1021/NL035100S.

(15) Borah, D.; Cummins, C.; Rasappa, S.; Senthamaraikannan, R.; Salaun, M.; Zelsmann, M.; Liontos, G.; Ntetsikas, K.; Avgeropoulos, A.; Morris, M.; et al. Nanopatterning via Self-Assembly of a Lamellar-Forming Polystyrene-Block-Poly(Dimethylsiloxane) Diblock Copolymer on Topographical Substrates Fabricated by Nanoimprint Lithography. *Nanomaterials* **2018**, *8* (1), 32. https://doi.org/10.3390/nano8010032.

(16) Jiang, X.; Bent, S. F. Area-Selective ALD with Soft Lithographic Methods: Using Self-Assembled Monolayers to Direct Film Deposition. https://doi.org/10.1021/jp905317n.

(17) Minaye Hashemi, F. S.; Birchansky, B. R.; Bent, S. F. Selective Deposition of Dielectrics: Limits and Advantages of Alkanethiol Blocking Agents on Metal-Dielectric Patterns. *ACS Appl. Mater. Interfaces* **2016**, *8* (48), 33264–33272. https://doi.org/10.1021/acsami.6b09960.

(18) Sadat, F.; Hashemi, M.; Birchansky, B. R.; Bent, S. F. Selective Deposition of Dielectrics: Limits and Advantages of Alkanethiol Blocking Agents on Metal − Dielectric Patterns. **2016**. https://doi.org/10.1021/acsami.6b09960.

(19) Mackus, A. J. M.; Merkx, M. J. M.; Kessels, W. M. M. From the Bottom-Up: Toward Area-Selective Atomic Layer Deposition with High Selectivity †. *Chem. Mater.* **2019**, *31* (1), 2–12. https://doi.org/10.1021/acs.chemmater.8b03454.

(20) Chen, R.; Li, Y. C.; Cai, J. M.; Cao, K.; Lee, H. B. R. Atomic Level Deposition to Extend Moore's Law and Beyond. *Int. J. Extrem. Manuf.* **2020**, *2* (2). https://doi.org/10.1088/2631-

7990/ab83e0.

(21) Färm, E.; Vehkamäki, M.; Ritala, M.; Leskelä, M. Passivation of Copper Surfaces for Selective-Area ALD Using a Thiol Self-Assembled Monolayer. *Semicond. Sci. Technol.* **2012**, *27* (7), 074004. https://doi.org/10.1088/0268-1242/27/7/074004.

(22) Nagata, T. *Material Design of Metal/Oxide Interfaces for Nanoelectronics Applications*, 1st ed.; Springer Japan, 2020.

(23) Prasittichai, C.; Pickrahn, K. L.; Minaye Hashemi, F. S.; Bergsman, D. S.; Bent, S. F. Improving Area-Selective Molecular Layer Deposition by Selective SAM Removal. *ACS Appl. Mater. Interfaces* **2014**, *6* (20), 17831–17836. https://doi.org/10.1021/am504441e.

(24) Mameli, A.; Merkx, M. J. M.; Karasulu, B.; Roozeboom, F.; Kessels, W. E. M. M.; Mackus, A. J. M. Area-Selective Atomic Layer Deposition of SiO 2 Using Acetylacetone as a Chemoselective Inhibitor in an ABC-Type Cycle. **2017**. https://doi.org/10.1021/acsnano.7b04701.

(25) Mameli, A.; Karasulu, B.; Verheijen, M. A.; Barcones, B.; Macco, B.; Mackus, A. J. M.; Kessels, W. M. M. E.; Roozeboom, F. Area-Selective Atomic Layer Deposition of ZnO by Area Activation Using Electron Beam-Induced Deposition. *Chem. Mater.* **2019**, *31* (4), 1250–1257. https://doi.org/10.1021/acs.chemmater.8b03165.

(26) Prasittichai, C.; Pickrahn, K. L.; Sadat, F.; Hashemi, M.; Bergsman, D. S.; Bent, S. F. Improving Area-Selective Molecular Layer Deposition by Selective. **2014**. https://doi.org/10.1021/am504441e.

(27) Chen, R.; Kim, H.; McIntyre, P. C.; Porter, D. W.; Bent, S. F. Achieving Area-Selective Atomic Layer Deposition on Patterned Substrates by Selective Surface Modification. *Appl. Phys. Lett.* **2005**, *86* (19), 1–3. https://doi.org/10.1063/1.1922076.

(28) Singh, J. A.; Thissen, N. F. W.; Kim, W.-H.; Johnson, H.; Kessels, W. (Erwin) M. .; Bol, A. A.; Bent, S. F.; Mackus, A. J. M. Area-Selective Atomic Layer Deposition of Metal Oxides on Noble Metals through Catalytic Oxygen Activation. *Chem. Mater.* **2017**, acs.chemmater.7b03818. https://doi.org/10.1021/acs.chemmater.7b03818.

(29) Färm, E.; Kemell, M.; Ritala, M.; Leskelä, M. Self-Assembled Octadecyltrimethoxysilane Monolayers Enabling Selective-Area Atomic Layer Deposition of Iridium. *Chem. Vap. Depos.* **2006**, *12* (7), 415–417. https://doi.org/10.1002/cvde.200604219.

(30) Chen, R.; Kim, H.; McIntyre, P. C.; Bent, S. F. Self-Assembled Monolayer Resist for Atomic Layer Deposition of HfO2 and ZrO2 High-κ Gate Dielectrics. *Appl. Phys. Lett.* **2004**, *84* (20), 4017–4019. https://doi.org/10.1063/1.1751211.

(31) Zhao, Y.; Sun, X. Molecular Layer Deposition for Energy Conversion and Storage. *ACS Energy Lett.* **2018**, *3* (4), 899–914. https://doi.org/10.1021/acsenergylett.8b00145.

(32) Vericat, C.; Vela, M. E.; Benitez, G.; Carro, P.; Salvarezza, R. C. Self-Assembled Monolayers of Thiols and Dithiols on Gold: New Challenges for a Well-Known System. **2010**. https://doi.org/10.1039/b907301a.

(33) Cummins, C.; Weingärtner, T.; Morris, M. A. Enabling Large-Area Selective Deposition on Metal-Dielectric Patterns Using Polymer Brush Deactivation. *J. Phys. Chem. C* **2018**, *122* (26), 14698–14705. https://doi.org/10.1021/acs.jpcc.8b04092.

(34) Cummins, C.; Shaw, M. T.; Morris, M. A. Area Selective Polymer Brush Deposition. **2017**, *1700252*, 1–6. https://doi.org/10.1002/marc.201700252.

(35) Lundy, R.; Yadav, P.; Selkirk, A.; Mullen, E.; Ghoshal, T.; Cummins, C.; Morris, M. A. Optimizing Polymer Brush Coverage to Develop Highly Coherent Sub-5nm Oxide Films by Ion Inclusion. *Chem. Mater.* **2019**. https://doi.org/10.1021/acs.chemmater.9b02856.

(36) Lundy, R.; Yadav, P.; Prochukhan, N.; Giraud, E. C.; O'Mahony, T. F.; Selkirk, A.; Mullen, E.; Conway, J.; Turner, M.; Daniels, S.; et al. Precise Definition of a "Monolayer Point" in Polymer Brush Films for Fabricating Highly Coherent TiO2Thin Films by Vapor-Phase Infiltration. *Langmuir* **2020**, *36* (41), 12394–12402. https://doi.org/10.1021/acs.langmuir.0c02512.

(37) Cummins, C.; Weingärtner, T.; Morris, M. A. Enabling Large-Area Selective Deposition on Metal-Dielectric Patterns Using Polymer Brush Deactivation. *J. Phys. Chem. C* **2018**, *122* (26), 14698–14705. https://doi.org/10.1021/acs.jpcc.8b04092.

(38) Kim, J.; Park, J.; Pham, D. P.; Yeo, M. S.; Rhee, H. S.; Kim, Y. S.; Cho, E. C.; Yi, J. Combination of Ultraviolet Exposure and Thermal Post-Treatment to Obtain High Quality HfO2 Thin Films. *Ceram. Int.* **2021**, *47* (7), 9643–9650. https://doi.org/10.1016/j.ceramint.2020.12.103.

(39) Jindal, S.; Manhas, S. K.; Gautam, S. K.; Balatti, S.; Kumar, A.; Pakala, M. Investigation of Gate-Length Scaling of Ferroelectric FET. *IEEE Trans. Electron Devices* **2021**, *68* (3), 1364–1368. https://doi.org/10.1109/TED.2021.3054720.

(40) Flynn, S. P.; Bogan, J.; Lundy, R.; Khalafalla, K. E.; Shaw, M.; Rodriguez, B. J.; Swift, P.; Daniels, S.; O'Connor, R.; Hughes, G.; et al. Nitrogen Reactive Ion Etch Processes for the Selective Removal of Poly-(4-Vinylpyridine) in Block Copolymer Films. *Nanotechnology* **2018**, *29* (35). https://doi.org/10.1088/1361-6528/aacae4.

(41) Salavati-Fard, T.; Vasiliadou, E. S.; Jenness, G. R.; Lobo, R. F.; Caratzoulas, S.; Doren, D. J. Lewis Acid Site and Hydrogen-Bond-Mediated Polarization Synergy in the Catalysis of

Diels-Alder Cycloaddition by Band-Gap Transition-Metal Oxides. *ACS Catal.* **2019**, *9* (1), 701–715. https://doi.org/10.1021/acscatal.8b03664.

(42) Hu, Z.; Mahdi, E. M.; Peng, Y.; Qian, Y.; Zhang, B.; Yan, N.; Yuan, D.; Tan, J. C.; Zhao, D. Kinetically Controlled Synthesis of Two-Dimensional Zr/Hf Metal-Organic Framework Nanosheets via a Modulated Hydrothermal Approach. *J. Mater. Chem. A* **2017**, *5* (19), 8954–8963. https://doi.org/10.1039/c7ta00413c.

(43) Lee, J.; Mishra, A. K.; Choi, C.; Kim, D.; Kim, E. Y.; Yong, K.; Kim, J. K. Three-Dimensional Nanoporous Metal Structures from Poly(2-Vinylpyridine)- Block -Poly(4-Vinylpyridine) Copolymer Thin Film . *ACS Appl. Mater. Interfaces* **2020**, *12* (13), 15667–15674. https://doi.org/10.1021/acsami.9b23009.

(44) Tan, T.; Liu, Z.; Lu, H.; Liu, W.; Tian, H. Structure and Optical Properties of HfO2 Thin Films on Silicon after Rapid Thermal Annealing. *Opt. Mater. (Amst).* **2010**, *32* (3), 432–435. https://doi.org/10.1016/j.optmat.2009.10.003.

(45) Park, M. H.; Chung, C. C.; Schenk, T.; Richter, C.; Opsomer, K.; Detavernier, C.; Adelmann, C.; Jones, J. L.; Mikolajick, T.; Schroeder, U. Effect of Annealing Ferroelectric HfO2 Thin Films: In Situ, High Temperature X-Ray Diffraction. *Adv. Electron. Mater.* **2018**, *4* (7), 1–10. https://doi.org/10.1002/aelm.201800091.

(46) Xiao, Z.; Kisslinger, K.; Chance, S.; Banks, S. Comparison of Hafnium Dioxide and Zirconium Dioxide Grown by Plasma-Enhanced Atomic Layer Deposition for the Application of Electronic Materials. *Crystals* **2020**, *10* (2), 1–12. https://doi.org/10.3390/cryst10020136.

(47) Das, S.; Guha, S.; Das, P. P.; Ghadai, R. K. Analysis of Morphological, Microstructural, Electrochemical and Nano Mechanical Characteristics of TiCN Coatings Prepared under N2 Gas Flow Rate by Chemical Vapour Deposition (CVD) Process at Higher Temperature. *Ceram. Int.* **2020**, *46* (8), 10292–10298. https://doi.org/10.1016/j.ceramint.2020.01.023.

(48) Kennemur, J. G. Poly(Vinylpyridine) Segments in Block Copolymers: Synthesis, Self-Assembly, and Versatility. *Macromolecules* **2019**, *52*, 1354–1370. https://doi.org/10.1021/acs.macromol.8b01661.

(49) Peng, Q.; Tseng, Y. C.; Darling, S. B.; Elam, J. W. A Route to Nanoscopic Materials via Sequential Infiltration Synthesis on Block Copolymer Templates. *ACS Nano* **2011**, *5* (6), 4600–4606. https://doi.org/10.1021/nn2003234.

(50) Zhang, Z.; Dwyer, T.; Sirard, S. M.; Ekerdt, J. G. Area-Selective Atomic Layer Deposition of Cobalt Oxide to Generate Patterned Cobalt Films. *Journal of Vacuum Science & Technology A*. 2019, p 020905. https://doi.org/10.1116/1.5066437.

(51) IEEE International Interconnect Technology Conference/Advanced Metallization Conference (IITC/AMC); 2016; pp 133–135.

(52) Lindvig, T.; Michelsen, M. L.; Kontogeorgis, G. M. A Flory-Huggins Model Based on the Hansen Solubility Parameters. *Fluid Phase Equilib.* **2002**, *203* (1–2), 247–260. https://doi.org/10.1016/S0378-3812(02)00184-X.

(53) Hansen, C. M. *Hansen Solubility Parameters: A User's Handbook*; CRC press, 2007.

(54) Barr, T. L.; Seal, S. Nature of the Use of Adventitious Carbon as a Binding Energy Standard. *J. Vac. Sci. Technol. A Vacuum, Surfaces, Film.* **1995**, *13* (3), 1239–1246. https://doi.org/10.1116/1.579868.

(55) Raczkowska, J.; Stetsyshyn, Y.; Awsiuk, K.; Zemła, J.; Kostruba, A.; Harhay, K.; Marzec, M.; Bernasik, A.; Lishchynskyi, O.; Ohar, H.; et al. Temperature-Responsive Properties of Poly(4-Vinylpyridine) Coatings: Influence of Temperature on the Wettability, Morphology, and Protein Adsorption. *RSC Adv.* **2016**, *6* (90), 87469–87477. https://doi.org/10.1039/c6ra07223b.

(56) Kumar, L.; Horechyy, A.; Bittrich, E.; Nandan, B.; Uhlmann, P.; Fery, A. Amphiphilic Block Copolymer Micelles in Selective Solvents: The Effect of Solvent Selectivity on Micelle Formation. *Polymers*. 2019. https://doi.org/10.3390/polym11111882.

(57) Ohtsu, N.; Tsuchiya, B.; Oku, M.; Shikama, T.; Wagatsuma, K. X-Ray Photoelectron Spectroscopic Study on Initial Oxidation of Hafnium Hydride Fractured in an Ultra-High Vacuum. *Appl. Surf. Sci.* **2007**, *253* (16), 6844–6847. https://doi.org/10.1016/j.apsusc.2007.01.117.

(58) Morant, C.; Galán, L.; Sanz, J. M. An XPS Study of the Initial Stages of Oxidation of Hafnium. *Surf. Interface Anal.* **1990**, *16* (1–12), 304–308. https://doi.org/10.1002/sia.740160163.

(59) Aizawa, M.; Buriak, J. M. Block Copolymer Templated Chemistry for the Formation of Metallic Nanoparticle Arrays on Semiconductor Surfaces. *Chem. Mater.* **2007**, *19* (21), 5090–5101. https://doi.org/10.1021/cm071382b.

4.7 Appendix:

Fabrication of high-k dielectric metal oxide films on patterned substrates: polymer brush assisted depositions for modern device architectures.

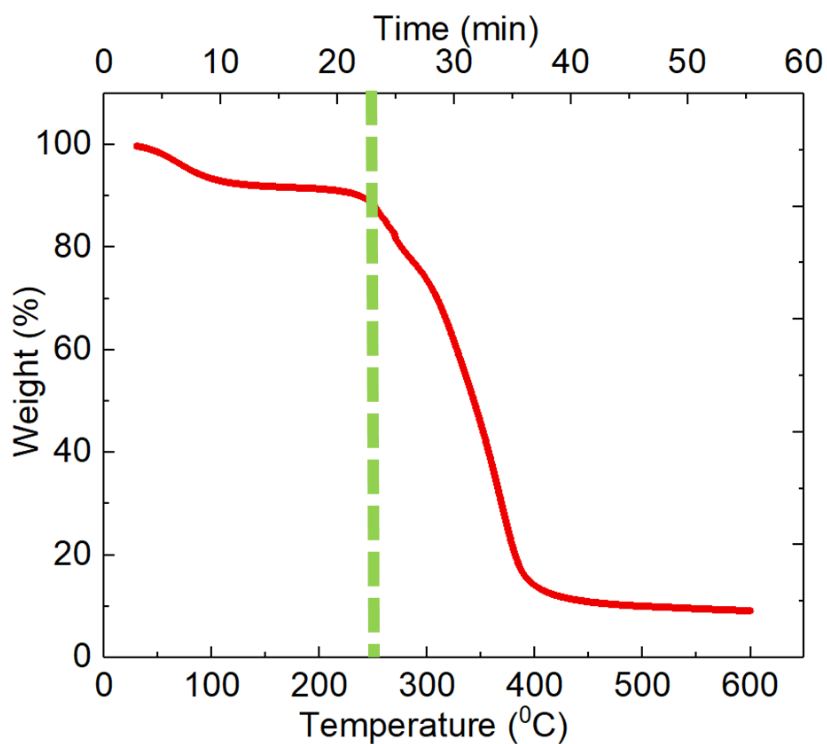

Figure S4.7.1: Thermogravimetric analysis was performed on the 5.5 $kmol^{-1}$ P4VP-OH at temperature range of 25-600^{0}C for 60 minute. Polymer undergo thermal degradation at 250^{0}C indicating optimum temperature for the grafting process.

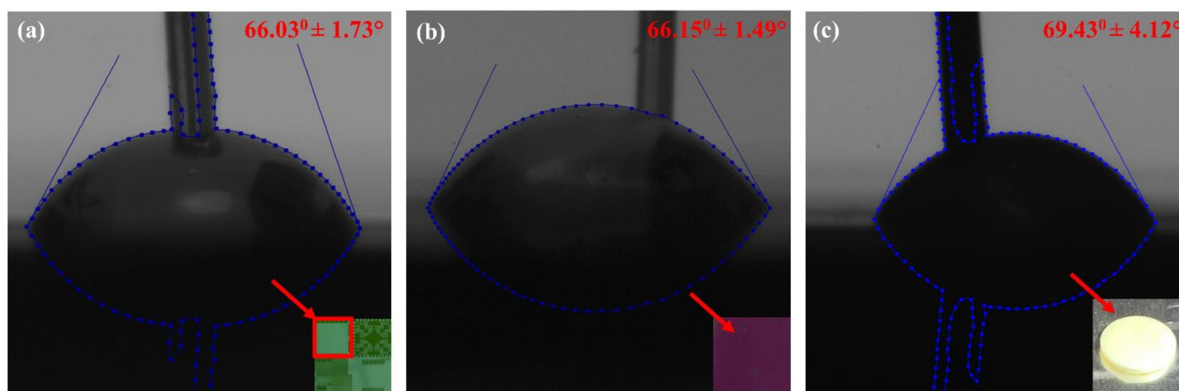

Figure S4.7.2: (a) water contact angle of grafted P4VP polymer brush measured at plane region of topographically patterned substrate (b) water contact angle of thick-coated P4VP film on plane silicon substrate (c) water contact angle of P4VP homopolymer pressed pellet.

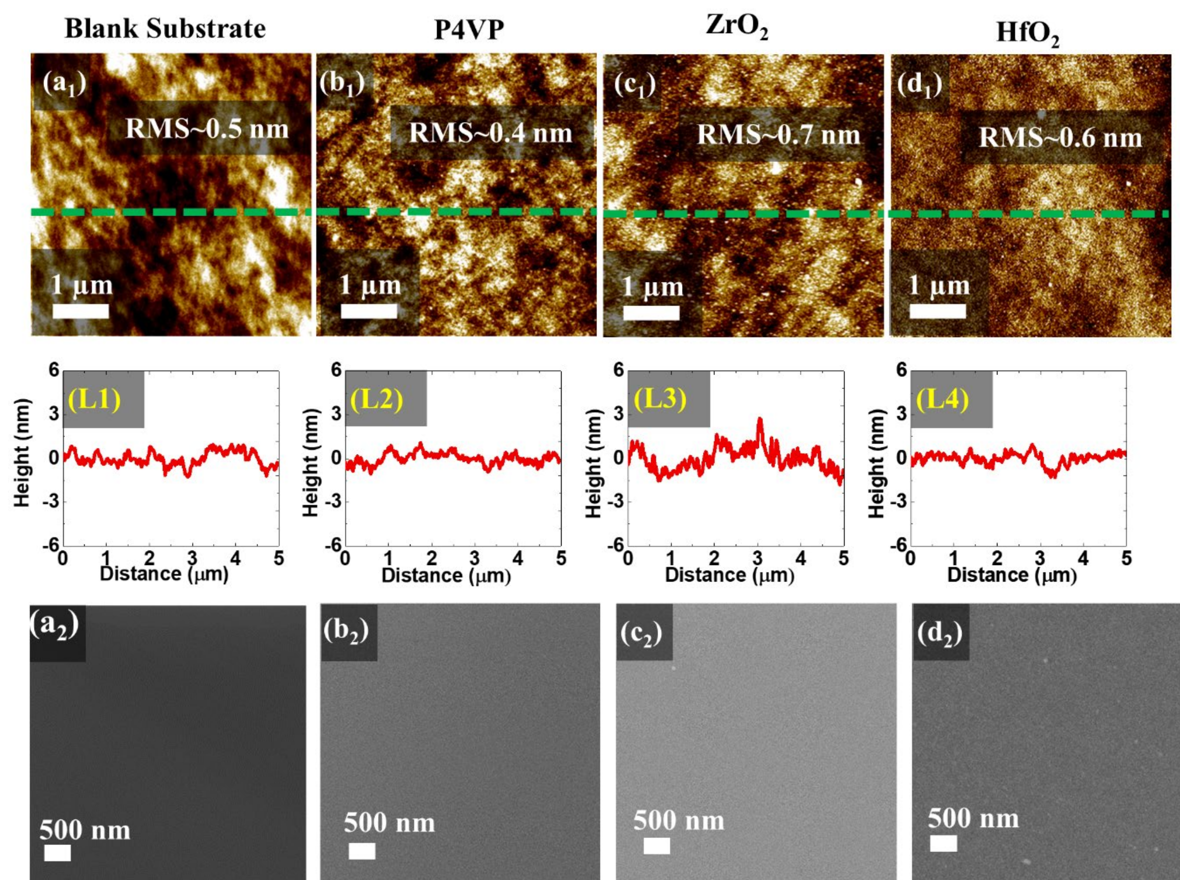

Figure S4.7.3: AFM image of (a_1-d_1) with line profile plotted at (L1-L4) and SEM images (a_2-d_2) for blank substrate (a_1, L1, a_2), P4VP grafted brush (b_1, L_2, b_2), ZrO_2 (C_1, L3, C_2) and HfO2 (d_1, L2, d_2) films.

Chapter 5. Polymethyl methacrylate template assisted deposition of uniform zirconium oxide films on copper substrate through liquid phase for area selective deposition application.

5.1 Abstract:

In this chapter, we demonstrate a polymer brush assisted approach for the fabrication of continuous zirconium oxide (ZrO_2) films over the large areas with high uniformity (pin-hole free) on Copper (Cu) substrates. This approach involves the use of a thiol-terminated poly-(methyl methacrylate) (PMMA-SH) as the template layer for the selective infiltration of zirconium oxynitrate (ZrN_2O_7) dissolved in ethanol. The preparation of a uniform covalently grafted polymer monolayer on the Cu substrate is critical for the eventual even metal oxide distribution across the surface, determined by the chemical interactions within the polymer functional group and the metal precursor. The subsequent reductive H_2 plasma annealing process results in a homogeneous formation of ZrO_2 film on Cu, while the formed Cu_2O oxide layer reduced at the Cu/Cu_2O interface. Fundamental analysis of the infiltration process and the resulting ZrO_2 film was determined by X-ray photoelectron spectroscopy (XPS), and Grazing Angle Fourier transformed infrared spectroscopy (GA-FTIR). Results derived from these techniques confirms the inclusion of the ZrN_2O_7 into the polymer films. On the other hand, cross-sectional transmission electron microscopy (TEM) and energy dispersive X-ray (EDX) mapping analysis corroborate the formation of ZrO_2 layer on the Cu substrate. We believed that this quick and facile methodology to prepare ZrO_2 films, potentially scalable to other high-κ dielectric materials of high interest in microelectronic applications.

5.2 Introduction:

The progressively reduction in electronic devices size and the challenges associated with the top-down photolithography approach has created the demand for controlled deposition of nanoscale materials *via* bottom-up processes.[1] In this scenario, the substrate coating of selected regions with active materials offers an attractive strategy that eliminates multiple patterning and etching steps used in the photolithography technique.[2] There are several approaches complimenting photolithography include block copolymer (BCP) lithography,[3-12] nanoimprint lithography, and, lately, area selective deposition (ASD) techniques.[13–16] These bottom up approaches are considered as promising processing methods for the selective infiltration of active materials such as metals and dielectrics for the fabrication of future nanoelectronics.[17] Specifically, the potential of ASD to produce highly coherent metal and oxide films is pivotal for their successful integration into silicon device architecture.[14] Several inspired approaches in the ASD technology arena have been explored in the past, including self-assembled monolayers (SAMs) in conjunction with atomic layer deposition (ALD) to demonstrate substrate specific selectivity. Selectivity in area selective deposition, is accomplished by carefully altering the substrate surface chemistry for the controlled infiltration of the inorganic materials.[18,19,20] Furthermore, the combination of SAMs based ALD have been broadly studied to facilitate deposition of materials onto the desired region of the substrate.[21] In this technique, the efficient fabrication of the material patterns relies on the chemical reaction of vapour phase precursors with pre deposited SAMs molecule. Several leading material research groups have investigated the practicality of SAM molecules. For example, Bent and co-workers demonstrated the well-defined techniques to achieve coating on Cu/SiO_2 line space.[18,20,22–24] Chen et al. have demonstrated promising efficacies of SAMs in the selective deposition of high-κ dielectric materials such as HfO_2 and ZrO_2.[24] However, defects (pin hole) generated by SAMs and long processing times required for grafting, makes it industrially less favorable.[25] Similarly, unreactive polymer

layers, such as poly(methyl methacrylate),[26] poly(imide),[27,28] poly(vinyl pyrrolidone),[29] chemically amplified resists,[30–32] and some physical approaches such as plasma treatment[33] have also been investigated to perform material patterning.

Chemical grafting of brushes, in particular, is regarded as the preferable way of substrate modification due to its compatibility with a variety of deposition processes. Polymers with different end terminating functional groups have different surface binding strengths. The surface reactivity of a polymer brush can be altered by adjusting the polymer brush's end-terminated group. In our previous works, we thoroughly investigated the key parameters governing the grafting process of high quality polymer brushes on silicon substrates.[34,35] High coverage interfacial polymer brush layer is critical in fabrication of nanometal oxide films. Various metal oxides (Al_2O_3, TiO_2, CuO and Co_3O_4) have been successfully infiltrated on grafted polymer brushes using liquid and vapour phase deposition techniques.[34–40] The utilization of readily available precursors, the simplicity of the processes, and the low cost of liquid aided depositions of inorganic salts are all advantages.

In this chapter, we develop a liquid phase insertion of zirconium oxynitrate (ZrN_2O_7) on chemically grafted PMMA brushes in order to obtain ZrO_2 thin films on a copper substrate. The fabrication of uniform polymer brush layer was crucial in the infiltration method leading to ZrO_2 films. With the aim to the develop future nanoelectronic devices, the avail of methods to synthesize advanced materials directly on various targeted surfaces without complicated processing steps is a critical challenge. Here, we address the effect of hydrogen plasma annealing in the oxidation of the ZrN_2O_7 to ZrO_2 and removal of the polymer brush layer. The past studies have reported the decomposition of the templating organic layer and oxidation of inorganic precursor through high temperature route such as the calcination followed by acetic acid treatment to reduce the formed copper oxide at the interface.[43] Herein, we successfully achieved both processes in a single step using reductive H_2 plasma annealing.

5.3 Experimental section:

5.3.1 Materials

Blank Cu substrate was received from Intel Corporation Ireland. Thiol end terminated poly (methyl methacrylate) (PMMA-SH) (number-average molecular weight-6.5 X 10^3 g/mol and polydispersity-1.3) was purchased from Polymer Source Inc. (Canada) and used without further purification. PMMA-SH was dissolved in toluene and stirred overnight to obtain 0.6% wt. solution. Zirconium (IV) oxynitrate hydrate (99% purity) and citric acid (ACS reagent>99.5 %) were purchased from Merck & Co. (Ireland). High performance liquid chromatography grade ethanol, deionised water (ρ=18.2 MΩ.cm), and toluene (99.99% purity) were purchased from Merck & Co. (Ireland), too, and used as received.

5.3.2 Substrate surface functionalisation, polymer coating, metal salt infiltration, and hydrogen plasma etching:

Figure 5.1 schematically shows the experimental approach for the fabrication of ZrO_2 on the Cu Substrate. Copper substrates were first degreased ultrasonically in toluene for 10 min and dried using a nitrogen gas flow. Organic adsorbents on Cu surface were removed using an oxygen plasma treatment for 2 min (40 kHz, 50W barrel asher). The Cu substrate was immersed in 1% wt. citric acid solution for 5 minute in order to reduce interfacial oxide layer and to activate the copper surface as confirmed by X-ray photon spectroscopy (XPS) previously.[37] The citric acid treated substrate was then rinsed with water and dried using soft N_2 gas blow. PMMA-SH solutions were spin coated at 3000 rpm for 25 sec with the ramp of 5 sec. Thereafter, spin coated samples were immediately annealed at 170 ºC for 10 minutes and subsequently were ultra-sonicated in toluene for 30 min (2 x 15 min) to remove physically adsorbed polymer molecules and yield a monolayer coverage. This monolayer coverage of polymer brush was further infiltrated with the ethanolic solution of zirconium oxynitrate (0.4% wt.) at 3000 rpm for 25 sec with the ramp of 5 sec. To achieve a uniform

ZrO_2 deposit on Cu surface and eliminate grafted polymers, the samples were annealed at 200 °C in presence of hydrogen gas.

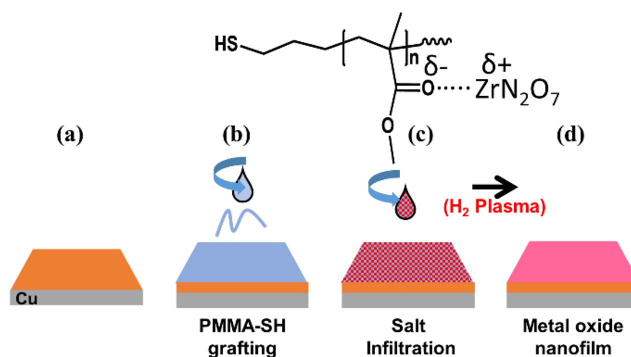

Figure 5.1: Schematic representation of the process for the (a) functionalization of Cu substrate, (b) fabrication of polymer brush film, (c) metal salt inclusion into polymer film (d) reductive polymer ashing.

5.3.3 Characterisation:

A high-resolution field emission scanning electron microscopy (Carl Ziess ultra) with a secondary electron detector operating at an accelerating voltage of 5 kV was used to scan top-down images of the samples. Atomic force microscopy (AFM, park system XE7) was used with the non-contact cantilever (AC 160TS, force constant ~ 26 nm^{-1}, resonant frequency ~ 300 kHz). The lamella was prepared using focused ion beam etching (FIB, Helios Nanolab 460) with typical high kV milling and a final low kV polish, which made the lamella electron transparent, showing that it is an adequate thickness for TEM. Platinum was employed as a capping layer. Brightfield and STEM imaging were used in transmission electron microscopy (FEI Osiris). The detector lengths during STEM were 220, 550, and 770 mm. 200 kV was used as the accelerating voltage. The EDX beam current was 1 nA, with a 30 minute acquisition period.

For eliminating the polymer and reducing the oxidised copper, a H_2 plasma treatment was used. Plasma processing was performed in an Oxford Instruments FlexAL system (base pressure 1 X 10^{-5} mbar). The sample was heated to 200 °C, and 50 sccm of H_2 gas was

supplied at a pressure of 40 mTorr along with 300W of RF power to produce a hydrogen plasma. The heated sample which was located downstream from the plasma source was processed for 30 minutes. XPS analysis was performed on a Scienta Omicron monochromatic Al Kα X-ray source (base pressure 1 X 10^{-8} mbar), equipped with a 128 channel Argus CU detector. The XPS was coupled in-situ to the FlexAl system via a transfer chamber (base pressure 5 X 10^{-7} mbar) to allow for the analysis of the plasma processed samples without breaking vacuum. The transfer time between the FlexAL and XPS chambers was approximately 1 minute. XPS data analysis was performed using Casa XPS software. The binding energy scale was referenced to the C 1s peak of adventitious carbon at 284.8eV.[44] For survey scans, an analyser pass energy was set to 100 eV while a pass energy of 50 eV was used to obtain high-resolution spectra of characteristic core levels.

Dyanamic contact angle (CA) measurements (custom built system) equipped with a high speed camera (60 Hz sampling rate) was used to capture advancing and receding water contact angle on five different regions of each substrate. Water was placed with the flow rate of the 5 nl.s^{-1} using 35 gauze needle with droplet volume between 40 to 100 nano litre. TGA pyris (1) was performed on the PMMA-SH brush at the temprature range of the 30-600 °C with the rate of 10°/min.

GA-FTIR was performed using a Nicolet iS50 FTIR Spectrometer equipped with a Harrick VariGATR attachment. Prior to sample analysis the germanium crystal was cleaned using butanone before acquiring a background of the atmosphere. Each sample was placed face down on the crystal and a force of approximately 600 N was applied to the sample to ensure sufficient sample-crystal contact. The sample was scanned at an unpolarised angle of incidence of 65° for a total of 128 scans at 8 cm^{-1} resolutions.

5.4 Results and discussion:

5.4.1 PMMA-SH brush grafting on Cu surface.

Cu substrate was cleaned by dipping it in 1 wt.% citric acid solution for 5 min in order to etch interfacial oxide layer as described in detail elsewhere.[37,45] XPS data shows that the citric acid treatment removes the interfacial oxide layer and activated the surface for further modification (see **Figure S5.7.1).** PMMA-SH dissolved in toluene (0.6% wt.) was coated on the copper substrate immediately after the citric acid treatment and annealed at 170 °C for 5 min. Heat treatment enabled the uncoiling of polymer chain and the rapid reaction between reactive end thiol group and copper metal results in the formation of uniform polymer brush on the surface. Contact angle measurements were performed immediately after the citric acid treatment and polymer brush grafting. The reference citric acid treated copper substrate showed an average advancing water contact angle (WCA) of θ_{Cu}=17.45 ± 2.6º. After the PMMA-SH brush grafting, the average WCA was recorded to be θ_{PMMA}=75.95 ± 1.6°, in close agreement to the value acquired for the pressed homopolymer methyl methacrylate pellet 77.64 ± 1.4° (see **Figure S5.7.2).** Surface coverage of the polymer brush deposited on the copper substrate was calculated using the Cassie Baxter equation.[46,47]

$$\Phi = \left(\frac{\cos\theta_{PMMA}}{\cos\theta_{Cu}} - 1\right) \Big/ \left(\frac{\cos\theta_{PMMA(max)}}{\cos\theta_{Cu}} - 1\right), (\mathbf{1})$$

Where Φ is the apparent surface coverage of the coated PMMA brush, θ_{PMMA} is the advancing water contact angle (θ_a) of the deposited PMMA-SH brush, θ_{Cu} is the θ_a of the citric acid treated copper substrate and $\theta_{PMMA(max)}$ is the θ_a of the pressed homopolymer pellet. By solving the above equation, surface coverage of the polymer brush is estimated to be 96%.

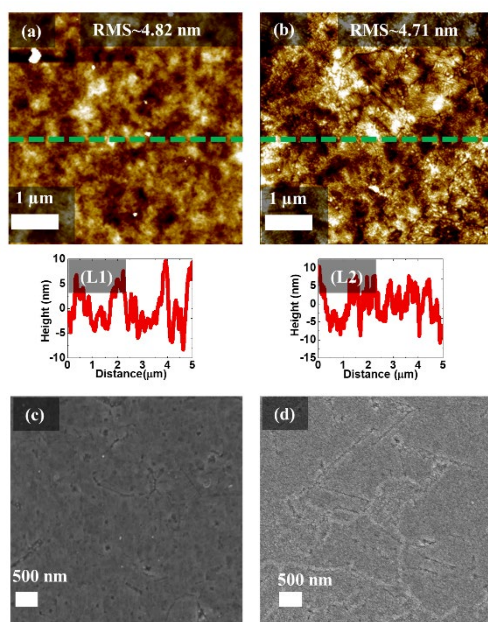

Figure 5.2: AFM images of (a) citric acid treated copper substrate (5 min) with roughness profile at L1, (b) grafted PMMA brush with line profile at L2. (c) and (d) are the respective SEM images of the functionalised Cu substrate and PMMA-SH grafted brush.

Morphology of the grafted polymer brush film was analysed using atomic force microscopy (AFM) and scanning electron microscopy (SEM). It is observed from **Figure S5.7.3** that solvent washing is not effective in removing contamination from the copper substrate and long-time aggressive ultrasonic cleaning is not suggested as it can potentially damage the copper layer. For high quality pinhole free polymer brush grafting, it is critical to reduce interfacial oxide layer and eliminate possible organic fragments adsorbed on the copper surface. Citric acid treatment is proven to be a successful step to reduce the Cu_2O/CuO interface to metallic copper and remove impurity particles from the substrate surface. This is confirmed by **Figures 5.2 (a)** and **(c),** which show that post citric acid treatment samples became plane and smoother. Namely, the root mean square (RMS) roughness value for as received copper substrate was calculated to be of 5.69 nm (**Figure S5.7.3**), while citric acid treated substrate of 4.82 nm (see **Figure 5.2a**), and grafted PMMA-SH brush of 4.71 nm (**Figure 5.2b**). The RMS value was used to estimate the grafting of polymer brush on the copper surface. Low RMS values observed for the deposited polymer brush shows highly

regular and uniform film coating. **Figures 5.2 (c)** and **(d)** are correspond to SEM images obtained for the citric acid treated Cu substrate and polymer coated Cu substrate, respectively. The representative SEM images show the absence of any micro roughness or irregularities in the formed polymer brush films.

5.4.2 PMMA-SH ion infiltration and fabrication of ZrO2:

The grafted PMMA-SH monolayer 6 kg,mol^{-1} brush was infiltrated to ethanolic solution of zirconium (IV) oxynitrate and subsequently converted to ZrO_2 nanofilm by H_2 reductive plasma annealing. XPS survey scans for the grafted brush presented in **Figure S5.7.4 (a)** shows that the respective elements (C, O, Cu) are present on the surface. Survey spectrum in **Figure S5.7.4 (b)** depicts that the infiltration on copper substrate without a deposited polymer layer leads to significantly less retention (~0.6%) of Zr. On the contrary, the deposition of zirconium oxynitrate solution onto the grafted brush reveals the inclusion of zirconium metals into the polymer film (see **Figure S5.7.4 (c)**). Finally, after the H_2 plasma treatment the carbon C 1s signal was remarkably reduced, attributed to the reductive elimination of the PMMA brush (see **Figure 5.7.4 (d)**)

The core-level XPS spectra of C 1s, O 1s, Zr 3d, and Cu 2p of the grafted PMMA brush, metal precursor infiltrated brush and post H_2 plasma treated samples are shown in **Figure 5.3.** C1s data from the samples containing PMMA brush are fitted into three different components as described by Piere et al.[48] For the bare PMMA brush, the C 1s peaks positioned at 284.9, 286.6 and 288.8 are associated with C-C, C-O-CH_3, and O-C=O of grafted PMMA brush.[49,50] This peak retains its position at the same binding energy after metal salt infiltration. Fallowing, the hydrogen plasma treatment, the C=O peak of PMMA no longer visible, illustrating the complete breakdown of the PMMA into volatile fragments. Additionally, the lower signal-to-noise ratio also indicates the C surface concentration decrease by the polymer removal, as displayed in **Table S5.7.2**.

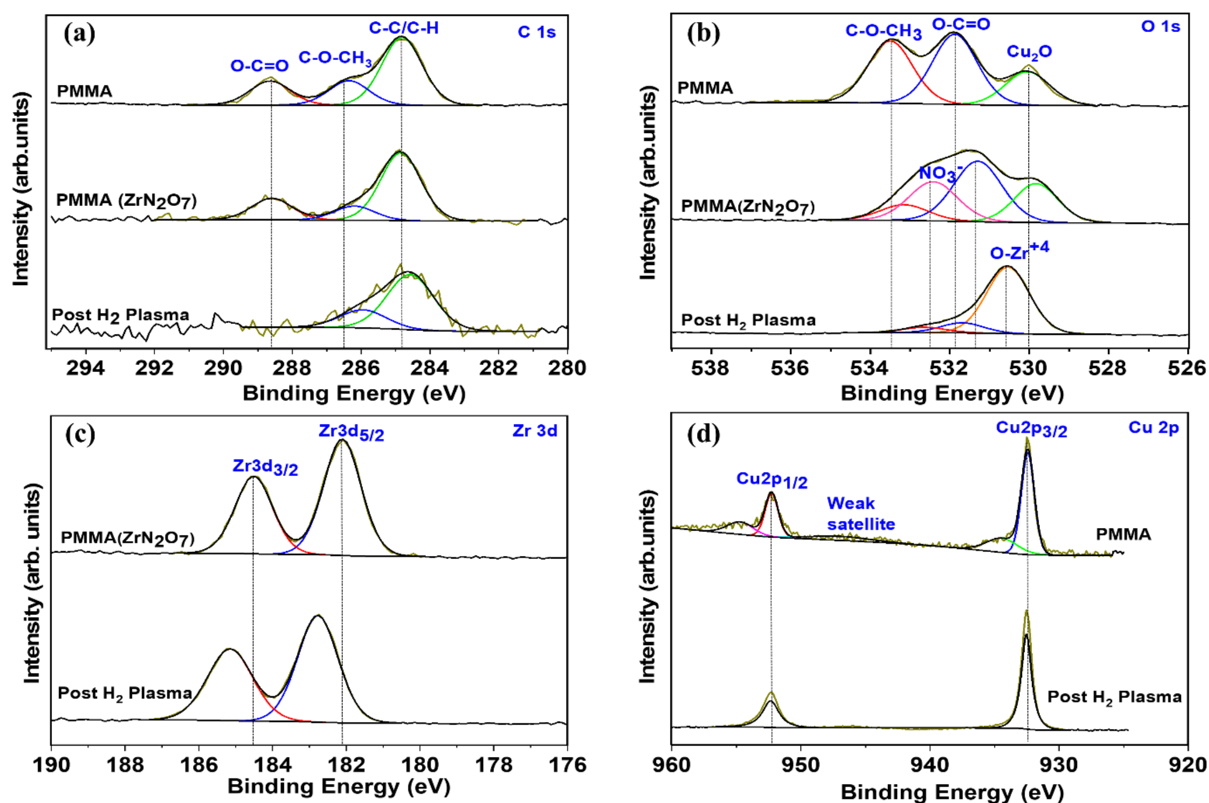

Figure 5.3: High resolution C 1s and O 1s (a and b) XPS spectra of the grafted polymer brush, metal infiltrated sample and H_2 plasma annealed substrate, (c) Zr 3d, pre and post plasma treated (d) Cu 2p substrate after the polymer brush grafting and H_2 plasma treatment.

The O 1s XPS spectra shown in **Figure 5.3b** reveal that for the grafted PMMA brush, three different O species can be discerned at 530, 531.8 and 533.5 eV. These peaks are associated with copper(I) oxide, methoxy oxygen and carbonyl oxygen of PMMA.[39,52,53] Interestingly, after the zirconium salt infiltration a negative shift in carbonyl oxygen peak is observed (by –0.5 eV), indicating the coordination of the Zr salt into the active site of the polymer. Additionally, one extra peak at 532.6 eV is detected, corresponding to the nitrate oxygen of zirconium oxynitrate.[54] In the post H_2 plasma sample, the polymeric oxygen peak and copper(I) oxide oxygen signal are eliminated, while new peaks appear at 530.6 eV attributed to the presence of zirconium oxide.[55] The second component at 531.8 eV can be ascribed to the formation of Zr-OH or C-O fragments of polymer.[56] After the reductive plasma annealing

no measurable nitrate oxide peak observed, suggesting the complete conversion of metal precursor to the metal oxide.

Zr 3d peak for the infiltrated sample display single spin-orbit doublet as shown in **Figure 5.3 (c)**. The peaks at 182.1 and 184.6 eV are associated to the Zr $3d_{5/2}$ and Zr $3d_{3/2}$ contributions, respectively.[57] After the hydrogen plasma exposure, a positive shift of +0.7 eV is observed , which could be due to the formation of ZrO_2.[58] These results are highly in agreement with the peaks observed in the O 1s region at 530.6 eV, associated to the O-Zr^{+4}.[59] Thus, the data suggest that the oxidation of the zirconium film occurs. On the other hand, the Zr loading present on surface after the reduction process increased by 14% (see **Figure S5.7.4 and Table S5.7.2**), consistent with the polymer ashing.

Figure 5.3d displays Cu 2p XPS spectra for the PMMA brush grafted sample and the hydrogen plasma treated metal infiltrated brush substrate. This region exhibits two peaks at 932.5 and 952.5 eV for the grafted brush, associated with the spin-orbit coupling compounds Cu $2p_{3/2}$ and Cu $2p_{1/2}$, respectively.[60] A weak satellite peak at ~946.2 eV and two minor peaks at 935.2 and 955.2 eV are additionally observed which correspond with the presence of residual CuO.[61] Oxidized copper oxide species could be formed during the annealing of the polymer brush at 170 ºC. The oxidation of underlying copper substrate for the grafted brush further was confirmed by the shift in the Cu LMM peak kinetic energy to 916.6 eV, as this peak is very sensitive to the copper oxidation state.[62] After the H_2 plasma treatment, the Cu LMM peak shifts back to 919.0 eV and the weak satellite peak and minor peaks are reduced indicating the complete reduction of CuO/Cu_2O to metallic Cu (see **Figure S5.7.5**).

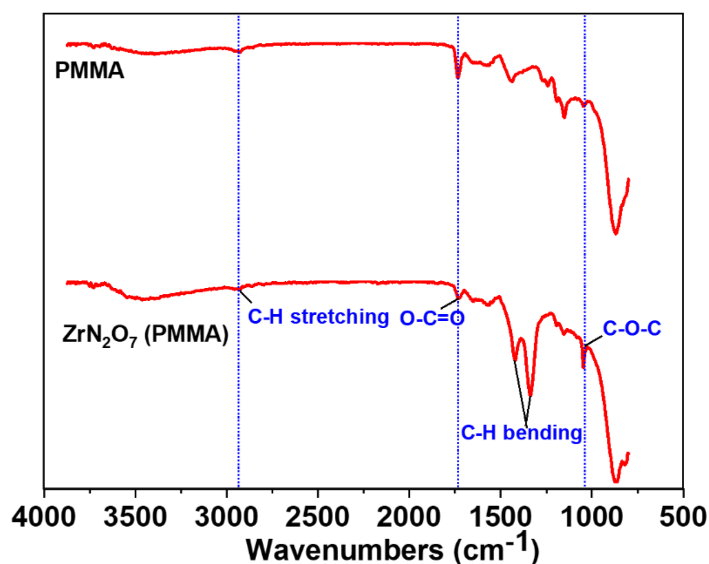

Figure 5.4: The FTIR spectra of PMMA and zirconium oxynitrate infiltrated PMMA brush.

The FTIR spectra of grafted PMMA brush and infiltrated zirconium oxynitrate brush are shown in **Figure 5.4.** In the grafted PMMA brush IR spectrum, the strong peak appears at 1734 cm^{-1} is the characteristic stretching band of the acrylate carbonyl group.[63] The peaks observed at 2967, and 2936, cm^{-1} correspond to the C-H band stretching vibrations of methyl and methylene groups of PMMA. The peaks present at 1421 and 1336 cm^{-1} are ascribes to the bending –C-H vibrations of the methyl group.[64] The peak at 1048 cm^{-1} is associated with the C-O stretching vibration.[65] The FTIR spectra of the grafted PMMA brush were compared with the zirconium oxynitrate deposited sample, revealing the decrease in the acrylate carbonyl band and the increase in intensity for C-O vibration mode in the infiltrated sample. The observed changes can be explained by the coordination of Zr metal ions with the carbonyl unit of the PMMA brush.[66]

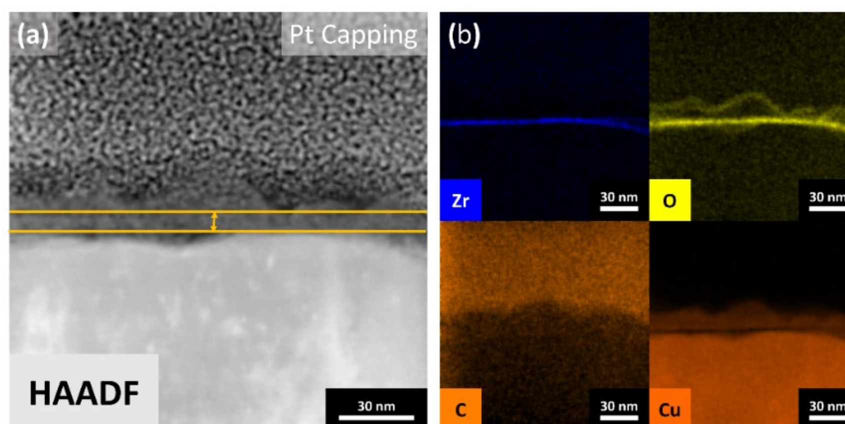

Figure 5.5 (a) STEM high-angle annular dark field (HAADF) images of hydrogen plasma annealed infiltrated sample and (b) EDX maps of (Zr, O, C, and Cu).

Figure 5.5 illustrates scanning tunnelling electron microscopy (STEM) images and electron dispersive X-ray spectroscopy (EDX) maps of hydrogen plasma annealed infiltrated PMMA brush sample. STEM cross-section was performed to analyse the zirconium oxide deposition on the copper substrate. The STEM cross-section (HAADF) image in **Figure 5.5 (a)** confirms the fabrication of a ~ 4 nm thick ZrO_2 layer on the copper substrate, whose elemental distribution is depicted by EDX mappings in **Figure 5.5 (b).**

5.5 Conclusion:

In conclusion, we propose a reliable method for the infiltration of a high-k material using a polymer brush activation strategy, which has a considerable importance in selective area deposition technology. Here, we demonstrate the solvent phase uniform deposition of thiol end-terminated PMMA brush coating onto a copper substrate. The described liquid phase infiltration technique can be used to fabricate thin films of zirconium oxide and potentially extended to other elements. This study describes a detailed analysis of the material infiltrations into the polymer brush film. XPS and FTIR analysis of the grafted brush, and infiltrated samples indicate the inclusion of the zirconium ions into the polymer film. A reductive hydrogen plasma treatment was carried out to eliminate polymer brush and reduce the formed CuO_x layer. TEM and EDX mapping of the hydrogen plasma treated sample shows that the Zirconium oxide is uniformly formed across the substrate, demonstrating that the technique has a great potential for integration into semiconductor processing and corrosion technology.

5.6 References:

(1) Mackus, A. J. M.; Merkx, M. J. M.; Kessels, W. M. M. From the Bottom-Up: Toward Area-Selective Atomic Layer Deposition with High Selectivity †. *Chem. Mater.* **2019**, *31* (1), 2–12. https://doi.org/10.1021/acs.chemmater.8b03454.

(2) Mackus, A. J. M.; Bol, A. A.; Kessels, W. M. M. The Use of Atomic Layer Deposition in Advanced Nanopatterning. *Nanoscale* **2014**, *6* (19), 10941–10960. https://doi.org/10.1039/C4NR01954G.

(3) Cummins, C.; Bell, A. P.; Morris, M. A. Creating Active Device Materials for Nanoelectronics Using Block Copolymer Lithography. *Nanomaterials* **2017**, *7* (10). https://doi.org/10.3390/nano7100304.

(4) Cummins, C.; Morris, M. A. Using Block Copolymers as Infiltration Sites for Development of Future Nanoelectronic Devices: Achievements, Barriers, and Opportunities. *Microelectron. Eng.* **2018**, *195*, 74–85. https://doi.org/10.1016/J.MEE.2018.04.005.

(5) Lundy, R.; Cummins, C.; Flynn, S. P.; Ghosh, A.; Collins, M. N.; Dalton, E.; Kelleher, S. M.; Daniels, S.; Morris, M.; Enright, R. Block Copolymer Enabled Nanoporous Membrane Fabrication for High Heat Flux Dissipation Applications. In *Poster Presentation at EMRS Spring Meeting; Lille, France*; 2015.

(6) Cheng, J. Y.; Ross, C. A.; Thomas, E. L.; Smith, H. I.; Vancso, G. J. Fabrication of Nanostructures with Long-Range Order Using Block Copolymer Lithography. *Appl. Phys. Lett.* **2002**, *81* (19), 3657–3659. https://doi.org/10.1063/1.1519356.

(7) Jeong, S. J.; Kim, J. Y.; Kim, B. H.; Moon, H. S.; Kim, S. O. Directed Self-Assembly of Block Copolymers for next Generation Nanolithography. *Mater. Today* **2013**, *16* (12), 468–476. https://doi.org/10.1016/j.mattod.2013.11.002.

(8) Cummins, C.; Borah, D.; Rasappa, S.; Chaudhari, a; Ghoshal, T.; O'Driscoll, B. M. D.; Carolan, P.; Petkov, N.; Holmes, J. D.; Morris, M. a. Self-Assembly of Polystyrene-Block-Poly(4-Vinylpyridine) Block Copolymer on Molecularly Functionalized Silicon Substrates: Fabrication of Inorganic Nanostructured Etchmask for Lithographic Use. *J. Mater. Chem. C* **2013**, *1* (47), 7941–7951. https://doi.org/Doi 10.1039/C3tc31498g.

(9) Ross, C. a; Berggren, K. K.; Cheng, J. Y.; Jung, Y. S.; Chang, J.-B. Three-Dimensional Nanofabrication by Block Copolymer Self-Assembly. *Adv. Mater.* **2014**, *26* (25), 4386–4396. https://doi.org/10.1002/adma.201400386.

(10) Giraud, E. C.; Mokarian-Tabari, P.; Toolan, D. T. W.; Arnold, T.; Smith, A. J.; Howse, J. R.; Topham, P. D.; Morris, M. A. Highly Ordered Titanium Dioxide Nanostructures via a Simple

One-Step Vapor-Inclusion Method in Block Copolymer Films. *ACS Appl. Nano Mater.* **2018**, *1* (7), 3426–3434. https://doi.org/10.1021/acsanm.8b00632.

(11) Arras, M. M. L.; He, B.; Jandt, K. D. High Molar Mass Amphiphilic Block Copolymer Enables Alignment and Dispersion of Unfunctionalized Carbon Nanotubes in Melt-Drawn Thin-Films. *Polymer (Guildf).* **2017**, *127*, 15–27. https://doi.org/10.1016/j.polymer.2017.08.030.

(12) Lundy, R.; Flynn, S. P.; Cummins, C.; Kelleher, S. M.; Collins, M. N.; Dalton, E.; Daniels, S.; Morris, M. A.; Enright, R. Controlled Solvent Vapor Annealing of a High χ Block Copolymer Thin Film. *Phys. Chem. Chem. Phys.* **2017**, *19* (4), 2805–2815. https://doi.org/10.1039/C6CP07633E.

(13) Vos, M. F. J.; Chopra, S. N.; Verheijen, M. A.; Ekerdt, J. G.; Agarwal, S.; Kessels, W. M. M.; Mackus, A. J. M. Area-Selective Deposition of Ruthenium by Combining Atomic Layer Deposition and Selective Etching. *Chem. Mater.* **2019**, *31*, 3878–3882. https://doi.org/10.1021/acs.chemmater.9b00193.

(14) Stevens, E.; Tomczak, Y.; Chan, B. T.; Altamirano Sanchez, E.; Parsons, G. N.; Delabie, A. Area-Selective Atomic Layer Deposition of TiN, TiO_2, and HfO_2 on Silicon Nitride with Inhibition on Amorphous Carbon. *Chem. Mater.* **2018**, *30* (10), 3223–3232. https://doi.org/10.1021/acs.chemmater.8b00017.

(15) Mameli, A.; Karasulu, B.; Verheijen, M. A.; Barcones, B.; Macco, B.; Mackus, A. J. M.; Kessels, W. M. M. E.; Roozeboom, F. Area-Selective Atomic Layer Deposition of ZnO by Area Activation Using Electron Beam-Induced Deposition. *Chem. Mater.* **2019**, *31* (4), 1250–1257. https://doi.org/10.1021/acs.chemmater.8b03165.

(16) Minaye Hashemi, F. S.; Birchansky, B. R.; Bent, S. F. Selective Deposition of Dielectrics: Limits and Advantages of Alkanethiol Blocking Agents on Metal-Dielectric Patterns. *ACS Appl. Mater. Interfaces* **2016**, *8* (48), 33264–33272. https://doi.org/10.1021/acsami.6b09960.

(17) Chen, R.; Li, Y. C.; Cai, J. M.; Cao, K.; Lee, H. B. R. Atomic Level Deposition to Extend Moore's Law and Beyond. *Int. J. Extrem. Manuf.* **2020**, *2* (2). https://doi.org/10.1088/2631-7990/ab83e0.

(18) Sadat, F.; Hashemi, M.; Prasittichai, C.; Bent, S. F.; Science, M.; Engineering, C.; Present, U. S. Self-Correcting Process for High Quality Patterning by Atomic Layer Deposition. **2015**, No. 9, 8710–8717. https://doi.org/10.1021/acsnano.5b03125.

(19) Parsons, G. N.; Clark, R. D. Area Selective Deposition : Fundamentals , Applications and Future Outlook North Carolina State University , Raleigh NC. **2020**, No. May, 0–93. https://doi.org/10.1021/acs.chemmater.0c00722.

(20) Kim, W. H.; Minaye Hashemi, F. S.; Mackus, A. J. M.; Singh, J.; Kim, Y.; Bobb-Semple, D.; Fan, Y.; Kaufman-Osborn, T.; Godet, L.; Bent, S. F. A Process for Topographically Selective Deposition on 3D Nanostructures by Ion Implantation. *ACS Nano* **2016**, *10* (4), 4451–4458. https://doi.org/10.1021/acsnano.6b00094.

(21) Fang, M.; Ho, J. C. Area-Selective Atomic Layer. *ACS Nano* **2015**. https://doi.org/10.1021/acsnano.5b05249.

(22) Singh, J. A.; Thissen, N. F. W.; Kim, W.-H.; Johnson, H.; Kessels, W. (Erwin) M. .; Bol, A. A.; Bent, S. F.; Mackus, A. J. M. Area-Selective Atomic Layer Deposition of Metal Oxides on Noble Metals through Catalytic Oxygen Activation. *Chem. Mater.* **2017**, acs.chemmater.7b03818. https://doi.org/10.1021/acs.chemmater.7b03818.

(23) Sadat, F.; Hashemi, M.; Birchansky, B. R.; Bent, S. F. Selective Deposition of Dielectrics: Limits and Advantages of Alkanethiol Blocking Agents on Metal − Dielectric Patterns. **2016**. https://doi.org/10.1021/acsami.6b09960.

(24) Chen, R.; Kim, H.; McIntyre, P. C.; Bent, S. F. Self-Assembled Monolayer Resist for Atomic Layer Deposition of HfO2 and ZrO2 High-κ Gate Dielectrics. *Appl. Phys. Lett.* **2004**, *84* (20), 4017–4019. https://doi.org/10.1063/1.1751211.

(25) Vericat, C.; Vela, M. E.; Benitez, G.; Carro, P.; Salvarezza, R. C. Self-Assembled Monolayers of Thiols and Dithiols on Gold: New Challenges for a Well-Known System. **2010**. https://doi.org/10.1039/b907301a.

(26) Färm, E.; Kemell, M.; Ritala, M.; Leskelä, M. Selective-Area Atomic Layer Deposition Using Poly(Methyl Methacrylate) Films as Mask Layers. *J. Phys. Chem. C* **2008**, *112* (40), 15791–15795. https://doi.org/10.1021/jp803872s.

(27) Zhang, C.; Vehkamäki, M.; Pietikäinen, M.; Leskelä, M.; Ritala, M. Area-Selective Molecular Layer Deposition of Polyimide on Cu through Cu-Catalyzed Formation of a Crystalline Interchain Polyimide. *Chem. Mater.* **2020**, *32* (12), 5073–5083. https://doi.org/10.1021/acs.chemmater.0c00898.

(28) Forouzmehr, M.; Zambou, S.; Lahtonen, K.; Honkanen, M.; Nazmul Anam, R. M.; Ruhanen, A.; Rokaya, C.; Lupo, D.; Berger, P. R. Selective Atomic Layer Deposition on Flexible Polymeric Substrates Employing a Polyimide Adhesive as a Physical Mask. *J. Vac. Sci. Technol. A* **2021**, *39* (1), 012405. https://doi.org/10.1116/6.0000566.

(29) Färm, E.; Kemell, M.; Santala, E.; Ritala, M.; Leskelä, M. Selective-Area Atomic Layer Deposition Using Poly(Vinyl Pyrrolidone) as a Passivation Layer. *J. Electrochem. Soc.* **2010**, *157* (1), K10. https://doi.org/10.1149/1.3250936.

(30) Wojtecki, R.; Ma, J.; Cordova, I.; Arellano, N.; Lionti, K.; Magbitang, T.; Pattison, T. G.;

Zhao, X.; Delenia, E.; Lanzillo, N.; Hess, A. E.; Nathel, N. F.; Bui, H.; Rettner, C.; Wallraff, G.; Naulleau, P. Additive Lithography−organic Monolayer Patterning Coupled with an Area-Selective Deposition. *ACS Appl. Mater. Interfaces* **2021**, *13* (7), 9081–9090. https://doi.org/10.1021/acsami.0c16817.

(31) Sinha, A.; Hess, D. W.; Henderson, C. L. A Top Surface Imaging Method Using Area Selective ALD on Chemically Amplified Polymer Photoresist Films. *Electrochem. Solid-State Lett.* **2006**, *9* (11). https://doi.org/10.1149/1.2335939.

(32) Chen, H. L.; Chu, Y. H.; Kuo, C. I.; Liu, F. K.; Ko, F. H.; Chu, T. C. Rapidly Selective Growth of Nanoparticles by Electron-Beam and Optical Lithographies with Chemically Amplified Resists. *Electrochem. Solid-State Lett.* **2005**, *8* (2), 54–57. https://doi.org/10.1149/1.1845051.

(33) Xiao, Z.; Kisslinger, K.; Chance, S.; Banks, S. Comparison of Hafnium Dioxide and Zirconium Dioxide Grown by Plasma-Enhanced Atomic Layer Deposition for the Application of Electronic Materials. *Crystals* **2020**, *10* (2), 1–12. https://doi.org/10.3390/cryst10020136.

(34) Lundy, R.; Yadav, P.; Selkirk, A.; Mullen, E.; Ghoshal, T.; Cummins, C.; Morris, M. A. Optimizing Polymer Brush Coverage to Develop Highly Coherent Sub-5nm Oxide Films by Ion Inclusion. *Chem. Mater.* **2019**. https://doi.org/10.1021/acs.chemmater.9b02856.

(35) Lundy, R.; Yadav, P.; Prochukhan, N.; Giraud, E. C.; O'Mahony, T. F.; Selkirk, A.; Mullen, E.; Conway, J.; Turner, M.; Daniels, S.; Mani-Gonzalez, P. G.; Snelgrove, M.; Bogan, J.; McFeely, C.; O'Connor, R.; McGlynn, E.; Hughes, G.; Cummins, C.; Morris, M. A. Precise Definition of a "Monolayer Point" in Polymer Brush Films for Fabricating Highly Coherent TiO2Thin Films by Vapor-Phase Infiltration. *Langmuir* **2020**, *36* (41), 12394–12402. https://doi.org/10.1021/acs.langmuir.0c02512.

(36) Cummins, C.; Weingärtner, T.; Morris, M. A. Enabling Large-Area Selective Deposition on Metal-Dielectric Patterns Using Polymer Brush Deactivation. *J. Phys. Chem. C* **2018**, *122* (26), 14698–14705. https://doi.org/10.1021/acs.jpcc.8b04092.

(37) Cummins, C.; Shaw, M. T.; Morris, M. A. Area Selective Polymer Brush Deposition. **2017**, *1700252*, 1–6. https://doi.org/10.1002/marc.201700252.

(38) Snelgrove, M.; Zehe, C.; Lundy, R.; Yadav, P.; Rueff, J.-P.; O'Connor, R.; Bogan, J.; Hughes, G.; McGlynn, E.; Morris, M.; Mani-Gonzalez, P. G. Surface Characterization of Poly-2-Vinylpyridine—A Polymer for Area Selective Deposition Techniques. *J. Vac. Sci. Technol. A* **2019**, *37* (5), 050601. https://doi.org/10.1116/1.5115769.

(39) Mani-Gonzalez, P. G.; Snelgrove, M.; Rueff, J.-P.; Lundy, R.; Yadav, P.; Bogan, J.; O'Connor, R.; Morris, M.; Hughes, G. Analysis of Al and Cu Salt Infiltration into a Poly 2-

Vinylpyridine (P2vP) Polymer Layer for Semiconductor Device Patterning Applications. *J. Phys. D. Appl. Phys.* **2019**, 1–20. https://doi.org/10.1088/1361-6463/ab60e8.

(40) Snelgrove, M.; McFeely, C.; Shiel, K.; Hughes, G.; Yadav, P.; Weiland, C.; Woicik, J. C.; Mani-Gonzalez, P. G.; Lundy, R.; Morris, M. A.; McGlynn, E.; O'Connor, R. Analysing Trimethylaluminum Infiltration into Polymer Brushes Using a Scalable Area Selective Vapor Phase Process. *Materials Advances*. 2021, pp 769–781. https://doi.org/10.1039/d0ma00928h.

(41) Akiyoshi, K.; Kameyama, T.; Yamamoto, T.; Kuwabata, S.; Tatsuma, T.; Torimoto, T. Controlling the Oxidation State of Molybdenum Oxide Nanoparticles Prepared by Ionic Liquid/Metal Sputtering to Enhance Plasmon-Induced Charge Separation †. **2020**. https://doi.org/10.1039/d0ra05165a.

(42) Clark, R. D. Emerging Applications for High K Materials in VLSI Technology. *Materials (Basel).* **2014**, *7* (4), 2913–2944. https://doi.org/10.3390/ma7042913.

(43) Minaye Hashemi, F. S.; Prasittichai, C.; Bent, S. F. Self-Correcting Process for High Quality Patterning by Atomic Layer Deposition. *ACS Nano* **2015**, *9* (9), 8710–8717. https://doi.org/10.1021/acsnano.5b03125.

(44) Barr, T. L.; Seal, S. Nature of the Use of Adventitious Carbon as a Binding Energy Standard. *J. Vac. Sci. Technol. A Vacuum, Surfaces, Film.* **1995**, *13* (3), 1239–1246. https://doi.org/10.1116/1.579868.

(45) Hoppe, E. W.; Seifert, A.; Aalseth, C. E.; Bachelor, P. P.; Day, A. R.; Edwards, D. J.; Hossbach, T. W.; Litke, K. E.; McIntyre, J. I.; Miley, H. S.; Schulte, S. M.; Smart, J. E.; Warren, G. A. Cleaning and Passivation of Copper Surfaces to Remove Surface Radioactivity and Prevent Oxide Formation. *Nucl. Instruments Methods Phys. Res. Sect. A Accel. Spectrometers, Detect. Assoc. Equip.* **2007**, *579* (1), 486–489. https://doi.org/10.1016/j.nima.2007.04.101.

(46) Cassie, A. B. D.; Baxter, S. Wettability of Porous Surfaces. *Trans. Faraday Soc.* **1944**, *40*, 546–551.

(47) Lundy, R.; Byrne, C.; Bogan, J.; Nolan, K.; Collins, M. N.; Dalton, E.; Enright, R. Exploring the Role of Adsorption and Surface State on the Hydrophobicity of Rare Earth Oxides. *ACS Appl. Mater. Interfaces* **2017**, *9* (15), 13751–13760. https://doi.org/10.1021/acsami.7b01515.

(48) Mani-Gonzalez, P. G.; McFeely, C.; Snelgrove, M.; Shiel, K.; Hernandez Marquez, J. A.; O'Connor, R. Titanium Infiltration into Ultrathin PMMA Brushes. *J. Vac. Sci. Technol. A* **2021**, *39* (4), 040403. https://doi.org/10.1116/6.0001061.

(49) Beamson, G.; Bunn, A.; Briggs, D. High-resolution Monochromated XPS of Poly(Methyl Methacrylate) Thin Films on a Conducting Substrate. *Surf. Interface Anal.* **1991**, *17* (2), 105–

115. https://doi.org/10.1002/sia.740170206.

(50) Ton-That, C.; Shard, A. G.; Daley, R.; Bradley, R. H. Effects of Annealing on the Surface Composition and Morphology of PS/PMMA Blend. **2000**. https://doi.org/10.1021/ma000792h.

(51) Cara, E.; Murataj, I.; Milano, G.; De Leo, N.; Boarino, L.; Lupi, F. F. Recent Advances in Sequential Infiltration Synthesis (Sis) of Block Copolymers (Bcps). *Nanomaterials* **2021**, *11* (4), 1–26. https://doi.org/10.3390/nano11040994.

(52) Poulston, S.; Parlett, P. M.; Stone, P.; Bowker, M. Surface Oxidation and Reduction of CuO and Cu2O Studied Using XPS and XAES. *Surf. Interface Anal.* **1996**, *24* (12), 811–820. https://doi.org/10.1002/(SICI)1096-9918(199611)24:12<811::AID-SIA191>3.0.CO;2-Z.

(53) Snelgrove, M.; Mani-Gonzalez, P. G.; Bogan, J.; Lundy, R.; Rueff, J. P.; Hughes, G.; Yadav, P.; McGlynn, E.; Morris, M.; O'Connor, R. Hard X-Ray Photoelectron Spectroscopy Study of Copper Formation by Metal Salt Inclusion in a Polymer Film. *J. Phys. D. Appl. Phys.* **2019**, *52* (43). https://doi.org/10.1088/1361-6463/ab35b2.

(54) Wiame, H.; Centeno, M. A.; Picard, S.; Bastians, P.; Grange, P. Thermal Oxidation under Oxygen of Zirconium Nitride Studied by XPS, DRIFTS, TG-MS. *J. Eur. Ceram. Soc.* **1998**, *18* (9), 1293–1299. https://doi.org/10.1016/s0955-2219(98)00056-9.

(55) Morant, C.; Sanz, J. M.; Galán, L.; Soriano, L.; Rueda, F. An XPS Study of the Interaction of Oxygen with Zirconium. *Surf. Sci.* **1989**, *218* (2–3), 331–345. https://doi.org/10.1016/0039-6028(89)90156-8.

(56) Wong, P. C.; Li, Y. S.; Zhou, M. Y.; Mitchell, K. A. R. XPS Investigations of the Interactions of Hydrogen with Thin Films of Zirconium Oxide I. Hydrogen Treatments on a 10 Å Thick Film. *Appl. Surf. Sci.* **1995**, *89* (3), 255–261. https://doi.org/10.1016/0169-4332(95)00031-3.

(57) Muneshwar, T.; Cadien, K. Comparing XPS on Bare and Capped ZrN Films Grown by Plasma Enhanced ALD: Effect of Ambient Oxidation. *Applied Surface Science*. 2018, pp 367–376. https://doi.org/10.1016/j.apsusc.2017.11.104.

(58) Wang, Y. M.; Li, Y. S.; Wong, P. C.; Mitchell, K. A. R. XPS Studies of the Stability and Reactivity of Thin Films of Oxidized Zirconium. *Appl. Surf. Sci.* **1993**, *72* (3), 237–244. https://doi.org/10.1016/0169-4332(93)90192-E.

(59) Lackner, P.; Zou, Z.; Mayr, S.; Diebold, U.; Schmid, M. Using Photoelectron Spectroscopy to Observe Oxygen Spillover to Zirconia. *Physical Chemistry Chemical Physics*. 2019, pp 17613–17620. https://doi.org/10.1039/c9cp03322j.

(60) Espinós, J. P.; Morales, J.; Barranco, A.; Caballero, A.; Holgado, J. P.; González-Elipe, A. R.

Interface Effects for Cu, CuO, and Cu2O Deposited on SiO2 and ZrO2. XPS Determination of the Valence State of Copper in Cu/SiO2 and Cu/ZrO2 Catalysts. *J. Phys. Chem. B* **2002**, *106* (27), 6921–6929. https://doi.org/10.1021/jp014618m.

(61) Ivanova, T. M.; Maslakov, K. I.; Sidorov, A. A.; Kiskin, M. A.; Linko, R. V.; Savilov, S. V.; Lunin, V. V.; Eremenko, I. L. XPS Detection of Unusual Cu(II) to Cu(I) Transition on the Surface of Complexes with Redox-Active Ligands. *Journal of Electron Spectroscopy and Related Phenomena*. 2020. https://doi.org/10.1016/j.elspec.2019.06.010.

(62) Biesinger, M. C. Advanced Analysis of Copper X-Ray Photoelectron Spectra. *Surf. Interface Anal.* **2017**, *49* (13), 1325–1334. https://doi.org/10.1002/sia.6239.

(63) Wang, N.; Wu, X.; Liu, C. S. Abnormal Segmental Dynamics of Poly(Methyl Methacrylate)/Poly(Vinylidene Fluoride) Blends by Mechanical Spectroscopy. *AIP Adv.* **2019**, *9* (1). https://doi.org/10.1063/1.5081758.

(64) Arul, K. T.; Ramanjaneyulu, M.; Ramachandra Rao, M. S. Energy Harvesting of PZT/PMMA Composite Flexible Films. *Curr. Appl. Phys.* **2019**, *19* (4), 375–380. https://doi.org/10.1016/j.cap.2019.01.003.

(65) Tu, J. S.; Perevedentseva, E.; Chung, P. H.; Cheng, C. L. Size-Dependent Surface CO Stretching Frequency Investigations on Nanodiamond Particles. *Journal of Chemical Physics*. 2006. https://doi.org/10.1063/1.2370880.

(66) Ajibade, P. A.; Mbese, J. Z. Synthesis and Characterization of Metal Sulfides Nanoparticles/Poly(Methyl Methacrylate) Nanocomposites. *Int. J. Polym. Sci.* **2014**, *2014*. https://doi.org/10.1155/2014/752394.

5.7 Appendix

Polymethyl methacrylate template assisted deposition of uniform zirconium oxide films on copper substrate through liquid phase for area selective deposition application.

5.7.1 Substrate cleaning and sample activation:

Interfacial Cu_2O, and CuO oxide layer is reduced to metallic copper by citric acid treatment. Few minutes of citric acid cleaning is sufficient for ashing oxide layer and removing the impurity from surface. After the citric acid treatment, thee samples were thoroughly washed in water to get rid of residual acid. Subsequent polymer brush deposition and annealing process yield homogeneous polymer film.

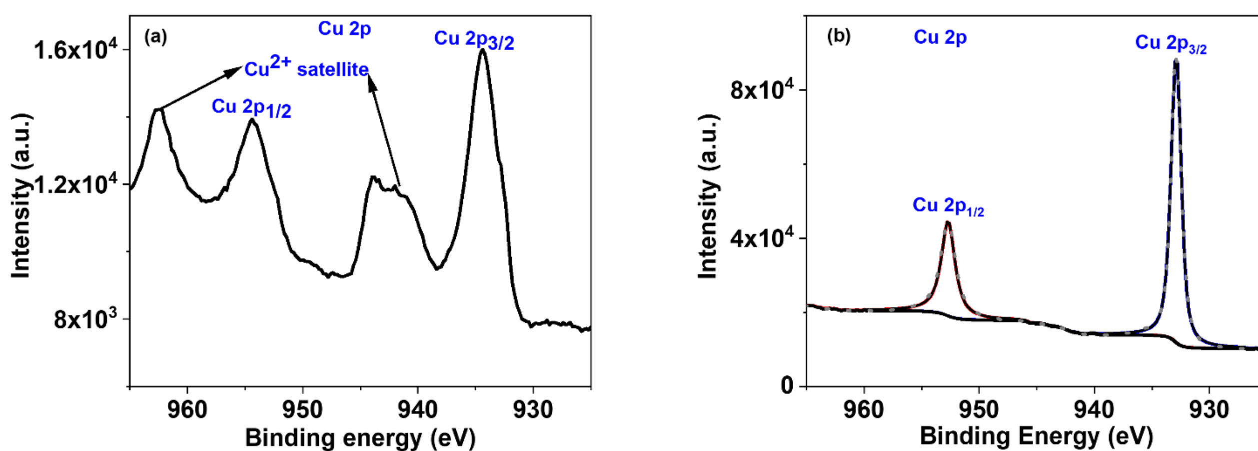

Figure S5.7.1: high resolution XPS spectra of Cu 2p of (a) blanket copper substrate and (b) post-citric acid treated sample (5 min).

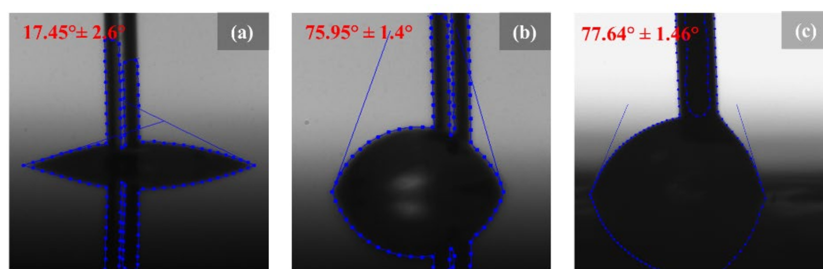

Figure S5.7.2: Advancing water contact angle of the a) citric acid treated substrate, b) PMMA brush coated substrate, and c) pressed homopolymer pellet.

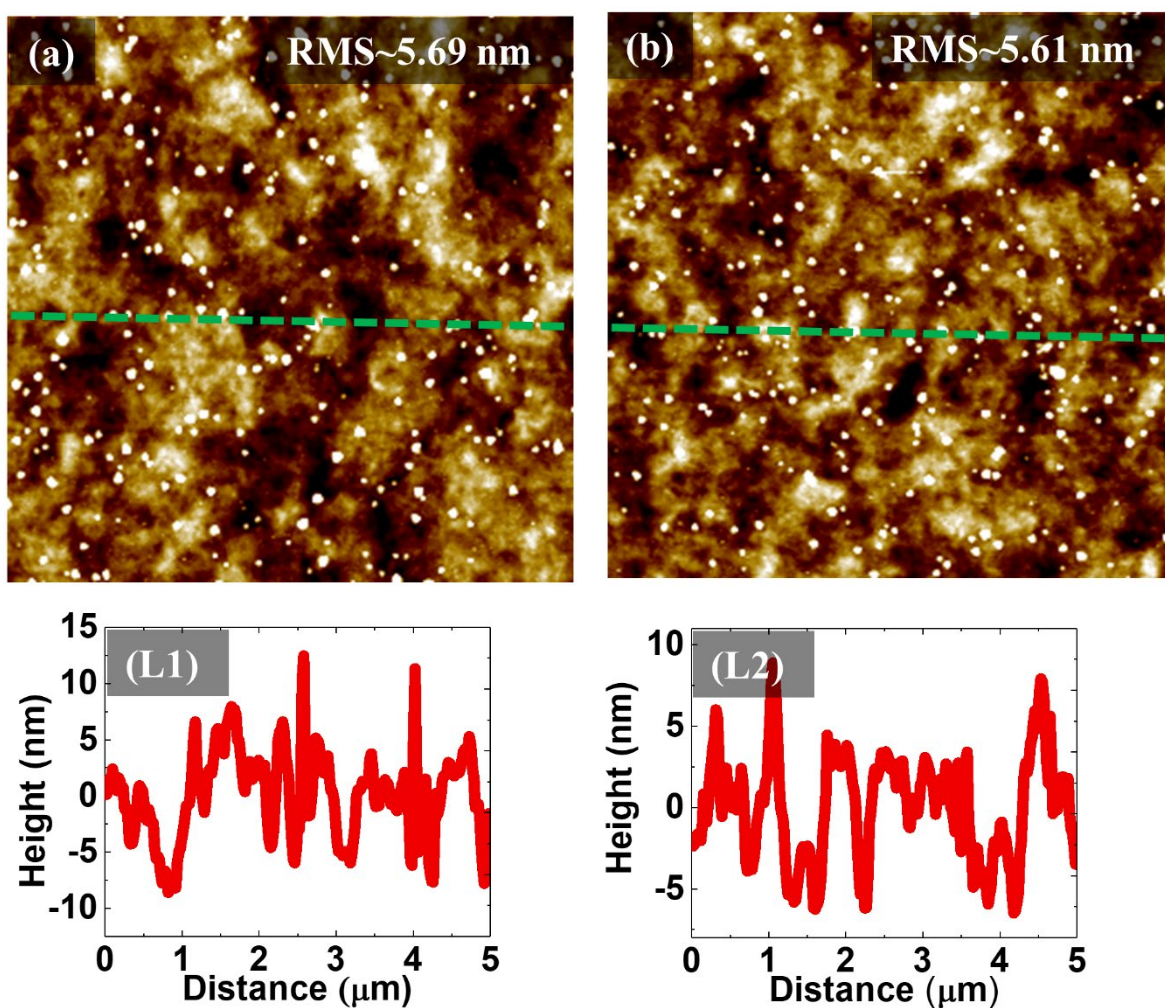

Figure S5.7.3: AFM images of the copper substrate (a) as received Cu sample and corresponding line images at L1 (b) toluene washed substrate and respective line image at L2.

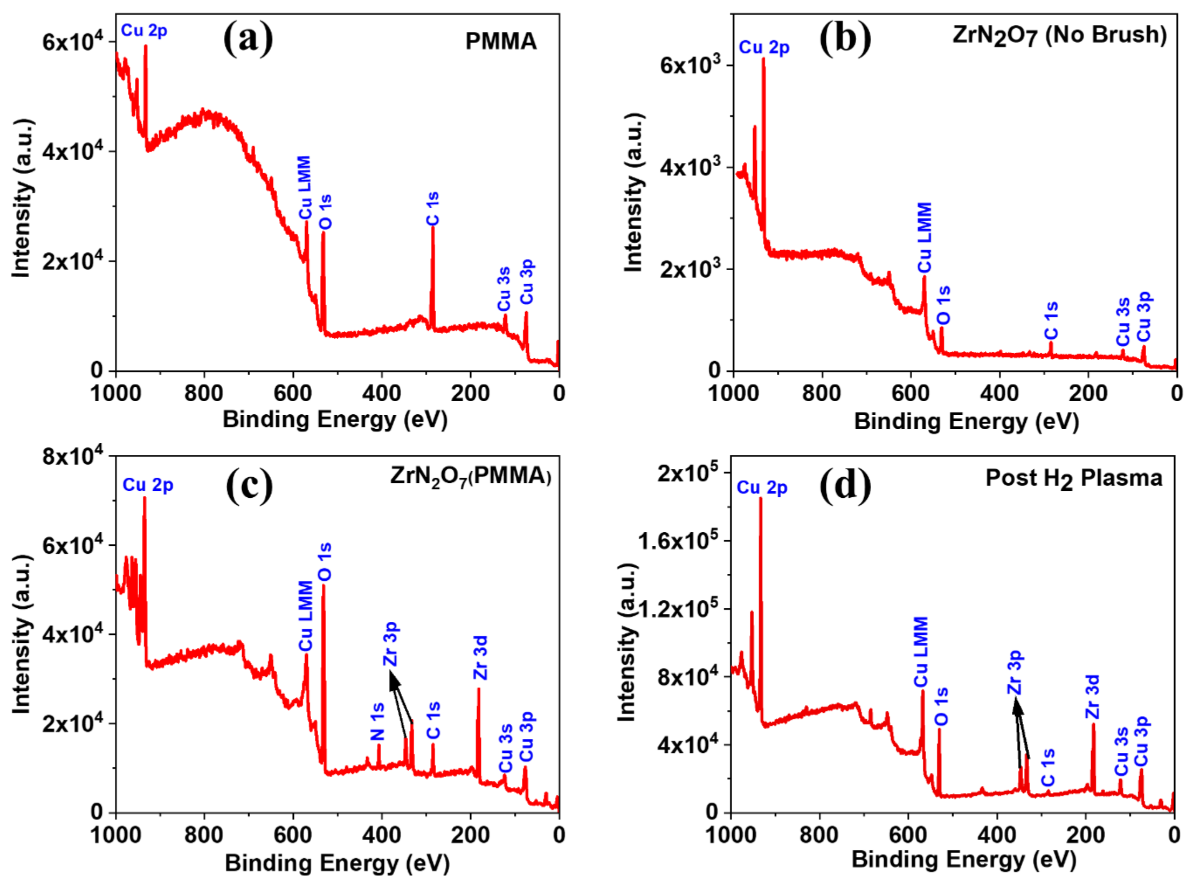

Figure S5.7.4: Wide energy XPS survey spectrum of (a) grafted PMMA-SH brush on the copper substrate (b) infiltrated zirconium oxynitrated with no brush (c) spin deposited zirconium oxynitrate on PMMA brush and (c) post reductive H_2 plasma annealed substrate.

Table S5.7.1: Elements and their respective binding energy

Binding Energy (eV)	**element**
29.7	Zr 4p
74.1	Cu 3p
121.6	Cu 3s
183	Zr 3d
284.8	C 1s
333	Zr $3p_{3/2}$
346	Zr $3p_{1/2}$
407	N 1s
431	Zr 3s
531.8	O 1s
566.8	Cu (LMM)
931.6	Cu $2p_{3/2}$
951	Cu $2p_{1/2}$

Table S5.7.2 Elements and atomic wt.%

At%	C 1s	O 1s	N 1s	Zr 3d	Cu 2p
PMMA	69.13	28.85	--	--	2.02
ZrN_2O_7 (No Brush))	46.84	33.95	0.4	0.6	18.21
ZrN_2O_7 (PMMA)	22.23	60.31	2.10	5.63	9.73
Post H_2 plasma	12.00	51.69	--	19.04	17.27

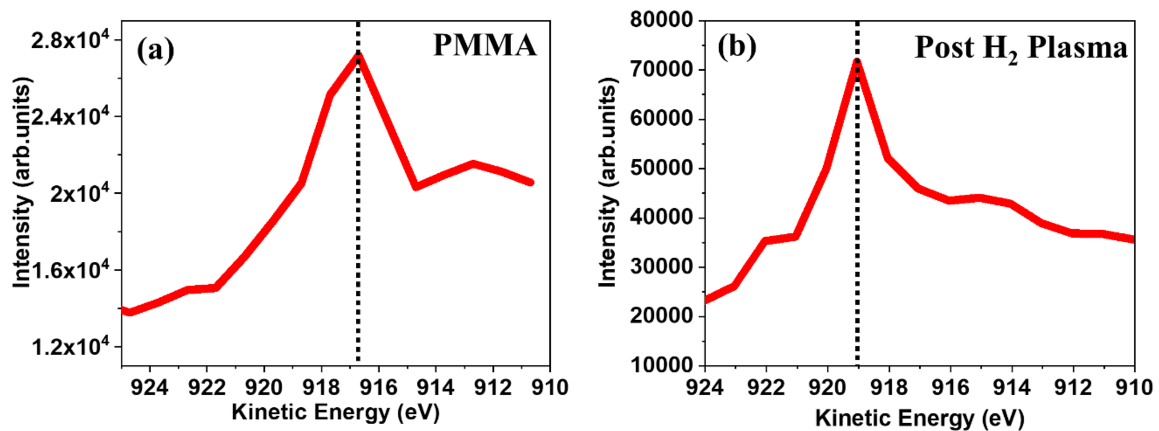

Figure S5.7.5: Cu (LMM) spectra extracted from survey spectrum for (a) PMMA brush grafted (b) post H_2 plasma sample

Chapter 6. Conclusions and future work

6.1 Conclusions:

Shrinking device dimensions and on chip complexity demand precise control of nanoscale patterning and development of new methods for material deposition. Several methods have been demonstrated to increase the device packing density and thereby enhance the performance and scalability of electronic devices while providing a route to reduced processing time.[1] Conventional patterning techniques (photolithography) have reduced the size of electronic devices from micrometers to nanometers (~ 10 nm). A further reduction in devise feature size has however introduced new fabrication challenges in terms of misalignment of features, line edge roughness etc.[2] Bottom up approaches such as block copolymer lithography and ASD has shown promise in addressing these challenges.[3] ASD techniques, in particular, have proven successful in developing consistent selective deposition of materials on substrates.[4,5]

This research concentrated on exploring the potential of a new methodology for fabricating uniform sub-5 nm metal oxide (Al_2O_3, TiO_2, RuO_2, HfO_2 and ZrO_2) coatings on substrates such as SiO_2, Cu and topographically patterned Si_3N_4. We developed a polymer brush grafting technique with potential for industrial integration. The polymer brush template allowed the infiltration of ethanolic solutions of metal salts. Subsequent oxygen plasma or UV ozone treatment enabled a simultaneous oxidation of the metal salt and the removal of the polymer brush template to produce robust homogeneous metal oxide films.[6] The potential of the polymer brush technique to develop similar uniform coatings on topographically patterned substrates as well as Cu substrates has been investigated.

Hydroxy terminated poly-(2-vinyl pyridine), poly-(4-vinyl pyridine) and poly-(methyl methacrylate) have been used as polymer brush materials on silicon substrates. The hydroxy end group of the polymer brushes reacts with the hydroxy group of the plasma

treated silicon substrate. Upon thermal annealing the as deposited polymer chains uncoil and successfully locate the surface to overcome the thermodynamic reaction barrier to condensation.[7] For Cu substrates, the high affinity of the thiol and amino groups for metal ions has been exploited to form defect-free coatings. The thiol and amino terminated polymer brush molecules formed co-ordinate bonds with the metal surface by donating loan pair of the electron. Different molecular weights of polymer brushes were then used to develop coatings/templates of varied thickness. The study showed that by selecting the molecular weight of the polymer brush molecule, the thickness of the metal oxide coating can be tuned. We have shown that a careful selection of the polymer brush can produce uniform metal oxide films of thickness as low as 2 nm. A synergistic effect of solvent assisted swelling and functional chemical group assisted metal ion linkage facilitated the efficient material infiltration yielding uniform deposits.

In chapter 2 and 3, we investigated the usefulness of P2VP-OH molecules for forming monolayer coverage on silicon substrates. A detailed investigation on the effects of polymer end group density, solution concentration, speed of spin coating, annealing temperature and the time of grafting on the final film formation has been carried out. We observed that low molecular weight of P2VP-OH (up to 6 $kgmol^{-1}$) at concentrations between 0.2 wt. % to 0.8 wt. % yield highly ordered monolayer coverage.[8] This high coverage P2VP brush were then used as a template to produce large-scale high quality inorganic films. Specifically, Al_2O_3 films have been effectively deposited using P2VP/P4VP templates. The selective metal inclusion facilitated by the pyridine moiety of the poly (vinyl pyridine) brush (P2VP/P4VP) enabled the formation of a highly uniform Al_2O_3 layer. The significant role played by solvent swelling in including the metal ions into the polymer brush is demonstrated using high-resolution TEM cross section images.

The examination of data/results showed the defining role played by the polymer brush templates in forming uniform metal oxide films. The data highlights that very high

coverage reactive polymer brush films with uniform thickness can be prepared in seconds when P2VP molecules are used. While P2VP is an ideal system for small ions, it would hinder the infiltration of large ions such as gold due to steric hindrance resulting from the proximity of pyridinic nitrogen with the polymer chain. A detailed investigation showed that, in contrast to P2VP, P4VP with a highly accessible geometry is a more ideal polymer brush template for binding large radii ions via the nitrogen atom.

The polymer brush film assisted metal oxide deposition can be used to produce large area films is a promising technique that may be adapted to dip or spray coating for a variety of technologies such as glass coating technology, digital displays, energy harvesting screens, and stimuli responsive surface. While the methodology is promising for deposition of metal oxide films, integrating this technique with reductive processes such as hydrogen plasma to reduce the metal films will enable extension to other applications such as catalysis.

In chapter 3, the P2VP film template was used to deposit high quality ultrathin titania films. For this, a simple apparatus enabling the vapour phase infiltration of the titanium (IV) isopropoxide into the monolayer P2VP film was designed and demonstrated. P2VP-OH brush was exposed to TTIP vapour phase precursor in the apparatus and the conversion to TiO_2 is carried out via UV/Ozone surface treatment. High coverage, pin hole-free, uniform TiO_2 films with varied thickness could be prepared by adjusting the molecular weight of P2VP. The morphology of the films were observed by SEM and TEM cross section images and the formation of TiO_2 was evidenced by XPS analyses.

Although P2VP brushes allowed the incorporation of a sufficient quantity of TTIP precursor for thin film formation, developing thicker films (> 5 nm) with P2VP was found to be challenging. Above its critical agglomeration concentration (CAC), i.e. 2 wt. % of P2VP, the strong intermolecular forces brings the molecules together and instead of homogeneous films, islands of agglomerates were formed.[6] Therefore, less sterically

hindered brush molecules such as PMMA, P4VP may be more useful for fabricating thicker inorganic films or by developing a solvent swelling technique to expand the polymer template during TTIP exposure. Further, we have shown that PS brushes have the potential to inactivate/passivate the substrate surface for material infiltration. Chapter 3 also discusses the implications of using material blockers (PS) and brushes (P2VP, P4VP and PMMA) together to selectively block/deposit materials of choice.

In chapter 4, we described ultrathin conformal coating of high-k dielectric materials (HfO_2 and ZrO_2) on topographically patterned substrates with silicon nitride capping layer. The results presented in this chapter indicate that polymer brushes with reactive groups can be used to develop thin inorganic films on substrates with trenches and pitches. Comparison between P4VP and PS brushes shows that the inclusion of the material into the polymer system is facilitated via solvent-assisted swelling and diffusion of the metal ions. Ethanol has high swelling affinity for pyridine based molecular systems. The deposited ethanol/salt solutions readily swell the P4VP brush to facilitate metal ion inclusion. The ion uptake (Zr^{+4} and Hf^{+4}) capability of P4VP with the other reactive brush systems such as P2VP and PMMA was compared. P4VP had ~ 60% more uptake compared with the next reactive brush, P2VP, while PMMA had the lowest ion uptake. The results show that using the reactive P4VP molecule, a highly conformal ultrathin inorganic oxide film with uniform thickness across the trenches can be prepared in minutes. An ethonolic solution of hafnium (IV) chloride and zirconium (IV) oxynitrate was infiltrated into a high quality grafted P4VP-OH brush. Cross-section TEM analysis confirmed that the subsequent oxygen plasma treatment produced a ~5 nm thick oxide layer. In conclusion, precisely deposited polymer films on topographically patterned substrates to create thin high-k dielectric oxide films.

In Chapter 5, we demonstrated selective deposition of dielectric materials (ZrO_2) on a metal surface (Cu). We developed a liquid phase infiltration technique by selectively grafting

PMMA-SH on the metal surface to perform uniform dielectric film deposition on copper. The metal surface can be activated with a polymer brush with the reaction centre to produce a dielectric film of equal quality to that produced by ALD or CVD-derived processes.

6.2 Future work:

Several key areas of additional research are required based on the results and experimental section discussed from chapter 2 to 5. These include infiltration studies of inorganic ions of different groups using liquid and vapour phase approach. Between these, the liquid phase approach is strictly an area selective path in ASD process for developing uniform pin-hole free metal oxide films. The high-resolution N 1s XPS spectra presented in Chapter 2 show metal ion interactions with the reaction centers present within the polymer brush. In comparison to the liquid phase approach, the vapour phase infiltration process shows less interaction between the grafted polymer brush and the inorganic ions. A possible solution to enhance metal ion incorporation is to construct a specialized chamber that allows for increased precursor partial pressure along with provision to expose the polymer film with suitable solvent(s). This technique would allow the polymer brush film to be stretched vertically, maximizing metal cation infiltration.

Surface modification using the polymer brush technique has various applications in surface chemistry including biomedical implants and nanofabrication.[9,10] Polymer brush chemistry is an emerging technique that could potentially replace conventional methods of nanofabrication. This work has optimized monolayer coverage of covalently grafted polymer brushes to deposit thin films of inorganic oxide materials with precise selectivity. A follow up detailed electrical characterisation of the developed sub 5 nm films is required.

In this thesis, although we have focussed mostly on sub 5 nm metal oxides fabrication, we have shown that thicker films can also be developed by using polymers of higher molecular weight. We have demonstrated that the steric hindrance in P2VP brushes could prevent the

fabrication of thicker brush at higher concentrations or higher molecular weight. This could be due to the week intermolecular interaction or pi-pi stacking interaction in the solution. On the other hand, sterically unhindered polymers such as poly methyl methacrylate (PMMA), poly-4-vinyl pyridine (P4VP), and poly ethylene oxide (PEO) are appealing for the fabrication of thick metal oxide films.

Monolayer polymer brush films developed using these methods has the potential to prepare bimetallic layer films.[11] Metal infiltration can be used to deposit the first layer of metal onto the formed polymer brush. The oxidation step involves removing the polymer brush and oxidizing the metal oxide film, after which a layer of polymer brush can be deposited and used to prepare the second layer of metal oxide films. Finally, the reduction plasma treatment can be used to reductively remove the polymer and reduce the metal oxide. Such bimetallic films are increasingly important to enhance the catalytic activity and have various applications in the field of surface plasmon resonance and electro catalysis. Grafted polymer brush should also be tested for the infiltration of metal matrix composites. This would extend its application in the field of general engineering, automotive and aerospace.

Tailoring the polymer brush film thickness is another crucial area of research. A thicker polymer brush film could provide the precise information of metal infiltration process and their chemistries. It has been noted that a thicker metal oxide film can be created using the higher molecular weight of the polymer. Thick nano-inorganic coating has significant application in the field of food packaging and glass coating. The barrier properties of nano inorganic coatings developed on polyethylene terephthalate (PET) using various techniques are very useful in preventing the diffusion of microbes, gas etc. This barrier coating can also prevent the leaching of any flavours. The majority of barrier coatings on food packaging materials are currently made with sol-gel chemistry[12] or the CVD technique.[13] When compared to these technique, polymer brush assisted coating can provide the ability to deposit inorganic oxide uniformly and offers a chip alternative. Some

biopolymers such as poly lactic acid (PLA)[14] and polyethylene furanoate (PEF)[15] show enhanced barrier properties as compare to PET thus can be used as thin film coating on PET.

In addition to this, polymer brush could be effectively utilized to increase the strength of glass, in particular thin-long glass. The strength of very thin, ultra-tough glass has been demonstrated dramatically in the videos with the gorilla glass being one of the top brands. When chemically strengthened glass is hit by force it absorbs the force and rebounds, this is particularly more obvious for the thin long glass sheets. To some extent, the production of the ultra-tough glass is made using glass screen protection technology to hold the covid-19 vaccine. These covid-19 vials are made from chemically strengthened alumina-silicate glass. In alumina-silicate glass, a large percentage of silica is replaced by alumina, making the glass inherently strong. Mustafa et.al produced modified soda lime glass which when chemically strengthened showed four times flexural strength increase over the base glass.[16] Similarly, Carturan et.al. applied sol-gel coating on 2 mm thick soda-lime glass to increase its strength.[17] Wasylak et.al developed hot end coating by nano-particles of alumina. A coating of aluminium nano-particle approx. 10 nm thick was applied onto the external container of 300 ml beer bottles using $Al(OH)_3$ as the base materials. Some of the other research shows chemical vapour deposition of inorganic material on glass to increase its strength. Polymer can afford the coating of inorganic material onto glass using simple methods. Polymer-assisted nano-metal oxide coatings are expected to strengthen glass materials and are thus proposed for use in the future.

6.3. References:

(1) Lu, W.; Lieber, C. M. Nanoelectronics from the Bottom Up. *Nanosci. Technol. A Collect. Rev. from Nat. Journals* **2009**, 137–146. https://doi.org/10.1142/9789814287005_0014.

(2) Xu, H.; Kosma, V.; Giannelis, E.; Ober, C. K.; Sakai, K. EUV Photolithography: Resist Progress and Challenges. **2018**, *1058306* (March 2018), 2. https://doi.org/10.1117/12.2302759.

(3) Mackus, A. J. M.; Merkx, M. J. M.; Kessels, W. M. M. From the Bottom-Up: Toward Area-Selective Atomic Layer Deposition with High Selectivity †. *Chem. Mater.* **2019**, *31* (1), 2–12. https://doi.org/10.1021/acs.chemmater.8b03454.

(4) Cummins, C.; Weingärtner, T.; Morris, M. A. Enabling Large-Area Selective Deposition on Metal-Dielectric Patterns Using Polymer Brush Deactivation. *J. Phys. Chem. C* **2018**, *122* (26), 14698–14705. https://doi.org/10.1021/acs.jpcc.8b04092.

(5) Chen, R.; Kim, H.; McIntyre, P. C.; Porter, D. W.; Bent, S. F. Achieving Area-Selective Atomic Layer Deposition on Patterned Substrates by Selective Surface Modification. *Appl. Phys. Lett.* **2005**, *86* (19), 1–3. https://doi.org/10.1063/1.1922076.

(6) Lundy, R.; Yadav, P.; Prochukhan, N.; Giraud, E. C.; O'Mahony, T. F.; Selkirk, A.; Mullen, E.; Conway, J.; Turner, M.; Daniels, S.; Mani-Gonzalez, P. G.; Snelgrove, M.; Bogan, J.; McFeely, C.; O'Connor, R.; McGlynn, E.; Hughes, G.; Cummins, C.; Morris, M. A. Precise Definition of a "Monolayer Point" in Polymer Brush Films for Fabricating Highly Coherent TiO2Thin Films by Vapor-Phase Infiltration. *Langmuir* **2020**, *36* (41), 12394–12402. https://doi.org/10.1021/acs.langmuir.0c02512.

(7) Ipekci, H. H.; Arkaz, H. H.; Onses, M. S.; Hancer, M. Superhydrophobic Coatings with Improved Mechanical Robustness Based on Polymer Brushes. *Surface and Coatings Technology*. 2016, pp 162–168. https://doi.org/10.1016/j.surfcoat.2016.05.026.

(8) Lundy, R.; Yadav, P.; Selkirk, A.; Mullen, E.; Ghoshal, T.; Cummins, C.; Morris, M. A. Optimizing Polymer Brush Coverage to Develop Highly Coherent Sub-5nm Oxide Films by Ion Inclusion. *Chem. Mater.* **2019**. https://doi.org/10.1021/acs.chemmater.9b02856.

(9) Skovdal, S. M.; Jørgensen, N. P.; Petersen, E.; Jensen-Fangel, S.; Ogaki, R.; Zeng, G.; Johansen, M. I.; Wang, M.; Rohde, H.; Meyer, R. L. Ultra-Dense Polymer Brush Coating Reduces Staphylococcus Epidermidis Biofilms on Medical Implants and Improves Antibiotic Treatment Outcome. *Acta Biomater.* **2018**, *76*, 46–55. https://doi.org/10.1016/j.actbio.2018.07.002.

(10) Senaratne, W.; Andruzzi, L.; Ober, C. K. Self-Assembled Monolayers and Polymer Brushes in Biotechnology: Current Applications and Future Perspectives. *Biomacromolecules* **2005**, *6* (5), 2427–2448. https://doi.org/10.1021/bm050180a.

(11) Thomas, V.; Namdeo, M.; Mohan, Y. M.; Bajpai, S. K.; Bajpai, M. Review on Polymer, Hydrogel and Microgel Metal Nanocomposites: A Facile Nanotechnological Approach. *J. Macromol. Sci. Part A Pure Appl. Chem.* **2008**, *45* (1), 107–119. https://doi.org/10.1080/10601320701683470.

(12) Startek, K.; Marczak, J.; Lukowiak, A. Oxygen Barrier Enhancement of Polymeric Foil by Sol-Gel-Derived Hybrid Silica Layers. *Polymer (Guildf).* **2020**, *195* (April), 122437. https://doi.org/10.1016/j.polymer.2020.122437.

(13) Mitschker, F.; Steves, S.; Gebhard, M.; Rudolph, M.; Schücke, L.; Kirchheim, D.; Jaritz, M.; Brochhagen, M.; Hoppe, C.; Dahlmann, R.; Böke, M.; Benedikt, J.; Giner, I.; De los Arcos, T.; Hopmann, C.; Grundmeier, G.; Devi, A.; Awakowicz, P. Influence of PE-CVD and PE-ALD on Defect Formation in Permeation Barrier Films on PET and Correlation to Atomic Oxygen Fluence. *J. Phys. D. Appl. Phys.* **2017**, *50* (23). https://doi.org/10.1088/1361-6463/aa6e28.

(14) Apicella, A.; Scarfato, P.; Di Maio, L.; Incarnato, L. Sustainable Active PET Films by Functionalization With Antimicrobial Bio-Coatings. *Front. Mater.* **2019**, *6* (October), 1–10. https://doi.org/10.3389/fmats.2019.00243.

(15) Ayhan, Z.; Yeom, H. W.; Howard Zhang, Q.; Min, D. B. Flavor, Color, and Vitamin C Retention of Pulsed Electric Field Processed Orange Juice in Different Packaging Materials. *J. Agric. Food Chem.* **2001**, *49* (2), 669–674. https://doi.org/10.1021/jf000984b.

(16) Ünal, M.; Nasser, H.; Günöven, M.; Sökmen, I.; Tankut, A.; Turan, R. Effect of Aluminum Thickness and Etching Time of Aluminum Induced Texturing Process on Soda Lime Glass Substrates for Thin Solar Cell Applications. *Phys. Status Solidi Curr. Top. Solid State Phys.* **2015**, *12* (9–11), 1201–1205.

https://doi.org/10.1002/pssc.201510125.

(17) Carturan, G.; Khandelwal, N.; Tognana, L.; Sglavo, V. M. Strengthening of Soda-Lime-Silica Glass by Surface Treatment with Sol-Gel Silica. *J. Non. Cryst. Solids* **2007**, *353* (16–17), 1540–1545. https://doi.org/10.1016/j.jnoncrysol.2007.01.037.